

THERMO-MECHANICAL FATIGUE OF CAST  
ALUMINIUM ALLOYS FOR ENGINE APPLICATIONS  
UNDER SEVERE CONDITIONS

Christian Kliemt

Submitted for the degree of Doctor of Philosophy

Heriot-Watt University

School of Engineering and Physical Sciences

2012

The copyright in this thesis is owned by the author. Any quotation from the thesis or use of any of the information contained in it must acknowledge this thesis as the source of the quotation or information.

## **ABSTRACT**

The increase in target performance of engines and hence the loading of their structural materials has dictated the need for more information about the behaviour of cast aluminium alloys under severe conditions up to 400°C. This study was therefore conducted in order to determine how different cooling rates, different pre-treatments and different alloying elements can improve the performance of cast aluminium (Al) alloys under thermo-mechanical fatigue (TMF) loading compared to a reference alloy and condition, AlSi6Cu4-T6. An existing TMF test rig was modified to allow an investigation of temperature gradients corresponding to those prevailing in real cylinder heads.

The measured data were implemented in a Chaboche damage model and in an FEM tool in order to simulate low cycle fatigue (LCF) and TMF behaviour. These models provide a possibility to simulate LCF and TMF behaviour taking into account microstructural changes.

On metallographic examination, a dependence of crack initiation on secondary dendrite arm spacing (SDAS) and on porosity was observed. Here, a smaller SDAS and a HIP modified microstructure led to a longer lifetime. Furthermore, clusters of brittle Si particles, decohesion or intermetallic phases were also found to initiate cracks. Stage I crack behaviour was seen at low strain amplitudes, where the crack propagates along the interface between the Al matrix and the intermetallic phases. Stage II behaviour was observed for higher strain amplitudes with crack propagation taking place along intermetallic phase boundaries such as Al<sub>2</sub>Cu,  $\alpha$ -phase and  $\beta$ -phase or through pores. An increasing proportion of matrix cracks was observed for low strain amplitudes. Investigation of the decohesion behaviour revealed decohesion under high strain amplitudes and in areas with a high particle fracture volume attributable to high notch stresses. A refinement of the microstructure, particularly the particles, was found with increased Si content, associated with an increase in particle density. Following all TMF tests, an orientation of particles dependent on the loading conditions was observed, and this seemed to have had an influence on crack behaviour. A drift of stress was also found after long term high temperature exposure for strain amplitudes of 0.2%, attributed to creep.

## **ACKNOWLEDGEMENT**

There is a great number of people who account for the success of this research. A major gratitude is indebted to Peter who was a competent help in questions of scanning microscopy, data acquisition and further hardware problems. Without his persistent encouragement and support, much of this work would not have been possible.

Exceptionally, I would like to thank Professor Robert Reuben for the possibility of accomplishment of this research, his mentoring and interest on the progression of this thesis. Furthermore, I would like to thank Professor Joachim Hammer for his continual and trend-setting discussions. His advice and guidance throughout this work has been of immeasurable help not only in academic work, but also in my development as a whole.

I would like to appreciate all the students who have aided me with their work. Especially Rita, Franz, Quirin, Wolfgang, Johannes, Martin and all the other students which were not named. It has been a pleasure to work with them.

Beyond that, I would like to thank all members and staff of the laboratory who attended me during my work for the familiar atmosphere.

The biggest tribute for the support during this thesis goes to my family.

Above all, I would like to express my deepest gratitude to my girlfriend Elisabeth, for her love and support during this work.

ACADEMIC REGISTRY  
**Research Thesis Submission**



Name:	Christian Klient		
School/PGI:	Heriot Watt University, School of Engineering and Physical Sciences		
Version: <i>(i.e. First, Resubmission, Final)</i>	Final	Degree Sought (Award and Subject area)	PhD

**Declaration**

In accordance with the appropriate regulations I hereby submit my thesis and I declare that:

- 1) the thesis embodies the results of my own work and has been composed by myself
- 2) where appropriate, I have made acknowledgement of the work of others and have made reference to work carried out in collaboration with other persons
- 3) the thesis is the correct version of the thesis for submission and is the same version as any electronic versions submitted\*.
- 4) my thesis for the award referred to, deposited in the Heriot-Watt University Library, should be made available for loan or photocopying and be available via the Institutional Repository, subject to such conditions as the Librarian may require
- 5) I understand that as a student of the University I am required to abide by the Regulations of the University and to conform to its discipline.

\* Please note that it is the responsibility of the candidate to ensure that the correct version of the thesis is submitted.

Signature of Candidate:		Date:	09/05/2012
-------------------------	--	-------	------------

**Submission**

Submitted By <i>(name in capitals)</i> :	
Signature of Individual Submitting:	
Date Submitted:	

**For Completion in the Student Service Centre (SSC)**

Received in the SSC by <i>(name in capitals)</i> :	
<i>Method of Submission</i> <i>(Handed in to SSC; posted through internal/external mail):</i>	
<i>E-thesis Submitted (mandatory for final theses)</i>	
Signature:	Date:

Please note this form should bound into the submitted thesis.

Updated February 2008, November 2008, February 2009, January 2011



# CONTENTS

ABSTRACT .....	ii
ACKNOWLEDGEMENT .....	iii
CONTENTS .....	v
LIST OF TABLES .....	viii
LIST OF FIGURES .....	x
GLOSSARY .....	xvii
LIST OF PUBLICATIONS AND IMPORTANT TALKS .....	xxii
CHAPTER 1 – INTRODUCTION .....	1
CHAPTER 2 – DESIGN REQUIREMENTS AND DAMAGE MECHANISMS IN POWER TRAIN COMPONENTS .....	3
CHAPTER 3 – LITERATURE REVIEW .....	6
3.1 ALLOY DEVELOPMENT .....	6
3.1.1 <i>Casting and alloying</i> .....	6
3.1.2 <i>Heat treatment</i> .....	11
3.2 STATIC MECHANICAL BEHAVIOUR .....	14
3.2.1 <i>Tensile properties</i> .....	14
3.2.2 <i>Creep</i> .....	17
3.3 COMPARISON OF MECHANICAL LOADINGS AND IMPACT OF TEMPERATURE .....	19
3.3.1 <i>Low Cycle Fatigue with constant temperature</i> .....	22
3.3.2 <i>Low Cycle Fatigue with alternating temperature (TMF)</i> .....	23
3.3.2.1 <i>Influence of heat treatment</i> .....	26
3.3.2.2 <i>Influence of casting procedure</i> .....	26
3.3.2.3 <i>Influence of alloying elements</i> .....	26
3.3.2.4 <i>Influence of loading conditions</i> .....	27
3.4 DAMAGE MECHANICS COMPUTATION AND SIMULATION .....	28
3.5 SUMMARY .....	34
CHAPTER 4 – MATERIALS AND METHODS .....	35
4.1 MATERIALS .....	35
4.2 HEAT TREATMENT .....	36
4.3 MECHANICAL TEST SPECIMEN GEOMETRY .....	38
4.4 TEMPERATURE CONTROL .....	38
4.5 ISOTHERMAL LOW CYCLE FATIGUE TESTS .....	38
4.6 CERT, CREEP TESTS .....	40
4.7 THERMO-MECHANICAL FATIGUE TESTS .....	41
4.8 METALLOGRAPHY .....	43
4.8.1 <i>Optical microscopy</i> .....	44
4.8.2 <i>Scanning Electron Microscopy</i> .....	44

4.8.3 <i>Transmission Electron Microscopy</i> .....	45
4.9 <b>IMAGE ANALYSIS</b> .....	45
4.10 <b>MICRO CT</b> .....	46
4.11 <b>HARDNESS MEASUREMENT</b> .....	46
4.12 <b>SUMMARY OF TESTS</b> .....	47
<b>CHAPTER 5 - RESULTS</b> .....	49
5.1 <b>INITIAL MICROSTRUCTURES</b> .....	49
5.2 <b>TEMPER TESTS</b> .....	51
5.2.1 <i>Initial condition</i> .....	51
5.2.2 <i>Overageing (e.g. phases and grains)</i> .....	51
5.2.3 <i>Change of hardness values</i> .....	52
5.2.4 <i>Summary of temper tests</i> .....	54
5.3 <b>CERT</b> .....	55
5.4 <b>CREEP TESTS</b> .....	57
5.5 <b>ISOTHERMAL LOW CYCLE FATIGUE TESTS</b> .....	59
5.5.1 <i>Cyclic stress-strain behaviour</i> .....	59
5.5.2 <i>Lifetime behaviour</i> .....	63
5.5.3 <i>Microstructural observations</i> .....	64
5.6 <b>THERMO-MECHANICAL FATIGUE OF ALSI6CU4–T6 REFERENCE ALLOY</b> .....	66
5.6.1 <i>Cyclic stress-strain behaviour</i> .....	66
5.6.2 <i>Lifetime behaviour</i> .....	72
5.6.3 <i>Microstructural observations</i> .....	72
5.7 <b>THERMO-MECHANICAL FATIGUE TESTS: EFFECT OF PRE-TREATMENT</b> .....	75
5.7.1 <i>Cyclic stress-strain behaviour</i> .....	75
5.7.2 <i>Lifetime behaviour</i> .....	80
5.7.3 <i>Microstructural observations</i> .....	81
5.7.3.1 <i>Effect of HIP-modification on T6 microstructure</i> .....	83
5.7.3.2 <i>Comparison of T7 vs. T6</i> .....	84
5.8 <b>THERMO-MECHANICAL FATIGUE TESTS: EFFECT OF SDAS</b> .....	87
5.8.1 <i>Cyclic stress-strain behaviour</i> .....	87
5.8.2 <i>Lifetime behaviour</i> .....	91
5.8.3 <i>Microstructural observations; comparison with reference alloy</i> .....	92
5.9 <b>THERMO-MECHANICAL FATIGUE TESTS: EFFECT OF ALLOYING ELEMENTS</b> .....	96
5.9.1 <i>Cyclic stress-strain behaviour</i> .....	96
5.9.2 <i>Lifetime behaviour</i> .....	101
5.9.3 <i>Microstructural observations; comparison with reference alloy</i> .....	103
<b>CHAPTER 6 - DISCUSSION</b> .....	108
6.1 <b>TEMPER TESTS</b> .....	108
6.2 <b>CERT</b> .....	111
6.3 <b>CREEP TESTS</b> .....	116
6.4 <b>ISOTHERMAL LOW CYCLE FATIGUE TESTS</b> .....	119
6.5 <b>THERMO-MECHANICAL FATIGUE BEHAVIOUR OF ALSI6CU4 REFERENCE ALLOY</b> .....	120
6.6 <b>EFFECT OF PRE-TREATMENT ON THERMO-MECHANICAL FATIGUE BEHAVIOUR OF THE ALSI6CU4 REFERENCE ALLOY</b> .....	124
6.7 <b>EFFECT OF SDAS ON THERMO-MECHANICAL FATIGUE BEHAVIOUR</b> .....	129

<b>6.8 EFFECT OF ALLOYING ELEMENTS ON MICROSTRUCTURE AND THERMO-MECHANICAL FATIGUE BEHAVIOUR</b> .....	130
<b>6.9 SUMMARY OF EFFECTS OF ALLOYING AND TREATMENT ON TMF PROPERTIES AND PROSPECTS FOR ALLOY DEVELOPMENT</b> .....	132
<b>6.10 SIMULATION AND MODELLING OF DAMAGE BEHAVIOUR OF ALSI6CU4</b> .....	137
<i>6.10.1 Modelling and simulation of microstructure during TMF</i> .....	137
<i>6.10.2 Cyclic stress-strain behaviour</i> .....	144
<i>6.10.3 Lifetime behaviour</i> .....	147
<i>6.10.4 Application to cylinder head geometry</i> .....	156
<b>CHAPTER 7 - CONCLUSIONS</b> .....	160
<b>7.1 EFFECT OF ALLOYING AND TREATMENT ON RESPONSE TO THERMAL EXPOSURE</b> .....	160
<b>7.2 HIGH TEMPERATURE FATIGUE BEHAVIOUR</b> .....	162
<b>7.3 DAMAGE EVOLUTION MODELS</b> .....	163
<b>7.4 IMPLICATIONS OF THE WORK FOR THE DESIGN, MATERIAL SELECTION AND SIMULATION OF AUTOMOTIVE CYLINDER HEADS</b> .....	165
<b>REFERENCES</b> .....	167
<b>APPENDIX</b> .....	I
<b>A. - USED EQUATIONS AND FORMULAS FOR CHABOCHE MODELLING AND ANSYS</b> .....	I
<b>B. - BACKGROUND MATERIALS AND METHODS</b> .....	II
<b>C. MICROSTRUCTURAL OBSERVATIONS</b> .....	V

## LIST OF TABLES

Table 2.1: Primary and secondary functions of cylinder heads [19,22].	3
Table 2.2: Production steps, loadings and damages [18].	5
Table 2.3: Factors influencing damage initiation.	5
Table 3.1: Results of RT tensile tests for cast aluminium alloys for a range of authors [15,163,164].	15
Table 3.2: Classification of the TMF behaviour according to Nitta and Kuwabara [219,229].	25
Table 4.1: Chemical composition of tested specimens in wt.-%.	36
Table 4.2: Heat treatments for the cast Al alloys tested.	36
Table 4.3: Overview of temper tests.	37
Table 4.4: LCF tests carried out on AlSi6Cu4-T6.	40
Table 4.5: CERT conditions used for the different Al-Si-Mg and Al-Si-Cu alloys.	40
Table 4.6: TMF overview of tested alloys and test conditions.	43
Table 4.7: Summary of tests.	48
Table 5.1: Micrographs showing the different initial microstructures of Al-Si-Mg and Al-Si-Cu alloys before testing. Vertical direction of the specimen axis runs from bottom to top of page.	49
Table 5.2: Initial hardness values after an ordinary T6 and T7 heat treatment.	51
Table 5.3: Comparison of mechanical parameters on AlSi6Cu4 with different pre-treatments at 200°C.	56
Table 5.4: Pre-test hardness values for different temper conditions of AlSi6Cu4.	81
Table 6.1: Summary of hardness changes in temper tests.	109
Table 6.2: Comparison of test temperature, proof stress and work hardening rates of the different alloys.	113
Table 6.3: Summary of different creep test data.	116
Table 6.4: Summary of the main effects on Al-Si-Cu and Al-Si-Mg alloys before and under CERT and TMF conditions.	135
Table 6.5: Hysteresis energy parameters for predicting lifetime.	148

Table 6.6: $P_{SWT}$ parameters for predicting lifetime. ....	149
Table 6.7: $P_{Ost}$ parameters for predicting lifetime. ....	149
Table 6.8: Best fit lines for average damage per cycle. ....	151
Table 7.1: Summary of Manson-Coffin-Basquin lifetime parameters for Al-Si-Cu and Al-Si-Mg alloys tested under TMF. ....	164
Table 7.2: Summary of the parameters for the equation line of the damage parameter of Ostergren for Al-Si-Cu and Al-Si-Mg alloys tested tested under TMF. ....	165
Table II.1: Overview of used etchants with detailed description of ingredients. ....	IV

## LIST OF FIGURES

Figure 1.1: Development of specific performance and ignition pressure of passenger car engines [12]. .....	2
Figure 2.1: Factors influencing the cylinder head lifetime. ....	4
Figure 3.1: Al-Si phase diagram [42]. ....	7
Figure 3.2: Effect of freezing rate on SDAS [78]. ....	10
Figure 3.3: A typical precipitation heat treatment cycle. ....	12
Figure 3.4: Formation of precipitates in relation to ageing temperature and ageing time. ....	13
Figure 3.5: Effect of particle diameter on dislocation hold-up mechanism. ....	14
Figure 3.6: Deformation mechanism chart for aluminium. ....	18
Figure 3.7: Classification of thermal fatigue [211]. ....	21
Figure 3.8: Chronological overview of damage mechanisms leading to failure [214]. ..	22
Figure 3.9: Damage mechanisms during one IP and OP cycle [217]. ....	23
Figure 3.10: Mechanical strain/ temperature variation under IP and OP TMF loading. ..	24
Figure 4.1: Mechanical test specimen geometry. ....	38
Figure 4.2: Schematic overview of controller, data acquisition, input and output signals for LCF test rig. ....	39
Figure 4.3: Schematic overview of controller, data acquisition, input and output signals for the TMF test rig. ....	41
Figure 4.4: Section planes of metallographic specimens cut from mechanical test pieces. ....	44
Figure 4.5: Pores in the gauge length in longitudinal and transverse $\mu$ -CT scans. ....	46
Figure 5.1: Hardness evolution of AlSi7Mg0.3(Cu) T6 on subsequent exposure at 200°C and 400°C. ....	52
Figure 5.2: Hardness evolution during high temperature exposure of the AlSi6Cu4 alloy at 200°C and 400°C starting from a T6 heat treatment. ....	53
Figure 5.3: Comparison of AlSi7Mg0.3(Cu) and AlSi6Cu4 tested after high temperature exposure at 400°C. ....	54

Figure 5.4: Comparison of CERT at 200°C and 400°C for AlSi6Cu4 in the non-HIPped T6 and HIPped condition. ....	55
Figure 5.5: Comparison of CERT on AlSi6Cu4 and AlSi9Cu3 in the T6 condition at 400°C. ....	56
Figure 5.6: Comparison of Al-Si-Mg alloys in the T6 condition subjected to CERT at 400°C. ....	57
Figure 5.7: Creep curves for AlSi6Cu4-T6 at 200°C with different stress values. ....	58
Figure 5.8: Creep curves for AlSi6Cu4-T6 at 400°C with different stress values. ....	59
Figure 5.9: Hysteresis loops of AlSi6Cu4-T6 at 200°C and 400°C at $N_f/2$ . ....	60
Figure 5.10: Mean inelastic strain of AlSi6Cu4-T6 at 200°C and 400°C under LCF loading at a strain amplitude of 0.2%. ....	61
Figure 5.11: Maximum stress of AlSi6Cu4-T6 at 200°C and 400°C tested under LCF loading with different strain amplitudes. ....	62
Figure 5.12: Comparison of maximum stress at 200°C and 400°C at $N_f/2$ under LCF loading with different strain amplitudes. ....	62
Figure 5.13: Mean inelastic strain at $N_f/2$ at 200°C and 400°C tested under LCF conditions with different strain amplitudes. ....	63
Figure 5.14: Mechanical strain amplitude – $N_f$ diagram of AlSi6Cu4-T6 under LCF loading conditions. ....	64
Figure 5.15: Crack through the $\alpha$ -matrix in AlSi6Cu4-T6 under LCF condition at 400°C and a strain amplitude of 0.35%. ....	65
Figure 5.16: Particle decohesion of AlSi6Cu4-T6 tested under LCF and a strain amplitude of 0.2%. ....	65
Figure 5.17: Hysteresis loops at $N=N_f/2$ for AlSi6Cu4-T6 under IP-TMF loading with different strain amplitudes. ....	67
Figure 5.18: Hysteresis loops at $N=N_f/2$ for AlSi6Cu4-T6 under OP-TMF loading with different strain amplitudes. ....	68
Figure 5.19: Mean inelastic strain of AlSi6Cu4-T6 under IP-TMF loading with different strain amplitudes. ....	69
Figure 5.20: Mean inelastic strain of AlSi6Cu4-T6 under OP-TMF loading with different strain amplitudes. ....	69
Figure 5.21: Maximum and minimum stresses of AlSi6Cu4-T6 specimens tested under IP TMF loading. ....	70

Figure 5.22: Maximum and minimum stresses of AlSi6Cu4-T6 specimens tested under OP-TMF loading. ....	71
Figure 5.23: Stress amplitudes of specimens tested under IP and OP-TMF loading at strain amplitudes of 0.2% and 0.5%. ....	72
Figure 5.24: Particle decohesion in AlSi6Cu4-T6 under IP-TMF loading and a strain amplitude of 0.7%. ....	74
Figure 5.25: Particle cracking as crack initiator in AlSi6Cu4-T6 under IP-TMF loading at a strain amplitude of 0.7%. ....	74
Figure 5.26: Internal voids just below the fracture surface of AlSi6Cu4-T6 under OP-TMF loading at a strain amplitude of 0.5%. ....	75
Figure 5.27: Hysteresis loops at $N=N_f/2$ for AlSi6Cu4 for different pre-treatments under IP-TMF loading. ....	76
Figure 5.28: Hysteresis loops at $N=N_f/2$ for AlSi6Cu4 with different pre-treatments under OP-TMF loading. ....	77
Figure 5.29: Evolution of mean inelastic strain of AlSi6Cu4 with different pre-treatments under IP-TMF loading. ....	77
Figure 5.30: Evolution of mean inelastic strain of AlSi6Cu4 with different pre-treatments under OP-TMF loading. ....	78
Figure 5.31: Evolution of stress amplitude and mean stress for AlSi6Cu4 with different pre-treatments under IP-TMF loading. ....	79
Figure 5.32: Evolution of stress amplitude and mean stress for AlSi6Cu4 with different pre-treatments under OP-TMF loading. ....	79
Figure 5.33: Mechanical strain amplitude vs. ductility factor for AlSi6Cu4 with different pre-treatments. ....	80
Figure 5.34: Mechanical strain amplitude vs. $N_f$ for AlSi6Cu4 with different pre-treatments under TMF loading. ....	81
Figure 5.35: Decrease of hardness for different amounts of TMF exposure for the different pre-treatments. ....	82
Figure 5.36: Fine striations near to the fracture surface for AlSi6Cu4-HIP at a strain amplitude of 0.2%. ....	83
Figure 5.37: Crack path for AlSi6Cu4-T7 at a strain amplitude of 0.5% under OP-TMF loading. The loading axis is in the vertical direction. ....	85
Figure 5.38: Laser scan micrograph showing particle cracking of the $\alpha$ -phase in AlSi6Cu4 under IP-TMF loading at a strain amplitude of 0.5%. ....	86



Figure 5.39: Hysteresis loops at $N=N_f/2$ for AlSi6Cu4 and AlSi9Cu3 under IP-TMF loading. ....	87
Figure 5.40: Hysteresis loops at $N=N_f/2$ for AlSi6Cu4 and AlSi9Cu3 under OP-TMF loading. ....	88
Figure 5.41: Mean inelastic strain for AlSi6Cu4 and AlSi9Cu3 under IP-TMF loading. ....	89
Figure 5.42: Mean inelastic strain for AlSi6Cu4 and AlSi9Cu3 under OP-TMF loading. ....	89
Figure 5.43: Stress amplitudes and mean stresses for AlSi6Cu4 and AlSi9Cu3 under IP-TMF loading. ....	90
Figure 5.44: Stress amplitudes and mean stresses for AlSi6Cu4 and AlSi9Cu3 under OP-TMF loading. ....	91
Figure 5.45: Mechanical strain amplitude vs. $N_f$ for AlSi6Cu4 and AlSi9Cu3 under TMF loading. ....	92
Figure 5.46: Microstructure of AlSi9Cu3 in the T6 condition. The loading axis is in the vertical direction. ....	93
Figure 5.47: Hardness decrease for AlSi6Cu4 and AlSi9Cu3 under IP-TMF loading at a strain amplitude of 0.2%. ....	94
Figure 5.48: Cracks in Fe cluster of AlSi9Cu3 near to the surface of IP-TMF tested at a strain amplitude of 0.5%. The loading axis is in the vertical direction. ....	95
Figure 5.49: Cracks alongside of Si particles in AlSi9Cu3 tested under IP-TMF loading at a strain amplitude of 0.2%. The loading axis is in the vertical direction. ....	96
Figure 5.50: Hysteresis loops at $N=N_f/2$ for AlSi6Cu4 and Al-Si-Mg alloys under IP-TMF loading. ....	97
Figure 5.51: Hysteresis loops at $N=N_f/2$ for AlSi6Cu4 and Al-Si-Mg alloys under OP-TMF loading. ....	98
Figure 5.52: Mean inelastic strain for AlSi6Cu4 and Al-Si-Mg alloys under IP-TMF loading. ....	99
Figure 5.53: Mean inelastic strain for AlSi6Cu4 and Al-Si-Mg alloys under OP-TMF loading. ....	99
Figure 5.54: Stress amplitudes and mean stresses for AlSi6Cu4 and Al-Si-Mg alloys under IP-TMF loading. ....	100
Figure 5.55: Stress amplitudes and mean stresses for AlSi6Cu4 and Al-Si-Mg alloys under OP-TMF loading. ....	101

Figure 5.56: Mechanical strain amplitude vs. $N_f$ for AlSi6Cu4 and Al-Si-Mg alloys under IP-TMF loading. ....	102
Figure 5.57: Mechanical strain amplitude vs. $N_f$ for AlSi6Cu4 and Al-Si-Mg alloys under OP-TMF loading. ....	102
Figure 5.58: Hardness decrease of AlSi6Cu4 and Al-Si-Mg alloys under TMF loading at a strain amplitude of 0.2% during the lifetime. ....	104
Figure 5.59: Crack initiation at Si cluster in AlSi9Mg0.5 under OP-TMF loading and a strain amplitude of 0.5%. ....	106
Figure 5.60: Schematic overview of crack initiation and propagation in Al-Si-Mg alloys. ....	106
Figure 5.61: Oxide layer on the crack path of AlSi7Mg0.5 under IP-TMF loading and a strain amplitude of 0.2%. ....	107
Figure 6.1: Comparison of grain size vs. time of LCF and temper tests for AlSi6Cu4. ....	110
Figure 6.2: Comparison of hardness data resulting from simulation, LCF and TMF tests on AlSi6Cu4. ....	111
Figure 6.3: Schematic relation between stress vs. strain and $d\sigma/d\epsilon$ vs. strain for a specimen. ....	113
Figure 6.4: Micrographs showing AlSi6Cu4-T6 in the non-HIPped (left) and the HIPped (right) conditions. ....	114
Figure 6.5: Creep curve of AlSi6Cu4-T6 at 200°C with different stress ratios. ....	117
Figure 6.6: Creep curve of AlSi6Cu4-T6 at 400°C with different stress ratios. ....	117
Figure 6.7: Stress amplitude and inelastic strain vs. the mechanical strain amplitude for AlSi6Cu4-T6 under LCF and TMF conditions. ....	121
Figure 6.8: Comparison of stress amplitude of AlSi6Cu4-T6 under LCF and TMF conditions at $N=N_f/2$ . ....	122
Figure 6.9: Mechanical strain amplitude vs. $N_f$ of AlSi6Cu4-T6 under LCF and TMF conditions. ....	123
Figure 6.10: Brittle fracture surface of AlSi6Cu4-T6 under OP-TMF loading at a strain amplitude of 0.6%. ....	124
Figure 6.11: Relation between lifetimes for AlSi6Cu4 with different pre-treatments and under IP-TMF loading. ....	127
Figure 6.12: Improvement in TMF life offered by two different pre-treatments over the reference condition AlSi6Cu4-T6. ....	128

Figure 6.13: Effect of pre-treatments on the maximum stresses of AlSi6Cu4. ....	129
Figure 6.14: Maximum stress in OP-TMF tests at $N=N_f/2$ for the different Al-Si-Mg alloys in relation to AlSi6Cu4. ....	132
Figure 6.15: Comparison of stress amplitudes at mechanical strain amplitudes of 0.2% and 0.5% at $N=N_f/2$ of alloys tested under TMF loading. ....	133
Figure 6.16: Mechanical strain amplitude vs. cycles to failure under TMF loading for mechanical strain amplitudes of 0.2% and 0.5% of all alloys tested. ....	134
Figure 6.17: Schematic overview of input data and simulation procedure. ....	137
Figure 6.18: Simulation of hardness values of AlSi6Cu4 at 200°C and 400°C starting from T7. ....	139
Figure 6.19: Orientation of pores relative to the direction of loading. ....	139
Figure 6.20: Stress distribution around an elliptical pore for different orientations: (right) pore aligned in loading direction, (left) pore rotated by 90° to the loading direction. ....	141
Figure 6.21: Pore geometry. ....	141
Figure 6.22: Stress concentration factors vs. pore radius of two sizes. ....	142
Figure 6.23: Stress concentration factors for linear-elastic and Chaboche simulations vs. elliptical pore radius of curvature. ....	143
Figure 6.24: Interaction of pores under tension (left) and compression (right). ....	144
Figure 6.25: Comparison of hysteresis loops resulting from simulation with the Chaboche model and from tests. ....	145
Figure 6.26: Comparison of hysteresis loops at $N=10$ obtained from simulation with Ansys and from tests under IP-TMF loading. ....	147
Figure 6.27: Accumulated hysteresis energy of AlSi6Cu4-T6 specimens tested under IP and OP-TMF loading. ....	148
Figure 6.28: Damage parameters of Smith-Watson-Topper and Ostergren at $N=10$ of tested specimens under IP and OP-TMF loading for AlSi6Cu4-T6. ....	149
Figure 6.29: Evolution of damage based on secant modulus for AlSi6Cu4-T6 under IP and OP-TMF loading. ....	150
Figure 6.30: Average damage per cycle vs. mechanical strain amplitude of AlSi6Cu4-T6 under IP and OP-TMF loading. ....	151
Figure 6.31: Specific angles of interest of hysteresis loop under TMF loading. ....	153

Figure 6.32: Example evolution of the upper angle of the hysteresis loop during the lifetime of the reference alloy under IP-TMF loading. The circled point shows the fracture of the specimen. ....	153
Figure 6.33: Predictive lives vs. the experimentally determined cycles to failure under IP-TMF loading of AlSi6Cu-T6. ....	154
Figure 6.34: Predictive life vs. the experimentally determined cycles to failure under OP-TMF loading of AlSi6Cu4-T6. ....	155
Figure 6.35: Damage parameter of Ostergren of all tested alloys under TMF loadings. ....	155
Figure 6.36: Measured cycles to failure vs. predicted life using the Manson-Coffin-Basquin equation for all tested alloys under TMF loadings. ....	156
Figure 6.37: Cylinder head geometry showing the temperature distribution under OP-TMF loading at 400°C. ....	157
Figure 6.38: Results for equivalent stress (von Mises, in MPa) with the global elastic-plastic material model. ....	157
Figure 6.39: Crack at the valve bridge of a cylinder head after TMF loading. ....	158
Figure 6.40: Results from FEMFAT for fatigue damage (logarithmic scale) applied to cylinder head geometry. ....	159
Figure II.1: Test rig showing induction coil, specimen, thermocouple and extensometer. ....	II
Figure II.2: Effect of HIP procedure on a cylinder head. ....	II
Figure II.3: Overview of heat treatments and effects on tensile strength and hardness. ....	III
Figure III.1: Pore near to the surface of a specimen of cast Al. ....	V
Figure III.2: Intermetallic phase on the surface of a specimen with a crack. ....	V
Figure III.3: Cracks starting from internal voids and pores near to the surface. ....	VI

## GLOSSARY

A	Area [mm <sup>2</sup> ]
A	Constant
A319	Alloy
A356	Alloy
AC4CH	Alloy
Al	Aluminium
AlCuBiPb	Alloy
Al <sub>2</sub> Cu	Intermetallic Phase
Al <sub>2</sub> CuMg	Intermetallic Phase
Al <sub>4</sub> CuMg <sub>5</sub> Si <sub>4</sub>	Intermetallic Phase
Al <sub>3</sub> Fe	Intermetallic Phase
Al <sub>5</sub> FeSi	Intermetallic Phase
Al <sub>9</sub> Fe <sub>2</sub> Si	Intermetallic Phase
Al <sub>12</sub> Fe <sub>3</sub> Si <sub>2</sub>	Intermetallic Phase
Al <sub>8</sub> Mg <sub>3</sub> FeSi <sub>6</sub>	Intermetallic Phase
Al <sub>5</sub> Mg <sub>8</sub> Si <sub>6</sub> Cu <sub>2</sub>	Intermetallic Phase
Al <sub>6</sub> Mn	Intermetallic Phase
AlSi5Cu3	Alloy
AlSi6Cu4	Alloy
AlSi9Cu3	Alloy
AlSi7Mg0.3(Cu)	Alloy
AlSi7Mg0.5	Alloy
AlSi8Mg0.4	Alloy
AlSi8Cu3	Alloy
AlSi9Mg0.5	Alloy
AlSi10Mg	Alloy
AlSi12CuMgNi	Alloy
AS9U3G	Alloy
B	Constant
b	Material parameter for isotropic hardening
C	Constant

$c_1$	Constant
$c_2$	Constant
$c_3$	Constant
$c_4$	Constant
CERT	Constant Extension Rate Test
CO <sub>2</sub>	Carbon dioxide
CT	Computer tomograph
$C_i$	Material parameter for kinematic hardening
$C_\infty$	Material parameter for kinematic hardening
D	Damage factor [-]
DI	Direct injection
$D_{Sec}$	Damage parameter [-]
$D_{TMF}$	Damage parameter of Riedel [-]
$d_{T0}$	Initial diameter of particle [ $\mu\text{m}$ ]
$d_T$	Diameter of particle [ $\mu\text{m}$ ]
E	Young modulus [MPa]
EDS	Energy dispersive spectroscopy
$E_0$	Initial young modulus [MPa]
$E_{Sec}$	Secant modulus [MPa]
e.g.	For example (latin: <i>exempli gratia</i> )
F	Force [N]
F	Creep and dwell time parameter
Fe	Iron
FEM	Finite elements method
G	Shear modulus [MPa]
h, hr	Hour
HB	Brinell hardness
$H_{B0}$	Brinell hardness in the initial condition
$H_{BS}$	Brinell hardness in the complete overaged condition
HCF	High Cycle Fatigue
HIP	Hot Isostatic Pressing
HV <sub>0.1</sub>	Vickers hardness
IDI	Indirect injection
IP	In-Phase
K	Kelvin

K	Viscosity parameter [MPa]
$K_t$	Stress concentration factor [-]
k	Boltzmann constant [ $J \cdot K^{-1}$ ]
k	Ramberg Osgood parameter [MPa]
k	Temperature dependent constant
k	Temperature dependent constant of ripening
l	Length [ $\mu m$ ]
LCF	Low Cycle Fatigue
M	Material point
Mg	Magnesium
$Mg_2Si$	Intermetallic Phase
min	Minute
Mn	Manganese
MPa	Megapascal
mm	Millimetre
N	Newton
$N$	Number of cycles [-]
$N_f/2$	Number of cycles at half of lifetime [-]
$N_f$	Number of cycles to failure [-]
n	Norton exponent [-]
n	Hardening exponent [-]
n	Number of crossed dendrite arms
$n_m$	Material constant
OM	Optical microscopy
OP	Out-of-Phase
PLC	Portevin-Le Chatelier effect
PS	Proof stress [MPa]
$P_M$	Damage parameter of Morrow [-]
$P_{max}$	Maximum pressure [bar]
$P_{Ost}$	Damage parameter of Ostergren [-]
$P_{SWT}$	Damage parameter of Smith-Watson-Topper [-]
$\dot{p}$	Accumulated plastic equivalent strain rate
Q	Creep activation enthalpy [J/mol]
Q	Intermetallic phase
$Q_{SD}$	Activation energy for self diffusion [J/mol]

$Q_{\infty}$	Material parameter for isotropic hardening
R	Gas constant [Pa m <sup>3</sup> K <sup>-1</sup> mol <sup>-1</sup> ]
R	Variable of isotropic hardening
R	Freezing rate [°C/s]
R <sub>a</sub>	Surface roughness [μm]
RT	Room temperature
R <sup>2</sup>	Coefficient of determination [-]
r	Constant
s, sec	Seconds
s	Material parameter
SEM	Scanning electron microscopy
SCF	Stress concentration factor
Si	Silicon
SDAS	Secondary dendrite arm spacing [μm]
T	Temperature [°C]
t	Time [s]
T <sub>max</sub>	Maximum temperature [°C]
T <sub>min</sub>	Minimum temperature [°C]
TEM	Transmission electron microscopy
TMF	Thermo Mechanical Fatigue
T <sub>M</sub>	Melting temperature [°C]
$\dot{T}$	Heating rate [K/s]
T1	Heat treatment
T5	Heat treatment
T6	Heat treatment
T64	Heat treatment
T7	Heat treatment
UTS	Ultimate tensile strength [MPa]
vs.	Versus
WH	Work hardening
W <sub>p</sub>	Plastic strain energy
wt.-%	Weight percent
ΔW <sub>p</sub>	Dissipated plastic energy
X	Back stress tensor
Y	Damage energy discharge rate



$\alpha$	Kinematic hardening variable
$\alpha$	Intermetallic Phase
$\beta$	Variable
$\beta$	Intermetallic Phase
$\beta'$	Intermetallic phase
$\beta''$	Intermetallic phase
$\varepsilon$	Strain [mm/mm]
$\varepsilon_a$	Strain amplitude [mm/mm]
$\varepsilon_{a,t}$	Total strain amplitude [mm/mm]
$\varepsilon_{el}$	Elastic strain [mm/mm]
$\varepsilon_{max}$	Maximum strain [mm/mm]
$\varepsilon_{mech}$	Mechanical strain [mm/mm]
$\varepsilon_{min}$	Minimum strain [mm/mm]
$\varepsilon_p$	Plastic strain [mm/mm]
$\Delta\varepsilon_{pl}$	Plastic strain amplitude [mm/mm]
$\varepsilon_{th}$	Thermal strain [mm/mm]
$\varepsilon_{tot}$	Total strain [mm/mm]
$\dot{\varepsilon}_{st}$	Secondary creep rate [ $s^{-1}$ ]
$\sigma$	Creep stress [MPa]
$\sigma$	Stress tensor
$\sigma_a$	Stress amplitude [MPa]
$\sigma_{cy}$	0.2% yield strength [MPa]
$\sigma_{max}$	Maximum stress [MPa]
$\sigma_{max1}$	Maximum stress in cycle $N=1$ [MPa]
$\sigma_{min}$	Minimum stress [MPa]
$\sigma_m$	Mean stress [MPa]
$\sigma_n$	Nominal stress [MPa]
$\sigma_p$	Internal increased stress caused by dislocation hardening [MPa]
$\sigma_y$	Yield strength [MPa]
$\Delta\sigma_{I,eff}$	Von Mises stress [MPa]
$\Delta\sigma_e$	Comparative stress [MPa]
$\theta$	Intermetallic phase
$\theta'$	Intermetallic Phase
$\theta''$	Intermetallic Phase

$\gamma$   
°C

Material parameter for kinematic hardening  
Degree Celsius

### **LIST OF PUBLICATIONS AND IMPORTANT TALKS**

- Christian Kliemt, Thermo-mechanical fatigue behaviour of AlSi7Mg0.3(Cu), VW-AK Materials and Operating Procedure, Wolfsburg, Germany, 2008
- Christian Kliemt, TMF experiments on cast Al-Si-Mg and Al-Si-Cu alloys, IWM, Freiburg, Germany 2009
- Christian Kliemt, Low Cycle fatigue experiments on cast AlSi10Mg, VW-AK Loadings and Damage on Engine Components, Wolfsburg, Germany 2009

## **CHAPTER 1 – INTRODUCTION**

On the one hand, the automotive industry is driven by the guidelines of the European Union and other institutions to reduce the CO<sub>2</sub> emissions of internal combustion car engines to 95g/km by 2020 (Tier 4, Euro 6, ...) [1-5]. On the other hand, the industry's leading firms have set up the aim to reduce development times and endeavour to minimize the development costs of engines. Also, the climate policy of the European Union promotes fuel and weight saving methods such as downsizing, hybrid engines and automatic start-stop systems [6-11]. Downsizing and start-stop systems lead to higher loading and higher specific power and, as a result, to higher component temperatures and increasing ignition pressure. These increasing loads (Figure 1.1) stretch current materials to their limits.

The aims set up by the automotive sector have led to an intensified application of FEM in order to simulate loading conditions. Current methods, which have mostly been developed for cast iron, do not incorporate the damage mechanisms occurring in cast Al alloys at high temperatures. Substantial knowledge of the thermal and mechanical loading and damage mechanisms are a prerequisite for real time simulations of engine loading. Furthermore, a comprehensive data base is essential, incorporating the results of thermo-mechanical fatigue (TMF) tests, constant extension rate tests (CERT), creep, low-cycle fatigue (LCF) tests and tempering tests. The increasing specific power of direct and indirect injection engines also dictate the need for new simulation methods [12].

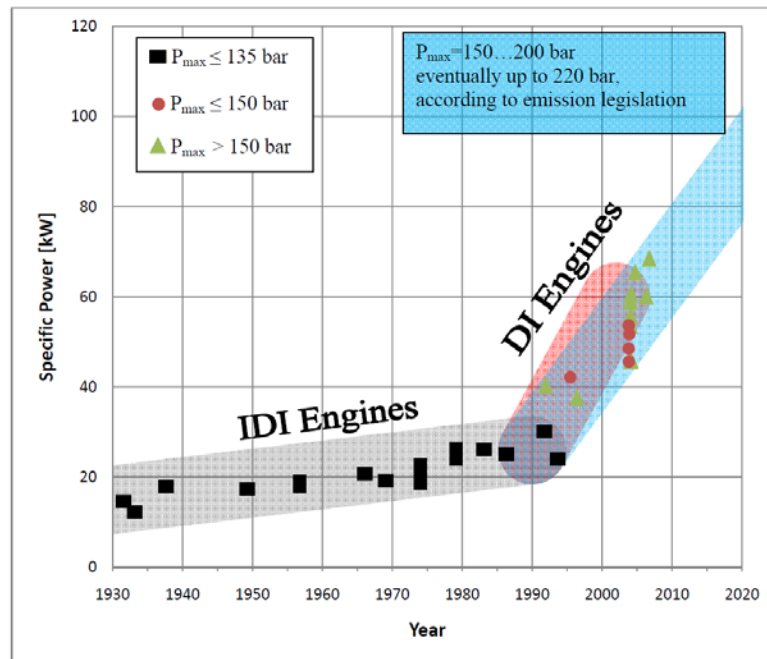


**Figure 1.1:** Development of specific performance and ignition pressure of passenger car engines [12].

Cylinder heads are exposed to static and dynamic stresses during their lifetime, especially in direct injection and supercharged diesel engines or petrol engines. Static stresses include the preload forces from bolted joints and those due to differential thermal expansion of components. Dynamic stresses are a result of combustion, and shorter-term thermal and inertial loadings. Because the engine needs to be cooled, components build up high temperature gradients and associated thermal stresses. Temperature is directly linked to the emissions and the fuel consumption of a vehicle [13-17] so there is a continual drive to increase operating temperatures.

The aim of the present research is to investigate and determine the influence of different cooling rates, pre-treatments and alloying elements on the TMF behaviour of Al-Si cylinder head alloys under severe conditions. To do this, the particular thermal characteristics of a cylinder head have to be considered in conjunction with the role of Si and other non-matrix phases on mechanical properties in a changing thermal environment. Accordingly, CERT, creep, LCF and temper tests have been carried out to determine the properties under isothermal and thermo-mechanical loading. The measured data were then incorporated into a computational tool in order to simulate mechanical behaviour in the engine.

## CHAPTER 2 – DESIGN REQUIREMENTS AND DAMAGE

### MECHANISMS IN POWER TRAIN COMPONENTS

An increase in most given engine operating characteristic, particularly peak pressure or heat input, implies an increase in thermal and mechanical loadings on power train components. During operation, the magnitude and distribution of the specific forces in the engine depend on component geometry, material properties and mechanical and thermal loadings. Components most affected by complex loadings are the cylinder head, the piston and the cylinder liner. Furthermore, these parts are also exposed to hot combustion gas, high combustion pressure or the dynamic movement of parts. Heat is dissipated through gallery walls to the cooling water, and the cooling system maintains a relatively steady-state temperature gradient once the engine has warmed up. The cylinder head, especially the valve bridge, is generally regarded as the critical part of the entire engine in terms of mechanical and thermal loading. Thus, any modifications in engine design and/ or performance will be felt most in changes of the cylinder head loading conditions. Therefore, it is essential to consider first what are the implications of any design modifications on mechanical performance and lifetime or failure behaviour of this part [13, 16, 18-31]. Generally, the functions and requirements of the cylinder head can be summarized as in Table 2.1 [19, 22]:

**Table 2.1:** Primary and secondary functions of cylinder heads. Compiled from [19, 22].

<b>Primary functions</b>	<b>Secondary functions</b>
Control of the combustion chamber: low flame ways, low heat absorption to the surface	Cooling: consistent component temperature
Regulate flow behaviour of the charge components in each cycle	Lubrication of moving parts
Switch charge motion	Oil return and ventilation
Sealing of the cylinder crankcase with the cylinder head gasket	Structural rigidity
Housing for the channels and controls	Fixtures and attachment of ancillary parts
Housing for the systems for the fuel mixture generation and ignition	

As these functions and requirements can be contradictory, it is necessary to balance properties to best meet the design options. The dictates of Table 2.1 can have separate implications for loading and damage mechanisms resulting from manufacturing and service [18]. In addition, the manufacturing step can be separated into “pure manufacturing” steps which include casting procedure, heat treatment, and alloying

elements which mostly affect the properties, and the loading conditions (including thermal ones in service) caused by assembly (Figure 2.1).

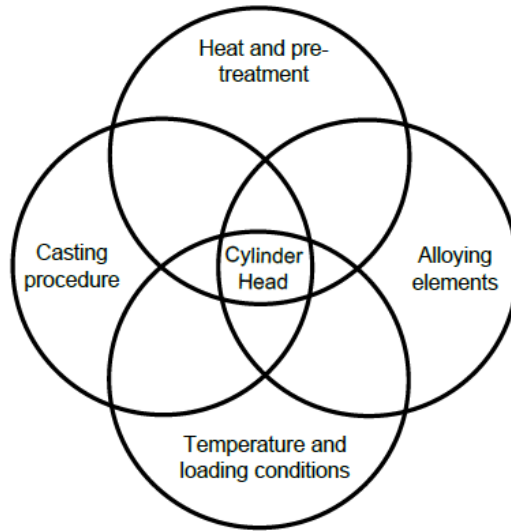


**Figure 2.1:** Factors influencing the cylinder head lifetime.

Table 2.2 lists the commonly used production steps and their associated damage mechanisms and manifestation of these affecting service performance.

**Table 2.2:** Production steps, loadings and damages [18].

<b>Production steps</b>	<b>Damage mechanism</b>	<b>Manifestation</b>
Casting and Solidification	<ul style="list-style-type: none"> <li>- Chemical Modification (e.g. Oxidation)</li> <li>- Inclusions</li> <li>- Blow holes</li> <li>- Different solidification times resulting from different wall thicknesses and solidification directions</li> </ul>	<ul style="list-style-type: none"> <li>- Irregular material composition</li> <li>- Notch effect</li> <li>- Notch effect, porosity</li> <li>- Residual stresses</li> </ul>
Heat treatment	Precipitation hardening = Solution annealing + Quenching: different thermal expansion	Residual stresses
Shape cutting	<ul style="list-style-type: none"> <li>- Thermal loadings resulting from high cutting speed</li> <li>- Mechanical loadings from fixation and cutting force</li> </ul>	<ul style="list-style-type: none"> <li>- Microstructural changes</li> <li>- Deformation, residual stresses</li> </ul>
Force fitting of valve seating, manipulation	Clamping forces resulting from oversize of force fitted components	Stress peaks, e.g. in valve crosspieces → crack – initiation
Assembly	Loadings from connection or surrounding components	Deformation of effective surfaces, pre-stress

These manifestations can lead to component failure or fracture and the likelihood of initiation depends upon service conditions as detailed in Table 2.3 [13, 16, 18-41].

**Table 2.3:** Factors influencing damage initiation.

<u>Driveability</u> <ul style="list-style-type: none"> <li>- Full load/ dynamic impulses</li> <li>- City traffic</li> <li>- Motorway traffic</li> </ul>	<u>Driver</u> <ul style="list-style-type: none"> <li>- Individual driving characteristics</li> <li>- Oil level and condition</li> <li>- Coolant level and condition</li> </ul>
<u>Temperature</u> <ul style="list-style-type: none"> <li>- Excessive combustion chamber temperature</li> <li>- Excessive temperature gradient</li> <li>- Excessive expansion</li> </ul>	<u>Material/ manufacturing process</u> <ul style="list-style-type: none"> <li>- Temperature stability</li> <li>- Elasticity</li> <li>- Creep resistance</li> <li>- Hardness</li> <li>- Thermal expansion</li> <li>- Microstructure</li> </ul>
<u>Engine control unit</u> <ul style="list-style-type: none"> <li>- Injection point</li> <li>- Start-Stop</li> </ul>	

## **CHAPTER 3 – LITERATURE REVIEW**

The state of knowledge of aluminium casting alloys for automotive engines can be divided into five distinct areas, all of which are relevant to this study. First, there is the development of the alloys themselves, in particular how alloying elements affect their microstructures and thermal stability. Next, there is the static mechanical behaviour of the relevant alloys, including at elevated temperatures the creep. The dynamic mechanical behaviour can be divided into isothermal low-cycle fatigue and thermo-mechanical fatigue. Finally, a section is included on how data from the foregoing areas can be used in simulation of damage mechanisms for design purposes.

### **3.1 ALLOY DEVELOPMENT**

Technical cast and wrought aluminium alloys can be classified as hardenable (heat-treatable) and non-hardenable [42-44]. For engine components, hardenable cast Al-Si alloys are the most commonly used Al alloys. The evaluation of the mechanical behaviour of Al alloys at elevated temperature, especially for varying temperature, takes account of physical properties, like thermal expansion, thermal conduction and oxidation behaviour, although all of these are relatively little affected by alloying. However, knowledge of the manufacturing process and its effect on microstructure is essential for the thermo-mechanical properties of the alloys. The factors affecting microstructure can be classified as those associated with the alloy preparation (casting and alloying) and those associated with post-casting heat-treatment.

#### ***3.1.1 Casting and alloying***

Figure 3.1 shows the Al-Si phase diagram, which is the basis of most cast aluminium alloys [45]. The eutectic point is at 12.5wt.% Si and a temperature of 577°C. Other alloying elements can have an effect on the Si content of the eutectic, shifting it either to higher or lower levels, and, often, the amount of eutectic in a cast alloy can be reduced if other strengthening mechanisms are used.



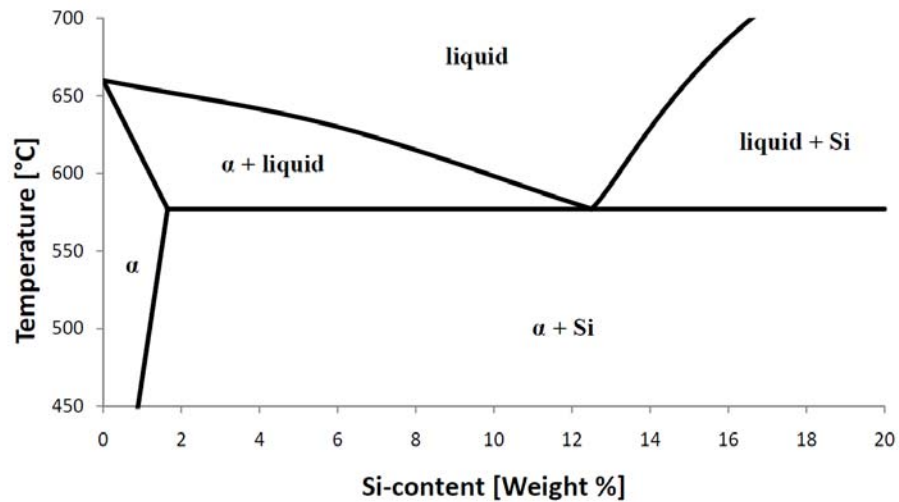


Figure 3.1: Al-Si phase diagram [42].

A principal factor affecting mechanical behaviour of the alloy is the amount and morphology of the eutectic [46] which is influenced by alloying elements, cooling rate and crystallisation behaviour. The eutectic microstructure is formed during solidification and can be broadly classified as; lamellar, coarse or refined [44, 47]. The refined microstructure is the only one considered to have good mechanical properties, attributable to the fine structure of the eutectic [44, 46-49].

Each of the alloying elements used in cast engine block alloys has a specific set of functions as follows:

**Silicon:** Silicon contents of between 5 and 12wt.% provide low shrinkage and, as a result, a low incidence of thermal cracking on solidification and cooling [12, 44, 50, 51]. Silicon is precipitated during solidification almost pure and, as such, provides dispersion strengthening, although too much silicon or too coarse a structure can produce crack-initiation sites. An excess of Si reduces the time to initiate strengthening during heat treatment when Mg is present as a precipitation hardening element. This is caused by an increase of the precipitation of fine, uniformly distributed  $\beta''$  particles, with a lower Mg:Si ratio in the embryonic zones/clusters and  $\beta''$  precipitates. Reducing the Mg:Si ratio also leads to

a decline in strength beyond the peak ageing condition [52]. Too low a Si content can result in a clustering of intermetallics and an increase of porosity [53]. The secondary dendrite arm spacing (SDAS) can also be decreased by an increase in Si content [54, 55], and various forms can be identified, depending on the level of modification; acicular (needles), blocky plates, lamellar, and refined fibrous structure [56, 57].

**Magnesium:** Magnesium (Mg) can refine the eutectic Si phase in Al-Si-Cu alloys [58]. Most importantly, additions of Mg lead to the formation of intermetallic phase:  $Mg_2Si$ .  $Mg_2Si$  is a coherent precipitate and so is responsible for precipitation hardening of alloys provided that an appropriate heat treatment is used. Increased Mg up to a content of 1wt.% produces increases in ultimate tensile strength (UTS), matrix strength, ultimate strain and hardness and improved mould filling behaviour although it concurrently decreases the ductility [12, 50, 59]. Ouellet and Samuel [60] refer to an improvement of heat treatment behaviour in the T5 and T6 tempers. However, negative effects on oxidation behaviour and porosity have been identified [61].

**Manganese:** Manganese (Mn) helps to reduce the detrimental effects of iron, which is difficult to eliminate entirely from aluminium alloys. It has been observed to change the morphology of Fe-intermetallics from relatively coarse platelets to “Chinese script”, thus improving tensile behaviour. The ratio of Fe to Mn should be around 2:1, and an excess reduces the amount of  $\beta$ -phase, promotes the formation of the  $\alpha$ -phase and leads to an increase in (undesirable) Fe-containing intermetallic phases [12, 50, 62-64].

**Copper:** Increased copper content changes the Al-Si eutectic to a ternary Al-Si-Cu eutectic. Furthermore, an increase in Cu leads to a decrease in SDAS [65]. This improves strength, creep resistance, hardness and chemical resistance in the as-cast and heat treated conditions [12, 20, 66]. Cu leads in AlCu and AlSi alloys to

enhancement of strength by formation of hardening precipitates during heat treatment process. A reduction in Cu leads to crack initiation associated with Si particles in the eutectic [53].

Iron: An increase of the Fe content concurrently lowers the ductility, tensile strength and castability and leads to enhanced porosity. In high pressure castings, iron additions are used to reduce adhesion to the mould walls. In Al-Si-Cu alloys, the solubility of Fe in  $\alpha$ -Al leads to it being able to form a range of intermetallic phases such as  $\text{Al}_3\text{Fe}$ ,  $\text{Al}_{12}\text{Fe}_3\text{Si}_2$  or  $\text{Al}_9\text{Fe}_2\text{Si}$ . At compositions of around 0.2wt.-% Fe acicular or flaky  $\text{Al}_9\text{Fe}_2\text{Si}$  forms and this has a detrimental effect on durability. A dramatic drop in ductility, characterised by a change from ductile to brittle fracture, can be observed if the Fe content increases beyond 0.7wt.%, so that the  $\text{Al}_5\text{FeSi}$  phase forms [50, 62, 66-70]. On the other hand, plate-like Fe-rich intermetallic particles in castings can inhibit the growth of small cracks and improve life [71]. In the absence of other detrimental effects, such as porosity, plate-like Fe intermetallics are dominant in influencing cracking.

The modifications applied to Al castings can be classified as follows [72]:

- Control of cooling rates and, consequently, phase transformation rates
- Superheating the melt
- Additions of refinement elements

A number of different casting procedures are used for engine/ power train components. Altenpohl [47] and others [66, 73-75] give an overview of the different process types. Whereas chill casting with sand cores is the current standard casting procedure for cylinder heads of mid-range cars [76], Thalmair [74] describes supplementary procedures for premium BMW cars, such as Rotacast, lost foam, gravity chill casting and low pressure chill casting. There are differences between the processes in terms of casting/ solidification time, shape and wall thickness of components, porosity content and cooling rates. For this reason, the resulting microstructure with its dendrites and intermetallics, which influence the static and dynamic properties of the solidified casting, vary as well.

The formation of dendrites can be influenced by the rate of movement of the solidification front, the temperature and its temporal and spatial distribution, and alloying elements. SDAS has been found to vary in a linear fashion with the freezing rate [67, 77-86], Figure 3.2. SDAS is a strong indicator of quality in Al-Si alloys because the fracture strain and fracture toughness both decrease with increasing SDAS. Garcia-Garcia *et al.* [80] found an inverse proportional relationship between the amount of interdendritic phases and SDAS.

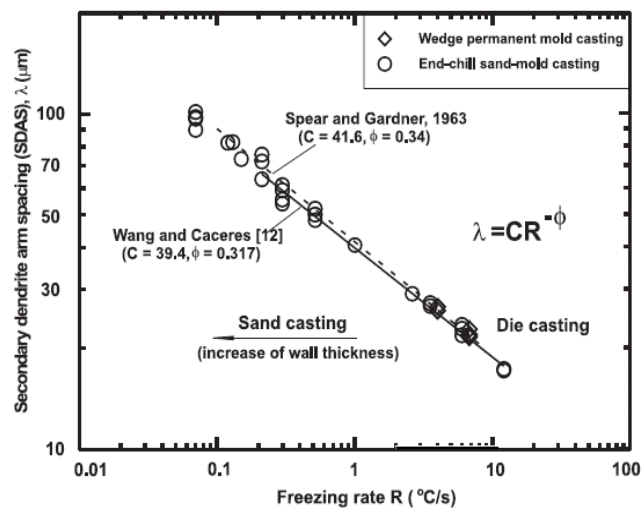


**Figure 3.2:** Effect of freezing rate on SDAS [78].

Porosity can be sub-divided into shrinkage and gas porosity [87, 88], reflecting their causes, which can be attributed to shrinkage, bulking, endogenic gas and exogenic gas [22]. Recently, a lot of effort has been expended to determine the influence of porosity and impurities on room temperature (RT) and elevated temperature behaviour of cast Al alloys [57, 78, 89-105], and a difference has been observed in the initiation of fatigue cracks. For example, Gao *et al.* [89] found that pore size inside the specimens can be described by a log-normal distribution but only large pores close to the surface lead to crack initiation. Yi *et al.* [106] observed a change of crack initiation site from pores to a microcell consisting of  $\alpha$ -Al dendrites and associated Si particles as the porosity content decreased. Ammar *et al.* [107] found crack initiation to be caused by porosity in nearly 90% of specimens tested. They established that fatigue strength decreases with increasing pore size and that surface pores had the greatest propensity to act as crack initiation sites. Arami *et al.* [108] detected, in tests, that an increase of porosity leads to a degradation in thermal fatigue behaviour.

Hot Isostatic Pressing (HIPing) reduces porosity and so leads to an increase of lifetime and improvement of properties. Since it is not a casting process, a detailed description of the HIP process is outside the scope of this review, but is covered in detail in [105, 106, 109-141], and a schematic description is given in Figure II.2 in Appendix B.

Franetovic *et al.* [142] developed a statistical model to describe how various alloy characteristics affect damage tolerance. Their results show that, as pore size and volume fraction decrease, other factors, such as clusters of particles or large particles begin to have a dominant influence on lifetime. They identified the amount of eutectic surrounding the primary phase as the so called “fatigue constitutive parameter”, and observed that pores smaller than half of the SDAS do not affect the lifetime in the LCF regime ( $N < 10^4$ ), but do have an influence on high cycle fatigue ( $N \geq 10^4$ ).

### **3.1.2 Heat treatment**

The strength of Al-Si alloys can be increased by increasing the dislocation density, by grain refinement, by solid solution strengthening, by dispersion strengthening, or by adding elements like Cu or Mg which produce coherent precipitates [44, 143, 144]. Increasing dislocation density requires cold working, which is not an option for castings, and the fineness of the grains will be determined largely by the casting procedure, in the same way as the dispersion of silicon is controlled (see previous section). Heat treatment concerns the balance between alloying elements that are in solid solution and as precipitates (either coherent or incoherent) [47]. The following pages concentrate on precipitation hardening, which is by far the most effective strengthening mechanism in aluminium alloys. Coherent precipitates restrict dislocation motion proportionately much more than do incoherent precipitates and thus strongly increase yield stress ( $\sigma_y$ ) and UTS [145].

Figure 3.3 shows a typical precipitation hardening heat treatment cycle. One prerequisite for precipitation hardening is an  $\alpha$ -solid solution (aluminium) which has a decreasing solubility of alloying elements with decreasing temperature and which can be cooled very rapidly so that it forms a supersaturated solid solution with the alloying elements [146]. The first treatment stage is therefore to heat the alloy to dissolve the precipitating alloying elements. The functions of such a solution treatment are homogenization, dissolution, fragmentation, and coarsening or spheroidization of non-

precipitating intermetallics in order to produce a homogenous  $\alpha$ -Al [147]. The temperature required to reach the  $\alpha$ -Al phase field (between solvus and solidus) is typically only 20°C below the melting point [43, 46, 144, 148, 149]. On quenching from the solution treatment temperature, the microstructure, including its high lattice vacancy density of nearly  $10^{-4}$ , is “frozen” [143]. The frozen-in vacancies enhance the diffusion of the substitutional precipitation atoms during subsequent ageing as well as holding the relevant elements in supersaturated solution [46, 146].

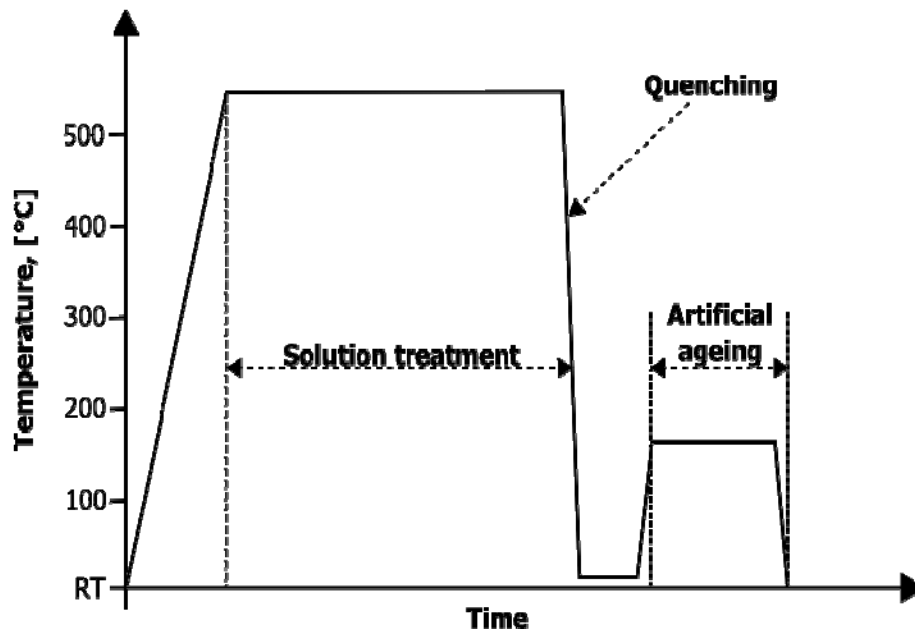


Figure 3.3: A typical precipitation heat treatment cycle.

The second prerequisite for precipitation hardening is the presence of alloying elements which form precipitates which are coherent with the parent aluminium lattice. These are mostly intermetallic compounds of Al, the archetypal one being between Cu and Al. Coherency is usually only obtained for small precipitates so, by controlling the time and temperature of ageing, mechanical properties can be adjusted in a range from high elongation (lower strength) to high strength (lower elongation) [149].

During ageing, Guinier Preston Zones (I and II) form first [150-152]. These zones are essentially ordered assemblages of atoms which are typically a few hundred atoms across and are fully coherent with the aluminium matrix; for example GP II Zones produce a tetragonal distortion of the matrix. With further holding times, a semi-coherent phase is formed and this is normally the stage of peak strengthening, beyond which the alloy becomes overaged and the precipitates less and less coherent. In the Al-Si-Mg system, peak ageing is obtained with the  $\beta'$ -phase which has a hexagonal

structure in the  $\langle 101 \rangle$  orientation. Above the optimum holding time and temperature, these particles evolve to form the incoherent  $\beta$ -phase [46, 153-155] which leads to a detrimental change in mechanical properties.

Which phases form depends on temperature and ageing time and Figure 3.4 gives a map of the stages in relation to ageing temperature and time. The small, coherent precipitates which form during the first period can be relatively easily cut by dislocations. As the phase equilibrium is approached, the larger precipitates grow at the expense of the smaller ones (Ostwald ripening) and so are further apart. Hence, it follows that dislocations will not cut the precipitates but will have to bypass them by the “Orowan Mechanism” [83, 143, 150]. Figure 3.5 shows schematically the relationship between particle radius and shear strength, a measure of the resistance to dislocations offered by the particles. The best strength (T6 condition) involves both coherent and semi-coherent particles and, for higher temperatures and longer times, the particles are coarser and hence less coherent (T7 heat treatment) [146]. Thus, in the T7 treatment, strength is sacrificed to improve dimensional stability over T6 [42, 156]. García-García *et al.* [80] observed a fragmentation, necking, spheroidization and coarsening of the Si particles during solution treatment. Firouzdor and colleagues [157] found  $\text{Al}_2\text{Cu}$ ,  $\text{Mg}_2\text{Si}$ ,  $\text{Al}_2\text{CuMg}$  and  $\text{Al}_4\text{CuMg}_5\text{Si}_4$  precipitates to have formed during T6 and T7 treatments. Caton, Jones and Allison [158] observed a higher crack growth rate in the T7 condition compared with the T6 heat treatment.

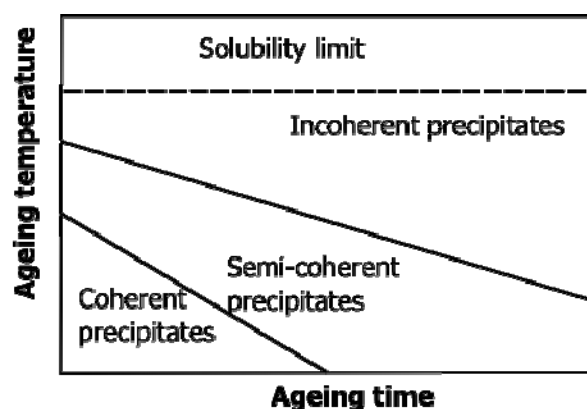


**Figure 3.4:** Formation of precipitates in relation to ageing temperature and ageing time.

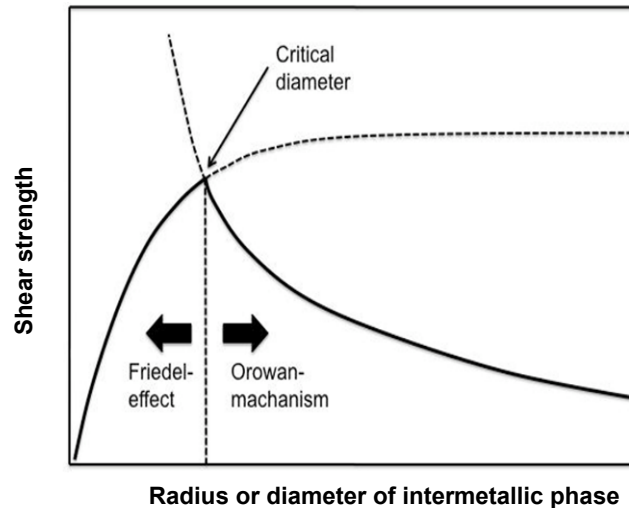


**Figure 3.5:** Effect of particle diameter on dislocation hold-up mechanism.

Some authors have attempted to calculate the increase or decrease of hardness during heat treatment and artificial ageing using physical or microstructural parameters [74, 143, 159-162]. Thalmer and Henne obtained good agreement with experiments using the model of Thomas *et al.* [162] comparing hardness values of some alloys which had been subjected to temperatures of up to 300°C.

## 3.2 STATIC MECHANICAL BEHAVIOUR

This section considers the state of knowledge of the effect of alloying of cast aluminium alloys on their static mechanical properties, namely the tensile and creep properties.

### 3.2.1 Tensile properties

Table 3.1 shows room temperature mechanical properties of a range of cast aluminium alloys in the T6 temper and the as cast condition. Despite the fact that there is quite a range in strength and ductility, there is no clear effect of any particular alloying element, most probably because these alloys have been developed to allow a reduction in silicon content without loss of strength. Besides Al and Si which result in dispersion strengthening by the eutectic, the alloys can be classed as those with secondary additions of Cu, Mg or both to provide precipitation hardening. Not surprisingly the higher Si contents tend to produce less ductile alloys, except where some of the Si is used for precipitation (as in Al-Mg-Si alloys), and higher Mg and Si content combined



tends to increase yield strength, except in the case of AlSi9Mg0.5. The discrepancies are most probably due to differences in phase distribution and grain size brought about by the alloying and, possibly, different casting procedures amongst the various investigators.

**Table 3.1:** Results of RT tensile tests for cast aluminium alloys for a range of authors [15, 163, 164].

<b>Alloy</b>	<b>Tensile Strength, [MPa]</b>	<b>Fracture Strain, [%]</b>	<b>Brinell Hardness, [HV<sub>0.1</sub>]</b>	<b>Yield Stress, [MPa]</b>
AlSi7Mg0.3(Cu)	272	4.1	90	207
AlSi7Mg0.5	320	3	100	240
AlSi8Mg0.4	260	1	90	220
AlSi9Mg0.5	290	4	90	210
AlSi6Cu4	276	3	95	-
AlSi9Cu3 as cast	240	1	80	140

A number of authors have reported that there is no clear yield point in the stress-strain curves at temperatures above 200°C [46, 143, 165]. Generally, stress-strain behaviour in cast aluminium alloys depends on five factors, which are:

- Casting procedure and conditions
- Alloying elements
- Heat treatment
- Temperature of testing
- Strain rate used during testing

Schneider and Feikus [166] assessed the effect of microstructural coarsening in specimens obtained from a range of casting wall thicknesses, which produced a range of solidification conditions and hence a change of mechanical properties. This was in broad accord with findings that a decrease of UTS is linked to coarsening [55]. Other authors [167, 168] have further observed that a high velocity of the solidification front leads to a decrease in SDAS and amount of secondary precipitate, especially  $\beta$ -Al<sub>3</sub>FeSi, both producing better mechanical performance. The effect on precipitation can be explained by an increased amount of dissolved Fe in Al and a reduced nucleation temperature with increasing solidification rate.

Some authors have analysed the effects of different alloying elements on mechanical behaviour of cast aluminium alloys [62, 169]. Döpp *et al.* [170] investigated the influence of Mg and Zn alone and in combination on mechanical properties and observed that an increase of both leads to an increase of UTS and hardness, whilst more than 4% Zn increases the risk of thermal cracking. Zak *et al.* [171] noted an effect on the formation of  $\beta$ -Al<sub>5</sub>FeSi by adding Mg to AlSi6Cu4, while Sarkar *et al.* [172] examined the influence of Fe on ductility and bendability. They found that neither  $\sigma_y$  nor tensile elongation is influenced by Fe additions, although true tensile ductility was reduced with Fe additions, which they attributed to the formation of the needle-like  $\beta$ -Al<sub>5</sub>FeSi phase.

Other authors [173-176] have commented on the change in mechanical properties associated with different solution times and solution temperatures during heat treatment. For all alloys, an increase in fracture strain, elasticity, UTS and hardness can be discerned (at least up to peak ageing) which is related to the influence of precipitation hardening phases, such as Al<sub>2</sub>Cu. Flaig [46] analysed the influence of an interruption of solution treatment on A319 alloys and found that a two-stage treatment improves mechanical properties. The author explained this by a reduction in size and refinement of distribution of the Cu rich phases in the alloy. Again working with A319 alloys, but in the T4 and T7 temper conditions tested between -90°C and 400°C, Rincón *et al.* [177] found that elongation increases and  $\sigma_y$  and UTS decrease above approximately 300°C, which they attributed to changes in particle size and also to particle/ matrix decohesion which the authors identified as a way of relaxing interfacial stresses. Some authors [177, 178] have detected cracking of Si particles during plastic deformation increased by an increase in dendrite cell size and plastic strain.

Dehler *et al.* [179] investigated the influence of strain rate and temperature on ageing of AlSi6Cu4 in the T64 condition and found an increase of elongation and decrease of UTS when the alloy is overaged. Whilst assessing the TMF resistance of alloys, Heikel [13] noted that gravity cast alloys tend to have higher UTS and  $\sigma_y$ . A number of authors [180-189] have described a somewhat erratic deformation behaviour under continuous loading during tensile tests leading to a zig-zag shape to the load extension curve. This effect has been attributed to the condensation of solute atoms near to dislocations, which subsequently require a higher shear stress to move them, rather like Cottrell

atmospheres in carbon steels. This “Portevin - LeChatelier” (PLC) effect increases with increasing temperature where solute atoms are more mobile.

### **3.2.2 Creep**

Creep in metals can be described as plastic deformation which increases with time at constant stress [190] and differs from creep in polymers due to its essentially plastic (irreversible) nature. A creep curve (plot of strain *vs.* time at constant stress and temperature) can be separated into three parts: primary creep, steady state creep and tertiary creep. Primary creep is affected by strain hardening which is characterised by a drop of the creep rate with time. During steady state creep, no change in creep rate is visible leading to a linear creep strain evolution with time and a balance between hardening and softening. In the final stage, the so called tertiary creep, the curve exhibits an increase of the creep rate with time, which is controlled by coarsening and microstructural damage [191]. Increasing the temperature or the stress (or both) causes the entire creep curve (all three stages) to become steeper and the time to rupture (creep failure) to become shorter.

In dynamic applications, creep failure is not usually the design-limiting consideration. Nevertheless, significant creep can occur during thermo-mechanical fatigue, depending upon the mean temperature relative to the melting point (homologous temperature).

Figure 3.6 [192, 193] gives an overview of the creep controlling mechanisms in temperature-stress space expressed by a normalised shear stress and homologous temperature. At low homologous temperatures (below  $0.4T_M$ ) plastic deformation is controlled by the normal mechanism of dislocation gliding under long- and short-range stress fields, limited by lattice friction. Some minor obstacles can be overcome by thermal activation [194-198] and, especially in face-centred cubic materials, some authors have remarked that cutting of forest dislocations at grain boundaries is the controlling mechanism. For temperatures above  $0.4T_M$ , plastic deformation is influenced by diffusion controlled processes, through which vacancies, grain boundaries and dislocations can move to allow non-slip-related plastic deformation.

At higher stresses, dislocation creep, involving climb of dislocations out of their slip planes to overcome obstacles, is the main mechanism. Climb is enabled by vacancy diffusion and, at higher temperatures, by volume diffusion. At lower stresses the

controlling mechanism depends on temperature, Coble creep between  $0.5T_M$  and  $0.9T_M$  and Nabarro-Herring creep at higher temperatures. Both of these mechanisms involve the diffusion of vacancies from areas of higher tensile stress to lower tensile or compressive stress, rather than diffusion-assisted movement of dislocations. The distinction between Nabarro-Herring and Coble creep is that the latter involves vacancy diffusion along grain boundaries and dislocations, which requires a lower activation energy than unassisted vacancy diffusion, hence its dominance at low temperatures.

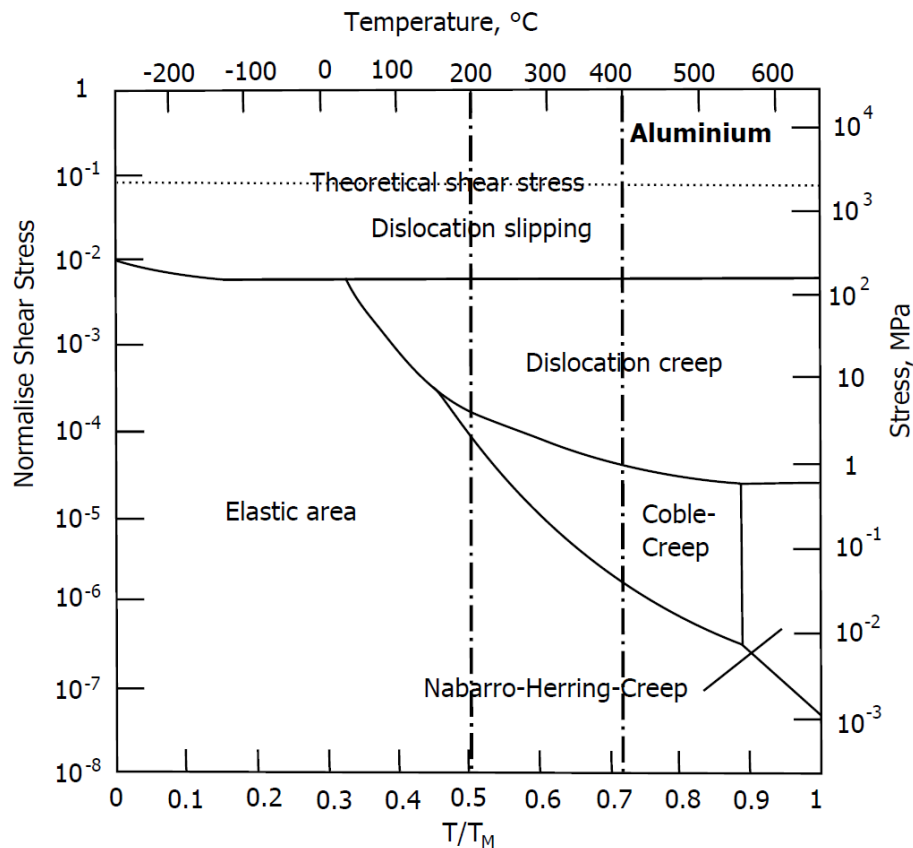


**Figure 3.6:** Deformation mechanism chart for aluminium [191, 192].

Literature data comparing creep in Al-Si-Cu and Al-Si-Mg hypoeutectic cast Al alloys used for engine/ power train components in the temperature range up to  $400^{\circ}\text{C}$  are very scarce. The alloys most commonly tested are based on Al-Mn, Al-Mg, fibre reinforced Al-Si or hypereutectic Al-Si-Mg alloys [199-205]. Creep rupture data are most often reported using a time-temperature parameter [206], such as: Larson-Miller, Orr-Sherby-Dorn, Manson-Succop or Sud-Aviation. Above  $50^{\circ}\text{C}$ , a decrease of stresses can be observed in most alloys. Sandström [199, 200, 207] has analysed creep rupture data taken from a number of sources using four time temperature parameters and also remarked that the mechanism controlling creep in AlSi6Cu4 was dislocation creep

meaning that obstacles are circumvented by dislocation climb. Jaglinski and Lakes [202] studied eutectic and hypereutectic Al alloys and observed lower strains to failure and shorter rupture times for hypereutectic alloys, which they attributed to casting defects rather than composition *per se*. Holecek *et al.* [208] observed that changes of Si or Cu had a smaller effect on creep rupture strength for hypereutectic alloys. Djakovic *et al.* [203] concluded that dislocation multiplication, particle coarsening and grain boundary cavity growth are important damage mechanisms in A2650-T8/ A2615 at 130°C-175°C in tensile creep tests. Overageing prior to creep tests generally leads to an increase in creep strain at a given stress and temperature. Dehler *et al.* [179] investigated the influence of stress and temperature on the creep behaviour of AlSi6Cu4 in the T64 condition and found that the alloy lost 35% of its creep strength due to overageing at 545K for 1hr. Nakajima *et al.* [209] observed an increase in the coarsening rate of  $\theta'$  during creep tests which they attributed to the so called “scavenging effect”, which is based on solute transport by dislocations. They explain the scavenging effect by the collection of solutes around moving dislocations. Furthermore, collected solutes diffuse to growing precipitates along dislocation cores because this is much easier than lattice diffusion in the creep regime. Luft [210] compared T6 and T7 heat treated AlSi7Mg and AlSi5Cu3 alloys and observed shorter creep rupture times and elongations for the T7 condition.

### **3.3 COMPARISON OF MECHANICAL LOADINGS AND IMPACT OF TEMPERATURE**

As far as cylinder heads are concerned, one can distinguish between an area with cold surroundings (cooling jacket) and one with warm surroundings (combustion chamber area). The thermo-mechanical loading situation in the engine and power train components are complex with all components being subject to cyclic loading due to both thermal and mechanical fluctuations at a range of frequencies. Current practice for lifetime assessment involves the following tests. Components with a required lifetime of  $10^2 \leq N_f \leq 10^4$  are tested both with cycling temperature (TMF) and at constant temperature (commonly called, low-cycle fatigue, LCF). Tests for components with a required lifetime of  $N_f \geq 10^4$  and subject to constant temperature with loadings which result in purely elastic strains, are classified as HCF tests. Löhé [211] provides a thorough overview of the various fatigue regimes, including temperature, the number of cycles to

failure and the relation between inelastic strains and the endurance limit, Figure 3.7. Thermal loadings can be classified in terms of the number of cycles ( $\leq 10^4$  LCF and  $\geq 10^4$  HCF) each having three categories [212]. Given that inelastic deformation is known to occur on components in the LCF range, these tests are normally carried out under strain control. If the temperature is constant during an LCF tests the strain rate is decoupled from temperature, but, in TMF tests, the strain rate is dependent on the heating and cooling rates [86, 198, 212, 213]. It is widely accepted that TMF tests simulate real conditions in engine and power-train components better than other tests. Nevertheless, lifetime calculations are mostly based on models featuring isothermal data. The following two sub-sections compare LCF and TMF tests in more detail.

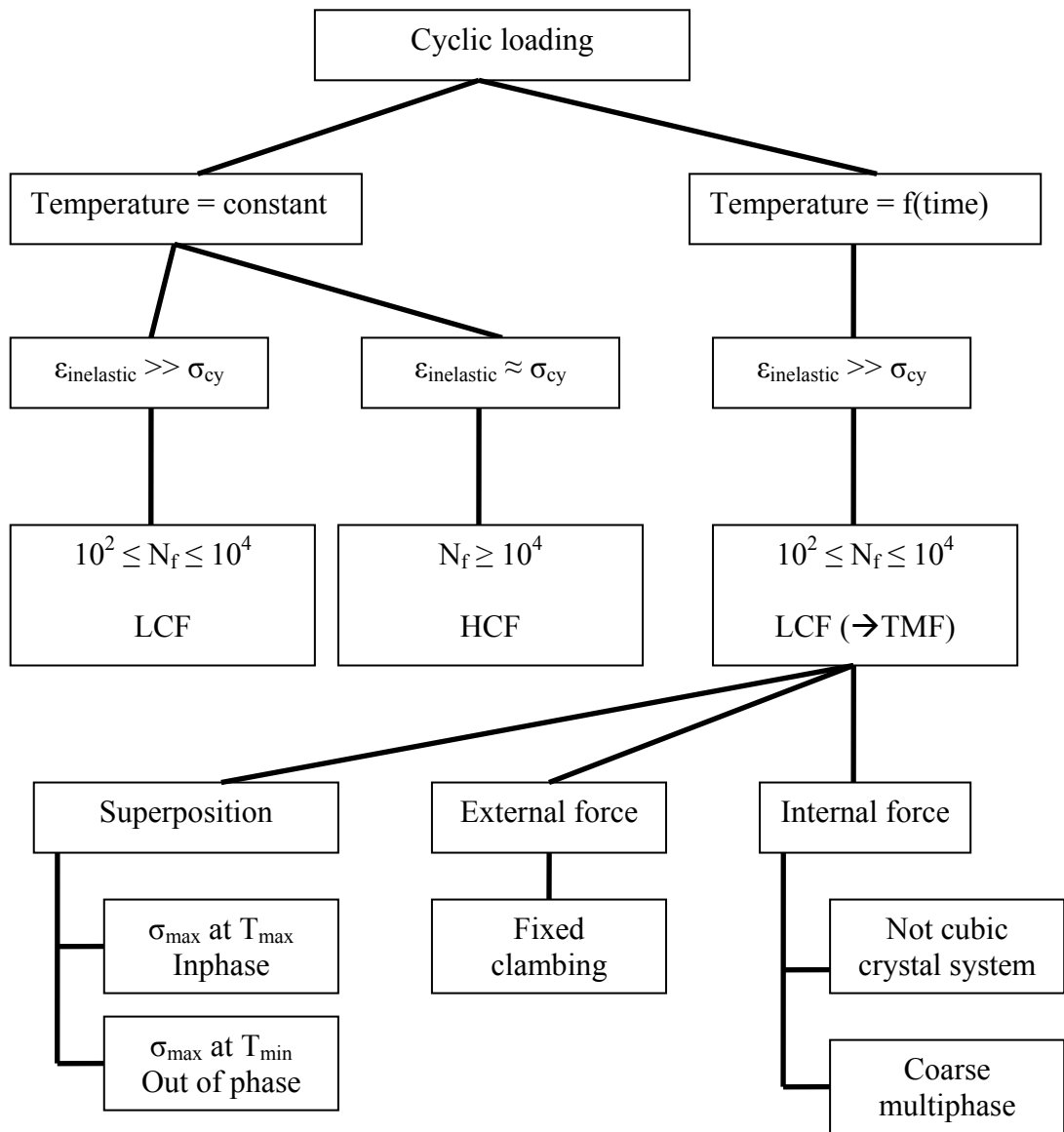


**Figure 3.7:** Classification of thermal fatigue [211].

### 3.3.1 Low Cycle Fatigue with constant temperature

Low cycle fatigue (LCF) is defined in ASTM E 519-74 and is characterized by cyclic plastic loadings, which leads to irreversible microstructural changes [214] even though global stresses may be below the yield strength. The reason for this is local microstructural changes at areas of stress concentration, which accumulate cycle upon cycle and have a macroscopic impact on the fatigue behaviour of the component [215]. Dislocations collect in ladder or cell structures under the reversals of loading and dislocation movements concentrate on a few slip bands, which produces relatively coarse slip steps and hence crack nuclei. Fatigue bands are considered to be caused to a large extent by screw dislocations cross-slipping [86]. Mughrabi and Christ [215, 216] have deduced those processes which can lead to fatigue of materials and components under cyclic loading and the associated dislocation behaviour (Figure 3.8). According to the material and loading situation, the nature and sequence of events may vary.

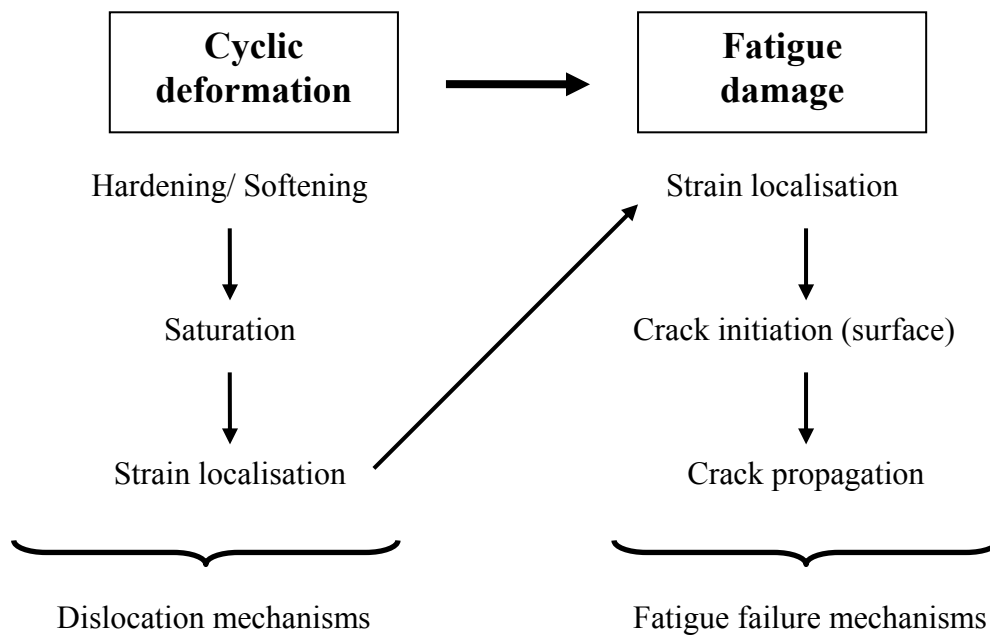


**Figure 3.8:** Chronological overview of damage mechanisms leading to failure [214].

Surface quality and the quality of material processing quality have a clear influence on micro cracking and hence on fatigue behaviour as well. Christ [215] lists the following:

- Material behaviour (grain sizes, intermetallic phase conditions)
- Loading conditions (loading amplitudes, cycle forms, frequencies)
- Process quality (surface qualities, residual stresses)



- Environment (air, vacuum, corrosive media)

as factors having an impact on lifetime.

### 3.3.2 Low Cycle Fatigue with alternating temperature (TMF)

In TMF, microstructural changes occur during each cycle, in LCF they progress over the duration of the tests. The point in the stress cycle at which the highest cyclic temperature occurs is also a factor and Figure 3.9 provides a comparison between in-phase (IP) and out-of-phase (OP) TMF [217]. Typically, microstructural evolve over many cycles in each type.

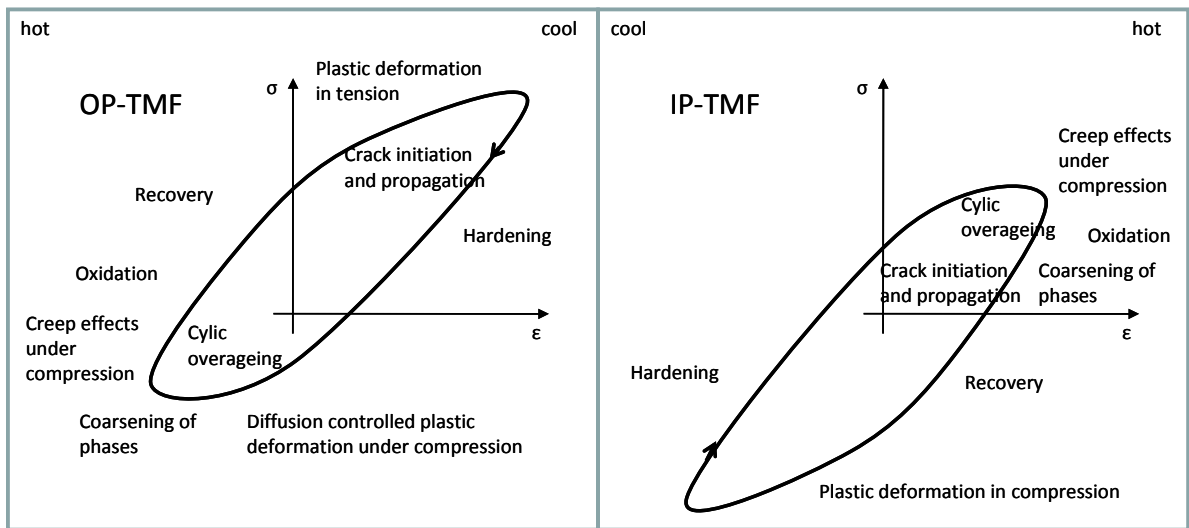


**Figure 3.9:** Damage mechanisms during one IP and OP cycle [217].

For example a cylinder head, there is an inhomogeneous distribution of thermal expansion caused by the cooling channels and the combustion chambers. During warm-up, thermal expansion of material around the combustion chamber is inhibited by the material close to the cooling channel. Such differential thermal expansion leads to compressive stresses in hotter areas during warm-up, and these stresses can relax if the temperature in the surrounding material is high enough. The cyclic mechanical deformation resulting from start-stop conditions leads to damage and failure of components [13-15, 50, 143, 210]. Valve bridges, which are the most heavily loaded areas in a cylinder head, experience tensile stresses when cooling down from combustion temperature, which can lead to crack initiation. As seen above, it is common to refer to the situation where tensile stresses occur under maximum

temperature as in-phase (IP) and where compressive stresses occur under maximum temperature as out-of-phase (OP).

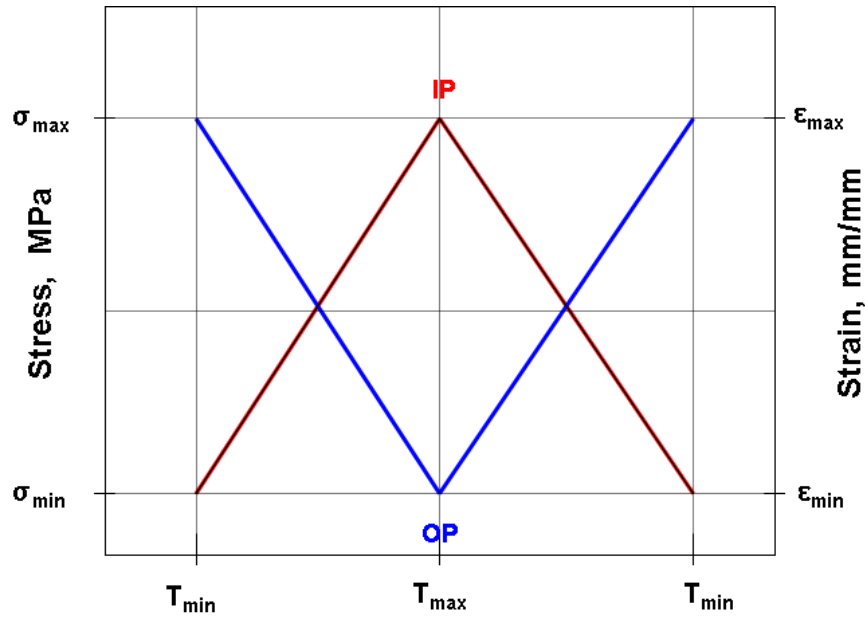


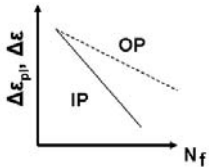
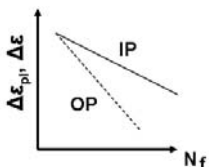
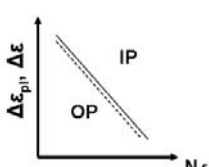
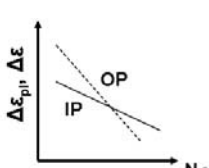
**Figure 3.10:** Mechanical strain/ temperature variation under IP and OP TMF loading.

The relationship between strain and temperature is based on geometry, temperature profile, heating and cooling rates and thermal expansion coefficients. Loadings of a cylinder head or other components under TMF can result in a complex behaviour including relaxation or creep under higher temperature, oxidation of the surface with a brittle oxide layer or overageing of precipitates evoked by long time exposures beyond the ageing temperature, all of which reduce the number of cycles to failure. Table 3.2 [218] shows the classification of TMF lifetime behaviour which was developed by Nitta and Kuwabara [219, 220], who identified four categories:

- **Type I** exhibits shorter lifetimes under IP conditions compared to OP caused by tensile stresses under maximum temperature which lead to creep damage effects. Fracture behaviour is intercrystalline because pores tend to form at diffusion paths.
- In contrast to Type I, **Type O** shows detrimental effects associated with tensile stresses at minimum temperature which lead to a reduced lifetime for the OP condition over the IP condition. These detrimental effects are associated with oxidation or diffusion.

- **Type E** shows no predominant damage modes so that the lifetime behaviour for IP and OP is nearly the same.
- **Type E'** shows a shorter lifetime for IP conditions (high stress at maximum temperature) under high strain amplitudes. Creep influences the damage behaviour only at higher strain amplitudes and higher temperatures.

**Table 3.2:** Classification of the TMF behaviour according to Nitta and Kuwabara [219, 220].

Type	Predominant damage mode
	<b>Type I:</b> IP-loading conditions cause earlier failure
	<b>Type O:</b> OP-loading conditions lead to shorter fatigue life
	<b>Type E:</b> IP- and OP-loading conditions show nearly the same fatigue life
	<b>Type E':</b> IP-loading conditions lead to short fatigue life at high strain amplitudes

The following paragraphs provide a brief overview of the main current foci of TMF research, discussed in terms of the factors influencing lifetime.

### **3.3.2.1 Influence of heat treatment**

In [221], TMF behaviour of A319-T7 was analysed and compared to a unified creep-plasticity constitutive model. Results revealed that the stress-strain behaviour of A319-T7 is influenced by decomposition of metastable  $\theta'$  precipitates within dendrites which lead to softening. Furthermore, a gradual coarsening of the  $\theta$  phase takes place. In [143, 210] the author investigated AlSi7Mg-T6, AlSi10Mg-T6, AlSi5Cu3-T7, AlSi6Cu4-T6/T7 and AlSi8Cu3-T1 with and without dwell times, a minimum temperature of  $T=50^{\circ}\text{C}$  and maximum temperatures of  $T=225^{\circ}\text{C}$ ,  $250^{\circ}\text{C}$ ,  $275^{\circ}\text{C}$  and  $300^{\circ}\text{C}$ . OP results in [210] reveal higher plastic strains for the peak aged alloy than for the T7 alloy. AlSi5Cu3-T7 shows higher stresses under tension and compression, which the author attributes to higher resistance to overageing. Softening of semi-coherent alloys only appears during higher testing temperatures in contrast to peak aged alloys which show hardening at a lower temperature and saturation at higher temperatures. Henne [143] investigated the influence of temperature and the relationship between  $\epsilon_{\text{th}}$  and  $\epsilon_{\text{mech}}$ . Furthermore, he analysed the influence of different heat treatment conditions on lifetime behaviour under TMF loadings. AlSi6Cu4, which was in the T7 temper condition, showed no influence which could have been caused by the heat treatment.

### **3.3.2.2 Influence of casting procedure**

The authors of [222-224] examined TMF behaviour of A319, especially the effect of different SDAS, and compared these data to a two-state-variable unified model. The maximum stresses reached for small SDAS are nearly 30% higher compared to larger SDAS. Properties can be improved by reducing SDAS and pore volume fraction. A modification of microstructure by adding strontium leads to a reduction of SDAS by a quarter and to a lifetime twice the original value.

### **3.3.2.3 Influence of alloying elements**

Sehitoglu *et al.* [225] investigated the influence of different Fe contents on TMF behaviour of an A319 alloy. Results showed higher stress levels for lower Fe contents and also more rapid softening for higher Fe levels. Bose-Filho *et al.* [226] mentioned an improvement by refining the microstructure or by a modifying the  $\alpha$ -phase. Working on AC4CH, Kaneso *et al.* [227] evaluated strontium modified Al alloys using tension-

TMF- and Charpy impact tests. Results showed that higher strain rates can be borne at higher strontium contents. Furthermore, lifetime can be improved by reducing the amount of plastic strain contents and by increasing tensile ductility. Flaig [46] worked with different alloys (AlSi10Mg, AlSi12CuMgNi and AlSi6Cu4) and assessed the influence of different maximum temperatures and the development  $\epsilon_{a,t}$  on the lifetime behaviour in OP tests. All alloys revealed a decrease in lifetime with increasing maximum temperature. For lifetimes between  $10^3 \leq N_f \leq 10^4$ , the best fit lines for the three alloys were nearly equal, but, for lifetimes below  $10^3$  cycles, AlSi10Mg exhibited shorter lifetimes than AlSi12CuMgNi or AlSi6Cu4.

#### **3.3.2.4 Influence of loading conditions**

A number of authors have examined the influence of a superimposed, intermittent HCF loading during TMF tests. In [143, 228] TMF tests with superimposed HCF were conducted on AlSi6Cu4, AlSi10Mg and AlSi8Cu3 in a temperature range between 50°C and 300°C. Above 250°C, a decrease of compressive stresses was observed, which is caused by dynamic relaxation and creep effects. The magnitude of this decrease was linked to temperature, increasing temperature leading to increased relaxation. This was attributed to diffusion controlled plastic deformation which is promoted by increasing temperature. Luft *et al.* [229] investigated the behaviour of AlSi7Mg-T6 under TMF with superimposed HCF, with a range of mechanical ( $\epsilon_{\text{mech}}$ ) to thermal ( $\epsilon_{\text{th}}$ ) strain ratios and dwell times. Results indicated that plastic strain increased when the maximum temperature is increased, which is a combined effect of increasing  $\epsilon_{\text{tot}}$  and decreasing  $\sigma_y$ , which is in turn caused by overageing. The overaged condition, which forms during the tests, was indicated by a coarsening of the Mg<sub>2</sub>Si phase. Besides this, the authors were able to show that overageing increases when maximum temperature rises. Above a threshold temperature of 250°C, they observed that mean stress rapidly decreased after the first cycle as a result of plastic deformation during heating up. By contrast, below this threshold, a slow decrease was apparent. Beck *et al.* [228] remarked that TMF tests with superimposed intermittent HCF loading exhibit a shorter lifetime than do TMF/HCF tests without dwell times. Furthermore, they observed that a superimposed HCF subjected to tensile loading for only 5s without dwell times leads to the same lifetime as seen in tests with HCF. In [228, 230], TMF tests with superimposed HCF loading and 120s dwell times at maximum temperature were conducted. The authors observed a

threshold of  $\varepsilon_{a,t}^{mech} = 0.02\%$ , below which lifetime effects by HCF loading were negligible, whereas, above this threshold, the number of cycles to failure decreased with increasing HCF amplitude and frequency. Cracks initiated at the interface between Si particles and  $\alpha$ -Al for both TMF and superimposed TMF tests. Cracks propagated along the eutectic regions for TMF which is a result of the thermal mechanical misfit of brittle components in contrast to a ductile matrix and cracks alongside slip bands in  $\alpha$ -Al crystals of superimposed TMF. By contrast, slip band density increased with increasing  $\varepsilon_{a,t}^{mech}$  in HCF. Toyoda and colleagues [231] reported an orientation of precipitates during TMF loading of an Al-Si-Cu-Mg alloy between 50°C and 250°C under OP conditions. Their results revealed a decrease of stresses under maximum and minimum temperature caused by overageing, which is indicative of a coarsening of the precipitates. Observations before and after testing showed the transformation of  $\theta''$  phase to  $\theta'$ -Al<sub>2</sub>Cu precipitates. Furthermore, the authors observed an orientation of the precipitates parallel to the loading axis. The authors explain this by a redissolution of the  $\theta''$  phase, followed by nucleation  $\theta'$  and Ostwald ripening. Here, precipitates which are perpendicularly orientated to the loading axis shrink, while precipitates, which are orientated parallel, grow. The preferential orientation mechanism of precipitate plates by stress-ageing is due to a large negative misfit in the perpendicular direction relative to the plate surface. When compressively loaded perpendicular to the surface of precipitate plates during ageing, the misfit strain adjusts by thermal processes so that strain energy of the entire matrix is lowered. It can be concluded that  $\theta'$  precipitates orient themselves preferentially in a single direction due to the application of compressive stresses at high temperature during TMF loading.

### 3.4 DAMAGE MECHANICS COMPUTATION AND SIMULATION

Simulation and modelling of materials and their behaviour have recently received significant attention, *inter alia* with regard to applications to engine blocks where add-ins for FEM software packages have been developed to simulate and model mechanical, thermal and TMF behaviour. However, some of these applications are limited in their capacity to simulate exact lifetime behaviour or stress-strain behaviour for want of data on the effect of alteration of aluminium alloy microstructure at elevated temperatures on their fatigue strength.

Danzer [232] was one of the first to categorise models and methods for LCF as follows:

- Physical models
- Damage mechanics models
- Fracture mechanics models
- Empirical models

Riedler [50] subclassified damage mechanics into models or methods for cyclic deformation behaviour and those describing lifetime behaviour.

Cyclic deformation behaviour has been further sub-classified [215] into:

- Empirical methods
- Continuum mechanics methods
- Material physical models
- Multi-component models

Fatemi and Yang [233] presented a survey of cumulative fatigue damage and life prediction theories for metals and alloys, and grouped them into six categories:

- Linear damage evolution and linear summation
- Nonlinear damage curve and two-stage linearization approaches
- Life curve modifications to account for loading interactions
- Approaches based on crack growth concepts
- Continuum damage mechanics
- Energy based approaches

The focus of the work in this thesis is on observing the cyclic stress-strain behaviour during TMF and in determining TMF lifetimes, so these aspects are discussed in more detail below.

#### ***3.4.1 Cyclic stress-strain behaviour per TMF cycle***

Continuum mechanics methods seek to calculate stress-strain-curves based on plastic and visco-plastic flow rules. A number of models have been developed in the automotive industry to simulate damage behaviour of components. One is the model of

Sehitoglu which is implemented in FEMFAT and which tries to simulate the TMF behaviour by separating damage in fatigue, oxidation and creep. It should be mentioned that their fatigue parameters are based on room temperature LCF tests [234-236]. Another method, which has been adopted and modified by several authors from Chaboche and Lemaitre [237-243] was used by Seifert. In [244], he used a Chaboche model in combination with the model of Gursson to calculate the thermo-mechanical fatigue behaviour of “porous” cast iron engine and power train components. Chaboche separated the total strain rate into an elastic, an inelastic and a thermal part [245]:

$$\dot{\varepsilon}_{tot} = \dot{\varepsilon}_{el} + \dot{\varepsilon}_{in} + \dot{\varepsilon}_{th} \quad (1)$$

The individual parts can be calculated in detail by the following formulas. The elastic strain rate is a result of the uni-axial relationship between stress and young modulus and can be obtained from:

$$\dot{\varepsilon}_{el} = \frac{\dot{\sigma}}{E} \quad (2)$$

The inelastic strain rate is a function of the back stress “ $\chi$ ” and the drag stress “R”. The back stress considers the “Bauschinger Effect” and the drag stress the translation or rotation of the yield surface by kinematic hardening.

$$\dot{\varepsilon}_{in} = \left\langle \frac{f}{Z} \right\rangle^n \text{sgn}(\sigma - \chi) \quad (3)$$

$$f = |\sigma - \chi| - R - k \leq 0 \quad (4)$$

The thermal strain rate considers the different thermal strains in the different temperature ranges during TMF tests.

$$\dot{\varepsilon}_{th} = \alpha_{th} \cdot \left( \dot{T}_{current} - \dot{T}_{initial} \right) \quad (5)$$

### 3.4.2 TMF lifetime behaviour

The models and methods of damage mechanics are based on continuum mechanics and were first developed by Rabotnov [246] and Kachanov [247], who attempted to explain



the development of cracks and pores in TMF. A typical example is the model of Chaboche [238] which has been modified by different authors in different ways. The model [248] is developed for creep-fatigue damage and considers the instantaneous damage per cycle ( $dD/dN$ ) to accumulate per cycle. When  $D=1$ , the accumulation is complete and the component has failed. The damage differential can be expressed:

$$dD = \left(\frac{\sigma}{A}\right)^r (1-D)^{-k} dt + \left[1 - (1-D)^{\beta+1}\right]^\alpha \cdot \left[\frac{\sigma_{\max} - \sigma_m}{M(1-D)}\right]^\beta dN \quad (6)$$

where  $\sigma_{\max}$  is the maximum stress,  $\sigma_m$  is the mean stress,  $M$  is a factor which takes into account the mean stress development and  $\alpha, k, \beta$  are parameters which take into account the temperature.

Dendorfer [249] took a different approach, using an integral damage parameter:

$$D = 1 - \frac{E_{Sec}}{E_0} \quad (7)$$

where  $E_{Sec}$  is the secant modulus per cycle and  $E_0$  is the initial Young's modulus, obtained from pre-tests. Again, following conventional fatigue damage terminology  $D=0$  corresponds to the undamaged condition and  $D=1$  corresponds to failure.

Empirical methods of lifetime prediction use parameters (such as temperature, strain, stress, frequency, dwell times, the Young's modulus) to describe material behaviour in a simple correlative way, which does not require a model for physical material behaviour. Such methods include:

- The Ramberg-Osgood model
- Damage parameters
- Energy density
- The Manson-Coffin-Basquin model
- Cumulative damage models

Nihei *et al.* [250] compared the damage parameters of Smith-Watson-Topper, Morrow, Morrow-Landgraf, Heitmann [251], Bergmann, Haibach and Nihei-Heuler-Boller-Seeger, all of which combine stress amplitudes or mean stress and strain amplitudes or

inelastic strains to calculate the cyclic deformation which acts during one cycle. They used structural steels, cast steel and two aluminium alloys tested under axial strain control for this comparison. They concluded that, for tests with a developing mean stress effect, the parameters of Smith-Watson-Topper,  $P_{SWT}$  [252], Ostergren,  $P_{Ost}$  [253] and Morrow [254]

$$P_{Ost} = (\sigma_a + \sigma_m) \cdot \Delta \varepsilon_p \quad (8)$$

$$P_{SWT} = [(\sigma_a + \sigma_m) \cdot E \cdot \varepsilon_a]^{0.5} \quad (9)$$

$$P_M = \frac{\sigma_a}{\left(1 - \frac{\sigma_m}{c_1}\right)} + E \cdot \varepsilon_p \quad (10)$$

cover the effect of mean stress best. The parameters of Bergmann [255] and Erdogan [256] gave the best estimation accuracy among the parameters tested [250]. All of the parameters mentioned above were developed for LCF, although some authors have attempted to apply them to TMF data [46, 257] as well. Unlike Flaig [46], Hallstein [257] found a good correlation between cycles to failure and  $P_{SWT}$  for cast iron. Flaig compared damage parameters resulting from isothermal LCF and TMF tests. He concluded that a linear relationship exists and, as far as damage is concerned, TMF tests result in shorter lifetimes. He attributes this to the microstructure which develops differently with varying the test frequencies.

The energy-based models and methods attempt to associate damage per cycle with the dissipation of energy caused by plastic deformation. A part of the irrecoverable energy in each cycle is absorbed due to inelastic strain absorption and another part is converted into heat [258, 259]. The first to describe the energy dissipated during one cycle was Bairstow [260] in 1910 and the cumulative energy dissipated during the lifetime is:

$$W_p = \Delta W_p \cdot N_f \quad (11)$$

where  $\Delta W_p$  is the dissipated inelastic energy per cycle (area of hysteresis loop) and  $N_f$  is the number of cycles to failure. Morrow [261, 262] showed that the lifetime dissipated energy in cyclic tests is twice that in tension tests. Riedler [263, 264], used the whole energy per cycle and, in his investigation of ductile AlCuBiPb alloys, found a good correlation of the type:

$$N_f = \frac{\Delta W_{\varepsilon_p, \sigma_a, N_f/2}^{mech}}{\varepsilon_{a,p, N_f/2}^{mech} \cdot \sigma_{a, N_f/2}} \quad (12)$$

Since tests can be done under stress-, strain-, force- or displacement-control, it is important to specify which is being used when reporting fatigue test results. Since cyclic strain is the root damaging factor responsible for fatigue, plots of strain amplitude against lifetime are the most useful. The strain amplitude-lifetime plot is a superposition of the elastic and plastic components and Manson-Coffin and Basquin have formulated this as follows [50, 232, 265, 266]:

$$\varepsilon_{a,t} = \varepsilon_{a,el} + \varepsilon_{a,p} = \frac{c_1}{E} \cdot (2N_f)^{-c_2} + c_3 (2N_f)^{-c_4} \quad (13)$$

Some authors use temperature-Wöhler-curves in their research on TMF which obscures the dependency between different strains [50]. Other authors use hardness values [267], the Young's modulus, dwell times, frequency, or other parameters to develop the Manson-Coffin and Basquin plots.

Boussac and Calais [161] developed a general formula to predict hardness as a function of time ( $t$ ) and temperature ( $T$ ) to reduce the number of temper tests which need to be done on a given alloy:

$$H_B(t, T) = H_{BS} + \frac{(H_{B0} - H_{BS}) - e^{A \cdot \ln T + B \cdot \ln t - C}}{1 + e^{A \cdot \ln T + B \cdot \ln t - C}} \quad (14)$$

where  $H_{B0}$  is the hardness in the initial state,  $H_{BS}$  is the hardness in the overaged state, and  $A$ ,  $B$  and  $C$  are constants. In principle, knowledge of the relevant constants allows hardness values to be used as a damage criterion as well.

### 3.5 SUMMARY

This review has shown the extensive work that has already been done in the area of TMF of aluminium casting alloys for automotive use. The contribution in this thesis will focus on the following aspects of research that have not sufficiently been established yet:

- Influence of time on the hardness development during elevated temperature exposure of cast aluminium
- Influence of elevated temperature and loadings on creep results
- Influence of strain rates and elevated temperature during LCF tests
- Influence of temperature gradients inside the gauge length of test specimen
- Stress and inelastic strain development of components which are related to a temperature gradient if temperature range is elevated up to 400°C
- Comparison between IP and OP TMF loadings
- Relationships encompassing all currently used cast aluminium alloys
- Effect of HIP pre-treatment
- Influence of varying alloying elements
- Significance of damage parameters for IP and OP loading with temperature cycling between 200°C-400°C

In addition, the possibility of implementing the test results in a “Chaboche” simulation model was examined.

## **CHAPTER 4 – MATERIALS AND METHODS**

In order to allow engines to work at higher temperatures, the TMF lifetime behaviour of cast aluminium alloys currently used for cylinder head alloys needs to be further evaluated. Also, after running the engine in practice, the material in the hot area of the cylinder head (injection plug, valve bridges) will be overaged, and so some developments in alloys and/ or treatments are likely to be necessary.

T6 is the standard heat treatment used in the automotive industry for currently-used (Al-Si-Mg and Al-Si-Cu alloys). For improvement, variations in the casting process which result in different SDAS values as well as different pre-treatments must be envisaged. Because of its established thermal performance, AlSi6Cu4 in the T6 condition is used as the reference alloy.

In order to quantify the potential of technically relevant Al-Si cast alloys, six conventional chill cast materials were tested in the T6 heat treatment condition. The testing focused on high temperature cylinder head applications and, accordingly, LCF and TMF experiments were carried out in the range 200-400°C. For additional information, creep tests and stress-strain experiments (CERT) were performed along with some heat treatment tests for temper response. Specific attention was focussed on microstructure, which was characterised before and after mechanical testing using optical microscopy (OM) and scanning electron microscopy (SEM). The latter was used in combination with energy dispersive spectroscopy (EDS).

### **4.1 MATERIALS**

The chemical compositions, obtained using spectroscopy (SPECTROMAXx), of the six alloys can be found in Table 4.1. Each of the alloys tested was from a single cast. The alloys were chosen to give a range of compositions around the reference alloy AlSi6Cu4, varying the Si and Cu contents, and replacing Cu with Mg.

**Table 4.1:** Chemical composition of tested specimens in wt.-%.

	Si	Mg	Cu	Fe	Mn	Zn	Ni	Cr	V	Ti	Al
<b>AlSi7Mg0.3(Cu)</b>	7.1	0.3	0.5	0.19	0.1	< 0.01	< 0.01	< 0.01	< 0.01	0.15	basis
<b>AlSi7Mg0.5</b>	6.22	0.5	0.49	0.35	0.21	< 0.01	< 0.01	< 0.001	< 0.01	0.2	basis
<b>AlSi8Mg0.4</b>	8.2	0.41	< 0.01	0.1	0.06	0.01	< 0.01	< 0.01	< 0.01	0.1	basis
<b>AlSi9Mg0.5</b>	9.16	0.49	0.24	0.14	0.04	< 0.01	< 0.01	< 0.01	< 0.01	0.18	basis
<b>AlSi6Cu4</b>	6.63	0.32	3.34	0.13	0.01	0.01	< 0.01	< 0.01	0.01	0.2	basis
<b>AlSi9Cu3</b>	8.08	0.2	2.22	0.91	0.26	1.12	0.12	0.05	< 0.01	0.04	basis

## 4.2 HEAT TREATMENT

The heat treatment parameters for each of the alloys tested are summarised in Table 4.2. All heat treatments were carried out in accordance with automotive industry standards, and furnace temperature was controlled within  $\pm 2^\circ\text{C}$ .

**Table 4.2:** Heat treatments for the cast Al alloys tested.

	Condition	Solution Temperature, [°C]	ST holding Time, [hr]	Quenching Temperature, [°C]	Ageing Temperature, [°C]	Ageing time, [hr]
<b>AlSi7Mg0.3(Cu)</b>	<b>T6</b>	530	14	RT	160	10
	<b>T7</b>	540	12	RT	225	8
<b>AlSi7Mg0.5</b>	<b>T6</b>	530	14	RT	160	10
<b>AlSi8Mg0.4</b>	<b>T6</b>	540	8	RT	170	7
<b>AlSi9Mg0.5</b>	<b>T6</b>	540	8	RT	170	7
<b>AlSi6Cu4</b>	<b>T6</b>	505	12	RT	155	3
	<b>T7B</b>	500	8	< 70	260	4
<b>AlSi9Cu3</b>	<b>T6</b>	505	12	RT	155	5

In addition to the mechanical test specimens, a set of heat-treated specimens of AlSi7Mg0.3(Cu) (representative of the Al-Si-Mg and Al-Si-Cu alloys studied) and AlSi6Cu4 (the reference alloy) were subjected to further high-temperature exposures. Specimens were machined to a diameter of 10mm and a length of 15mm and, following the T6 and T7, treatments were exposed to further ageing at the T6 or T7 temperature for periods up to 120hr. Also, specimens which had received a T6 treatment were exposed for the same times at 200°C or 400°C corresponding to the maximum and minimum temperatures of the TMF tests. Table 4.3 summarises the tests. The hardness and phase distribution were then assessed by carrying out micro hardness tests on the  $\alpha$ -Al and the size, morphology and orientation of: Si, Mg<sub>2</sub>Si, Al<sub>2</sub>Cu,  $\alpha$ ,  $\beta$  and  $\pi$  phases assessed. Particular attention was paid to the  $\beta$ -phase which has a deleterious effect on ductility and tensile strength.

**Table 4.3:** Overview of temper tests.

Temperature exposure	AlSi7Mg0.3(Cu)	AlSi6Cu4
T6	X	X
T6+200°C	X	X
T6+400°C	X	X
T7	X	—
T7+200°C	—	X
T7+400°C	—	X

### 4.3 MECHANICAL TEST SPECIMEN GEOMETRY

For the CERT, creep, LCF and TMF tests, cylindrical test specimens were machined (Figure 4.1) with a diameter in the gauge length of 10mm and a tolerance of  $\pm 0.02\text{mm}$ . To obtain a reproducible surface quality, all specimens were surface ground using up to 4000 grit before testing. Spot measurements of roughness lay in a range between  $R_a=0.1$  to  $0.4\ \mu\text{m}$ .

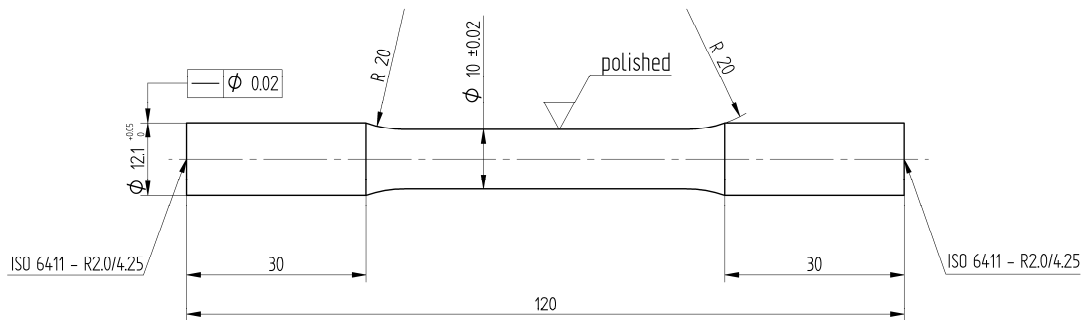


**Figure 4.1:** Mechanical test specimen geometry.

### 4.4 TEMPERATURE CONTROL

During all isothermal tests temperature was measured by thermocouples of the K-type and controlled by an [Omega Newport i8](#) PID controller. Additionally, an [Omega Newport TC-08](#) data acquisition device was used to record when a detrimental temperature deviation occurred. Before a test, a temperature calibration was done to obtain the temperature distribution within the chamber and along the gauge length of the specimen. For this purpose, five thermocouples were attached within the gauge length and calibration revealed a maximum deviation in the temperature of  $\pm 2^\circ\text{C}$  along the gauge length.

### 4.5 ISOTHERMAL LOW CYCLE FATIGUE TESTS

All LCF tests were conducted on a 100kN servo-hydraulic [MTS 810](#) test rig. Heating was applied using a two-batch convection furnace whose temperature was held within



$\pm 1^\circ\text{C}$  by a Eurotherm PID controller which also provided a 30mm length of isothermal temperature field over the gauge length. Specimens were fixed in water cooled grips. The test rig was equipped with alignment regulation using a 3D GOM-Aramis measurement system to measure and calibrate the orientation of the clamps before testing. Before running a test, specimens were heated up without load to ensure an appropriate temperature; then a holding time of 5min was used to guarantee a homogeneous temperature field in the specimen. Strain and force were measured using an MTS high temperature extensometer capable of operating up to  $400^\circ\text{C}$  and a 100kN load cell was fixed on the crosshead.

A schematic view of the test rig with input and output parameters is shown in Figure 4.2.

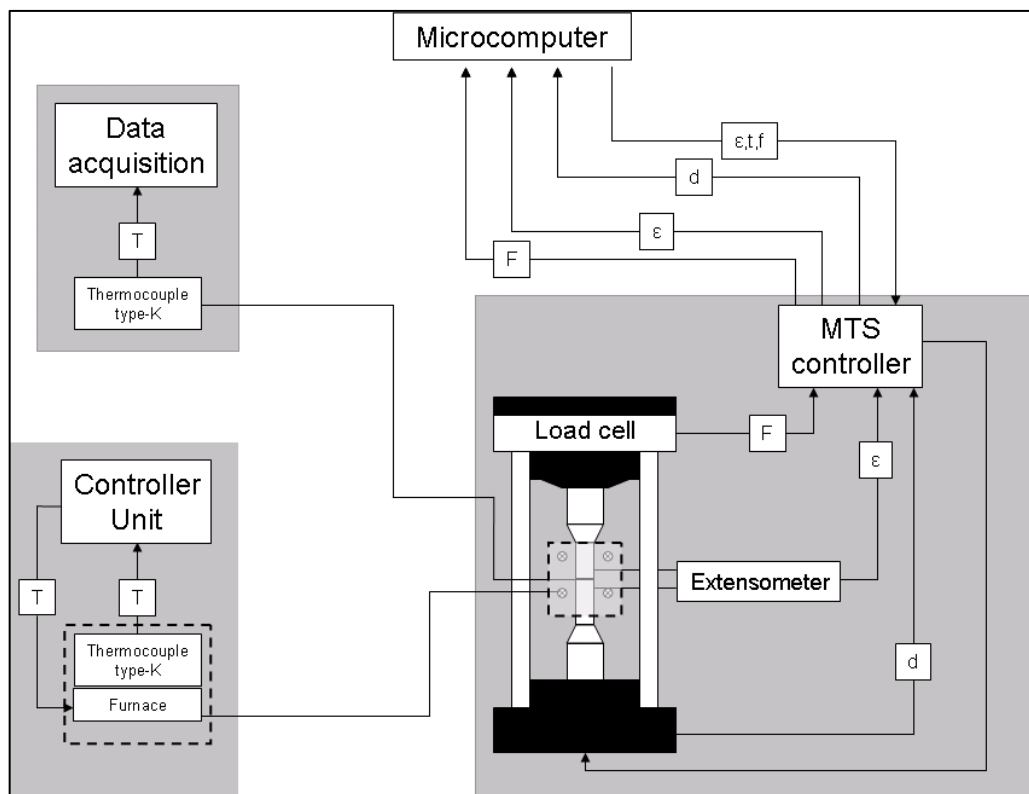


**Figure 4.2:** Schematic overview of controller, data acquisition, input and output signals for LCF test rig.

All isothermal LCF tests were conducted under total strain control. Following the parameters for the TMF tests, the LCF tests were carried in tension-compression with zero mean strain using a triangular waveform with a constant period of 80s and different strain amplitudes. To obtain a better performance for tests with higher plastic strain a

superordinate controller was used to adapt the control parameters to the changing material parameters. Tests were conducted for AlSi6Cu4 at 200°C and 400°C. An internal threshold controller enabled a defined stop before fracture or other user-defined criteria, which, in this case, were a 60% drop in maximum stress or at  $N=10^4$  cycles. A summary of the isothermal low cycle fatigue tests at 200°C and 400°C is given in Table 4.4.

**Table 4.4:** LCF tests carried out on AlSi6Cu4-T6.

Temper condition	Temperature, [°C]	$\Delta\varepsilon_{\text{mech}}/2$ , [%]	Strain rate, [ $s^{-1}$ ]
T6	200	0.2	$1 \times 10^{-4}$
T6	200	0.35	$1.75 \times 10^{-4}$
T6	200	0.5	$2.5 \times 10^{-4}$
T6	200	0.7	$3.5 \times 10^{-4}$
T6	400	0.2	$1 \times 10^{-4}$
T6	400	0.35	$1.75 \times 10^{-4}$
T6	400	0.5	$2.5 \times 10^{-4}$
T6	400	0.7	$3.5 \times 10^{-4}$

#### 4.6 CERT, CREEP TESTS

All CERT, creep tests were carried out on the test rig described above. Temperature ranges followed the ones used for the LCF tests, as did the procedure before running a test. The CERT, creep tests were terminated at a strain of 8%, as measured by a high temperature extensometer with a gauge length of 12mm. A summary of the alloys, heat treatments and temperatures used for the CERT is presented in Table 4.5.

**Table 4.5:** CERT conditions used for the different Al-Si-Mg and Al-Si-Cu alloys.

Material condition	Temperature, [°C]	Strain rate, [ $s^{-1}$ ]
AlSi6Cu4 (T6)	200	$3 \times 10^{-4}$
AlSi6Cu4 (T7)	200	$3 \times 10^{-4}$
AlSi6Cu4 (T6)+HIP	200	$3 \times 10^{-4}$
AlSi6Cu4 (T6)	400	$3 \times 10^{-4}$
AlSi6Cu4 (T7)	400	$3 \times 10^{-4}$
AlSi6Cu4 (T6)+HIP	400	$3 \times 10^{-4}$

AlSi9Cu3 (T6)	400	$3 \times 10^{-4}$
AlSi7Mg0.5 (T6)	400	$3 \times 10^{-4}$
AlSi8Mg0.4 (T6)	400	$3 \times 10^{-4}$
AlSi9Mg0.5 (T6)	400	$3 \times 10^{-4}$

#### 4.7 THERMO-MECHANICAL FATIGUE TESTS

All TMF tests were conducted on a rig based on a 250kN MTS 810 servo-hydraulic test machine. The rig was designed to be compliant with the European Standard, specifically devised for TMF tests [268]. This standard provides a detailed description of the test setup, pre-cycling procedure, test execution, analysis and reporting [268]. During the pre-cycling, the thermal strain,  $\epsilon_{th}$ , and Young's modulus are measured and a zero stress test is done. A schematic diagram of the test rig and data handling is given in Figure 4.3.

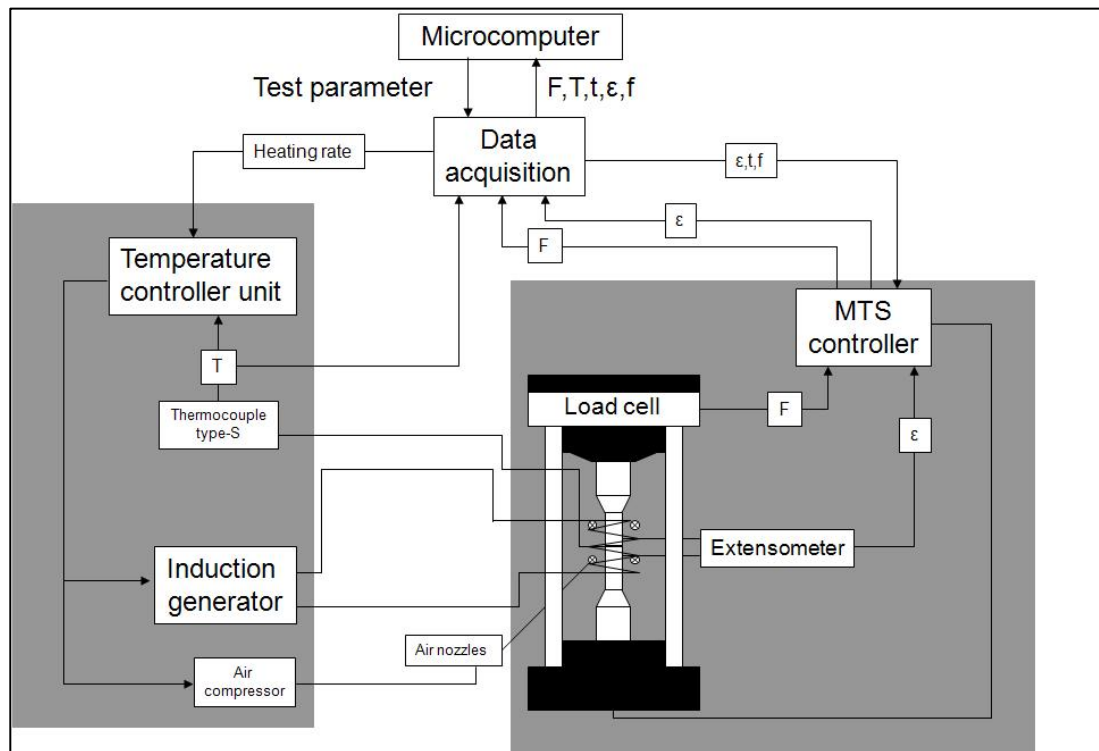


**Figure 4.3:** Schematic overview of controller, data acquisition, input and output signals for the TMF test rig.

Specimens were heated using a 5kW [Hüttinger](#) high frequency generator and an induction coil with the capability of raising the temperature at a rate,  $\dot{T} = 5K/s$  and cooling was achieved by conduction into the water cooled grips, thermal radiation and by forced convection using four air nozzles fixed into the ends of the gauge length. In contrast to the Code of Practice [268], which requires the axial temperature gradient along the gauge length to be confined to  $\pm 2\%$  of the temperature range, the temperature gradient was selected here to reflect the gradients in a typical cylinder head, where temperature differences of up to  $50^\circ\text{C}$  over 6mm can be experienced [269]. A special PID controller driving the high frequency generator or the valves for the air nozzles was used to regulate positive or negative deviations from the specified gradient and mean. The maximum frequency was determined from the heating rate to be 0.0125Hz corresponding to a cycle time of 80s. In the interest of minimising temperature deviation in the fixings and in the induction coil, an auxiliary temperature control device was used to provide a constant cooling air temperature of  $8^\circ\text{C}$  with a deviation of  $\pm 1^\circ\text{C}$ . During the tests, the temperature in the gauge length was determined using S-type thermocouples of diameter 0.1mm. Before running the tests, the temperature was calibrated with a thermal imaging camera system and also with a [Bartec](#) R2540 four channel pyrometer. Measured data were compared to data from a special calibration specimen which had five thermocouples distributed over the gauge length.

By switching from force control to mechanical strain control after the pre-cycling procedure was finished, the TMF tests were made to start at the mean temperature with a force of 0N, a mechanical strain,  $\varepsilon_{\text{mech}}=0$  and a dwell time of 40s at a time when the gauge length is completely heated up.

All of the tests were conducted in the temperature range between  $200^\circ\text{C}$  and  $400^\circ\text{C}$  to examine the consequences of an enhancement of temperature in cylinder heads. Also, in-phase (IP) and out-of-phase (OP) loading were applied. Mechanical strain amplitude values were varied between  $\Delta\varepsilon_{\text{mech}}/2 = 0.2\%$  and  $0.7\%$ . The internal threshold controller enabled the tests to be terminated before complete fracture or if there was a drop in maximum stress of 5%, sustained for fifteen consecutive cycles or when the number of cycles reached  $10^4$ . Some tests were not terminated at the point, but the specimens being allowed to run until fracture so that the fracture surface could be examined. Specimens which reached the threshold value of  $10^4$  were defined as run-outs, i.e. fatigue-tested specimens without failure.

A summary of the tested alloys, including heat and pre-treatments is presented in Table 4.6.

**Table 4.6:** TMF overview of tested alloys and test conditions.

<b>Material condition</b>	<b>Temperature range, [°C]</b>	<b>Mechanical Strain Amplitude, [%]</b>
AlSi6Cu4 (T6)	200-400	±(0.25-0.6)
AlSi6Cu4 (T7)	200-400	±(0.25-0.7)
AlSi6Cu4 (T6)+HIP	200-400	±(0.25-0.5)
AlSi9Cu3 (T6)	200-400	±(0.25-0.7)
AlSi7Mg0.5 (T6)	200-400	±(0.25-0.7)
AlSi8Mg0.4 (T6)	200-400	±(0.25-0.7)
AlSi9Mg0.5 (T6)	200-400	±(0.25-0.7)

#### 4.8 METALLOGRAPHY

The procedure for microstructural analysis was the same for all specimens, including those from the temper tests and from the untested materials. After high temperature testing, specimens were cut from the test pieces as shown in Figure 4.4 using a [Buehler Isomet](#) low speed saw. For the metallographic preparation the samples were mounted in [Technovit 4071](#) for optical microscopy and in [KEM70](#) for scanning electron microscopy. The surfaces were ground (to 4000 grit) and then polished down to 1µm, followed by fine polishing with [OP-S](#) suspension. Special attention was paid to preventing the specimen temperature from exceeding 60°C during preparation.

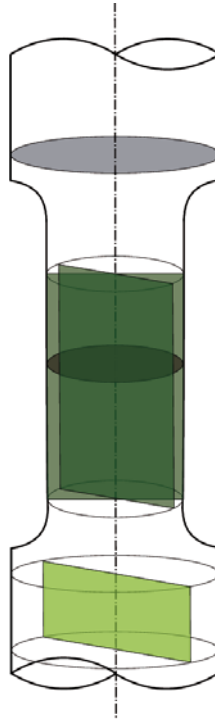


**Figure 4.4:** Section planes of metallographic specimens cut from mechanical test pieces.

#### ***4.8.1 Optical microscopy***

For the investigation of SDAS, large precipitates and crack length, specimens were examined using an [Olympus BX 51](#) optical microscope with colour camera and image analysis software. Specimens were examined in the non-etched condition and also after etching. A detailed description of etchants used is given in Table II.1 in the Appendix B. Examination for crack damage on the surface or damage in the volume used the longitudinal grinding pattern which ran along the specimen axis. Grinding patterns were analysed before and after etching, to give a clear differentiation between cracks, pores and intermetallic phases.

#### ***4.8.2 Scanning Electron Microscopy***

For higher resolution examination of precipitates, cracks, fatigue striations and fracture surfaces, a LEO 1455VP scanning electron microscope (SEM) was used, capable of magnifications of up to 50000 $\times$ . The instrument was also equipped with EDX and back scatter imaging, which allowed differentiation between the intermetallic phases.

### 4.8.3 Transmission Electron Microscopy

For the highest resolution, including precipitate formation, orientation, precipitate-free zones and dislocation behaviour a Hitachi H8100 transmission electron microscope (TEM) was used.

## 4.9 IMAGE ANALYSIS

Image analysis using established methods [270-274] was used to characterise the microstructure of the different alloys and treatments as acquired using optical microscopy on polished and etched sections. A proprietary image analysis tool “analySIS 3.0” was used within the “Matlab” environment, programmed specifically for:

- Determination of the SDAS
- Evaluation of particles and intermetallic phases
- Pore examination

Size, volume fraction, morphology, orientation and distribution were analysed for each component in each micrograph. A total of 80 to 120 micrographs were taken of each specimen along its gauge length to obtain a statistically significant result. SDAS was determined by running a line across the micrograph and counting the number of dendrite arms crossed according to:

$$SDAS = \frac{l}{n} \quad (15)$$

where  $l$  is the length of the line and  $n$  is the number of crossed dendrite arms. The analysis of the phases, pores or particles could be identified by means of their colour characteristics under a variety of etches.

#### 4.10 MICRO CT

A Micro CT system consisting of a “Comet” X-ray tube operating at 225kV, 315W and target current 1.4mA with a Perkin Elmer XRD 1640 AL ES detector was used to detect the type, direction and amount of pores and intermetallic phases in the mechanically tested specimens. The highest voxel resolution of the CT was 27.68 $\mu$ m.

The micro CT was also used to corroborate the above mentioned image analysis, to which end carefully-chosen specimens of each alloy were tested in the longitudinal and lateral directions. The results indicated a good match with the image analysis.

Figure 4.5 shows longitudinal and transverse scans of a non-HIPped AlSi6Cu4 alloy. The longitudinal figure reveals pores on the outer surface of the gauge length and in the transition zone to the grips. In the transverse scan, some globular and one elongated pore can be observed.

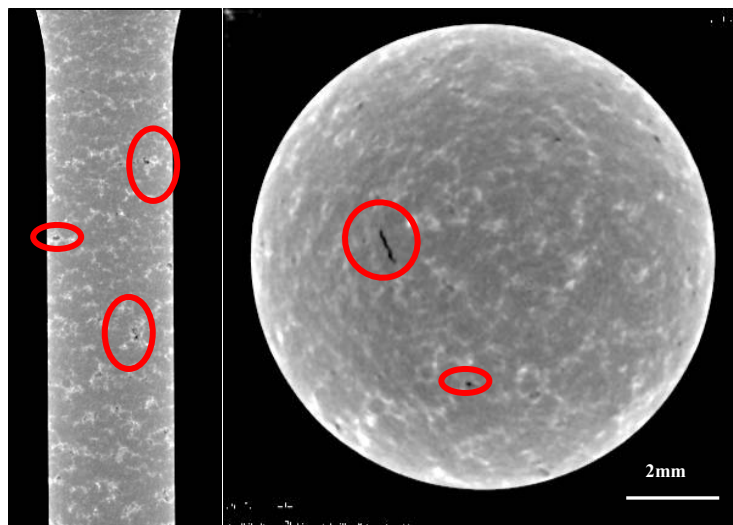


**Figure 4.5:** Pores in the gauge length in longitudinal and transverse  $\mu$ -CT scans.

#### 4.11 HARDNESS MEASUREMENT

All specimens from the temper tests, the isothermal and the TMF tests were examined using a Leitz Durimet II micro hardness tester in the longitudinal and lateral axes of the gauge length and in the clamped area after testing. A Vickers indenter with a 0.1kg load



was used giving hardness number on the HV<sub>0.1</sub> scale. An arithmetical average of 20 individual measurements was taken for each area measured.

#### **4.12 SUMMARY OF TESTS**

Table 4.7 summarises the experiments carried out in this work, in preparation for the presentation of results and discussion in the next two chapters. The main systematic tests (on all alloys and conditions, apart from the AlSiMgCu alloy) are the CERT and thermal fatigue tests which allowed the full range of materials to be assessed for their thermal and mechanical performance. The full set of tests was carried out on the reference alloy, allowing the different measures temper resistance, creep and LCF to be linked to the main tests.

**Table 4.7:** Summary of tests.

<b>Alloy/ condition</b>	<b>Temper</b>	<b>CERT</b>	<b>Creep</b>	<b>Isothermal LCF</b>	<b>Thermal fatigue (<math>\Delta T=200-400^{\circ}\text{C}</math>)</b>
AlSi6Cu4-T6	✓	200, 400°C	200, 400°C	200, 400°C: $\Delta\varepsilon/2 = 0.2, 0.35,$ 0.5, 0.7%	IP: $\Delta\varepsilon/2 = 0.2, 0.35, 0.4, 0.5, 0.7\%$ OP: $\Delta\varepsilon/2 = 0.2, 0.35, 0.5, 0.6, 0.7\%$
AlSi6Cu4-T7	✓	200, 400°C	✗	✗	IP/OP: $\Delta\varepsilon/2 = 0.2, 0.3, 0.35, 0.5, 0.7\%$
AlSi6Cu4- T6+HIP	✗	200, 400°C	✗	✗	IP/OP: $\Delta\varepsilon/2 = 0.2, 0.35, 0.5\%$
AlSi9Cu3-T6	✗	400°C	✗	✗	IP: $\Delta\varepsilon/2 = 0.2, 0.35, 0.4, 0.5, 0.7\%$ OP: $\Delta\varepsilon/2 = 0.2, 0.35, 0.5, 0.7\%$
AlSi7Mg0.3(Cu)	✓	✗	✗	✗	✗
AlSi7Mg0.5-T6	✗	400°C	✗	✗	IP/OP: $\Delta\varepsilon/2 = 0.2, 0.35, 0.5, 0.7\%$
AlSi8Mg0.4-T6	✗	400°C	✗	✗	IP/OP: $\Delta\varepsilon/2 = 0.2, 0.35, 0.5, 0.7\%$
AlSi9Mg0.5-T6	✗	400°C	✗	✗	IP/OP: $\Delta\varepsilon/2 = 0.2, 0.35, 0.5, 0.7\%$

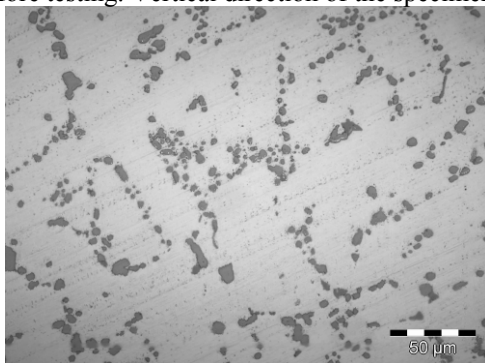
## CHAPTER 5 - RESULTS

This chapter gives a detailed description of the results of the various tests, including the starting microstructures and the tempering tests, followed by the CERT, creep and LCF tests. The LCF and TMF test results are each divided in sections dealing with observations on the cyclic stress-strain behaviour, the lifetime and the microstructures, respectively. The main results of the TMF tests are presented in four parts. The first part considers the TMF behaviour of the reference alloy AlSi6Cu4-T6, and the second deals with the effect of pre-treatment on its behaviour. The third part considers the influence of reducing SDAS on the performance of the AlSi6Cu4 and AlSi9Cu3 alloys. The last part compares the reference alloy with the different Al-Si-Mg alloys to assess the effect of modifying the alloying additions.

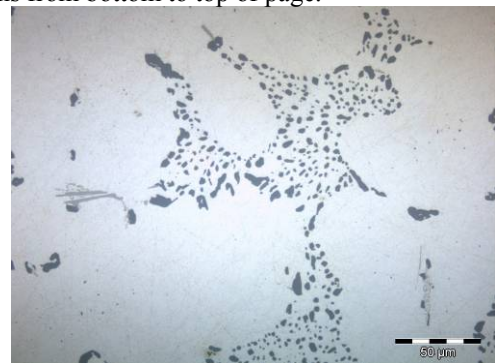
### 5.1 INITIAL MICROSTRUCTURES

Table 5.1 shows typical micrographs of each of the alloys in their starting condition. The sections have been etched to reveal the eutectic structure and are photographed at similar magnification to reveal changes in eutectic coarseness and matrix islet size. The structures all show primary  $\alpha$ -Al matrix in dendritic form, and there is a considerable range in coarseness from the AlSi9Mg0.5 to the AlSi9Cu3. Although it is not all that clear from Table 5.1, there is also a systematic increase in the amount of eutectic with Si content.

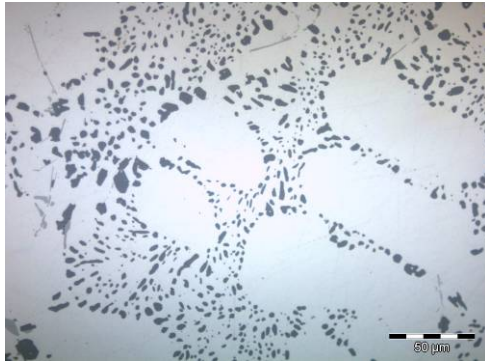
**Table 5.1:** Micrographs showing the different initial microstructures of Al-Si-Mg and Al-Si-Cu alloys before testing. Vertical direction of the specimen axis runs from bottom to top of page.



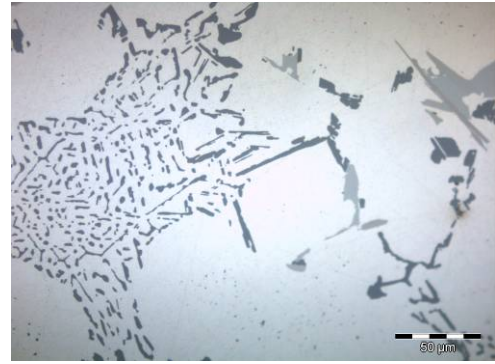
AlSi7Mg0.5



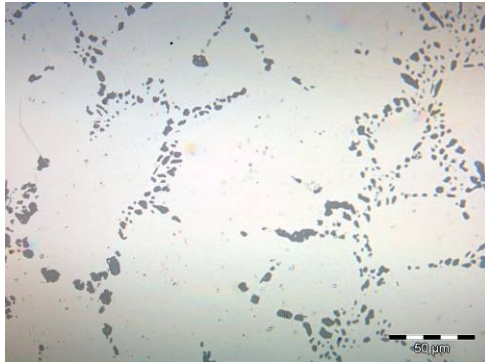
AlSi7Mg0.3(Cu)



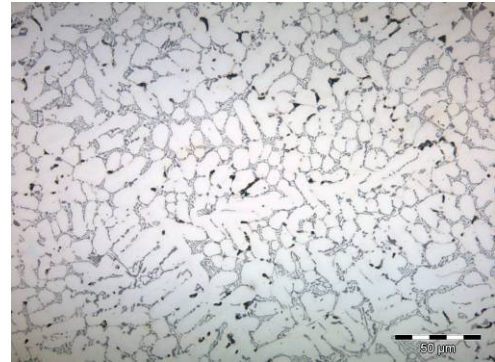
AlSi8Mg0.4



AlSi9Mg0.5



AlSi6Cu4



AlSi9Cu3

Because of the contrast between the (dark grey) eutectic Si particles and the (light grey) primary and eutectic  $\alpha$ -Al, some observations can also be made about the eutectic microstructure:

- AlSi7Mg0.3(Cu) = granular/ globular, coarse-medium
- AlSi7Mg0.5 = granular, medium
- AlSi8Mg0.4 = lamellar/ globular, coarse
- AlSi9Mg0.5 = acicular/ globular, coarse
- AlSi6Cu4 = globular/ granular, medium
- AlSi9Cu3 = lamellar, fine

In some micrographs, intermetallic phases with a Cu, Fe or Mg content are visible as well.

## 5.2 TEMPER TESTS

Temper tests were carried out on AlSi7Mg0.3(Cu) and on AlSi6Cu4 to assess the scale of decrease in hardness, the development of other phases and the level of grain coarsening associated with high temperature exposure in the absence of mechanical loading.

### 5.2.1 Initial condition

The alloys were representative of the Al-Si-Mg and Al-Si-Cu alloys studied. Table 5.2 gives an overview of the initial hardness values after an ordinary T6 and T7 heat treatment.

**Table 5.2:** Initial hardness values after an ordinary T6 and T7 heat treatment.

	<b>T6</b>	<b>T7</b>
<b>AlSi7Mg0.3(Cu)</b>	137HV <sub>0.1</sub>	117HV <sub>0.1</sub>
<b>AlSi6Cu4</b>	117HV <sub>0.1</sub>	97HV <sub>0.1</sub>

### 5.2.2 Overageing (e.g. phases and grains)

For both alloys, an increase in inter-particle distance and associated coarsening of the precipitates was observed in all specimens, commencing at the beginning of overageing.

For AlSi7Mg0.3(Cu) in the T6 and T7 specimens, the Si particles increased in size to almost 1.5 times the size in peak-aged condition with long time exposure, whereas the  $\beta$ -phase and  $\pi$ -phase coarsened to a lesser extent. The Mg<sub>2</sub>Si phase, exhibited coarsening in the T7 long time exposure tests, but not in the T6 long time exposure tests. The  $\beta$ -phase showed slight coarsening at 200°C and unknown possible slight refinement at 400°C. The  $\pi$ -phase was not modified at 200°C but displayed considerable coarsening during the 400°C exposure tests.

For AlSi6Cu4 the T6 peak-aged condition leads to a microstructure containing Q-phase as well as Al<sub>2</sub>Cu phases. The Si particles coarsened in all of the tests, becoming 20% higher after long time exposure at the peak-aged condition. The  $\beta$ -phase also coarsened, although a little less than did the Si particles. The Al<sub>2</sub>Cu phase changed shape during the further T6 artificial ageing, decreasing in one dimension and increasing in the other.

In general, more coarsening was observed in those samples which started in the T7 condition and this started immediately, in contrast to the T6 specimens which only started to change starting after around 1hr of treatment.

### 5.2.3 Change of hardness values

Figure 5.1 summarises the hardness evolution during the high temperature (200°C and 400°C) exposures of the AlSi7Mg0.3(Cu) starting from the peak-aged T6 condition. Given that the initial condition of the specimens exposed to high temperatures at 200°C and 400°C is the same (137HV<sub>0.1</sub>), it can be seen that a significant drop in hardness to below 60HV<sub>0.1</sub> has occurred at 400°C within the first 30min and that subsequent reduction over the remaining 100hr is relatively small. For the 200°C exposure, there is a relatively abrupt change in the (logarithmic) rate of softening after 10hr, corresponding to the commencement of significant overageing, the hardness dropping to about 80HV<sub>0.1</sub> after 100hr.

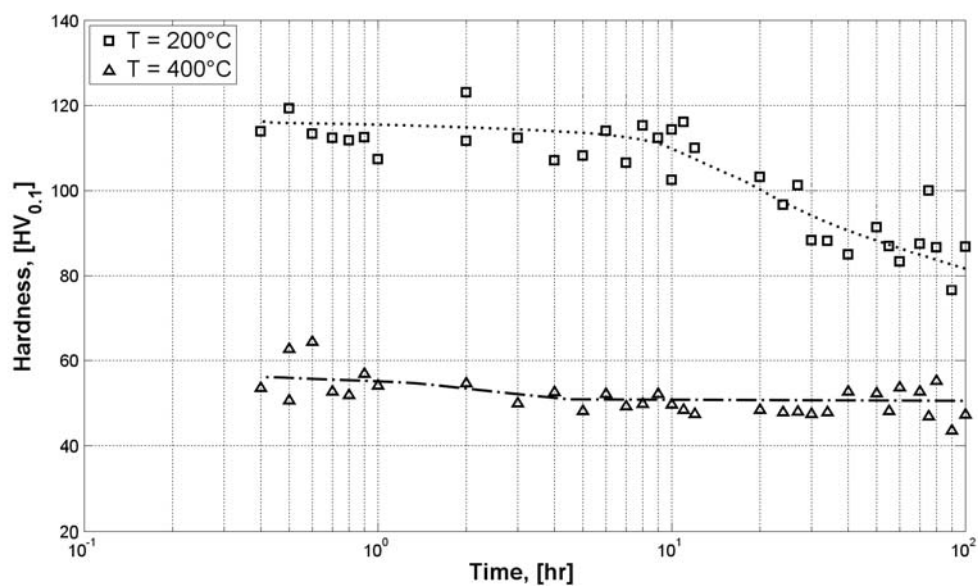


**Figure 5.1:** Hardness evolution of AlSi7Mg0.3(Cu) T6 on subsequent exposure at 200°C and 400°C.

For AlSi6Cu4 in the T6 condition (Figure 5.2), the hardness began to change significantly only after 600min and this was similar for the T7+200°C exposure. On the other hand, the specimens exposed at T6+400°C exhibited a rapid drop during the initial few minutes with little further change after 1hr. As can be seen, the saturated state is reached for the 400°C specimens after ~50min, with a very rapid drop in hardness

values during the initial 18min (given that the time scale is logarithmic). It was noted that the hardness of both the T6 and the T7 specimens exposed at 400°C settled to the same hardness value of  $\sim 60\text{HV}_{0.1}$ . Also, the decrease in hardness for the T6 heat treatment was delayed to longer exposure times compared to T7.

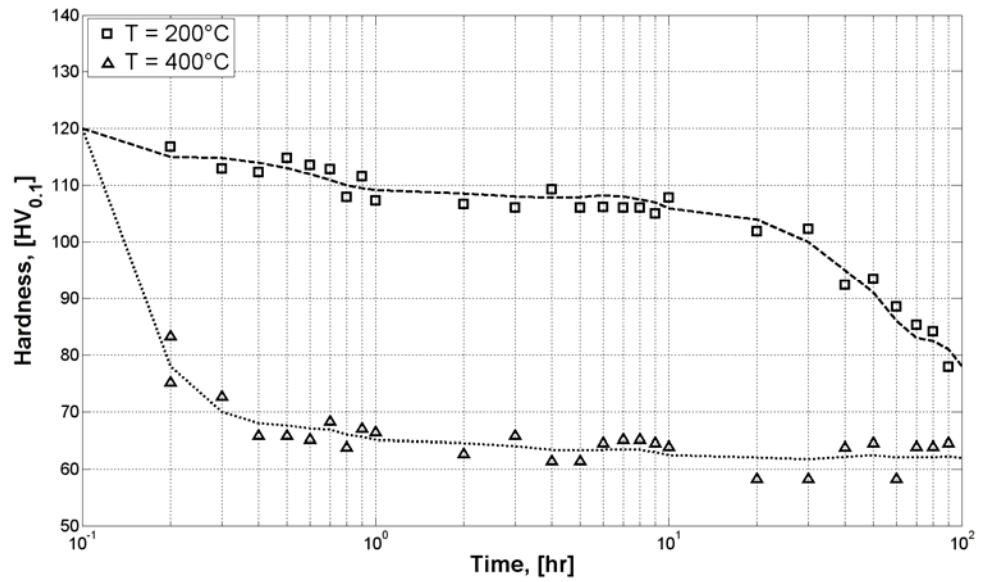


**Figure 5.2:** Hardness evolution during high temperature exposure of the AlSi6Cu4 alloy at 200°C and 400°C starting from a T6 heat treatment.

#### 5.2.4 Summary of temper tests

The 600min high temperature exposure is equivalent to 450 cycles with a cycle time of 80s in the LCF or TMF tests. This means that microstructural or strength changes observed in these tests are likely to affect the fatigue specimens as well.

Figure 5.3 compares the hardness evolution of specimens of the two alloys in the T6 heat treatment when exposed at 400°C. Whereas the AlSi6Cu4 exhibits a slightly higher initial hardness, it also shows a greater reduction during the long time exposure. After 2hr, both alloys reach a saturated value showing little further change for the next ~80hr.

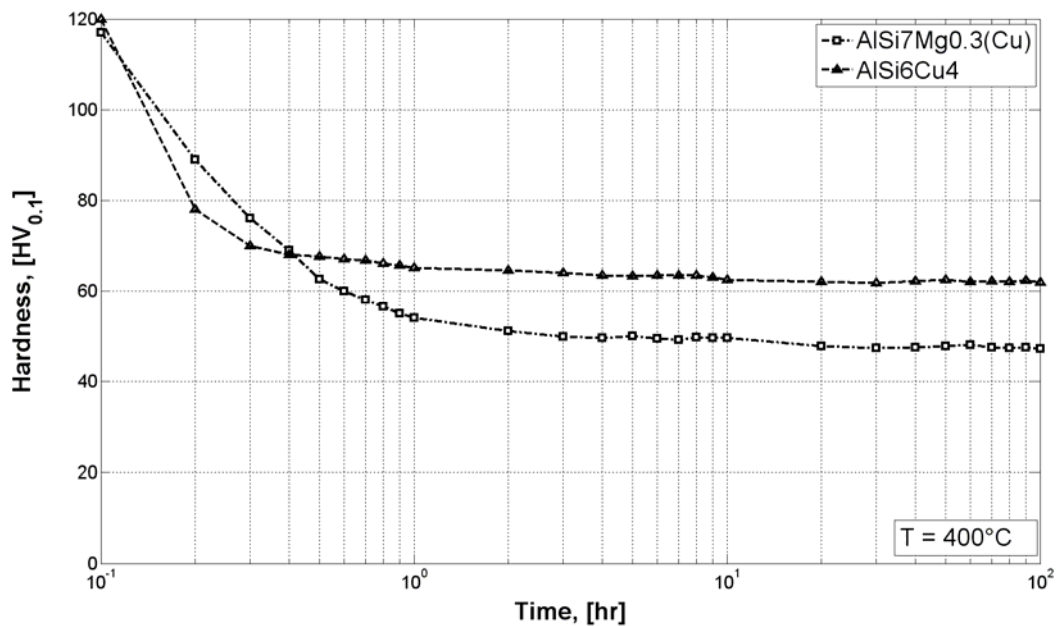


**Figure 5.3:** Comparison of AlSi7Mg0.3(Cu) and AlSi6Cu4 tested after high temperature exposure at 400°C.

Neither AlSi7Mg0.3(Cu) nor AlSi6Cu4 showed any reorientation of particles during long term exposure although this could happen during mechanical loading. For both alloys, a grain coarsening which increases with increasing temperature and temper time, was observed.



### 5.3 CERT

CERTs were conducted to investigate and to evaluate the high temperature elastic-plastic behaviour of the different alloys, the different temper conditions and the HIP process.

Figure 5.4 compares AlSi6Cu4 in the HIPped and T6 conditions tested at 200°C and 400°C. For both conditions, there is a marked decrease in  $\sigma_y$ , UTS and stiffness and an increase in fracture strain with increase of temperature. Also, the HIP process has more influence on the curve at the lower temperature (200°C) than at the higher temperature (400°C), amounting to about 25MPa increase in strength at 200°C and around 10MPa at 400°C. All curves exhibit the same gradient up to around 55MPa, after which the gradient decreases, less so at 200°C. Unlike the specimens tested at 400°C, specimens at 200°C display strain hardening until fracture.

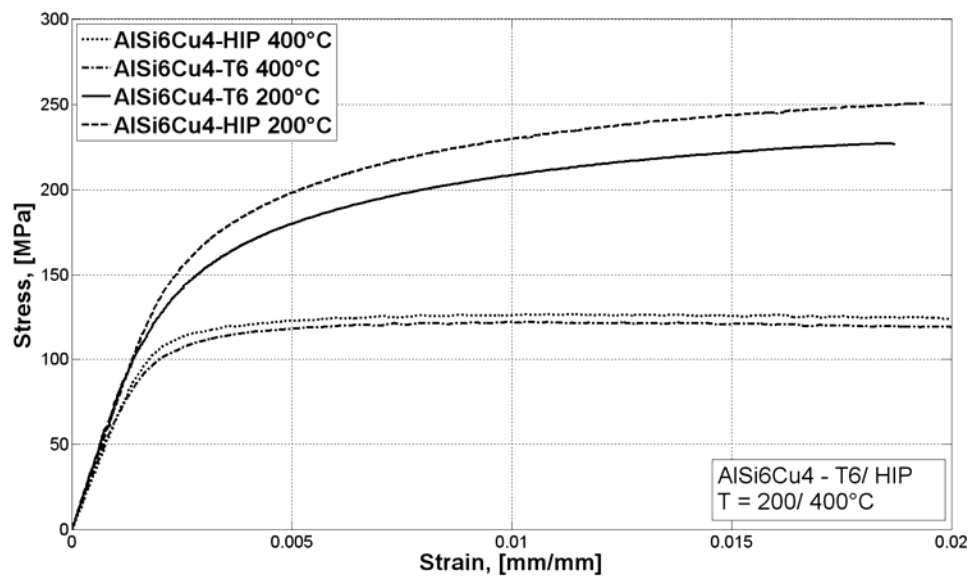


**Figure 5.4:** Comparison of CERT at 200°C and 400°C for AlSi6Cu4 in the non-HIPped T6 and HIPped condition.

**Table 5.3:** Comparison of mechanical parameters on AlSi6Cu4 with different pre-treatments at 200°C.

	Yield strength, [MPa]	Ultimate tensile strength, [MPa]
AlSi6Cu4-T6	170	225
AlSi6Cu4-T7	143	191
AlSi6Cu4-HIP+T6	194	250

Table 5.3 presents a comparison of AlSi6Cu4 at 200°C in the non-HIPped T6, T7 and the HIPped T6 conditions. The highest UTS values were reached for specimens modified with a HIP process followed by a T6 treatment. The HIP process leads to an increase of UTS of 10% and an increase of  $\sigma_y$  around  $\sim 13\%$  at 200°C. The corresponding increases at 400°C were around 4% for the UTS and around 6% for  $\sigma_y$ .

Figure 5.5 compares AlSi6Cu4 with AlSi9Cu3, which differ mainly in the SDAS, tested in the T6 condition at 400°C. Both alloys exhibit similar stress-strain behaviour up to a strain of 0.11%, at which point the smaller SDAS of AlSi9Cu3 leads to a higher UTS and  $\sigma_y$ .

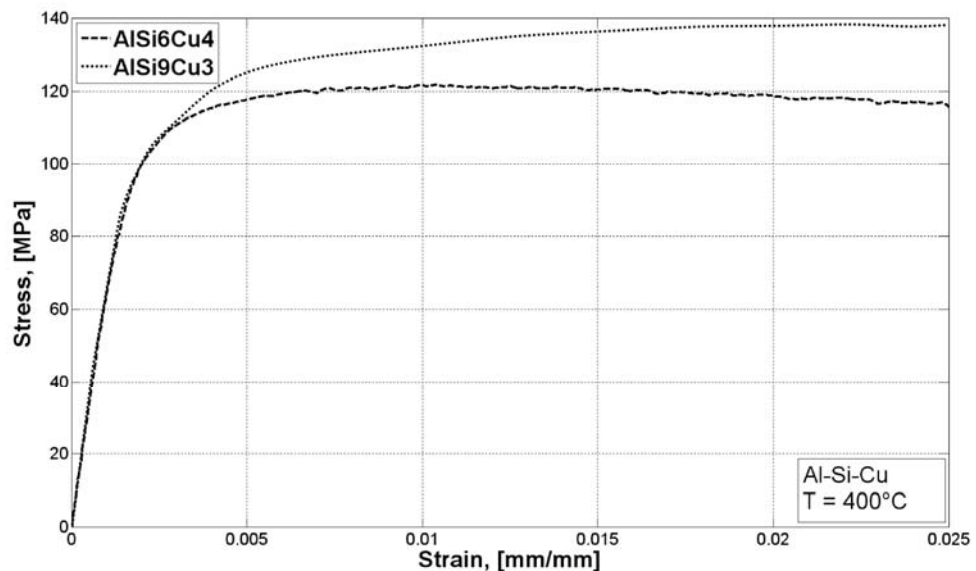


**Figure 5.5:** Comparison of CERT on AlSi6Cu4 and AlSi9Cu3 in the T6 condition at 400°C.

For the Al-Si-Mg alloys tested at 400°C (Figure 5.6), it can be seen that the UTS decreases with increasing Si content, as does the ratio UTS: $\sigma_y$ . At the UTS, the curves are relatively flat showing almost perfectly plastic behaviour, although the AlSi8Mg0.4

displays quite a lot of “noise” on the curve, presumably associated with some sort of dynamic recovery mechanism.

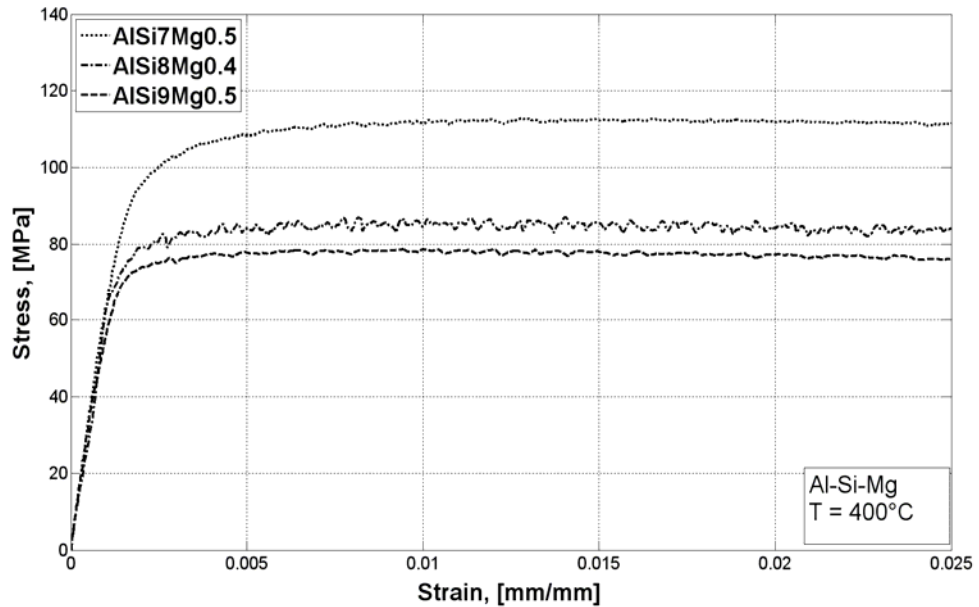
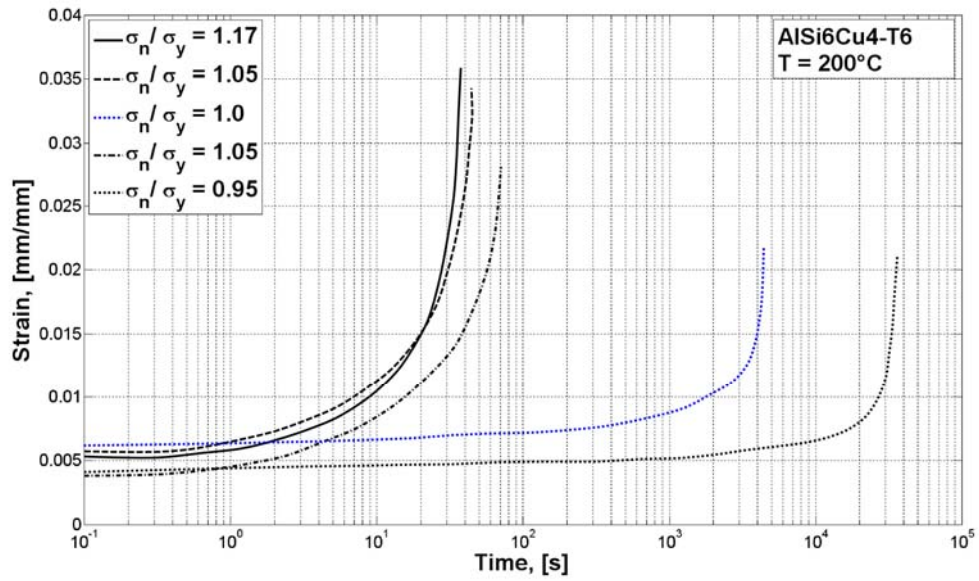


Figure 5.6: Comparison of Al-Si-Mg alloys in the T6 condition subjected to CERT at 400°C.

#### 5.4 CREEP TESTS

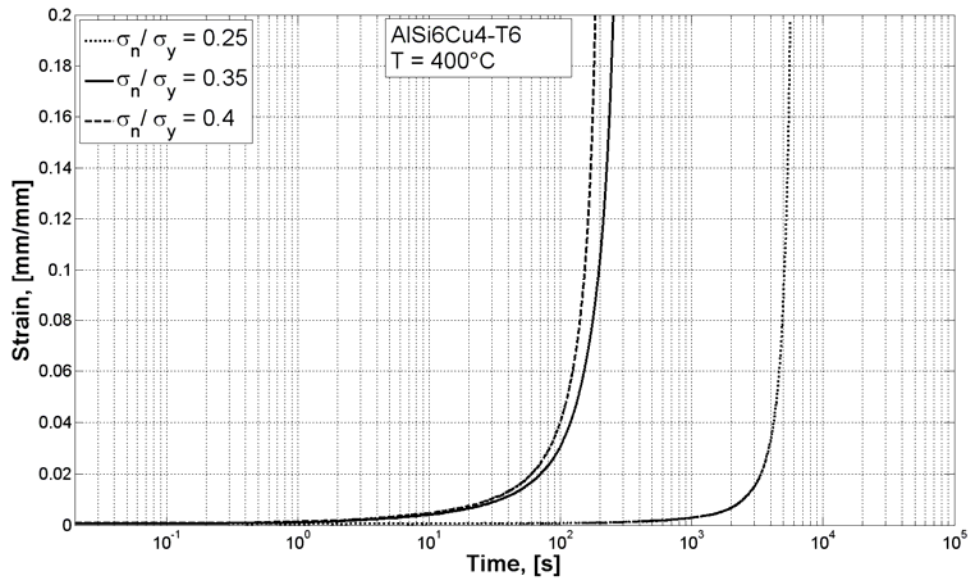
The creep tests were conducted only on the reference alloy at temperatures of 200°C and 400°C with loadings based on the CERTs, using various ratios of the (constant) creep stress,  $\sigma_n$ , to the yield stress,  $\sigma_y$ .

Figure 5.7 compares specimens tested at 200°C with different loadings. The test with a loading of  $\sigma_n/\sigma_y=1.05$  showed some scatter so two specimens were tested. Generally, the creep rate increases with increasing  $\sigma_n/\sigma_y$ , as might be expected, and the length of the steady creep region is longer as  $\sigma_n/\sigma_y$  decreases, again as would be expected. Curves with a  $\sigma_n/\sigma_y$  of 1.0 and 0.95 are almost parallel for the first 100s. Finally, with increasing  $\sigma_n/\sigma_y$ , the time to creep rupture decreases and the elongation at rupture increases.



**Figure 5.7:** Creep curves for AlSi6Cu4-T6 at 200°C with different stress values.

In comparison with the tests at 200°C, the 400°C tests showed a considerable increase in elongation, especially considering the substantially lower stresses relative to yield (Figure 5.8). The effect of  $\sigma_n/\sigma_y$  is similar to that observed at 200°C but with a more pronounced difference between the lower and higher values. Except for the specimen with a load ratio of 0.4, the creep specimens fractured at a strain of 0.2mm/mm, so this was considered to be the creep fracture strain for designing the TMF tests.



**Figure 5.8:** Creep curves for AlSi6Cu4-T6 at 400°C with different stress values.

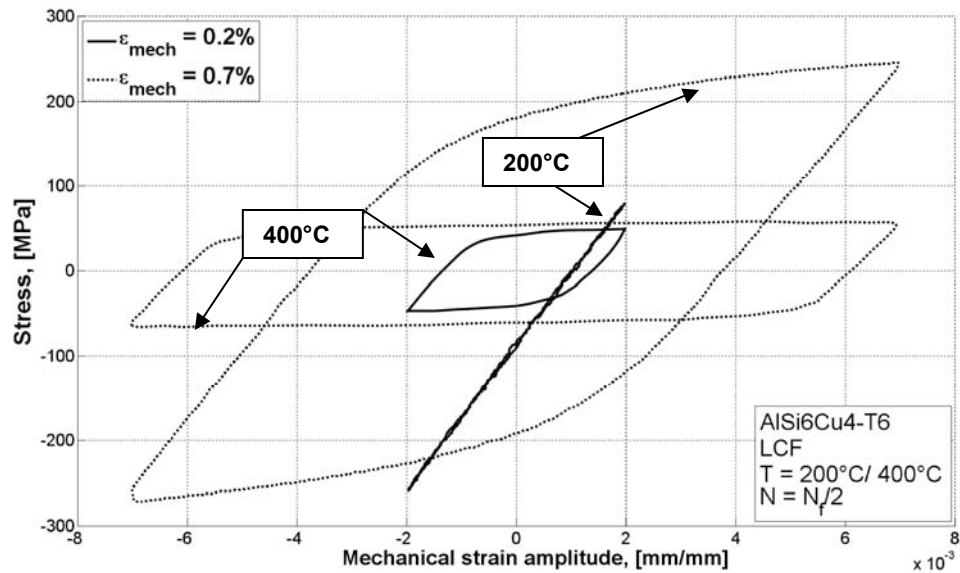
## 5.5 ISOTHERMAL LOW CYCLE FATIGUE TESTS

The LCF tests were conducted only on the reference alloy with a cycle time of 80s to match the TMF tests. The constant cycle time means that strain rates increase with increasing strain amplitude. The results are collected here in terms of observations on the stress-strain behaviour within cycles, followed by the lifetime behaviour and, finally, the observations on the microstructures.

### 5.5.1 Cyclic stress-strain behaviour

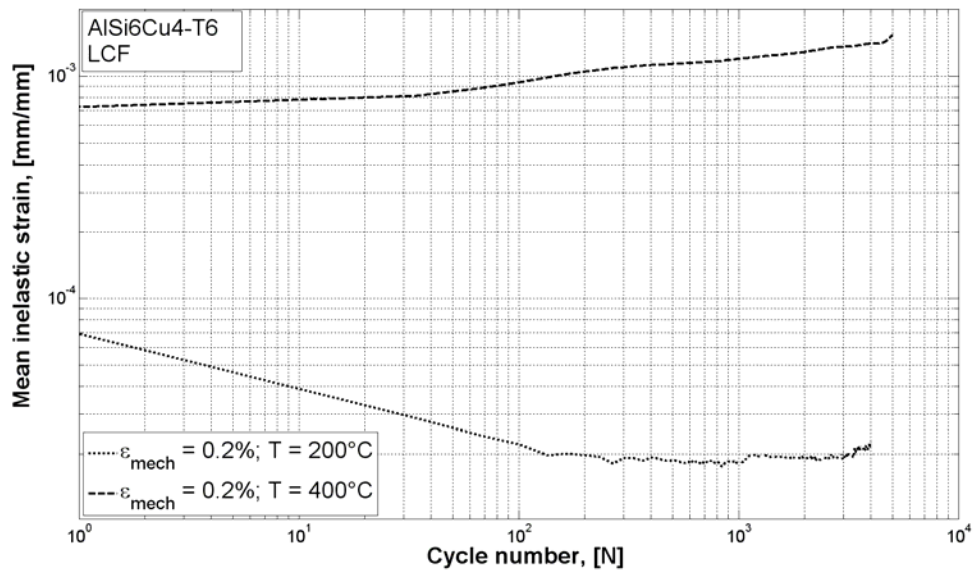
Figure 5.9 shows hysteresis loops for strain amplitudes of 0.2% and 0.7% at mid-way through the LCF life ( $N=N_f/2$ ) for specimens tested at 200°C and 400°C. The most obvious contrast between the two temperatures is that tests at 200°C exhibit a pronounced stress development, whereas the stress range at 400°C remains within the band  $\pm 70$ MPa. For the 0.2% strain amplitude, a rapid drop in mean compressive stress can be observed between the 200°C and 400°C test temperatures, the behaviour at 200°C being essentially elastic. For the 0.7% strain amplitude, the mean compressive stress is about the same at both temperatures, although there is again a significant drop in maximum stress. The increase in temperature causes maximum stresses to decrease by about 70% for the high strain amplitude and by about 35% for the low strain

amplitude. At the higher test temperature, which is above  $0.4T_M$ , the cyclic behaviour is affected by time depending processes. This can be seen particularly in the hysteresis loop at 0.7% strain amplitude, where the top and bottom of the loop are more linear and flat for the higher temperature.



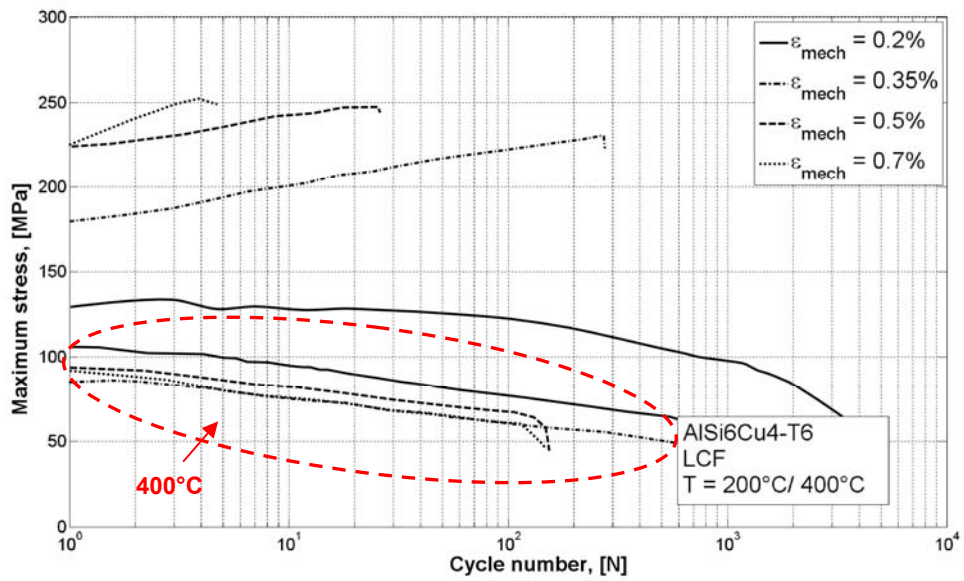
**Figure 5.9:** Hysteresis loops of AlSi6Cu4-T6 at 200°C and 400°C at  $N_f/2$ .

Figure 5.10 shows the development of the mean inelastic strain over the life of the longest lifetime samples (strain amplitude of 0.2%) at 200°C and 400°C. Since the stress remains below  $\sigma_y$  at 200°C, mean inelastic strain development is very small, and the curve shows a decrease up to  $N=1500$ , which is followed by an increase until fracture. Hence, this material displays slight hardening followed by slight softening until fracture. In contrast, specimens at 400°C show an increase of mean inelastic strain until fracture from the first cycle on.



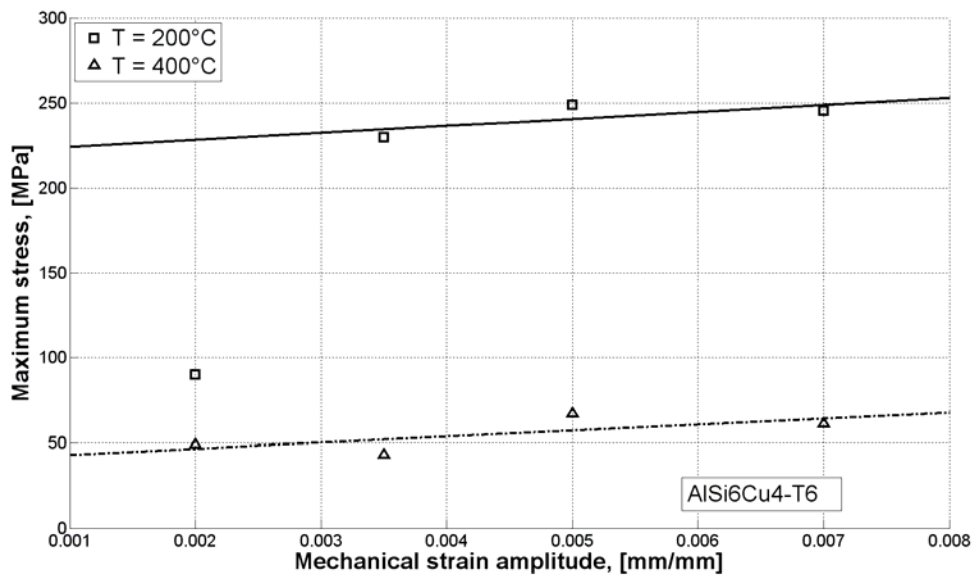
**Figure 5.10:** Mean inelastic strain of AISi6Cu4-T6 at 200°C and 400°C under LCF loading at a strain amplitude of 0.2%.

Figure 5.11 shows the development of maximum stress vs. the number of cycles  $N$  for specimens tested at 200°C and 400°C. For specimens tested at 200°C, all strain amplitudes above a threshold of 0.2% show hardening until fracture. For the 0.2% strain amplitude, hardening can be observed during the initial three cycles, followed by a relatively stable phase and softening above  $N=20$ . Small compressive mean stresses develop for all strain amplitudes tested at 200°C during their lifetime. Curves for the specimens tested at 400°C all exhibit broadly similar stresses, but with the highest stresses under tension and compression being at a strain amplitude of 0.2% and the lowest at a strain amplitude of 0.7%. All of the 400°C curves display softening, characterised by a decrease in stress, from the initial cycle on. The strain amplitudes of 0.2% and 0.35% show a decrease of maximum stress of 86% at fracture. It can also be observed that the stress evolution for strain amplitudes of 0.35% and 0.7% are almost the same between  $N=2$  and 100, whereas the hysteresis loop at  $N=N_f/2$  (Figure 5.9) indicates a decreasing stress with increasing strain amplitude.



**Figure 5.11:** Maximum stress of AlSi6Cu4-T6 at 200°C and 400°C tested under LCF loading with different strain amplitudes.

Comparing maximum stresses at  $N=N_f/2$  at 200°C and 400°C, Figure 5.12 demonstrates an increase in maximum stress with increasing strain amplitude.



**Figure 5.12:** Comparison of maximum stress at 200°C and 400°C at  $N_f/2$  under LCF loading with different strain amplitudes.



In contrast, Figure 5.13 shows the relationship between mean inelastic strain and mechanical strain amplitude, increasing at both temperatures with approximately the same gradient. Specimens tested at 400°C show a higher level of mean inelastic strain for a given mechanical strain amplitude.

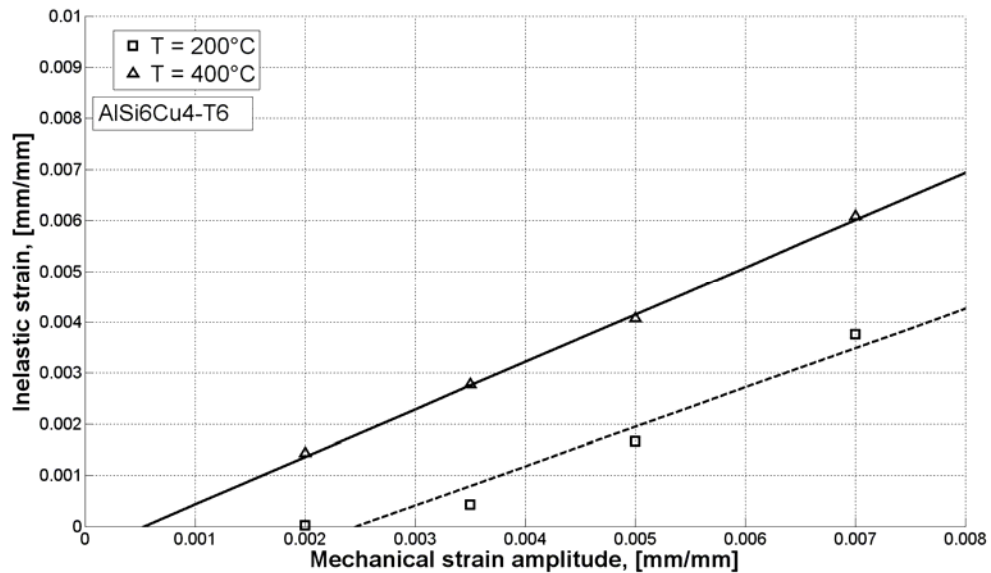


**Figure 5.13:** Mean inelastic strain at  $N_f/2$  at 200°C and 400°C tested under LCF conditions with different strain amplitudes.

### 5.5.2 Lifetime behaviour

Figure 5.14 summarises the lifetime behaviour of the AISi6Cu4-T6 alloy. The  $\Delta\epsilon_{\text{mech}}$  vs.  $N$  relationship shows a decrease in strain amplitude leading to a higher lifetime as expected. Specimens tested at 200°C exhibit a shorter lifetime than specimens tested at 400°C for a given  $\Delta\epsilon_{\text{mech}}$ . Only one of the specimens (one of the three tested with a strain amplitude of 0.2%) reached the defined criterion of  $N=10^4$  cycles, but was run on until fracture anyway.

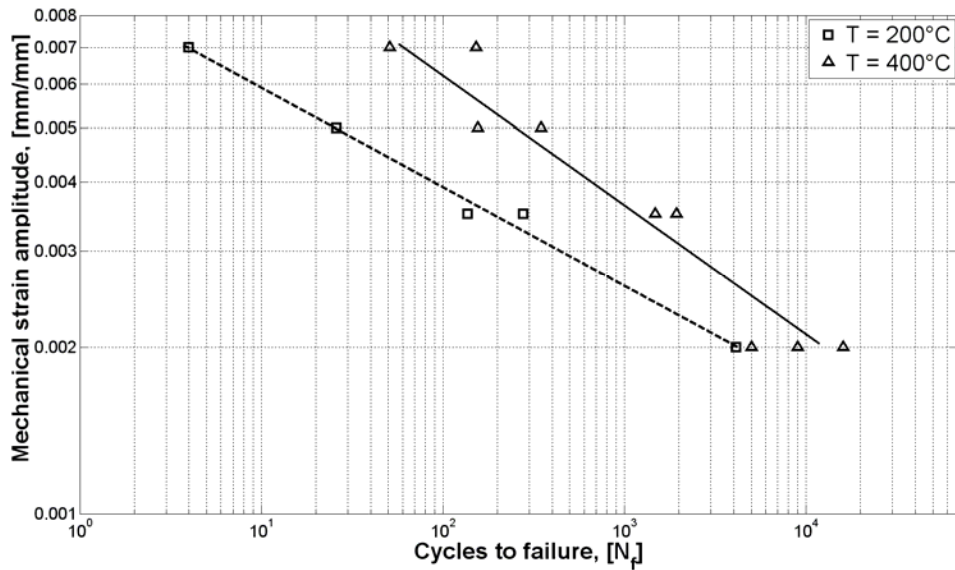


**Figure 5.14:** Mechanical strain amplitude –  $N_f$  diagram of AlSi6Cu4-T6 under LCF loading conditions.

### 5.5.3 Microstructural observations

In all specimens tested, cracks were found to initiate from pores near to the surface. Also, specimens tested at 200°C showed an increase in hardness with decreasing strain amplitude, whereas those tested at 400°C showed a continuous decrease in hardness with decreasing strain amplitude.

Grain coarsening, and coarsening and transformation of intermetallic phases was detected for specimens tested at 400°C, the  $\alpha$ -phase increasing by 10%, the  $\beta$ -phase decreasing by 15%, the Al<sub>2</sub>Cu phase increasing by 20% and Si particles decreasing by 10%. An analysis of the grain size before and after tests with a strain amplitude of 0.2% showed the grains have grown nearly eightfold at 400°C and by about one and a half times at 200°C. Also, the Si and  $\beta$ -phases re-orient along angles of  $\sim 45^\circ$  and  $\sim 130^\circ$  to the loading direction as they grow. While test specimen cracks propagate alongside Si particles and grain boundaries at 200°C, cracks propagate through the  $\alpha$ -matrix at 400°C (Figure 5.15). Both Si particles and Al<sub>2</sub>Cu phases support crack propagation and, furthermore, particle decohesion can be observed at 400°C, Figure 5.16.

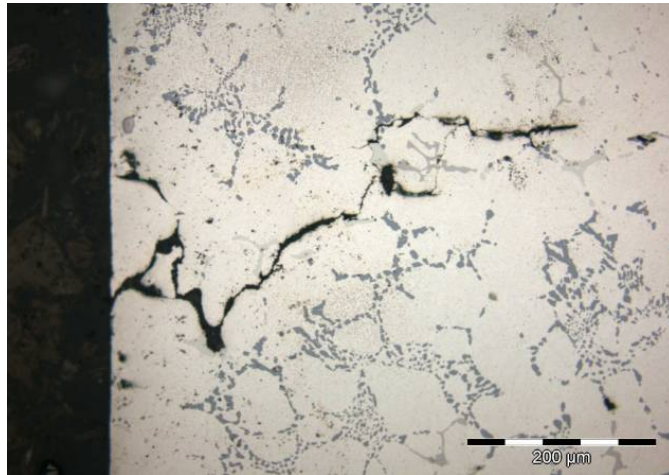


**Figure 5.15:** Crack through the  $\alpha$ -matrix in AlSi6Cu4-T6 under LCF condition at 400°C and a strain amplitude of 0.35%.

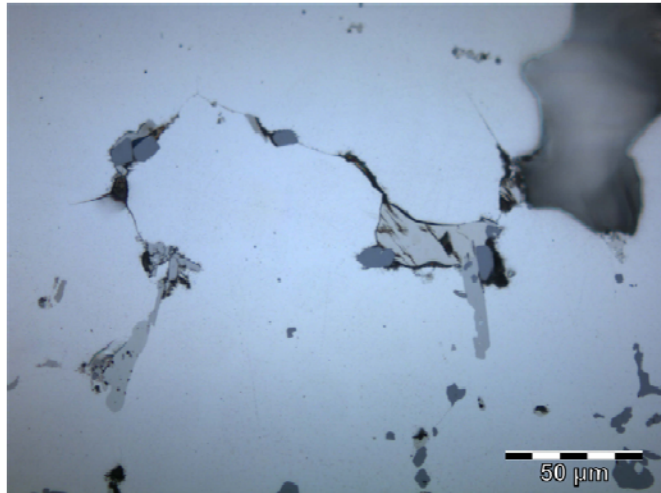


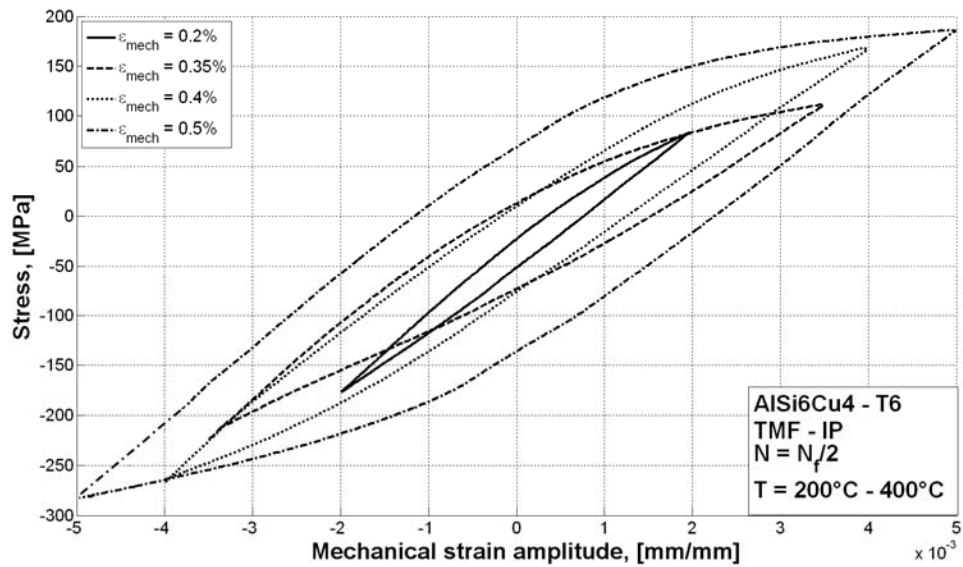
**Figure 5.16:** Particle decohesion of AlSi6Cu4-T6 tested under LCF and a strain amplitude of 0.2%.

## 5.6 THERMO-MECHANICAL FATIGUE OF ALSI6CU4-T6 REFERENCE ALLOY

As described earlier, the TMF tests were conducted at zero mean strain with a cycle time of 80s and the temperature cycling between 200°C and 400°C corresponding to maximum heating and cooling rates of 5°C/s. In this, the main series of tests, the influence of strain amplitude on stresses was studied as well as the effect on fatigue life. Both IP and OP tests were carried out with strain amplitudes between 0.2% and 0.6% in order to evaluate damage behaviour and to determine the strain amplitude where creep effects become significant. In this section, the cyclic stress-strain behaviour and associated microstructural observations are described, whereas the TMF lifetime behaviour is described alongside that of the other alloys and treatments in Section 5.7.

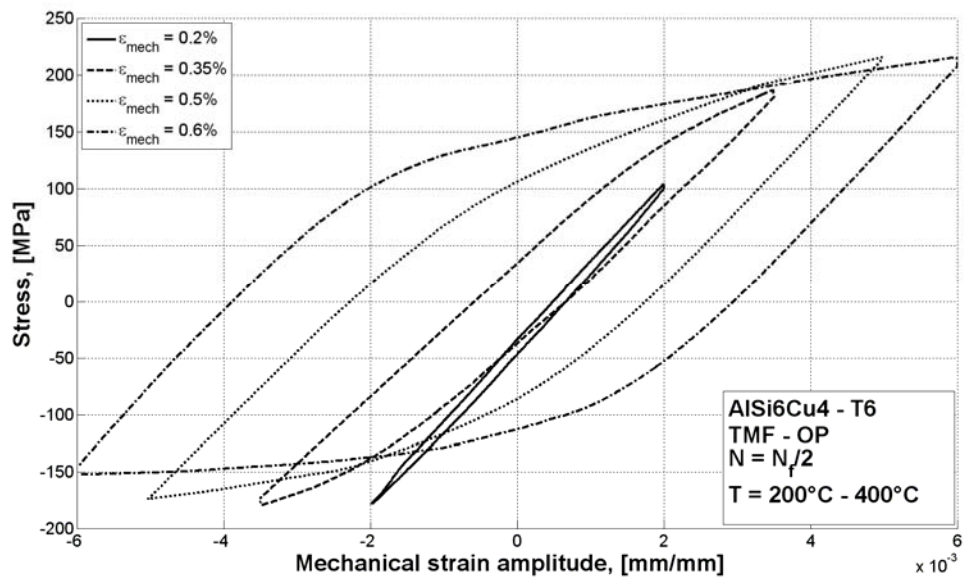
### 5.6.1 Cyclic stress-strain behaviour

Figure 5.17 shows cyclic stress-strain hysteresis loops at  $N=N_f/2$  under IP loading at different strain amplitudes. It is obvious that stress amplitude increases with increasing strain amplitude. Also, the included angle at the low temperature (compressive stress) tip of the hysteresis loop is more acute than at the high temperature (tension). Elastic-plastic behaviour is evident from  $N=1$  for all strain amplitudes which can be seen by the hysteresis broadening. An exception to this is a strain amplitude of 0.2% where only elastic behaviour is visible at  $N=N_f/2$ . Furthermore, a development of relaxation is taking place above a strain amplitude of 0.5% and all loops display the development of a compressive mean stress by  $N=N_f/2$ .



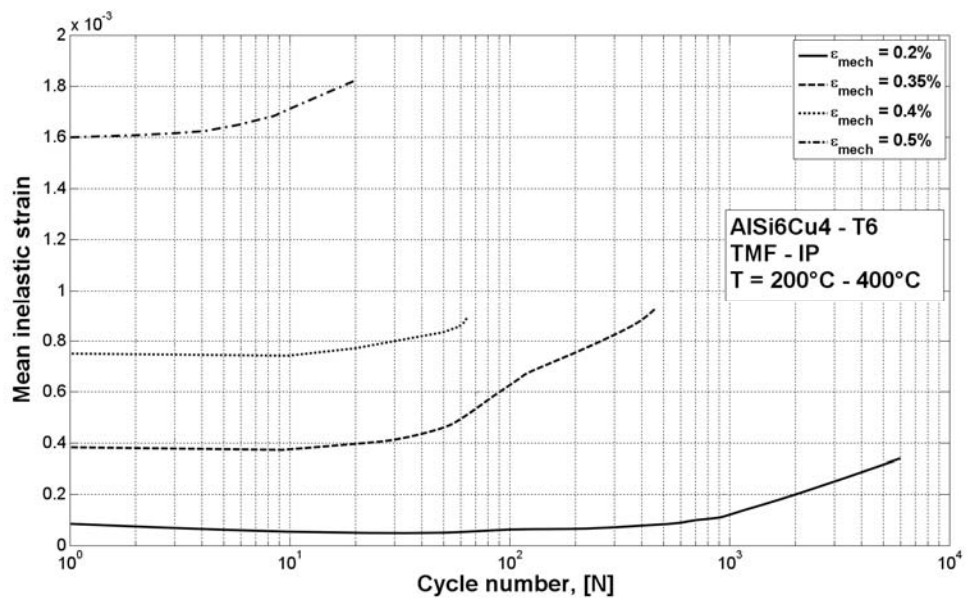
**Figure 5.17:** Hysteresis loops at  $N=N_f/2$  for AISi6Cu4-T6 under IP-TMF loading with different strain amplitudes.

Figure 5.18 shows the hysteresis loops for the OP tests under TMF loading at  $N=N_f/2$ . Compared with the corresponding IP loops, these are generally narrower (in terms of stress amplitude for a given strain amplitude) and more symmetrical at the high and low temperature tips. Also, the maximum compressive stress decreases with increasing strain amplitude. Furthermore, relaxation effects lead to a decrease of stresses under minimum temperature above a strain amplitude of 0.6%. For a strain amplitude of 0.2%, mostly elastic behaviour is visible at  $N=N_f/2$  with a shift to compressive mean stresses. For higher strain amplitudes, elastic-plastic behaviour was visible from cycle  $N=1$  on.



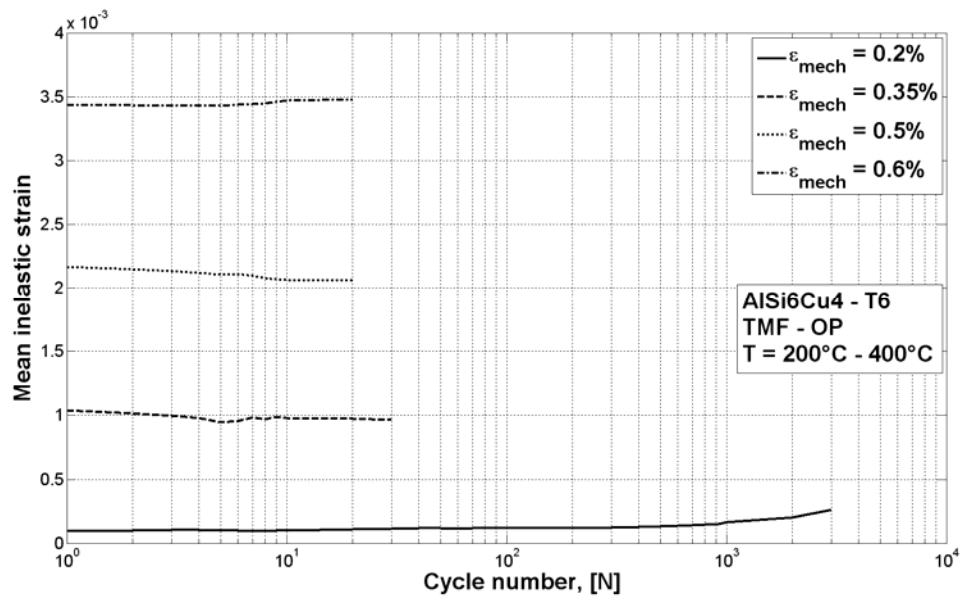
**Figure 5.18:** Hysteresis loops at  $N=N_f/2$  for AISi6Cu4-T6 under OP-TMF loading with different strain amplitudes.

Figure 5.19 shows the mean inelastic strain of specimens tested under IP loading. Generally, there is an increase of mean inelastic strain with increasing strain amplitude, although strain amplitudes  $\leq 0.4\%$  show a slight decrease during the initial ten cycles.



**Figure 5.19:** Mean inelastic strain of AISi6Cu4-T6 under IP-TMF loading with different strain amplitudes.

As seen in Figure 5.20, specimens tested under OP loading show higher mean inelastic strains than the IP tests, although there is relatively little, if any, increase over the lifetime.



**Figure 5.20:** Mean inelastic strain of AISi6Cu4-T6 under OP-TMF loading with different strain amplitudes.

Figure 5.21 shows the evolution of maximum and minimum stresses through the TMF lifetime for the IP tests. The decrease in lifetime with increasing strain amplitude is accompanied by an increase in maximum and minimum stresses, with no saturation being evident at any of the strain amplitudes above 0.2%. The 0.2% strain amplitude exhibits a peculiar behaviour in that the softening in tensile stress up to  $N=500$  is followed by a saturation phase where the maximum tensile stress does not change significantly until just before failure. In contrast to this, the maximum compressive stress shows hardening until  $N=600$ , followed by a saturation phase and then softening until fracture. The mean stress developed as expected for all specimens with an increase of compressive mean stress (from -4MPa and -48MPa) with increasing strain amplitude.

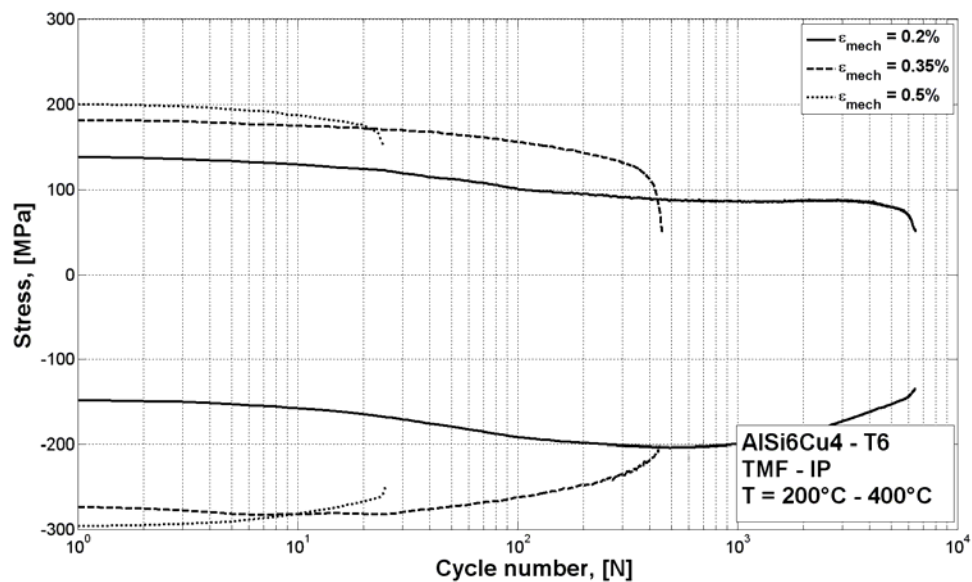


**Figure 5.21:** Maximum and minimum stresses of AISi6Cu4-T6 specimens tested under IP-TMF loading.

Figure 5.22 shows the corresponding evolutions of maximum and minimum stress under OP-TMF loading conditions. The specimens with strain amplitudes of 0.5% and 0.6% show almost the same maximum tensile stress values and evolution, whereas at maximum temperature (compression) the 0.5% strain amplitude shows higher stresses than the 0.6% strain amplitude does. The 0.2% strain amplitude exhibits the same shift towards compressive stresses as for IP loading. Within the first 10 cycles, all tensile stress curves are within 40MPa of each other, whereas there is a wider range for compression, around 110MPa. Also, for the higher strain amplitudes, the drop in



maximum tensile stress just before fracture is larger than the compressive one. The development of a mean tensile stress can be discerned with increasing strain amplitude.

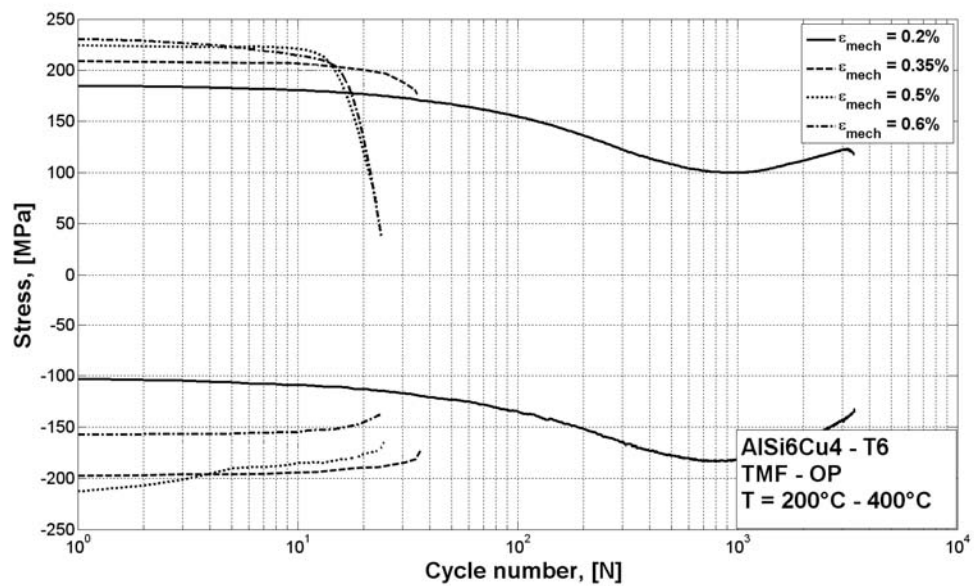


**Figure 5.22:** Maximum and minimum stresses of AISi6Cu4-T6 specimens tested under OP-TMF loading.

Figure 5.23 compares the stress amplitude evolutions under IP and OP TMF loading at strain amplitudes of 0.2% and 0.5%. It can be seen that the IP and OP evolutions are almost exactly the same for the 0.2% strain amplitude, with a slight increase in hardening which reaches its maximum between 150 and 200 cycles. For the 0.5% strain amplitude, the IP stress amplitude is significantly higher throughout the fatigue life, and the drop in amplitude prior to failure is much larger for the OP loading.

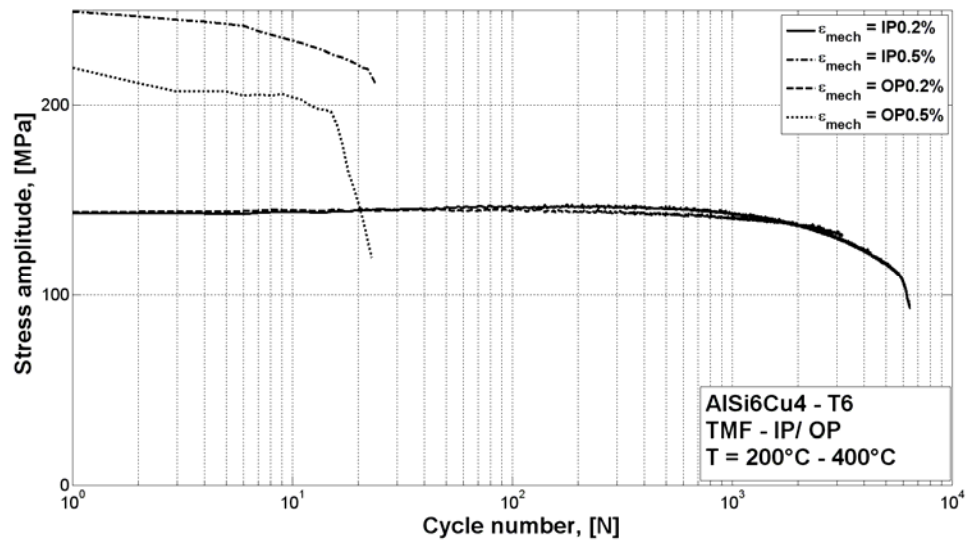


**Figure 5.23:** Stress amplitudes of specimens tested under IP and OP TMF loading at strain amplitudes of 0.2% and 0.5%.

### 5.6.2 Lifetime behaviour

The lifetime curves for AISi6Cu4-T6 can be found in sections 5.7.2, 5.8.2 and 5.9.2, alongside those for different pre-treatments, casting methods and alloying elements.

### 5.6.3 Microstructural observations

Both IP and OP TMF tests on AISi6Cu4-T6 exhibited a decrease in post-test hardness with increasing strain amplitude, in common with the LCF tests at 400°C but in contrast to the 200°C tests where an increase in hardness was seen with increasing strain amplitude.

During the IP tests, Si and  $\beta$ -phase particles were found to re-orient themselves to between angles of 357° to 4°, almost parallel to the loading direction. During the OP tests, the particles oriented themselves between 87° and 94°, almost perpendicular to the loading direction. Also, elliptical pores with axes almost perpendicular to the loading direction were found after the OP tests and nearly parallel to the loading direction after the IP tests. Additionally, an increase in the number of micropores, presumably caused by creep effects, was observed in association with the pore orientation. Crack propagation from pore to pore was observed in all pore-containing specimens.

Coarsening of the intermetallic phases and some particles was observed, particularly the Si particles, and this was more prevalent for the OP than the IP loading. The  $\beta$ -phase and  $\text{Al}_2\text{Cu}$  reduced in size and there was no clear difference for the  $\alpha$ -phase. Compared to the OP loading, the IP fracture surfaces appeared more ductile when observed in the SEM. Crack initiation seemed to be linked to pores, microstructural imperfections and debonding of Si particles near to the test piece surface (see Figures III.1, III.2 and III.3 in Appendix C).

Transdendritic crack propagation took place along Si particles at the interface between the Si and the  $\alpha$ -matrix. Whereas few Si particles contain fractures, most of the specimens revealed debonding (Figure 5.24). Fracture of Si particles was only seen when the particles were oriented parallel to the loading direction. The fracture behaviour depended on the strain amplitude, i.e. on the time of exposure. For low strain amplitudes (long times at high temperature), cracks propagated mainly through the  $\alpha$ -matrix by decohesion of the eutectic Si particles from the  $\alpha$ -matrix with few particle fractures. At high strain amplitudes, the short-time development of stresses leads to brittle behaviour of intermetallic phases, with them debonding and finally fracturing (Figure 5.25). For strain amplitudes smaller than 0.35%, the length of cracks in the matrix reduced.

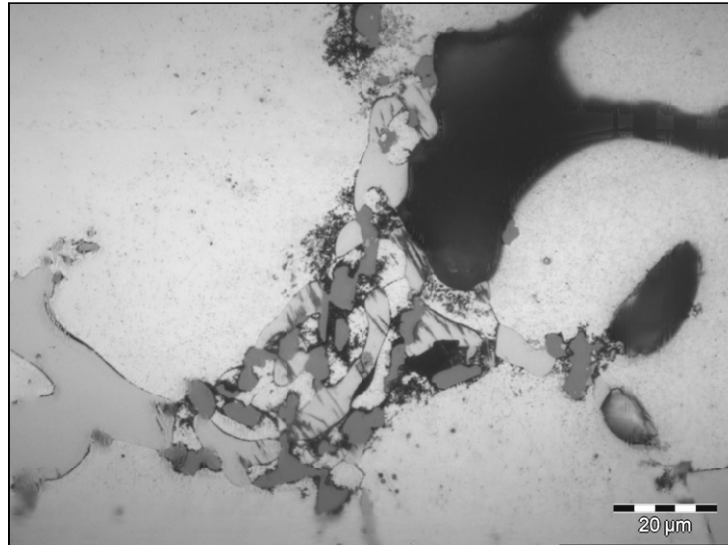


**Figure 5.24:** Particle decohesion in AlSi6Cu4-T6 under IP-TMF loading at a strain amplitude of 0.7%.

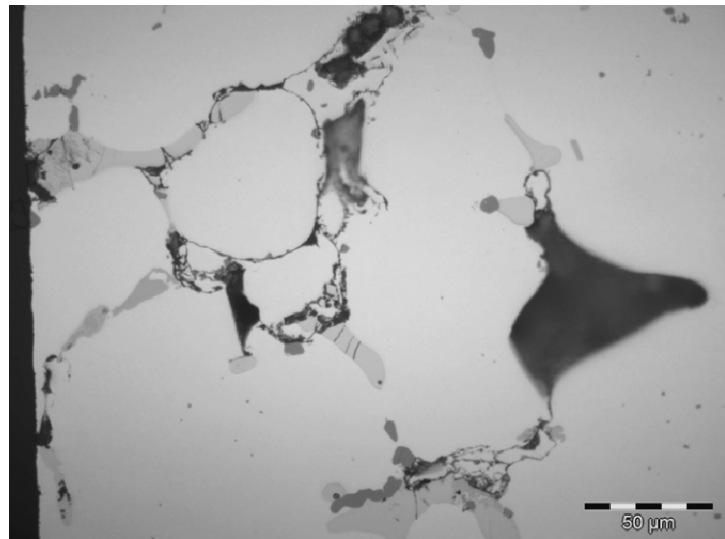


**Figure 5.25:** Particle cracking as crack initiator in AlSi6Cu4-T6 under IP-TMF loading at a strain amplitude of 0.7%.

Finally, internal voids were observed on the sample surface near to the fracture surface (Figure 5.26).

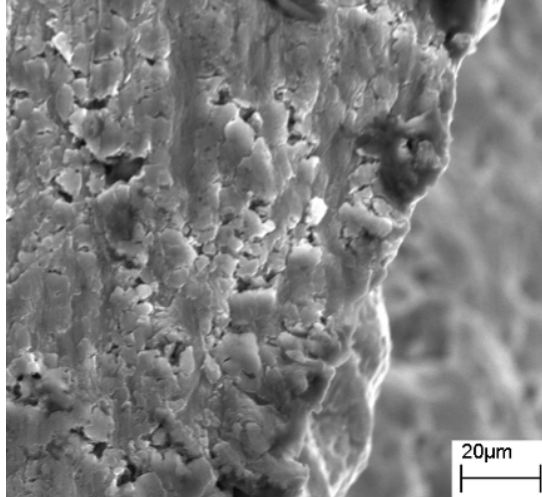


**Figure 5.26:** Internal voids just below the fracture surface of AlSi6Cu4-T6 under OP-TMF loading at a strain amplitude of 0.5%.

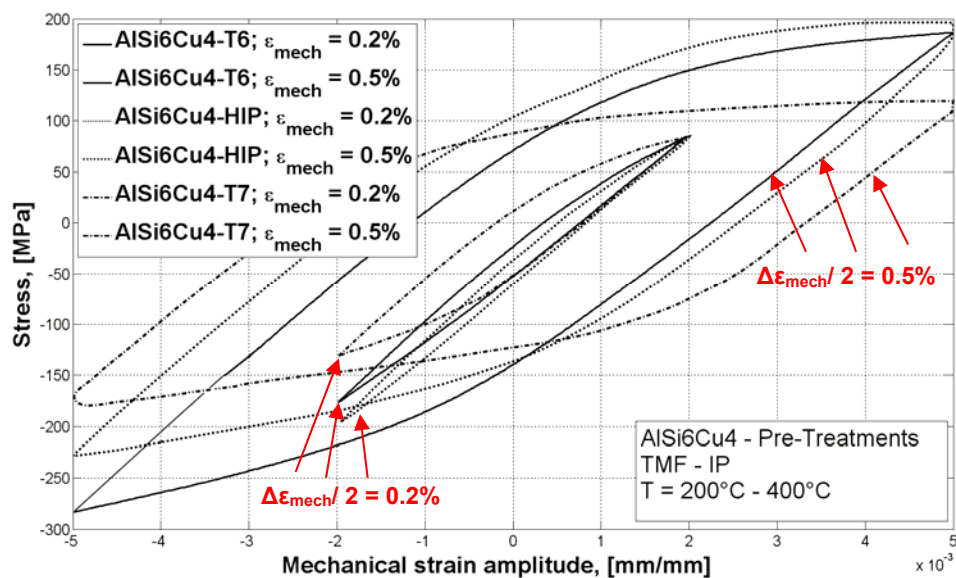
## 5.7 THERMO-MECHANICAL FATIGUE TESTS: EFFECT OF PRE-TREATMENT

This section describes the results of TMF tests on the reference alloy in the T7 and HIPped conditions, as well as in the T6 temper condition. Strain amplitudes of 0.2% and 0.5% were used and tests were carried out in under IP and OP conditions with the same temperature range as those reported in Section 5.6.

### 5.7.1 Cyclic stress-strain behaviour

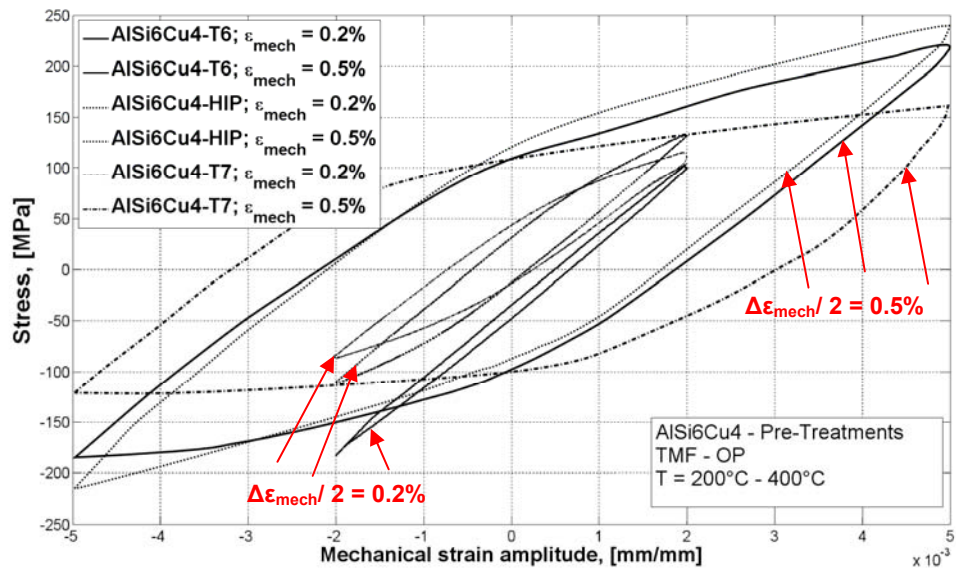
Figure 5.27 shows the IP TMF hysteresis loops at  $N=N_f/2$  for each of the three pre-treatments. At the lower strain amplitude, all developed almost the same maximum stress at the maximum strain (and temperature) but not at the minimum. At the minimum strain, the HIP-modified specimens exhibited the highest compressive stresses and the T7 the lowest. Also, both the HIP-modified and unmodified T6 heat-treated specimens showed nearly elastic behaviour at the low strain amplitude, unlike

the T7 specimen, which showed a broadening of the hysteresis loop. The area inside the hysteresis loops for the two T6 specimens is only about half that of the T7 specimen. At the higher strain amplitude, all three treatments exhibited elastic-plastic behaviour and the HIP-modified specimen had the highest tensile stress, with the unmodified T6 specimen exhibiting the highest compressive stress. The T7 specimen again showed the most pronounced elastic-plastic behaviour, as seen in a broadening of the loop. Furthermore, relaxation effects are visible for the unmodified T6 and T7 specimens at high temperature and high strain amplitudes, as seen by the decrease in gradient at the top right of the loops.



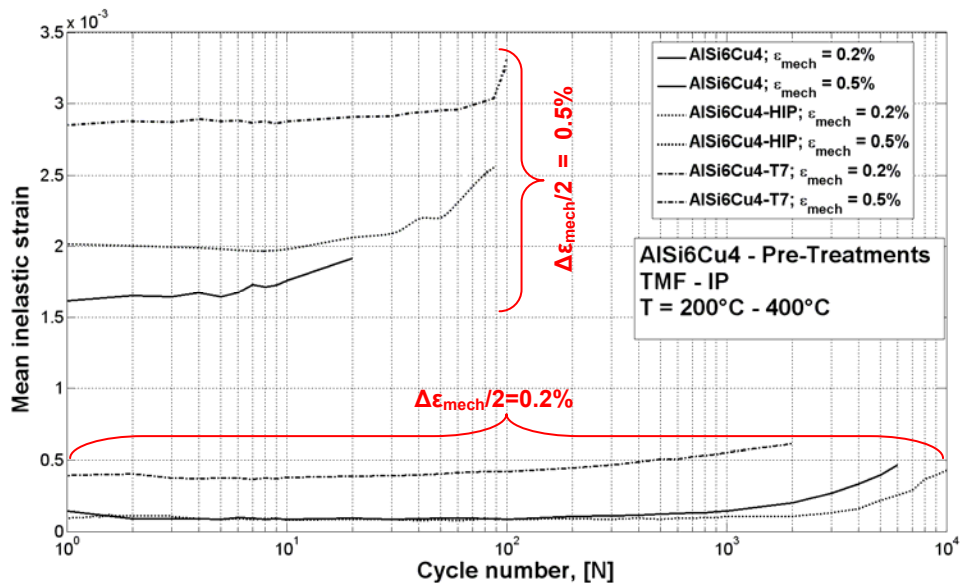
**Figure 5.27:** Hysteresis loops at  $N=N_f/2$  for AlSi6Cu4 for different pre-treatments under IP-TMF loading.

Figure 5.28 shows the corresponding hysteresis loops under OP TMF conditions at  $N=N_f/2$ . At the strain amplitude of 0.5%, the highest stresses at maximum and minimum temperature were reached for specimens with a HIP modification while the T7 heat treatment leads to the lowest stresses. Also, the hysteresis loops of the unmodified and HIP modified T6 heat treated specimens are almost the same, with a slight rotation (higher tensile and compressive maxima) for the HIP-modified. At the lower strain amplitude, the unmodified T6 specimen remains essentially elastic, although the HIP-modified specimen shows some broadening of the loop, the shift to compressive mean stresses being much stronger for the unmodified T6 specimen.



**Figure 5.28:** Hysteresis loops at  $N=N/2$  for AISi6Cu4 with different pre-treatments under OP TMF loading.

Figure 5.29 shows the evolution of mean inelastic strain during the IP TMF tests. The T7 heat treated specimens show the highest mean inelastic strains at both strain amplitudes whereas both T6 heat treated specimens show almost elastic behaviour at the lower strain amplitude up to around  $N=1000$ , where an increase in mean inelastic strain occurs for both specimens.



**Figure 5.29:** Evolution of mean inelastic strain of AISi6Cu4 with different pre-treatments under IP-TMF loading.

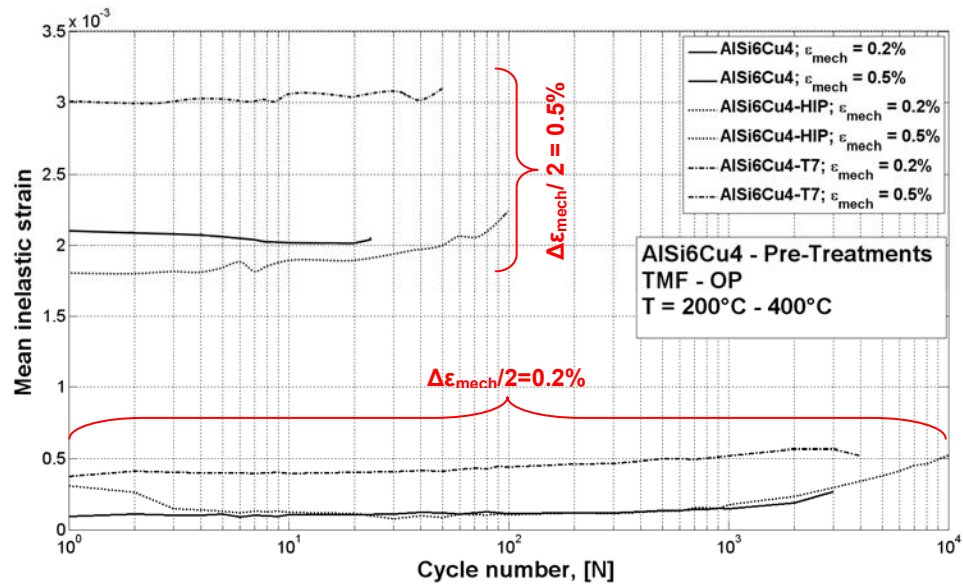


**Figure 5.30:** Evolution of mean inelastic strain of AISi6Cu4 with different pre-treatments under OP-TMF loading.

Figures 5.31 and 5.32 compare the evolutions of stress amplitudes and mean stresses for both strain amplitudes under IP and OP TMF loading, respectively. While a slight hardening can be discerned for high strain amplitudes under IP loading, the OP tests show no such behaviour. Also, both modified and unmodified T6 specimens show a gradually reducing displacement of mean stress in the compression direction during their lifetime, which did not occur for T7 specimens. The unmodified T6 and T7 specimens tested at high strain amplitudes under OP loading showed a significant drop in both maximum and mean stress approaching failure, a behaviour not seen in the IP tests. Under IP loading, the specimens tested with the lower strain amplitude showed more ductile failures, characterised by a continuous decrease of stresses towards the end, whereas only brittle fracture behaviour can be observed for the OP tests characterised by fracture without a prior rapid drop in stress. For low strain amplitudes, the evolution of stress is about the same for unmodified and HIP-modified T6 specimens, whereas the T7 heat treated specimens exhibited lower stresses.



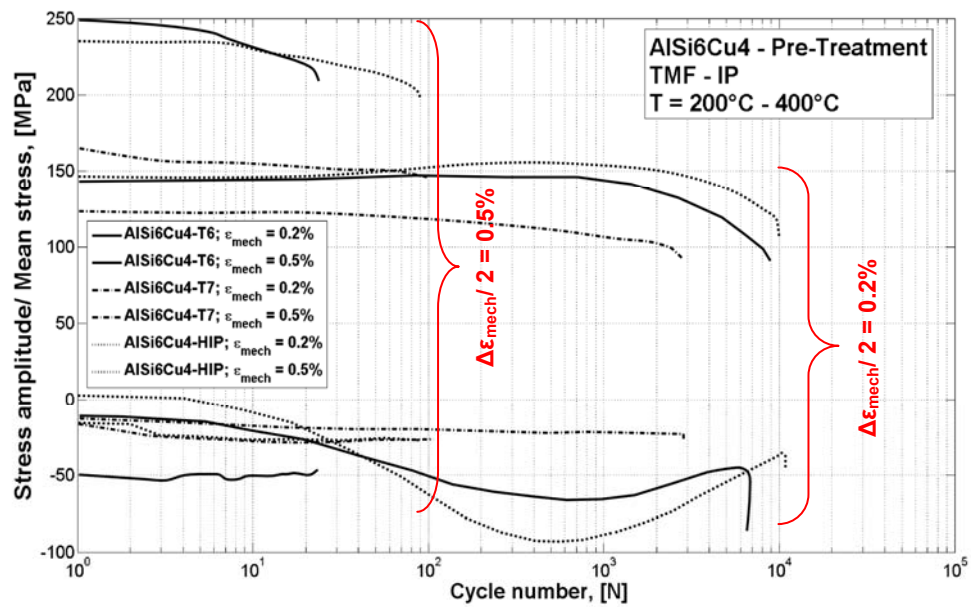


**Figure 5.31:** Evolution of stress amplitude and mean stress for AISi6Cu4 with different pre-treatments under IP TMF loading.

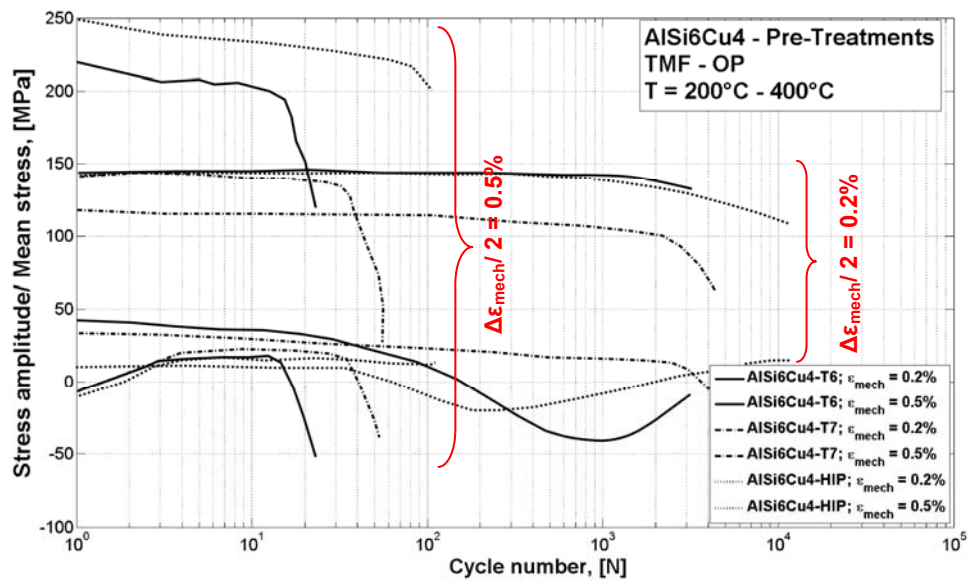


**Figure 5.32:** Evolution of stress amplitude and mean stress for AISi6Cu4 with different pre-treatments under OP TMF loading.

The TMF performance can be conveniently summarised with a parameter denominated “ductility factor”, which has been elaborated during the research. It is defined as the product of the maximum stress at  $N=N_f/2$  and the mean inelastic strain at  $N=N_f/2$ . Figure 5.33 shows how the ductility factor changes with mechanical strain amplitude. An

increase in strain amplitude up to about 0.5% leads to a lower increase in the ductility factor than the same increase in strain amplitude above 0.5%. The higher the mechanical strain rate is, the lower is the mean inelastic strain in relation to the strain rate. Changes in ductility factor can be seen in fracture and damage behaviour as well.

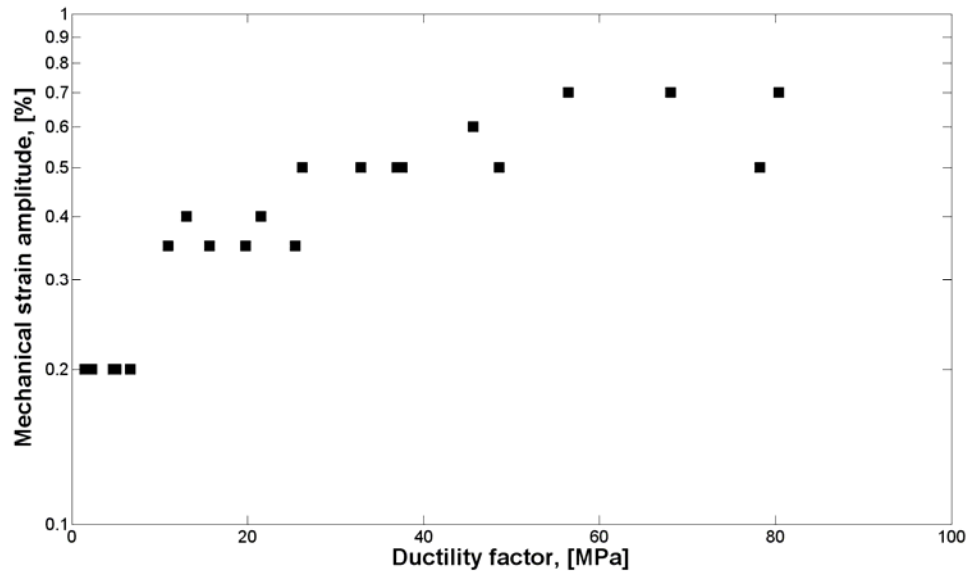


**Figure 5.33:** Mechanical strain amplitude vs. ductility factor for AlSi6Cu4 with different pre-treatments of IP and OP TMF tests.

### 5.7.2 Lifetime behaviour

Figure 5.34 summarises the TMF lifetimes of the three pre-treatments under IP and OP loading. As expected, the lifetime becomes shorter with increasing strain amplitude in an approximately linear fashion when plotted on a log-log scale. The HIP-modified specimens have the best overall TMF performance, reaching the threshold of  $10^4$  cycles without fracture at strain amplitudes of 0.2%. The HIP-modified specimens also demonstrate nearly the same lifetime behaviour for IP and OP loading.

The T7 heat treatment showed shorter lifetimes under OP than IP loading for high strain amplitudes and longer lifetimes for low strain amplitudes. The unmodified T6 and T7 specimens showed nearly the same behaviour under OP loading, but the T6 was markedly poorer than the T7 at lower strain amplitudes and better at higher strain amplitudes. An unambiguous assignment to the diagrams of Nitta and Kuwabara (Table 3.2) cannot therefore be done. For high strain amplitudes, HIP specimens reveal a higher lifetime under IP loading in contrast to lower strain amplitudes, whereas OP

loading results in higher lifetimes. The same behaviour can be observed for T7 heat treated specimens.

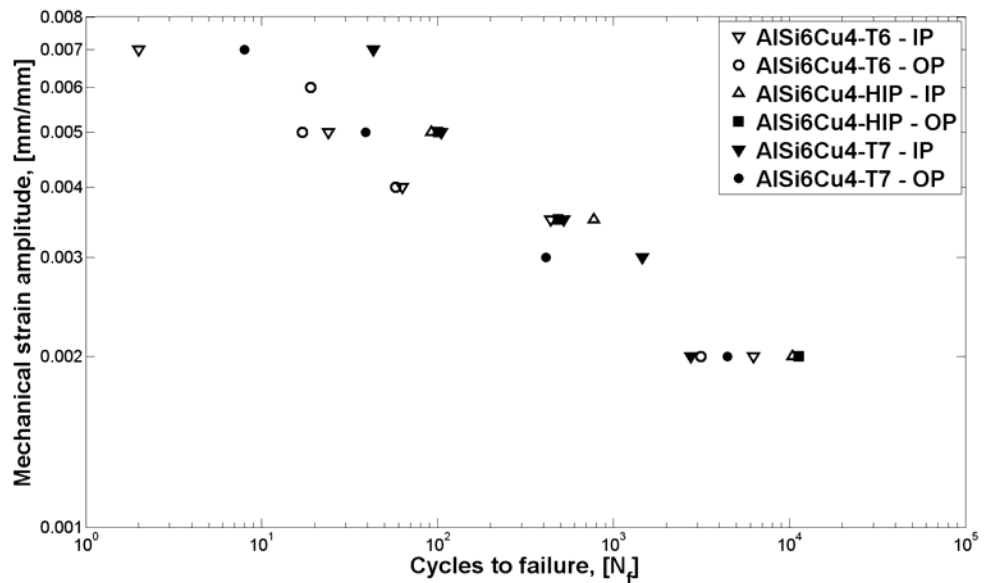


**Figure 5.34:** Mechanical strain amplitude vs.  $N_f$  for AlSi6Cu4 with different pre-treatments under TMF loading.

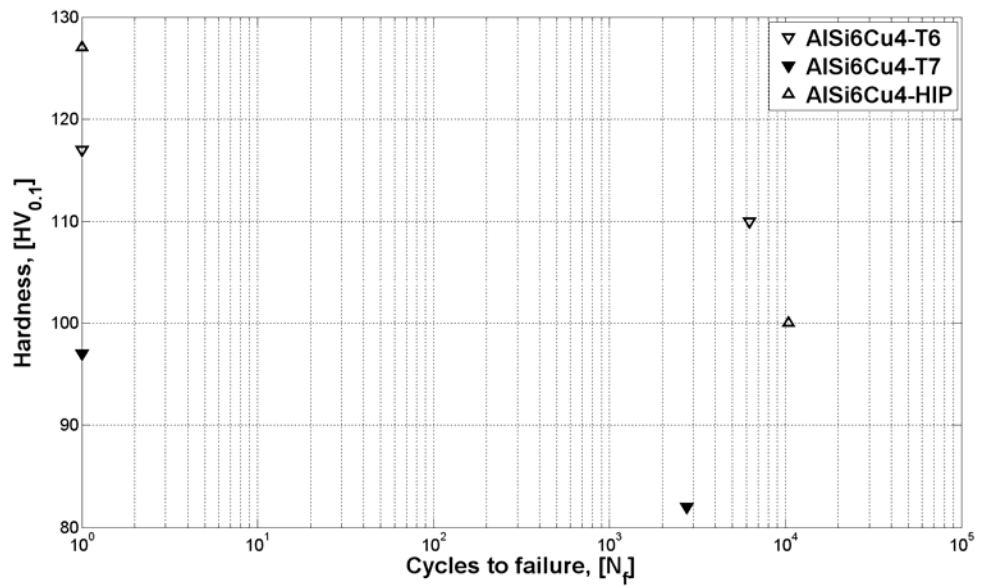
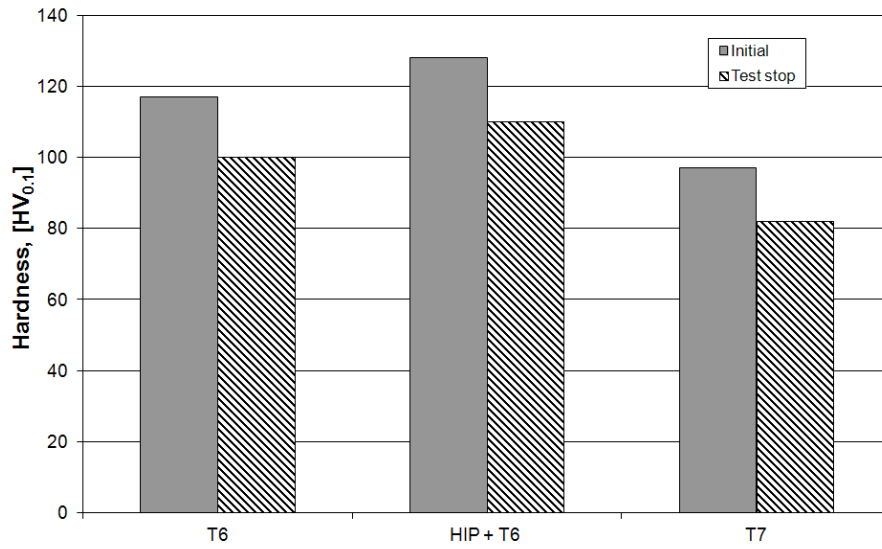
### 5.7.3 Microstructural observations

Table 5.4 summarises the pre-test hardness measurements which show that the T7 heat treatment leads to a reduction of hardness over T6 by about 30% whereas the HIP-modification produces about a 10% increase.

**Table 5.4:** Pre-test hardness values for different temper conditions of AlSi6Cu4.

Temper condition	Hardness, [HV <sub>0.1</sub> ]
T6	117
HIP+T6	128
T7	97

Figure 5.35 shows the post-test hardness for specimens tested under IP-TMF loading at a strain amplitude of 0.2%. The number of cycles to failure is essentially a measure of the degree of thermo-mechanical exposure and, as can be seen, all three conditions exhibit nearly the same gradient of hardness with exposure. The difference between the decreases is in approximate proportion to the differences in pre-test hardness.



**Figure 5.35:** Decrease of hardness for different amounts of TMF exposure for the different pre-treatments.

### **5.7.3.1 Effect of HIP-modification on T6 microstructure**

HIP-modification produced a reduction in porosity by about 82% to 0.03% and SEM examination of the fracture surfaces revealed no shrinkage porosity and only a small amount of gas porosity. The representative pore size was less than 17 $\mu\text{m}$ , smaller than the SDAS. No effect of HIP-modification on SDAS, grain size, or size and morphology of eutectic Si and other precipitates could be discerned. Furthermore, no new phases were observed as a result of HIP-modification.

The reduction of porosity leads to a change of crack initiation and failure mechanisms. While pores near the surface are crack initiators in specimens with a higher content of porosity, cracks initiate at Si particles and precipitates in HIP samples and lead to damage. In particular, a difference between IP and OP-TMF loading can be detected. Specimens under IP-TMF loading reveal a fracture behaviour which is more ductile than that observed under OP-TMF loading. Furthermore, fine striations near to the crack path can be detected so it seems that some propagation is plastic. No cracks were found to have been initiated at the remaining pores. The formation of micropores due to creep effects was not observed in TMF loaded HIP specimens. Whereas cracks propagate from pore to pore in pore-containing specimens, propagation in HIP-modified samples was observed to follow the intermetallic phases and the interface between Si and  $\alpha\text{-Al}$ . Fracture of  $\text{Al}_2\text{Cu}$  supported crack propagation in most of the specimens.

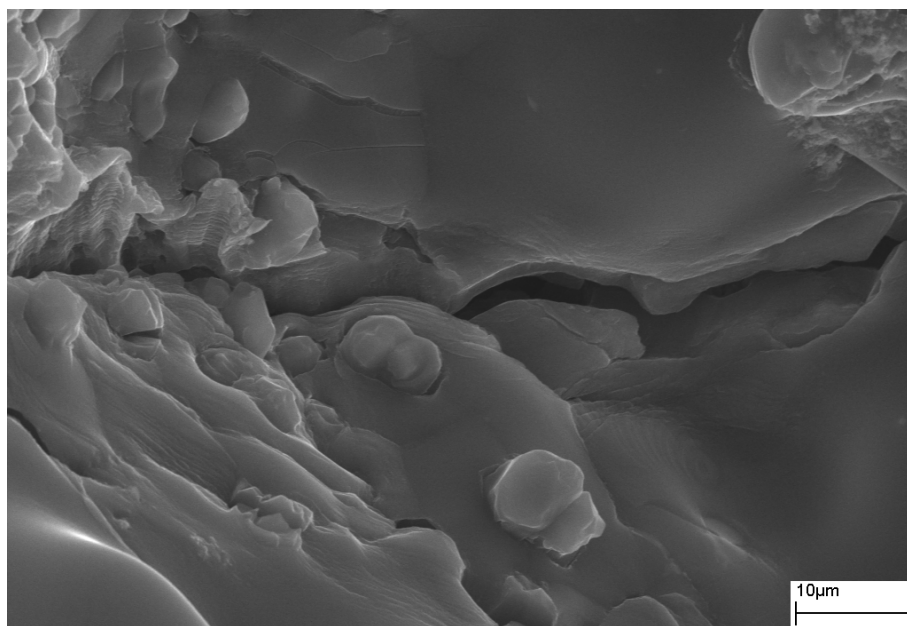


**Figure 5.36:** Fine striations near to the fracture surface for  $\text{AlSi6Cu4}$ -HIP at a strain amplitude of 0.2%.

The long time exposure for low strain amplitudes leads to grain growth in addition to the coarsening of precipitates. An increase of around 25% was found to have taken place to around  $40\mu\text{m}^2$  for all cases of 0.2% strain amplitude. At these low strain amplitudes fracture behaviour similar to the T6 specimens was observed, although the specimens tested under high strain amplitudes revealed intercrystalline crack propagation. No difference in the behaviour of IP and OP loaded could be discerned, which is reflected in their similar lifetime behaviour.

### **5.7.3.2 Comparison of T7 vs. T6**

The T7 pre-treatment leads to the formation of incoherent precipitates, so that dislocations can circumvent the precipitates by the “Orowan mechanism”. The larger inter-precipitate distances lead to a longer running time and ductility increases, whereas strength decreases, which can be seen in the CERT and in the comparison of hardness values.

Specimens tested with OP loading exhibited an orientation of Si particles, which form an angle of around  $90^\circ$  to the loading direction at all strain amplitudes, although this behaviour was only observed for IP loading above a strain amplitude of 0.35%. The same behaviour was seen for the  $\beta$ -phase under IP and OP loading. With increasing cycle time and hence with decreasing strain rate, an increase in grain size was detected. The T6 and HIP-treated specimens had a mean final grain size of  $30\mu\text{m}$ , whereas T7 specimens had a mean grain size  $63\mu\text{m}$  before starting the tests. In contrast to T6 and HIP specimens, the T7 specimens showed considerable grain coarsening during the TMF tests; for example at a strain amplitude of 0.2% for OP loading the grains coarsened by a factor of about 2.5. This coarsening before testing and during the tests prevents micropores caused by various creep effects from forming. This can be attributed to the lower number of grains and hence triple points. While Si particles and the  $\text{Al}_2\text{Cu}$  phase show no changes in size, a slight coarsening of  $\alpha$ - and  $\beta$ -phases during TMF tests can still be detected.

For low strain amplitudes ( $\leq 0.5\%$ ), Stage I crack initiation under IP and OP loading was observed, followed by Stage II. Here, damage of the matrix, cracks alongside the particles and through the intermetallic phases could be seen, with crack initiation Si clusters. Cracks propagated in a rectilinear fashion, indicating brittle, cleavage fracture

behaviour. At high strain amplitudes, the same behaviour as the ordinary T6 heat treated specimens was observed. Above threshold strain amplitude of 0.5%, only Stage II behaviour with damage along particle interfaces has taken place, as seen in Figure 5.37.

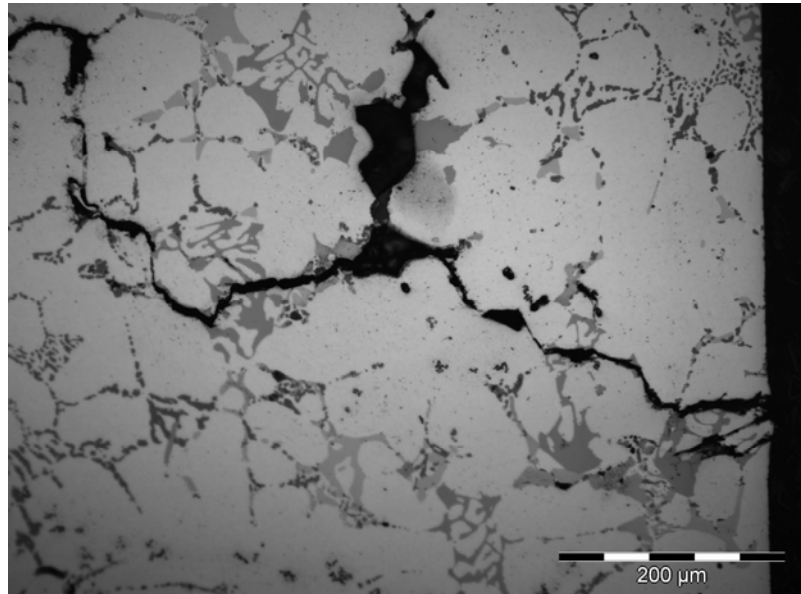


**Figure 5.37:** Crack path for AlSi6Cu4-T7 at a strain amplitude of 0.5% under OP-TMF loading. The loading axis is in the vertical direction.

Either Si particles are pulled out of the matrix or cracks through the  $Al_2Cu$ ,  $\alpha$ - or  $\beta$ -phases lead to damage. As already mentioned, the coalescence of pores supports crack propagation and no cracks were observed in Si particles. Cracking of both stages can be detected for iron-rich particles, as can be seen in Figure 5.38.

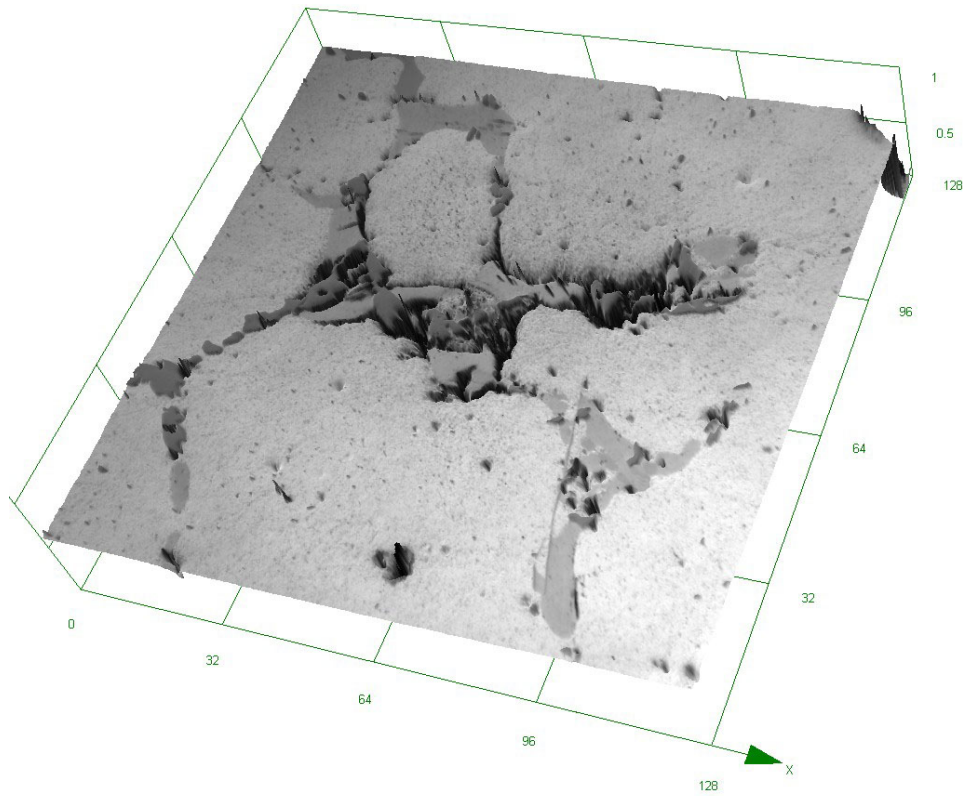


**Figure 5.38:** Laser scan micrograph showing particle cracking of the  $\alpha$ -phase in AlSi6Cu4 under IP-TMF loading at a strain amplitude of 0.5%. The loading direction is in the horizontal direction.

Cracks only occurred in the Si particles orientated at an angle of  $\sim 90^\circ$  to the loading direction. However, this only occurs if they have begun to dissolve out of the matrix. While pores or clusters of Si particles act as crack initiation points at low strain amplitudes, cracked particles act as initiation points at high strain amplitudes. The fracture surfaces of the T7 specimens showed brittle, rectilinear propagation under high strain amplitudes as did the specimens given an ordinary T6 heat treatment. For low strain amplitudes, cleavage fractures could be observed and the long time exposure leads to similar fracture behaviour under IP and OP loading.



## 5.8 THERMO-MECHANICAL FATIGUE TESTS: EFFECT OF SDAS

TMF tests were performed on AlSi9Cu3 and AlSi6Cu4 specimens in order to investigate the influence of different solidification rates on mechanical behaviour and lifetime.

### 5.8.1 Cyclic stress-strain behaviour

Figure 5.39 shows the hysteresis loops under IP loading at  $N=N_f/2$  for the extreme mechanical strain amplitudes 0.2 and 0.5%. At all mechanical strain amplitudes AlSi6Cu4 gave higher stresses at maximum and minimum temperature than AlSi9Cu3. The AlSi9Cu3 loops show a broadening which can be attributed to a higher amount of an elastic-plastic behaviour, which it displays from the initial cycle on. At low strain amplitudes the tensile stresses are almost equal as the compressive ones, although this effect was not found for higher strain amplitudes.

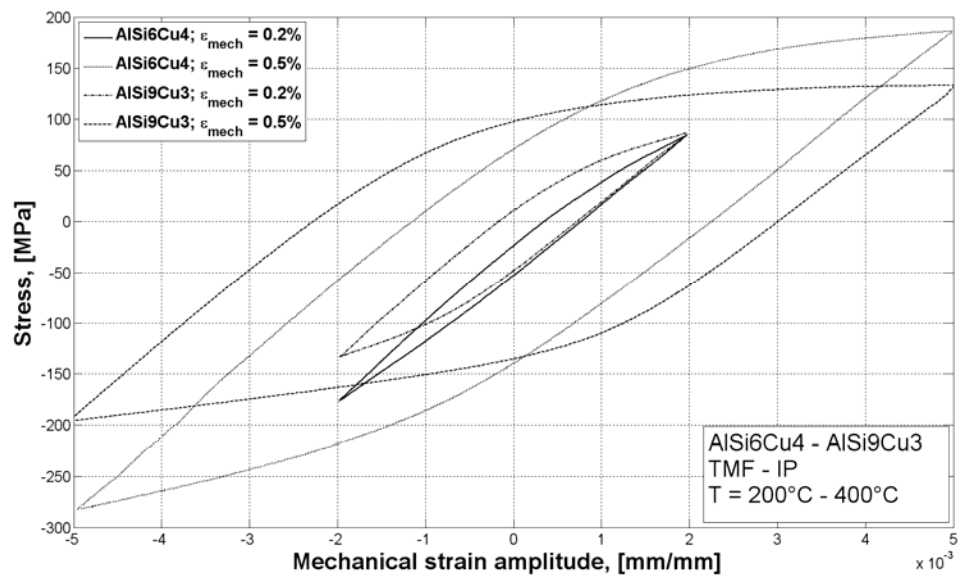
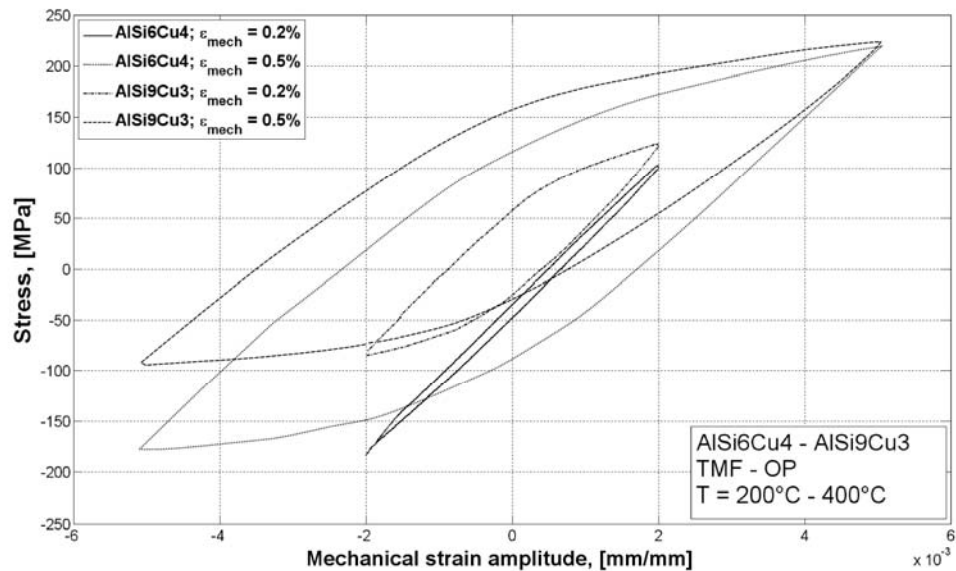


Figure 5.39: Hysteresis loops at  $N=N_f/2$  for AlSi6Cu4 and AlSi9Cu3 under IP-TMF loading.

At a strain amplitude of 0.5% the OP tests develop nearly the same stresses at minimum temperature at  $N=N_f/2$  for both alloys although they are distinct at lower strain amplitudes. AlSi6Cu4 only exhibits elastic behaviour at  $N=N_f/2$ , and AlSi9Cu3 shows pronounced elastic-plastic behaviour with a smaller shift towards compressive mean stresses.



**Figure 5.40:** Hysteresis loops at  $N=N_f/2$  for AlSi6Cu4 and AlSi9Cu3 under OP-TMF loading.

Figures 5.41 and 5.42 show the mean inelastic strain over the TMF lifetime for IP and OP loaded specimens. The mean inelastic strains are smaller for AlSi6Cu4 under both IP and OP conditions. The strains begin to increase beyond  $N=100$  for AlSi9Cu3 for low strain amplitudes under IP and OP, but a delay to longer times can be observed for AlSi6Cu4, where an increase occurs beyond  $N=500$  for IP and beyond  $N=1000$  for OP loading. Below these thresholds, only elastic behaviour was seen. In the OP condition, specimens tested at higher strain amplitudes revealed a slight decrease in mean inelastic strain up to  $N=10$ , followed by an increase until fracture. Mean inelastic strain increases from the initial cycle on for IP loading and higher strain amplitudes. Exceptionally, AlSi6Cu4 exhibits brittle behaviour under OP conditions so that an increase of mean inelastic strain can be observed in one cycle.

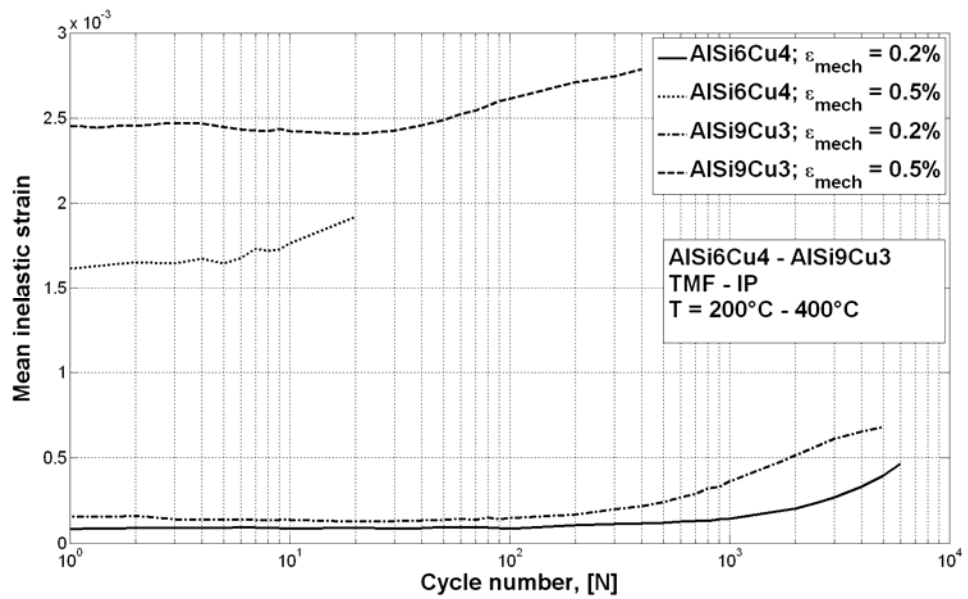


Figure 5.41: Mean inelastic strain for AlSi6Cu4 and AlSi9Cu3 under IP-TMF loading.

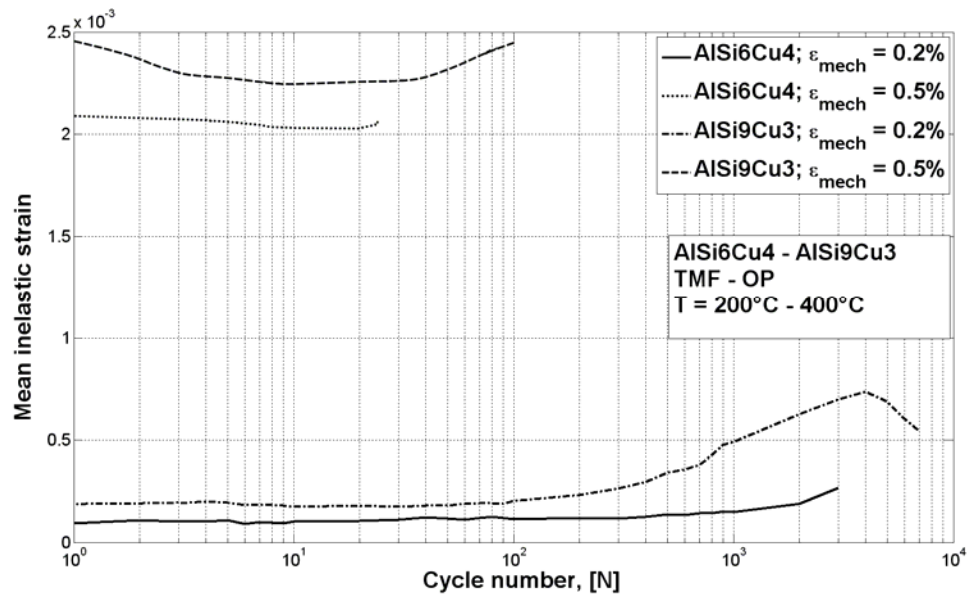
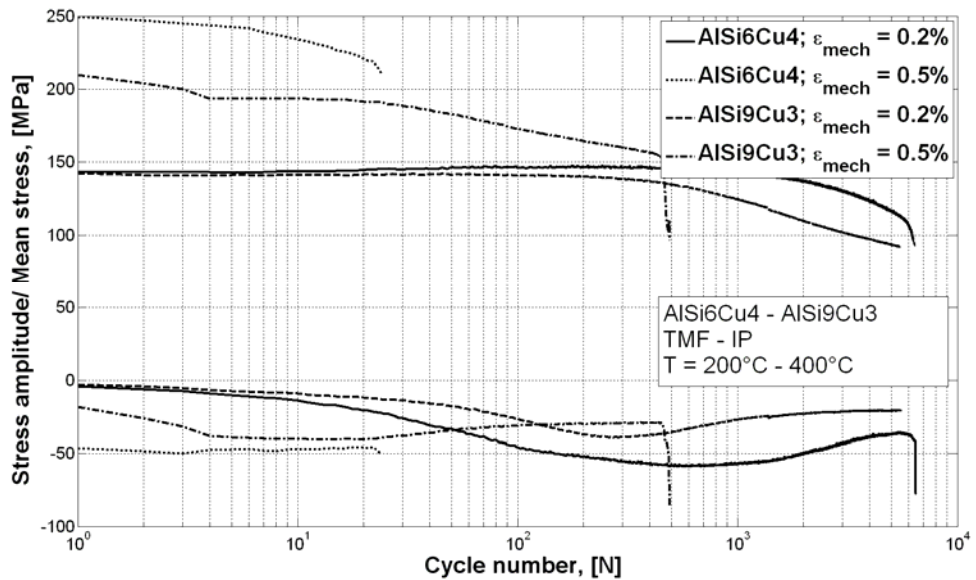


Figure 5.42: Mean inelastic strain for AlSi6Cu4 and AlSi9Cu3 under OP-TMF loading.

Stress amplitudes and mean stresses for IP and OP loading are shown in Figures 5.43 and 5.44. The IP and OP curves for a strain amplitude of 0.2% nearly all show the same evolution with a shallow increase until, around  $N=300$ , the AlSi9Cu3 curve shows an abrupt change in slope, whereas the AlSi6Cu4 curve begins to decrease more gently. The higher strain amplitudes give higher stress amplitudes and the curves exhibit a decrease from the beginning on, the curves for AlSi6Cu4 and AlSi9Cu3 nearly showing

the same values at the beginning for OP-TMF loading. AlSi6Cu4 IP0.5% and AlSi9Cu3 OP0.5% nearly demonstrate the same behaviour although AlSi6Cu4 shows higher stress amplitudes than AlSi9Cu3 for both lower and higher strain amplitudes. AlSi6Cu4 has higher negative mean stresses for IP-TMF loading than AlSi9Cu3, but no such distinction can be identified for OP-TMF.



**Figure 5.43:** Stress amplitudes and mean stresses for AlSi6Cu4 and AlSi9Cu3 under IP-TMF loading.

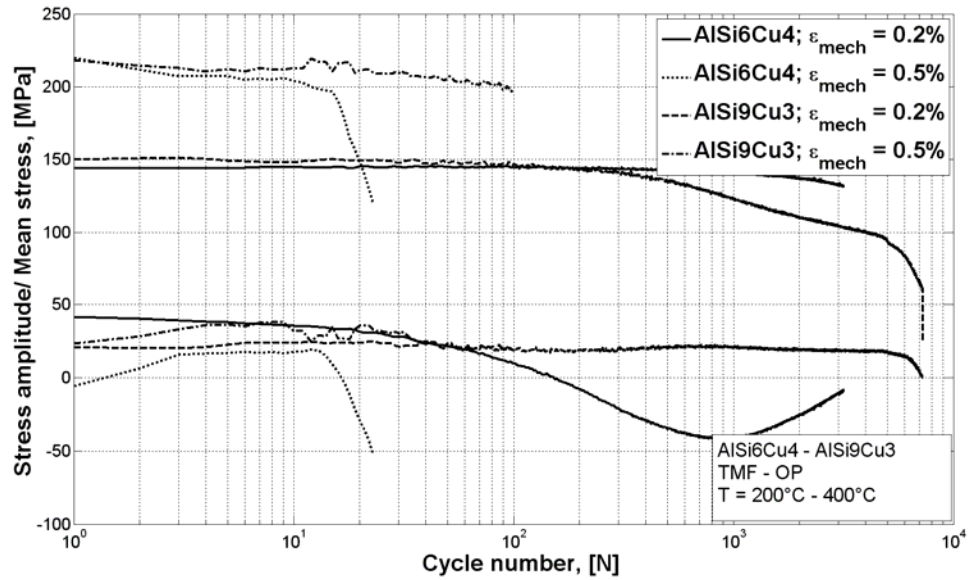


**Figure 5.44:** Stress amplitudes and mean stresses for AlSi6Cu4 and AlSi9Cu3 under OP-TMF loading.

### 5.8.2 Lifetime behaviour

Figure 5.45 shows the lifetimes of AlSi6Cu4 and AlSi9Cu3 for IP and OP loading in the usual log-log plot with the expected decrease in lifetime with increasing strain amplitude for both alloys. AlSi9Cu3 has longer lifetimes than AlSi6Cu4 under both IP and OP loading, and IP loading leads to shorter lifetimes than OP for both alloys. While AlSi9Cu3 exhibits lifetimes around an order of magnitude higher than AlSi6Cu4 for high strain amplitudes, this difference decreases with decreasing strain amplitude. The defined fatigue endurance limit of 10000 cycles was not reached by any of the specimens. Using the Nitta-Kuwabara classification scheme (Table 3.2), both AlSi6Cu4 and AlSi9Cu3 can be classed as showing type E' behaviour with creep damage being deferred to higher loading amplitudes in AlSi9Cu3.

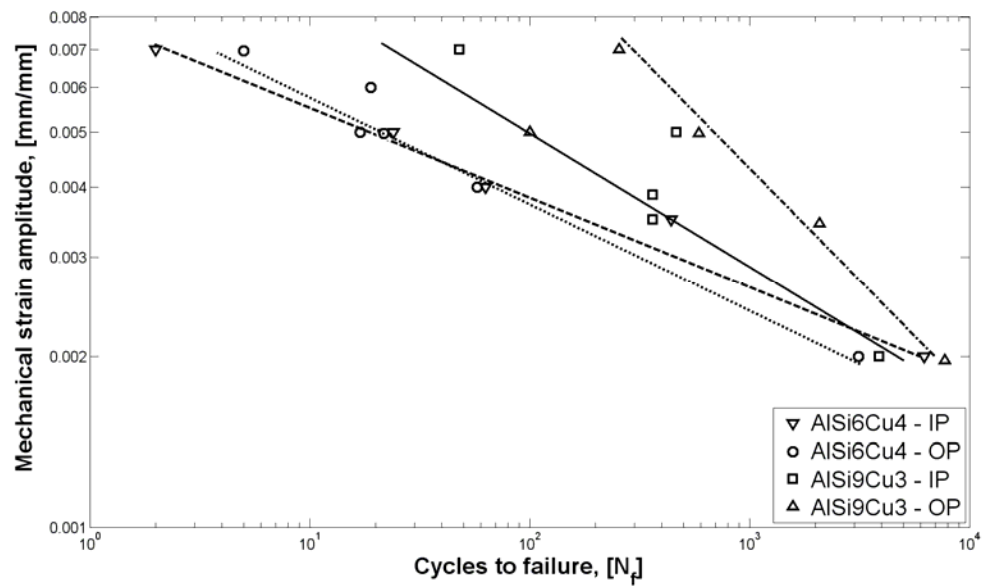


**Figure 5.45:** Mechanical strain amplitude vs.  $N_f$  for AlSi6Cu4 and AlSi9Cu3 under TMF loading.

### 5.8.3 Microstructural observations; comparison with reference alloy

Due to the lower SDAS, smaller intermetallic phase particles are observed, Figure 5.46. Furthermore, the higher proportion of  $\beta$ -phase results in a homogeneous distribution of finely dispersed Si particles. The orientation of intermetallic phases and particles for AlSi9Cu3-T6 is identical to that for AlSi6Cu4-T6 tested under TMF loading.

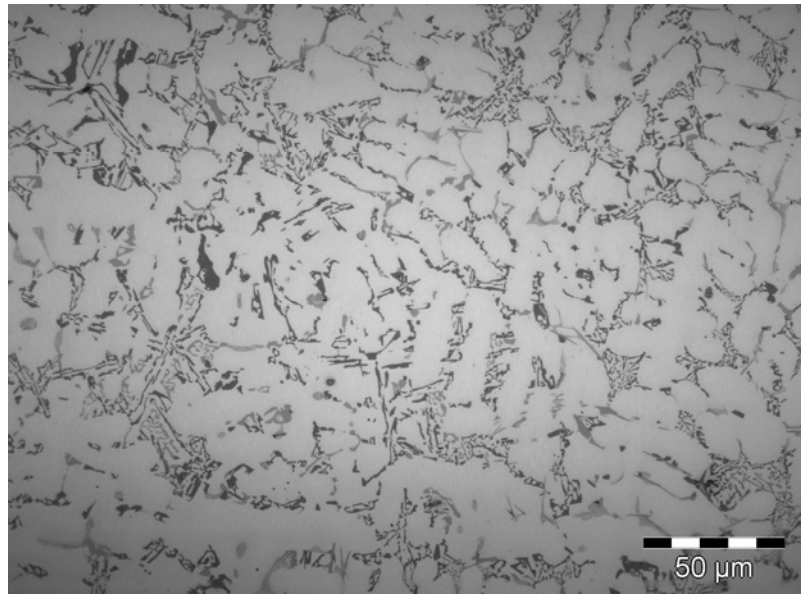


**Figure 5.46:** Microstructure of AlSi9Cu3 in the T6 condition. The loading axis is in the vertical direction.

Figure 5.47 gives an overview of the ageing effects on the two alloys. Rather than cyclic softening, the long term thermal exposure during IP-TMF loading gives a morphological change which is tantamount to a change from T6 to T7. Ageing is indicated by a hardness decrease until the onset of fracture for both, IP and OP loading.

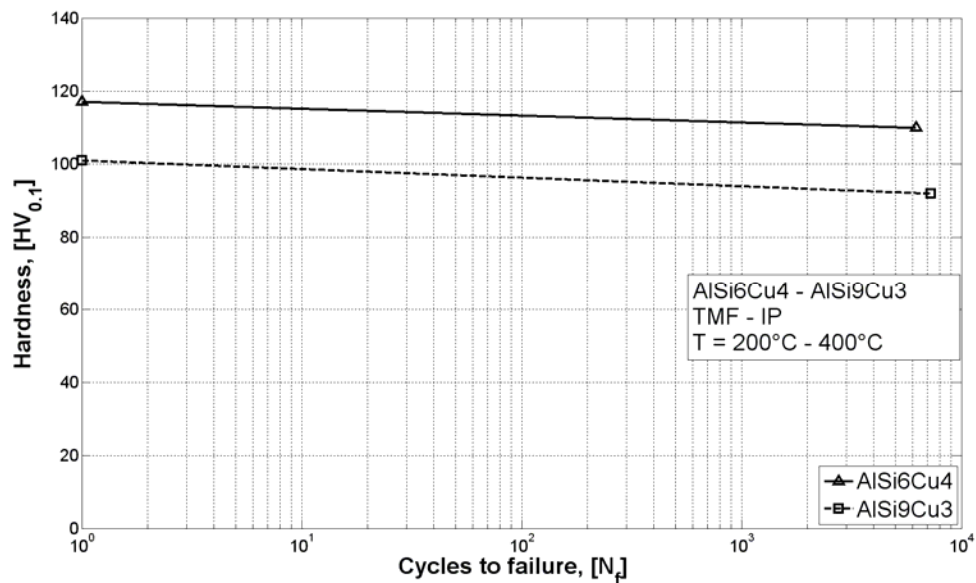
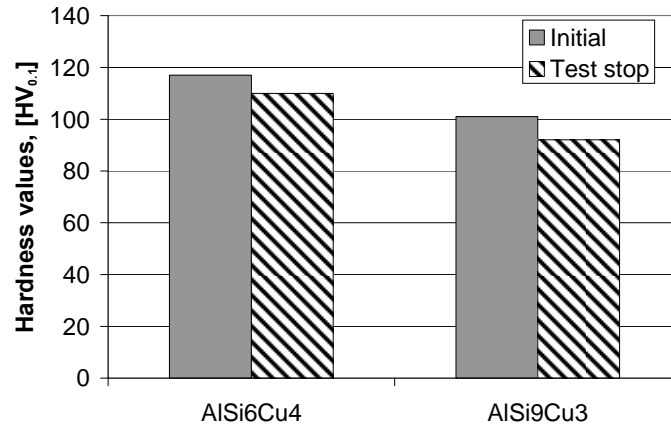


**Figure 5.47:** Hardness decrease during the lifetime for AISi6Cu4 and AISi9Cu3 under IP-TMF loading at a strain amplitude of 0.2%.

Due to the lower porosity, which can be attributed to the lower SDAS, crack initiation starts in precipitation clusters near to the surface. Furthermore, the low SDAS leads to controlled crack propagation along the interface between the  $\alpha$ -matrix and intermetallic phases. Also, the volume fraction of Si particles is higher than in AISi6Cu4. Induced by the higher Fe content, clustering of oversize  $\alpha$ -phase near to the surface could be observed, leading to crack initiation and propagation caused by the high notch stresses. Figure 5.48 shows such an Fe cluster near to the surface. A higher sensitivity for particle cracking can be observed for such Fe phases.



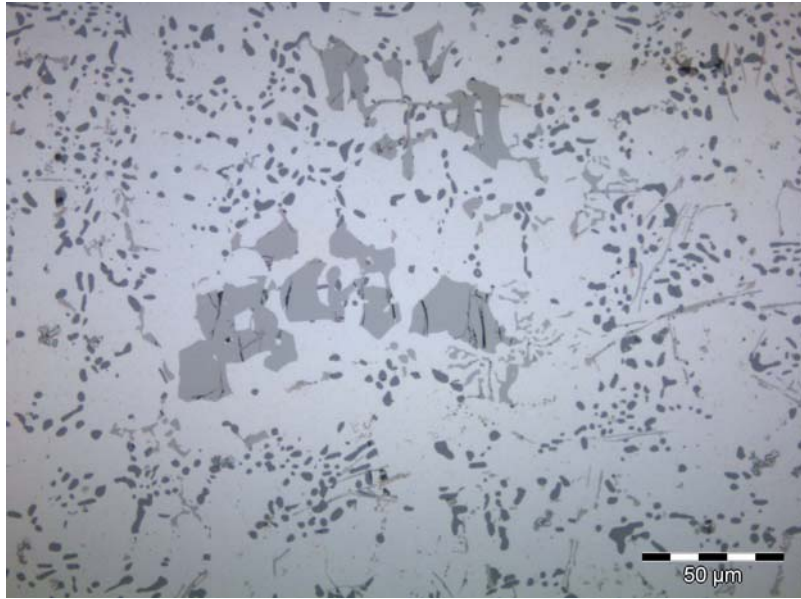


**Figure 5.48:** Cracks in Fe cluster in AlSi9Cu3 near to the surface of IP-TMF specimen tested at a strain amplitude of 0.5%. The loading axis is in the vertical direction.

Whereas no matrix separation was detected in the surface near regions for AlSi6Cu4 for low strain amplitudes, a separation of Si particles from the matrix was visible for AlSi9Cu3. In the bulk material, there was no Si decohesion but there was a clear indication for intermetallic phases. For higher strain amplitudes, the separation of particles in AlSi9Cu3 was at an angle of  $45^\circ$  to the loading direction. Particle clusters showed enhanced decohesion. In general, particle cracking was the main crack propagation mechanism for higher strain amplitudes. Figure 5.49 shows crack propagation along “debonded” particles, (IP-TMF 0.2%).

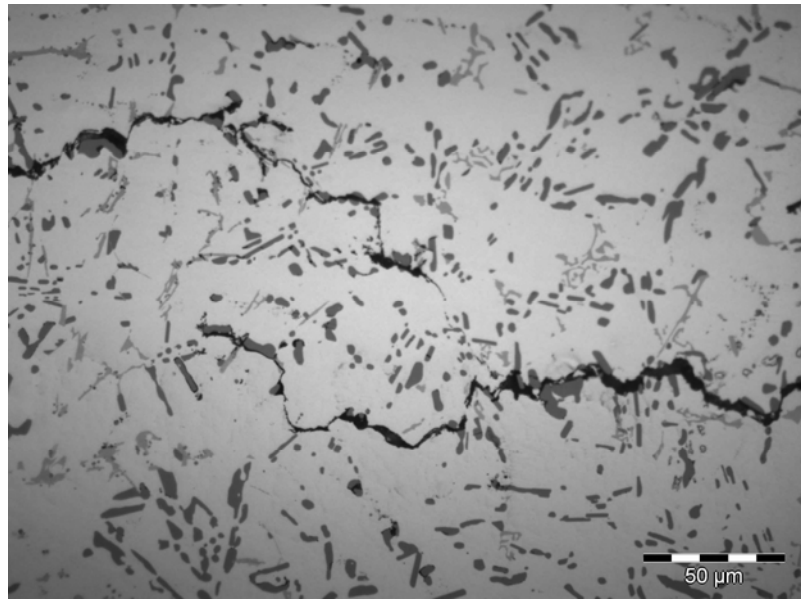


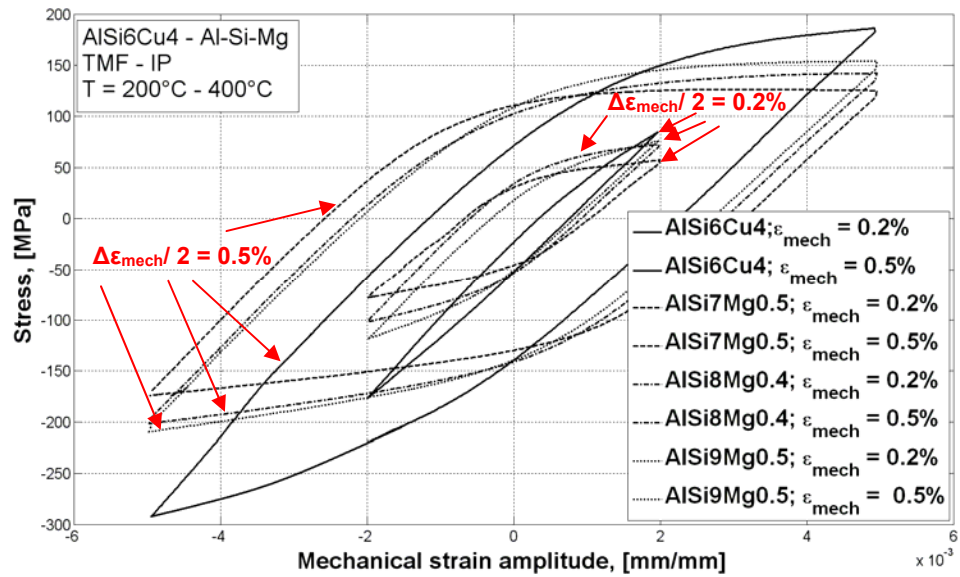
**Figure 5.49:** Cracks alongside Si particles in AlSi9Cu3 tested under IP-TMF loading at a strain amplitude of 0.2%. The loading axis is in the vertical direction

## 5.9 THERMO-MECHANICAL FATIGUE TESTS: EFFECT OF ALLOYING ELEMENTS

This section compares the alloys containing 0.4 or 0.5 Mg with the reference alloy, all in the T6 temper condition. Thus, as well as examining the effect of replacing Cu with Mg and Si, the influence of different Si contents on the alloys with Mg was examined.

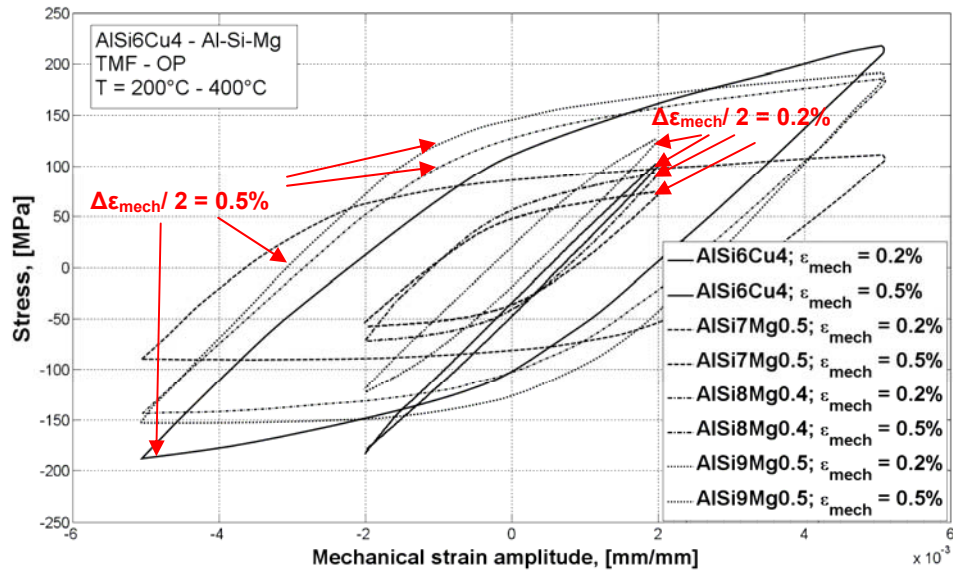
### 5.9.1 Cyclic stress-strain behaviour

Figure 5.50 shows the effect of the varying Si content of the Al-Si-Mg alloys on the stress-strain loops at  $N=N_f/2$  under IP-TMF loading against the background of the AlSi6Cu4 reference alloy. An increase in the magnitudes of both maximum and minimum stresses with increasing Si content can be seen for the Al-Si-Mg alloys, although none are as high as for the reference alloy. In all cases, the effect of alloying is more pronounced on the compressive stresses than on the tensile stress, at least for the in-phase loading shown in Figure 5.50. It might be noted that AlSi6Cu4 reaches higher stresses under compression for a strain amplitude of 0.2% than AlSi7Mg0.5 does for a strain amplitude of 0.5%. Furthermore, pronounced elastic-plastic behaviour can be discerned at  $N=N_f/2$  for all the Al-Si-Mg alloys.



**Figure 5.50:** Hysteresis loops at  $N=N_f/2$  for AlSi6Cu4 and Al-Si-Mg alloys under IP-TMF loading.

The differences between AlSi6Cu4 and AlSi7Mg0.5 are even more pronounced for OP-TMF loading, as are those between the Al-Si-Mg alloys (Figure 5.51). For example, the stresses in AlSi7Mg0.5 tested with a strain amplitude of 0.5% were exceeded by the stresses in AlSi9Mg0.5 tested with a strain amplitude of 0.2%. In general, increasing Si content leads to an increase in maximum and minimum stresses and a decrease in the breadth of the hysteresis loops. Furthermore, AlSi6Cu4 tested with a strain amplitude of 0.2% has a higher magnitude of minimum stresses than any of the Al-Si-Mg alloys with strain amplitudes  $\leq 0.5\%$ . Pronounced elastic-plastic behaviour is evident at  $N=N_f/2$  for AlSi7Mg0.5 and AlSi8Mg0.4 whereas AlSi9Mg0.5 and AlSi6Cu4 only reveal plastic behaviour.



**Figure 5.51:** Hysteresis loops at  $N=N_f/2$  for AlSi6Cu4 and Al-Si-Mg alloys under OP-TMF loading.

Creep effects occur above a strain amplitude of 0.5% for IP and OP-TMF loading conditions. Figures 5.52 and 5.53 illustrate the mean inelastic strain development during lifetime of IP and OP-TMF loaded specimens with a strain amplitude of 0.2% and 0.5%. While the Al-Si-Mg alloys tested at a strain amplitude of 0.2% all show nearly the same mean inelastic strain, those at the higher strain amplitude are higher the lower is the Si content from the initial cycle on. The mean inelastic strain is lower for the reference alloy than for any of the Al-Si-Mg alloys at both strain amplitudes.

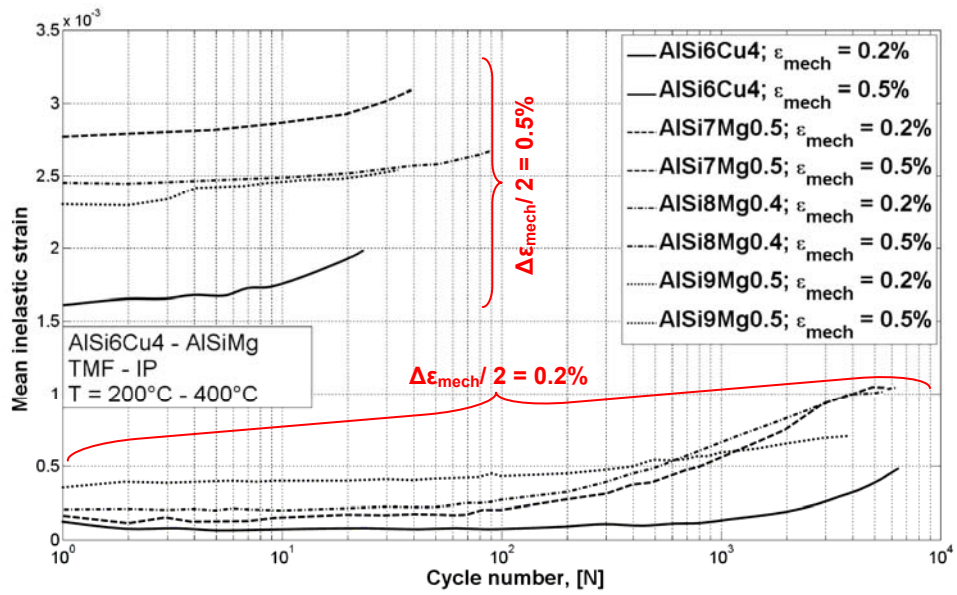


Figure 5.52: Mean inelastic strain for AlSi6Cu4 and Al-Si-Mg alloys under IP-TMF loading.

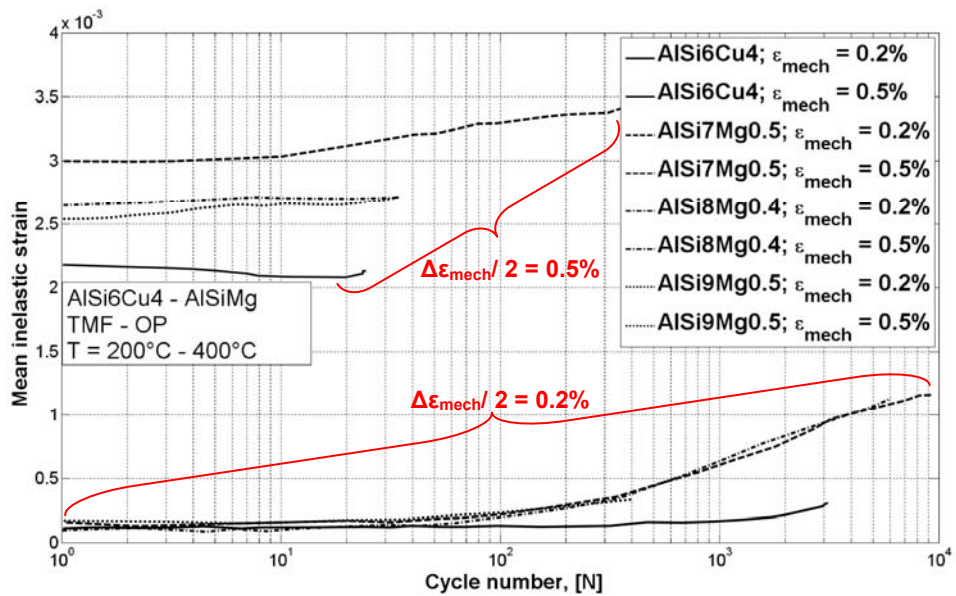
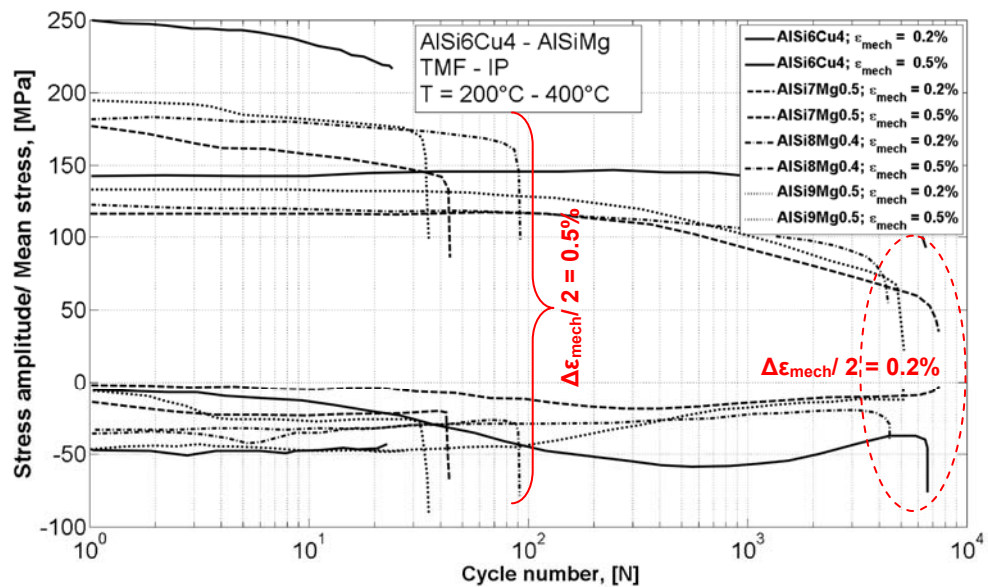


Figure 5.53: Mean inelastic strain for AlSi6Cu4 and Al-Si-Mg alloys under OP-TMF loading.

Generally, the stresses at maximum and minimum temperature decrease with decreasing Si content for the Al-Si-Mg alloys. As can be seen in Figure 5.54, the stress amplitudes under IP-TMF loading for AlSi6Cu4 are much higher than those for Al-Si-Mg alloys. Exceptionally, AlSi6Cu4 shows slight hardening for the lower strain amplitude during the first 400 cycles, followed by softening. For all the Al-Si-Mg alloys, softening has taken place after around one seventh of the lifetime and no hardening effects can be detected, softening starting from  $N=1$  on for the higher strain amplitude. Again exceptionally, the mean stress of AlSi6Cu4 for a strain amplitude of 0.2% does not drift in the compression direction in contrast to the behaviour at high strain amplitude. The mean stresses for all of the Al-Si-Mg tests almost converge after 300 cycles.



**Figure 5.54:** Stress amplitudes and mean stresses for AlSi6Cu4 and Al-Si-Mg alloys under IP-TMF loading.

Figure 5.55 shows the stress amplitude and mean stress development for OP-TMF loading. The AlSi9Mg0.5 shows linear softening accompanied by a gradual drift towards tensile mean stresses over about 50% of the lifetime followed by a rapid drop. In contrast, the AlSi7Mg0.5 and AlSi8Mg0.4 exhibit three phases of softening.



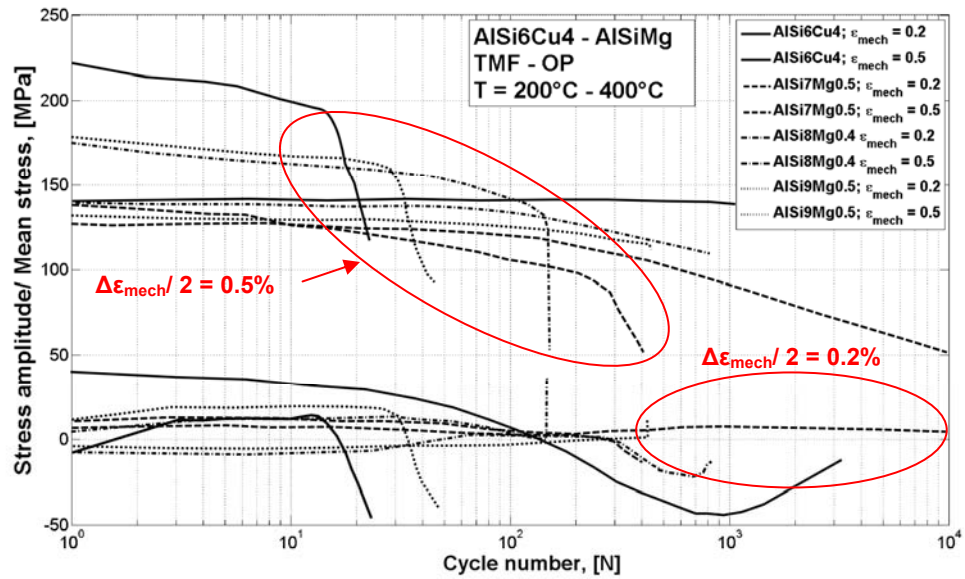


**Figure 5.55:** Stress amplitudes and mean stresses for AlSi6Cu4 and Al-Si-Mg alloys under OP-TMF loading.

In summary, at high strain amplitudes, above a threshold of 0.5%, relaxation effects can be seen for all alloys under the higher temperature. These relaxation effects are caused by a decrease of the material's resistance to plastic deformation at higher temperature and increasing rates of recovery processes.

### 5.9.2 Lifetime behaviour

Figures 5.56 and 5.57 show mechanical strain amplitude vs. lifetimes for IP and OP loading, respectively. For IP loading, AlSi6Cu4 exhibits shorter lifetimes than any of the Al-Si-Mg alloys at high strain amplitudes, but longer than any at low strain amplitudes, although it should be noted that the crossing of other lifetime curves is a consequence of extrapolating the regression curve. For the Al-Si-Mg alloys, the lifetimes tend to converge at low strain amplitudes, whereas, at high strain amplitudes, the lifetimes decrease with increasing silicon content. For OP-TMF loading, the shortest lifetimes were exhibited by AlSi9Mg0.5 for and the longest by AlSi7Mg0.5 at both low and high strain amplitudes.

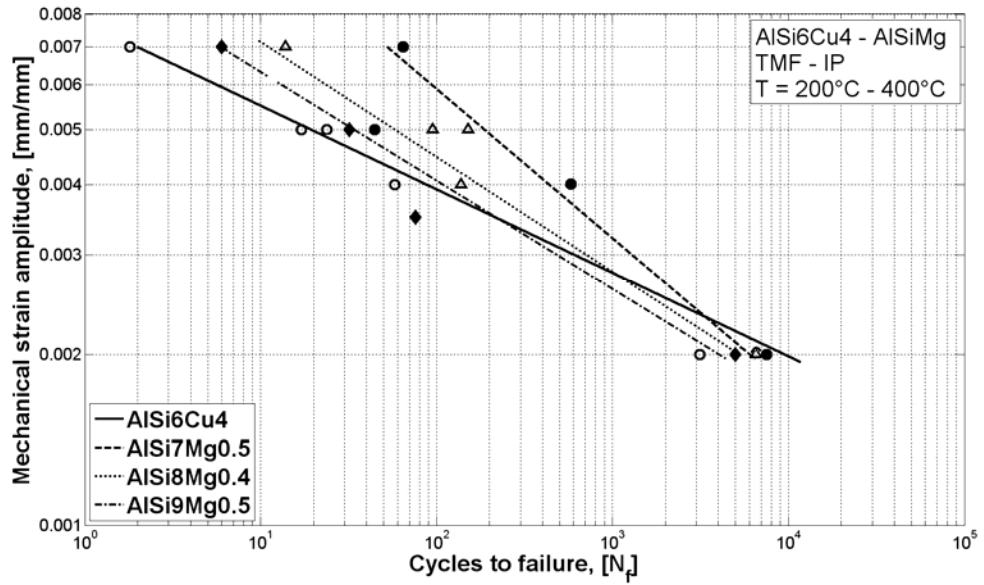


**Figure 5.56:** Mechanical strain amplitude vs.  $N_f$  for AlSi6Cu4 and Al-Si-Mg alloys under IP-TMF loading.

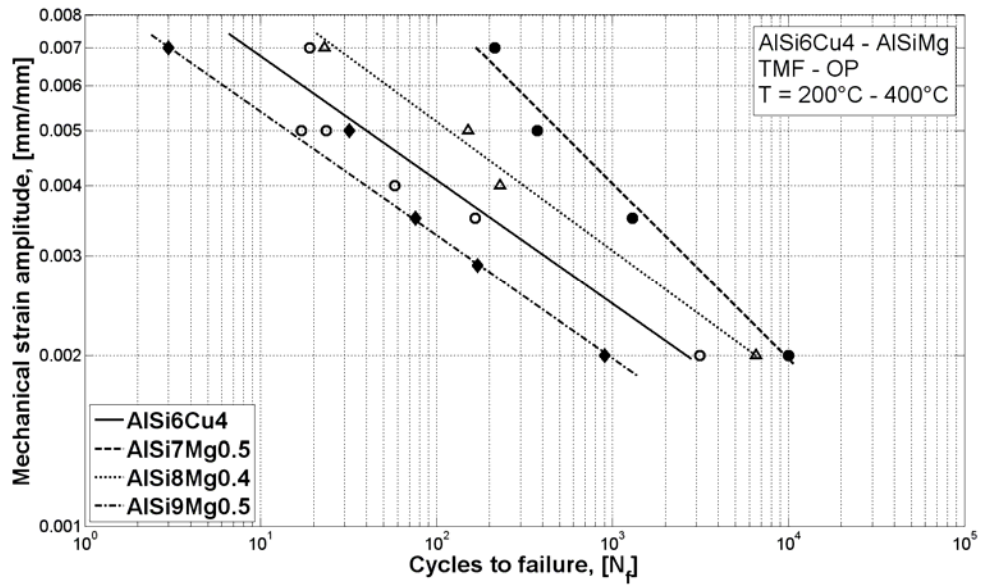


**Figure 5.57:** Mechanical strain amplitude vs.  $N_f$  for AlSi6Cu4 and Al-Si-Mg alloys under OP-TMF loading.



### ***5.9.3 Microstructural observations; comparison with reference alloy***

The porosity content in all samples was below 0.8%, separated into shrinkage and gas pores. Micro CT measurements and 2D analysis using SEM and OM suggested a mean pore diameter less than 11  $\mu\text{m}$ . Pores are one of the main initiators of cracks and damage during TMF, but initiation was only detected for shrinkage pores. Gas pores are generally of globular form giving rise to lower notch stresses than shrinkage pores.

Figure 5.58 shows how the mean hardness decreases during the lifetime for the different alloys, starting from a value determined by the T6 heat treatments. The gradients of the lines for AlSi7Mg0.5 and AlSi8Mg0.4 are nearly the same, as are those for AlSi6Cu4 and AlSi9Mg0.5, but lower. This means, for example, that, although AlSi8Mg0.4 and AlSi9Mg0.5 start with almost the same hardness, AlSi8Mg0.4 shows a much lower hardness by the end of its fatigue life.

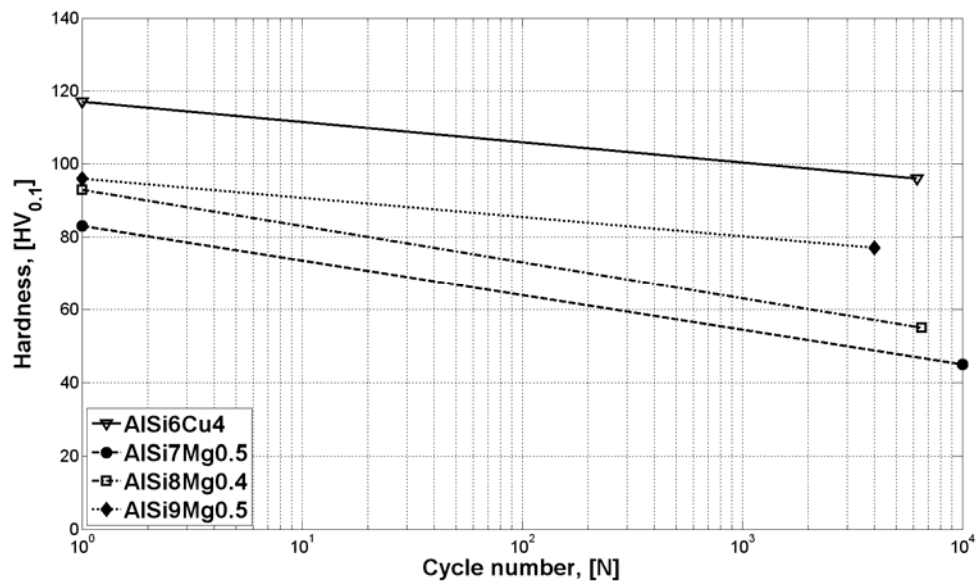
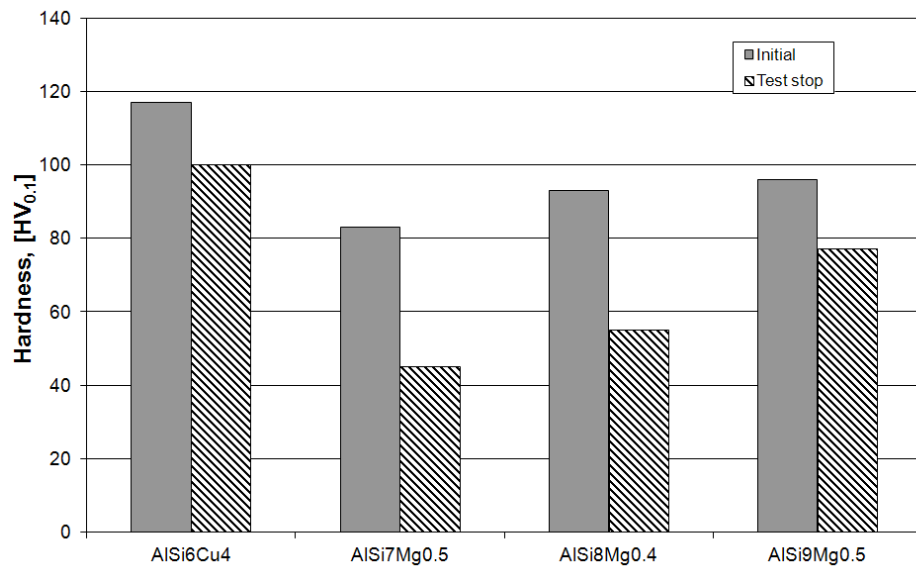


**Figure 5.58:** Hardness decrease of AlSi6Cu4 and Al-Si-Mg alloys under TMF loading at a strain amplitude of 0.2% during the lifetime.

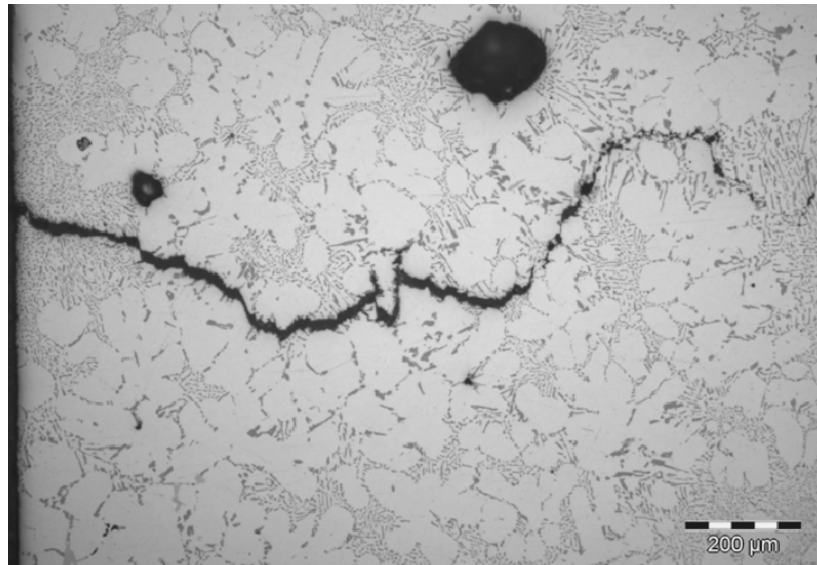
During the tests, a slight increase of Si particle size was detected and this was more pronounced the higher the Si content is. The form of the Si particles in AlSi7Mg0.5 and AlSi8Mg0.4 was nearly globular whereas, in AlSi9Mg0.5, a more plate-like form with aspect ratio of about 2:1 was observed, leading to higher notch stresses. Furthermore, these Si particles were observed to reorient during the IP and OP-TMF tests. Simultaneously, a decrease of Mg<sub>2</sub>Si size was noted, more evident with increasing Si

content. Coarsening of the  $\beta$ - phase and  $\pi$ -phase were also seen after both IP and OP-TMF loading.

For all the Al-Si-Mg alloys, an increase in microporosity was detected under IP-TMF loading, attributable to creep effects, given that they observed to be oriented along the loading direction. No such micropores were detected under OP-TMF loading. Creep pores grew by up to 42% for AlSi7Mg0.5, 24% for AlSi8Mg0.4 and 11% for AlSi9Mg0.5. TMF specimens tested with the highest strain amplitudes showed the highest content of creep pores.

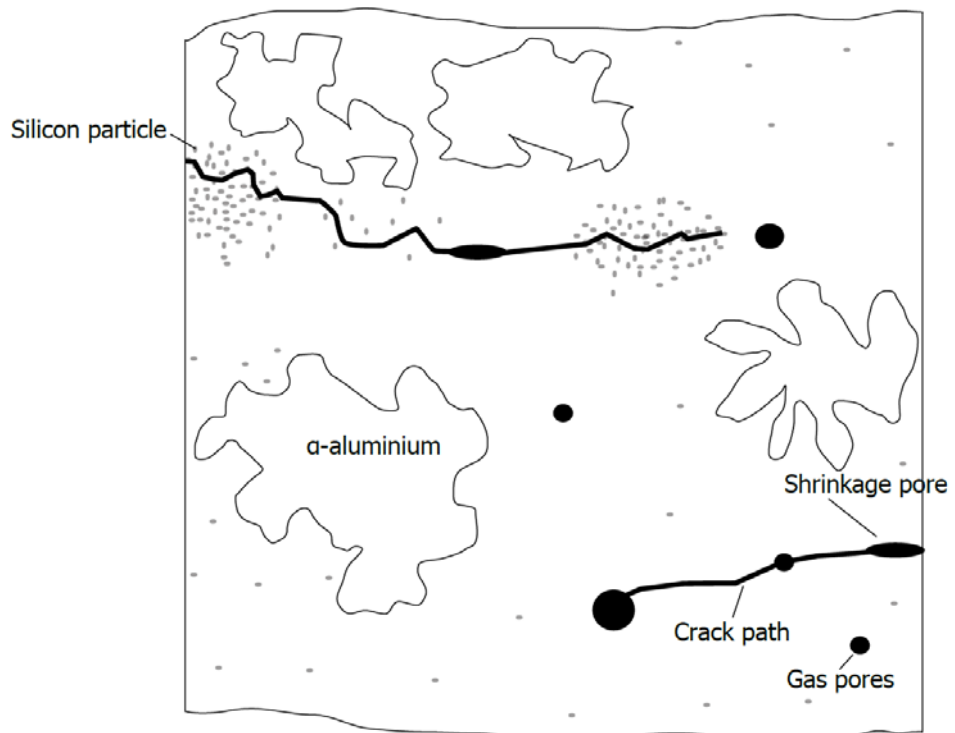
With increasing Si content and low strain amplitudes cracks showing the characteristics of stage I, could be observed in the material near to the surface. Crack initiation and propagation appeared sometimes to be influenced by phases containing iron. For high strain amplitudes, nearly brittle fractures were observed around the periphery of the fracture surfaces, which is similar to the reference alloy. In AlSi8Mg0.4, voids appeared to be responsible for the stress reduction, with pores being found near to the surface. Transdendritic crack propagation was found in AlSi9Mg0.5, where a higher content of microcracks was detected inside the gage length.

Apart from the strain amplitude, which simultaneously affects the strain rate and recovery processes, alloying elements have a direct influence on decohesion behaviour. In this context, the amount of decohesion increases with increasing Si content, an assertion that was verified by FEM analysis, which revealed higher stresses associated with the higher stiffness of Si in comparison with the  $\alpha$ -matrix. Local concentration of Si content leads to higher stresses and hence damage, and the amount of clustering of eutectic Si particles was observed to increase with increasing Si content. The enhanced stresses can lead to crack initiation near to the surface in these clustering zones, where cracking is caused by a differential thermal expansion between Si crystals and the Al matrix (Figure 5.59).



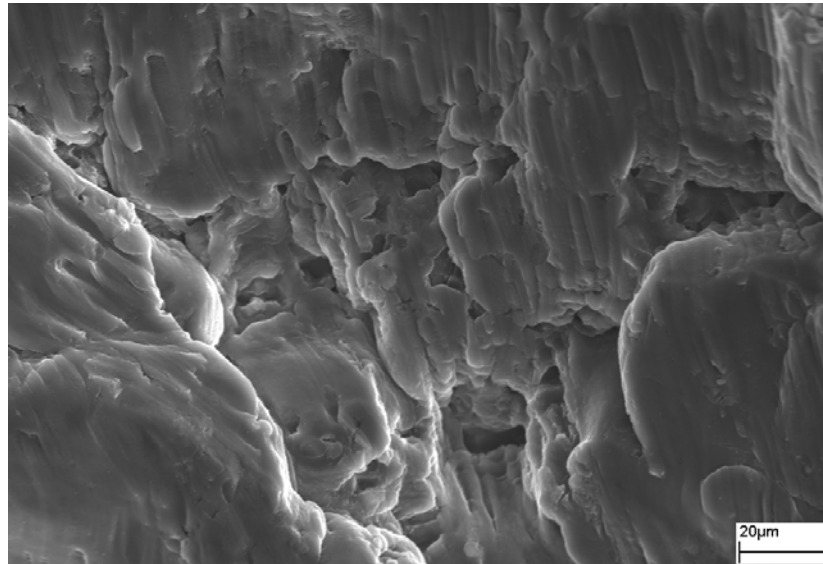
**Figure 5.59:** Crack initiation at Si cluster in AlSi9Mg0.5 under OP-TMF loading and a strain amplitude of 0.5%.

Figure 5.60 provides a schematic overview of the two different crack initiators in Al-Si-Mg alloys.



**Figure 5.60:** Schematic overview of crack initiation and propagation in Al-Si-Mg alloys.

For specimens tested under low strain amplitudes, another crack initiator was observed. In this, an oxide layer forms on the crack paths and continual tension-compression loading leads to spalling of the oxide layer which then acts as a further crack initiator (Figure 5.61).



**Figure 5.61:** Oxide layer on the crack path of AlSi7Mg0.5 under IP-TMF loading and a strain amplitude of 0.2%.

## **CHAPTER 6 - DISCUSSION**

This chapter discusses the significance of the results presented in Chapter 5 in terms of design and materials section for advanced automotive engine applications. The discussion is organised along the broad areas of investigation indicated by the summary of experiments (Section 4.12). First the findings of the auxiliary tests will be discussed, starting with the temper tests followed by the CERT and creep tests to give an overall assessment of the effects of thermal exposure on the phase distributions, grain size and dendrite arm spacing, and mechanical properties, as well as the other mechanical processes which may be going on along with the fatigue. Next, the isothermal LCF tests are discussed along with the TMF tests on the reference alloy to elucidate the effects of thermal cycling and alloy pre-treatment. Next, the TMF tests on the reference alloy and the AlSi9Cu3, both in the T6 conditions are compared to assess the effect of dendrite arm spacing. The main series of tests, TMF of all alloys, are next discussed to highlight the selection criteria for the engine application. At all of these stages, comparison will be made with the works of others to highlight new findings and/ or conflicting findings. Finally, the data from the reference alloy are used in a damage simulation model in order to compare the predictions using the new data with current design procedures.

### **6.1 TEMPER TESTS**

The long-time exposure tests were carried out to separate the relative influences of long time isothermal exposure and of cyclic loading under temperature. Others, e.g. Henne [143], have carried out temper tests at different temperatures and have used the same hardness simulation formula as used in this thesis, but his purpose was to demonstrate the validity of the formula and not, as it is the purpose of this work, to use the time and temperature during the tests to correlate with the hardness indicated by temper tests conducted at threshold minimum and maximum temperature. In the current work, the validity could be confirmed for the long-time exposure tests as well.

The changes in hardness (Table 6.1) resulting from long-time exposure at 200°C and 400°C following T6 and T7 heat treatment of the AlSi7Mg0.3(Cu) and AlSi6Cu4 alloys are qualitatively as might be expected from age-hardened alloys which overage and loss strength with with long term exposure for temperatures above the ageing temperature.

**Table 6.1:** Summary of hardness changes in temper tests.

Alloy	Treatment before	Hardness [84]		
		As treated	100hr at 200°C	100hr at 400°C
AlSi6Cu4	T6	117	80	60
AlSi6Cu4	T7	97	75	60
AlSi7Mg0.3(Cu)	T6	137	85	55
AlSi7Mg0.3(Cu)	T7	117	-	-

The T6 treatments will have been developed to allow optimum precipitation hardening, so that any exposure at or above the initial ageing temperature can be expected to result in overageing. The T7 treatments are usually designed to allow for a certain amount of overageing and are often specified for higher temperature applications [144, 156]. Thus, both alloys might be expected to suffer a loss in hardness after exposure at 200°C, although, for the T7 treatment the decrease of hardness during the long time exposure is not as severe as the T6. Both alloys in both conditions can be expected to overage to saturation after the 400°C exposure.

The difference between the hardness values of the AlSi7Mg0.3(Cu) temper test specimens in the T6 condition (137HV<sub>0.1</sub>) and the starting hardness of T6 TMF specimens (119HV<sub>0.1</sub>) can be explained by the test procedure. The TMF specimens were tested after a break of eight days taking into consideration typical times between heat treatment, manufacturing and assembly in the automotive industry.

Compared with the loss of coherency of the age-hardening precipitates, the effects of increasing grain size and coarsening of the non-ageing precipitates on alloy strength are minimal. Nevertheless, the grains continue to coarsen with time and temperature and, particularly for the specimens tested at less than 400°C, a blurring of grains oriented in the same direction could be observed. Figure 6.1 shows the grain size versus time at temperatures of 200°C and 400°C for the temper tests and the isothermal LCF tests. For fatigue tests at 400°C, the rate of increase in grain size is essentially the same as for the temper tests, indicating that mechanical effects are outweighed by thermal ones. However, at 200°C, a different behaviour can be observed. Here, an interaction between recrystallisation and strain hardening seems to have taken place, similar to the dynamic recrystallisation that occurs in hot forming operations, where the increase of dislocation density nucleates new grains more rapidly than in a normal recovery-recrystallisation process, leading to less rapid increase in grain size.

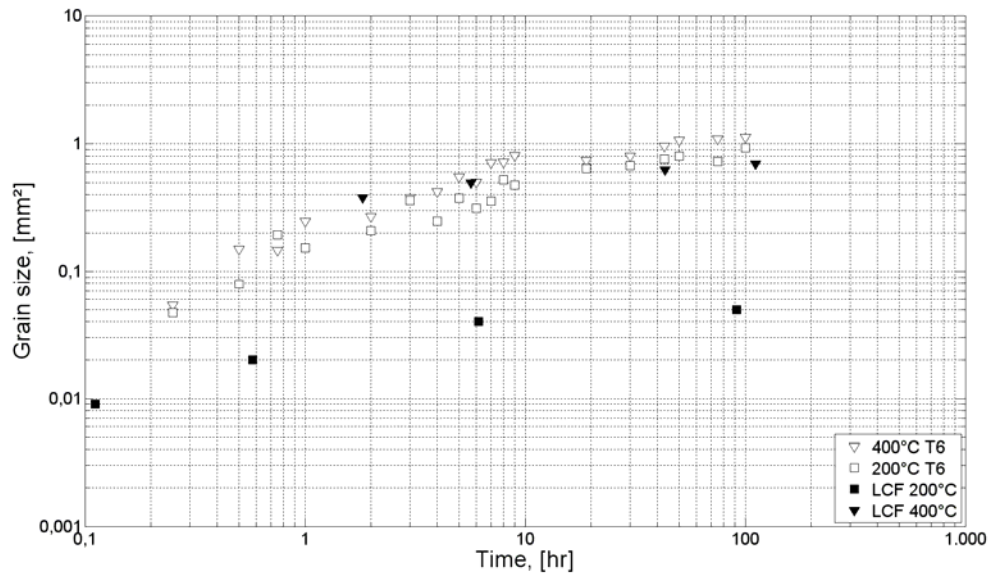


**Figure 6.1:** Comparison of grain size vs. time of LCF and temper tests for AlSi6Cu4.

The increase in the sizes of the various intermetallic phases can be explained by the Ostwald ripening effect, which occurs above  $0.4T_M$ , whereby larger particles grow at the expense of smaller particles dissolving to maintain the same volume fraction of precipitates (which is determined by the chemical composition of the alloy). The growth rate depends on the diffusion rates of the constituents of the precipitate (which are each functions of the temperature), although, for example, Lifshitz *et al.* [275] have described this behaviour with a simplified formula:

$$d_T^3 - d_{T0}^3 = k \cdot t \quad (16)$$

Figure 6.2 shows the hardness data before and after the TMF and LCF tests, as well as the data from the temper tests. For clarity, only test data of fatigue specimens which fall in the range of hardness simulation are plotted here, so higher hardness values and longer lifetimes have been omitted. Also shown in Figure 6.2 is the calculated hardness-time profile for 200°C and 400°C using the Boussac-Calais model [161] (Chapter 3.4, formula 14) with constants  $A=3.2056$ ,  $B=1.3801$ ,  $C=28.8023$  for 200°C and  $A=18.0358$ ,  $B=2.5$ ,  $C=105.897$  for 400°C.



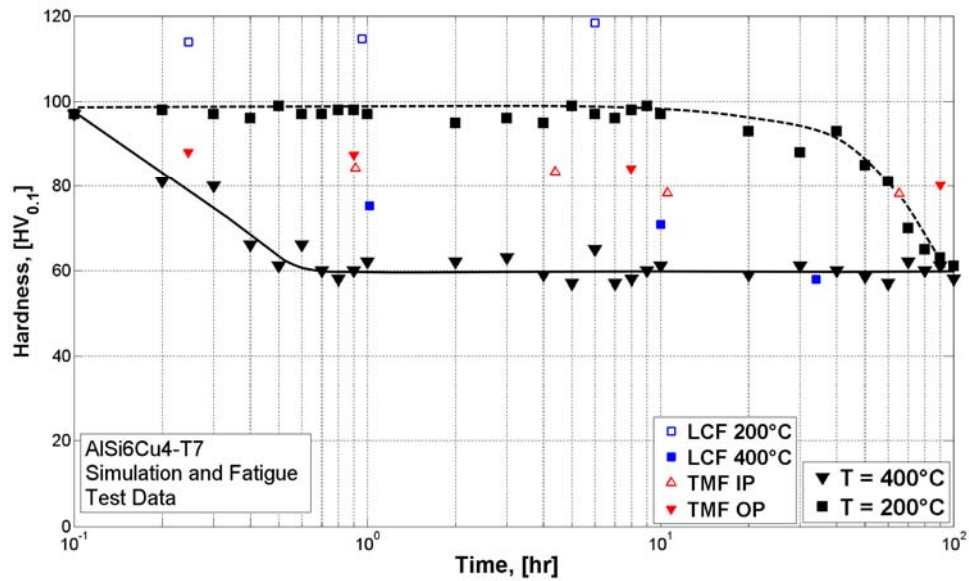


**Figure 6.2:** Comparison of hardness data resulting from simulation, LCF and TMF tests on AlSi6Cu.

As can be seen, the simulation fits the temper tests very well indeed. For the (isothermal) LCF tests at 400°C, the initial rapid softening is delayed considerably, whereas for those at 200°C the material hardens slightly. For both the IP and OP TMF tests, where the average temperature is 300°C the hardness profile sits between the two temper tests with little distinction between the IP and OP.

## 6.2 CERT

Taking into account the inhomogeneous temperature distribution during the TMF tests, itself based on the temperature gradient inside cylinder heads, the CER tests were conducted at a strain rate of  $3 \times 10^{-4} \text{s}^{-1}$ . A number of different test procedures have been reported in the literature making it difficult to compare the results on the basis of the initial microstructure. For example, Henne [143] used a strain rate of  $1.8 \times 10^{-4} \text{s}^{-1}$  and a soaking time of 60s, Flaig [46] used a strain rate of  $5 \times 10^{-2} \text{s}^{-1}$  and a soaking time of 25min and Rincón *et al.* [177] used a soaking time of 10min and a strain rate of  $10^{-4} \text{s}^{-1}$ . At the most extreme, Eady and Smith [276] used a soaking time of 30min, in which case the effect of this heat treatment on the microstructure cannot be neglected, as seen in the temper tests. In comparing any elongation-based measurements (including work-hardening rate) with the literature, it needs to be considered that the attachment and cooling methods used for the extensometers can have significant influence on the

measured values, especially during prolonged high temperature exposure. For example, Riedler [50] estimated the influence of gauge length of extensometers, and found a decrease in ultimate strain and proportional elongation when increasing the gauge length. Furthermore, the position of the specimen in the casting from which it is cut is also important. Whilst single cast specimens using a permanent mould usually display a homogeneous SDAS within the gauge length, specimens extracted from cylinder heads show a more inhomogeneous distribution caused by the different cooling rates in the complex geometry, for example around cooling channels [32].

Table 6.2 summarises the CERT results as 0.2% proof stress (PS) at 200°C and 400°C, and the work hardening (WH) rate, estimated as the average ascending slope of the stress-strain curve starting at 0.2% PS. As can be seen in Figure 6.3, the gradient quickly becomes constant and, after the UTS becomes negative, due to plastic instability.

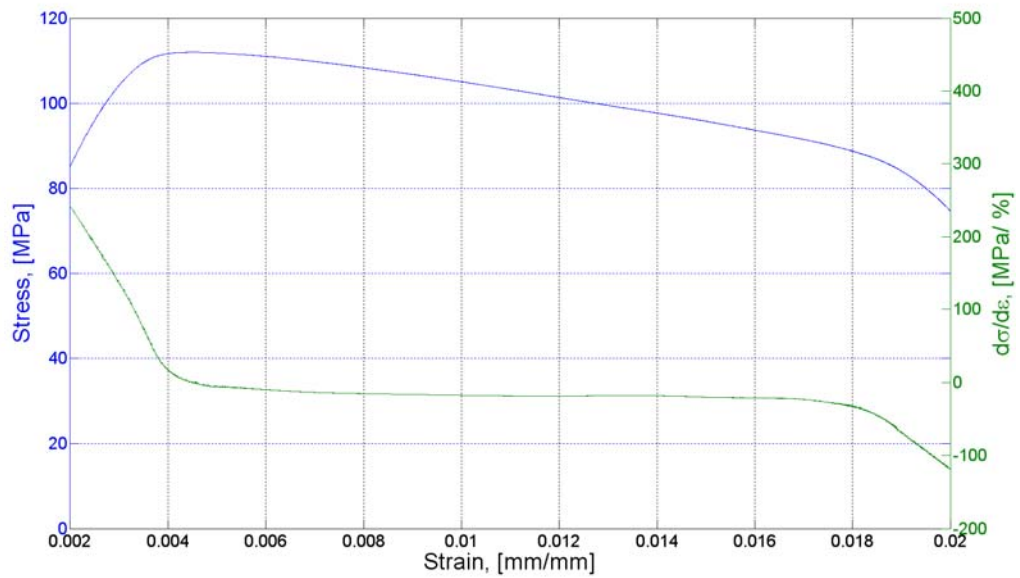


**Figure 6.3:** Schematic relation between stress vs. strain and  $d\sigma/d\varepsilon$  vs. strain for a specimen.

**Table 6.2:** Comparison of test temperature, proof stress and work hardening rates of the different alloys.

Alloy/treatment	0.2% PS at 200°C, [MPa]	0.2% PS at 400°C, [MPa]	WH rate at 200°C, [MPa/%]	WH rate at 400°C, [MPa/%]
AlSi6Cu4-T6	173	114	53	7.5
AlSi6Cu4-T7	138	106	52	7.2
AlSi6Cu4-T6-HIP	195	125	56.3	7.9
AlSi9Cu3-T6	-	105	-	36
AlSi7Mg0.5-T6	-	106	-	7.9
AlSi8Mg0.4-T6	-	83	-	3.3
AlSi9Mg0.5-T6	-	77	-	2.1

The CERTs give further information on the loss of mechanical properties with time, differing from the tempering tests in that the specimens are strained during exposure at a rate approximately the same as in the TMF tests. The increase of elongation with increasing test temperature and the significant drop in strength is caused by increasing overageing, which reduces the effectiveness of the precipitates as obstacles to dislocations, as well as the increased thermal activation of dislocations, given that temperature and stress put the tests in the regime of dislocation creep (Figure 3.6). The

ageing temperature of T6 specimens before the CERT was between 155°C and 170°C so that to the overageing effect might be expected to occur more quickly and to a greater final extent when testing at 400°C which is clearly seen in the CERTs for AlSi6Cu4 alloy.

AlSi6Cu4-T6 specimens which had been subjected to a HIP procedure showed a higher work hardening rate both at 200°C and 400°C and also a higher yield strength, as well as a slightly higher ductility. The increase of strength with the HIP process can be attributed to the reduction of porosity and healed voids, which can be seen in Figure 6.4. Nevertheless, over the range of interest in this study, time and temperature dependent effects such as overageing and creep have a much greater effect on monotonic properties at high temperatures than do porosity or voids. This can be seen, for example, in the strength which decreases by about 50% when the temperature increases, whereas it only increases by 10-15% when applying a HIP pre-treatment. Furthermore, a slight coarsening might be expected during the HIP due to the high processing temperature of about ~500°C. The influence of exposure temperature was also observed by Ostermeier *et al.* [277], who examined the influence of a HIP procedure after a T6 heat treatment. They found a decrease in room temperature yield strength and tensile strength, coupled with an increase in the ultimate strain, which they attributed to the exposure during hipping to temperatures of 480°C to 510°C. The observed increase in ultimate strain with increasing test temperature for all alloys is mentioned by a number of other authors [46, 143].

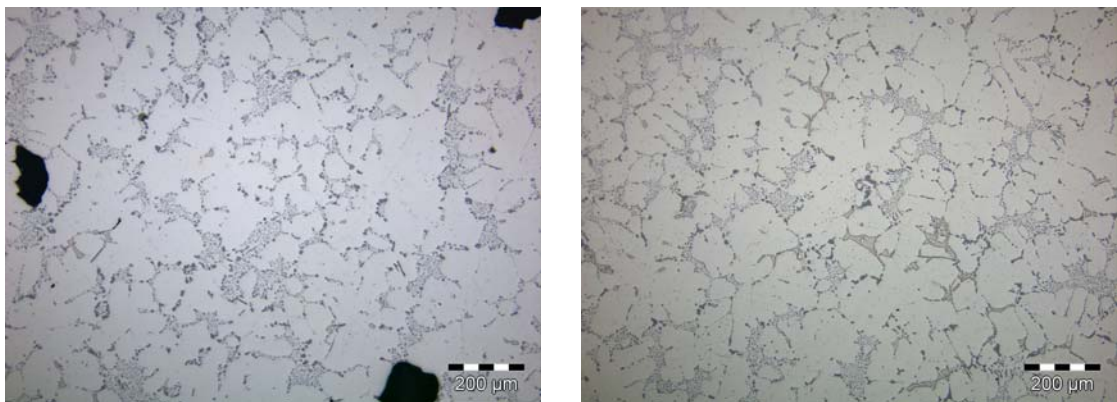


**Figure 6.4:** Micrographs showing AlSi6Cu4 T6 in the non-HIPped (left) and the HIPped (right) conditions.

The AlSi6Cu4-T7 specimen showed a slightly lower work hardening rate, associated with a reduction of the ratio of UTS to yield strength, and the overaged condition of the specimen before testing leads to lower values of 0.2% PS and UTS. Other authors have made similar observations, such as Rincon *et al.* [177] who used a strain rate of  $10^{-4} \text{ s}^{-1}$ , and obtained values for an A319 alloy 50MPa lower for UTS and  $\sigma_y$  for the T7 heat treated condition over the T6.

The CERT curves and microstructural observations for the 200°C specimens indicate a significant influence of the brittle fracture of Si particles. In contrast, fracture behaviour is ductile at 400°C, due to the thermally activated processes which lead to relaxation of stresses at the brittle particle/ matrix interfaces and, ultimately, dimples and a higher ultimate strain. The increase in ductility is reflected in a dramatic decrease in the work hardening rate from around 50MPa/% to around 7MPa/%. For all the AlSi6Cu4 variants; T6, T7 and T6 HIP, tested at 400°C, the behaviour is almost perfectly plastic, characterised by a reduction in the work hardening rate of about 85%. According to other authors [81, 88, 278-282], higher values of work hardening rate can be obtained using a shorter soaking time, a higher strain rate, a lower SDAS and/ or a different casting procedure.

Comparing the AlSi9Cu3-T6 alloy with AlSi6Cu4-T6 (and also with the other alloys) at 400°C, the most striking effect is the massive enhancement in the work hardening rate. This increase is almost certainly associated with dislocation interaction with the finer microstructure. The SDAS in AlSi9Cu3 is about one third of the value of AlSi6Cu4 although it needs to be noted that the Si content and the other alloying elements will have an effect as well. Including the work hardening rate and PS for AlSi9Mg0.5 in the comparison helps to highlight the effect of SDAS on the work hardening rate.

For the Al-Si-Mg alloys, an increase of PS and work hardening rate with decreasing Si content can be observed when testing at 400°C. This is the opposite to what might be expected at room temperature and is likely to be associated with the enhanced notch stresses between matrix and the acicular particles (Table 5.1) with increasing Si, promoting plastic flow in the matrix.

### 6.3 CREEP TESTS

The main results of the creep tests on AlSi6Cu4 in the T6 condition are summarised in Table 6.3. The creep parameter  $A$  has been obtained from the steady-state (minimum) creep rate and the loading ratio  $\left(\frac{\sigma}{\sigma_y}\right)$  from:

$$\dot{\varepsilon}_{st} = A \cdot \left(\frac{\sigma}{\sigma_y}\right)^n \quad (17)$$

where the temperature-independent exponent  $n=2.5$  is an average value from Stoeckl *et al.* [283] determined for test temperatures of 250°C, 300°C and 350°C on the same alloy. The values obtained for the pre-exponential term vary a little according to stress (which they should not do), but the principal difference is related to temperature.

**Table 6.3:** Summary of creep test data.

Temperature, [°C]	Loading ratio, [ $\sigma/\sigma_y$ ]	Pre-exponential term, $A$ , [ $s^{-1}$ ]	Time for steady state creep, [s]	Rupture time, [s]	Strain at rupture, [%]
200	0.95	15.8	622	36458	0.2
	1.0	21.0	72	1422	0.21
	1.05	27.5	< 1	71	0.28
	1.05	27.5	< 1	44	0.34
	1.17	49.8	< 1	38	0.35
400	0.25	$2.9 \times 10^{-3}$	111	-	stopped at 20%
	0.35	$1.9 \times 10^{-2}$	< 1	-	stopped at 20%
	0.4	$3.9 \times 10^{-2}$	< 1	-	stopped at 20%

Primary creep is not discernible in Figure 5.7 or 5.8 at either temperature probably because both test temperatures (200°C and 400°C) are quite high. A decrease in the time for steady state creep can be observed with increasing the load ratio at both temperatures. Figures 6.5 and 6.6 show the first derivatives (strain rate) of the data behind Figures 5.7 and 5.8, both plotted against strain rather than time. The erratic behaviour during the initial stage is due to transients in the test equipment and does not reflect the creep behaviour of the specimen. The high stress ratios used in the 200°C testing put them in the category of “impact” or “high velocity” creep in which no

recovery or diffusion effects are expected. The hardening is therefore expected to be generated by dislocation formation, cutting and pile-up, leading to the observed rapid drop in the strain rate of more than an order of magnitude in one second.

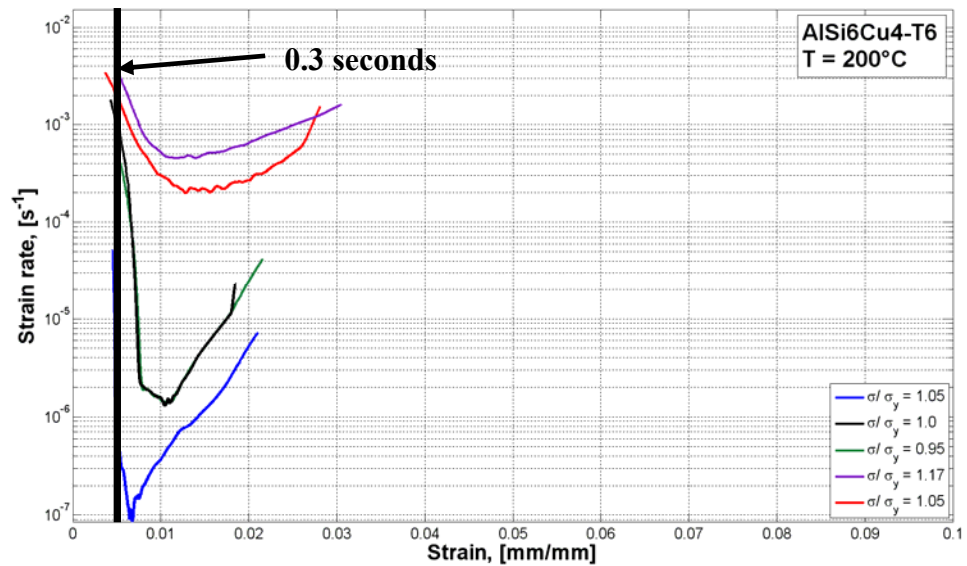


Figure 6.5: Creep curve of AlSi6Cu4-T6 at 200°C with different stress ratios.

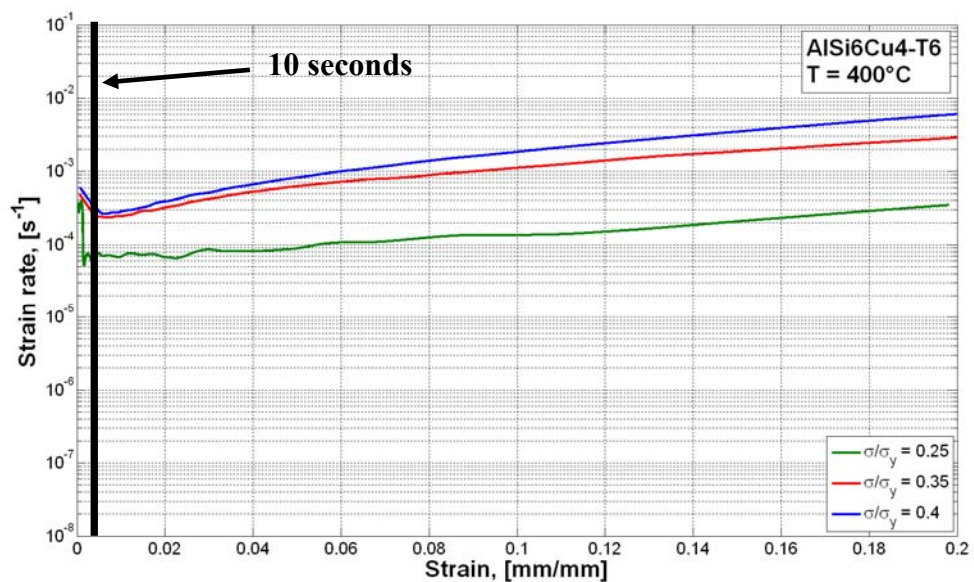


Figure 6.6: Creep curve of AlSi6Cu4-T6 at 400°C with different stress ratios.

As indicated in the tempering tests, overaging at 400°C in the AlSi6Cu4 alloy continues over a period of about 1000s and is still going on after  $3.6 \times 10^5$ s at 200°C. This means that microstructural changes are going on throughout the steady-state creep

in all of the measurements, so that the observed creep rate is a combination of the rates of creep processes and of microstructural change.

As expected, creep rupture times decrease with increasing temperature at a given stress. The general increase in strain to rupture at 400°C is caused by their higher degree of overageing at a given time, which leads to an increase in ductility as well. The increased strain to rupture as stress is reduced for a given temperature can similarly be ascribed to this effect. At 400°C, as well as overageing, there is significant grain coarsening and coarsening of larger second phase particles. This coarsening, especially of the  $\beta$ -phase, has a deleterious effect on creep life because these particles act as stress raisers and cracks initiate more easily in larger  $\beta$ -phase particles.

Besides the work of Stoeckl *et al.* [283], Dehler *et al.* [179] also carried out a creep study, working on the same alloy specification, although over the temperature range between 149°C and 299°C. At 272°C, they found the creep rate to increase with strain in roughly the same way as in the current work at 400°C, except at the higher loads where they observed a similar rapid initial drop, similar to the current work at 200°C. They also found the rupture time to decrease substantially with increasing load, again in accord with the current work at 200°C.

However, the observed minimum creep rates in this work lay between 0.3% and 1.5% strain (Figure 6.5 and 6.6), in contrast to Dehler *et al.* [179] who found minimum creep rates between 0.1% and 0.3% strain and also lower Norton exponents. As well as the generally lower temperature range, Dehler *et al.* used an alloy with slightly different composition (lower Si, lower Cu, lower Mg, higher Fe, higher Mn, higher Zn, higher Cr), a different temper condition (T64 with a higher ageing temperature), a different test configuration through a three zone furnace (which produces a different temperature profile and hence a different integral strain distribution) and a holding time of 1hr before starting the test. This longer holding time, in particular, has a large effect on the microstructure and hence the creep parameters such as the Norton exponent and minimum creep rate, as observed in the temper tests, where holding at 400°C led to a very rapid drop in hardness. Furthermore, it seems that the creep tests conducted by Dehler *et al.* [179] were not recorded with an extensometer and may be based on displacement of the crosshead. Finally, the tests on aluminium alloys in [283] have



shown that minimum creep rates measured in compression tests are generally lower than those measured in tension.

#### 6.4 ISOTHERMAL LOW CYCLE FATIGUE TESTS

The hardening behaviour seen in samples of the reference alloy tested at 200°C is probably caused by the build-up of interactions between dislocations and coherent precipitates. High strain amplitudes lead to a movement of dislocations which pile up in front of small precipitates and at grain and phase boundaries, making subsequent dislocation movement more difficult and increasing dislocation density.

A similar behaviour to the CERTs, where a reduction by half of the values of UTS and  $\sigma_y$  was observed when increasing the LCF test temperature from 200°C to 400°C. In the 400°C tests, which were conducted well above the ageing temperature, precipitates were subjected to Ostwald ripening and the consequent increase in particle size and inter-particle distance, resulting in reduced dislocation-particle interaction and hence softening. For example, when starting from the same strain amplitude, an increase of temperature from 200 to 400°C leads to an increase in inelastic strains of around 0.12%. At the higher temperature, thermal activation allows dislocations to circumvent precipitates by processes such as climbing and also enhances dislocation rearrangement and dislocation annihilation, all of which would further contribute to softening even if there was no overageing.

At each temperature, the cyclic stress response curves (as illustrated, for example, by the change in maximum stress over the fatigue life, Figure 5.11) exhibit two stages. At 200°C, there is cyclic hardening, followed by a rapid drop in stress at the end of life, most likely due to macroscopic crack growth. At 400°C, there is progressive softening, followed by a steeper drop during the last 20 to 50 cycles, again likely caused by macroscopic crack growth. When expressed in terms of mechanical strain amplitude *vs.* cycles to failure (Figure 5.14), it can be seen that overageing and creep considerably improve fatigue life at 400°C. However, in applications where fatigue is driven by temperature gradients in a single material, this merely means that the hotter parts will fail later than the colder ones.

A number of other workers, e.g. Minichmayr [14], working with AlCuBiPb alloys, and Bose-Filho *et al.* [226], working with an AlSi7Mg alloy have reported contrasting behaviour where a decrease of fatigue life is observed when increasing temperature. This effect can be attributed to the condition of the microstructure when starting the test series. If the hardening phases in these alloys were not aged to the peak value of hardness and, if the transition from partially coherent to incoherent particles was not complete early in the test, the benefit of grain growth and coarsening including a higher ductility, a lower grain boundary sliding quotient and a lower enthalpy when increasing the test temperature would not be obtained. Furthermore, not all Al-Si alloys used in automotive applications are given a heat treatment, e.g. AlSi6Cu4, commonly used for cylinder heads and AlSi9Cu3, for cylinder crankcases. Tests on AlSi10Mg by Flaig [46] and A319-T7B by Engler-Pinto *et al.* [284] revealed a small difference in fatigue life when increasing the temperature. Also, the casting conditions can alter such microstructural features as SDAS, size and distribution of any oxides, and porosity, all of which affect fatigue life. Bose-Filho [226] indicated that the SDAS in the alloys they studied was 20 $\mu$ m, Engler-Pinto [284] determined theirs to be 15-30 $\mu$ m, although Minichmayr [14] did not mention SDAS dimensions at all.

## **6.5 THERMO-MECHANICAL FATIGUE BEHAVIOUR OF ALSI6CU4 REFERENCE ALLOY**

In contrast to the LCF tests, which were conducted under isothermal conditions with a homogeneous temperature in the gauge length, the TMF specimens were tested in a more realistic situation where the temperature was ramped up and down at a fixed rate, and could be either in-phase or out-of-phase with the applied mechanical strain.

As expected, both the mean inelastic strain and stress amplitude increase when increasing strain amplitude (Figure 6.7) for both TMF and LCF on the reference alloy. In the logarithmic plot, the inelastic strain increases in an approximately linear fashion vs. the mechanical strain amplitude but with a considerably steeper slope than does the stress amplitude.

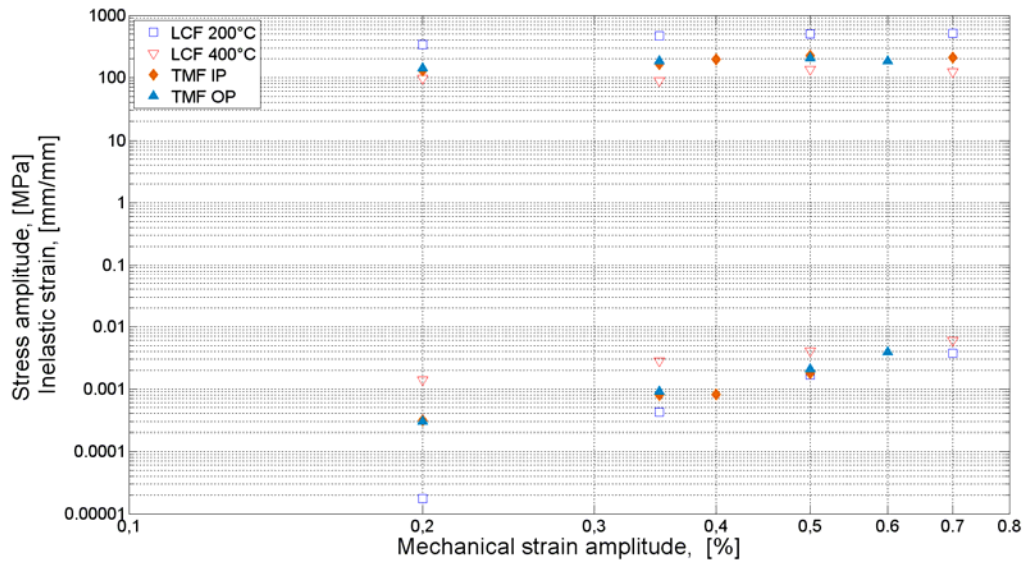


**Figure 6.7:** Stress amplitude and inelastic strain vs. mechanical strain amplitude for AlSi6Cu4-T6 under LCF and TMF conditions.

All of the data points in Figure 6.7 are based on a value of  $N=N_f/2$ , which means that the exposure time also increases with mechanical strain amplitude in the same way as does the fatigue life. It can be seen that, again, both the stress amplitudes and inelastic strains for IP and OP TMF tests lie between the maximum (400°C) and minimum (200°C) temperature values of the LCF tests reflecting what was found in the CERT, suggesting that the same factors affecting creep are also affecting the LCF and TMF performance. The lower inelastic strains in the TMF tests are associated with sharper angles at the reversal points of the hysteresis loops and in their more open form. This is a result of a change of the integral strain distribution from LCF to TMF.

The result of softening and hardening during both types of tests can be seen in Figure 6.8. Here, the stress amplitude at  $N=N_f/2$  is plotted vs. the number of cycles to failure and two distinct regimes can be identified, the first including the IP and OP TMF and the LCF at 400°C the values of specimens tested at 200°C in LCF lying along a different line.

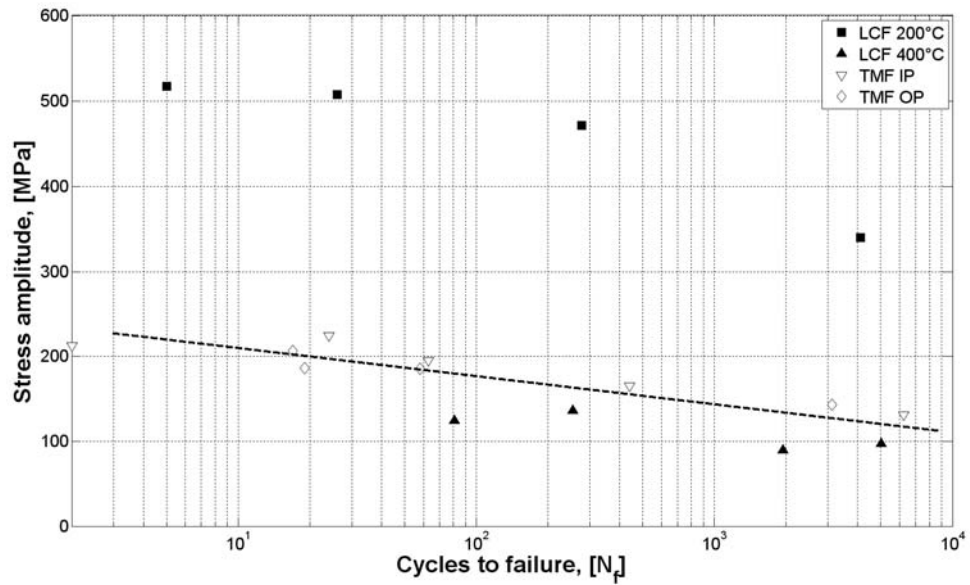


**Figure 6.8:** Comparison of stress amplitude of AlSi6Cu4-T6 under LCF and TMF conditions at  $N=N_f/2$ .

This different behaviour between LCF and TMF must be seen in the context of test procedure. The highest (LCF 200°C) and lowest (LCF 400°C) stress amplitudes are in direct relation to the dislocation behaviour at that test temperature. At 200°C, hardening is a result of dislocation pile-up so that here the lowest inelastic strains develop whereas, at 400°C, overageing effects like grain growth and coarsening lead to softening so that here the lowest stress amplitudes, highest inelastic strains and longest lifetimes can be obtained, Figure 6.9. For both types (IP and OP) of TMF tests, no hardening takes place, presumably because the hardening (at the cooler temperature) and softening (at the higher temperature) are roughly in balance.

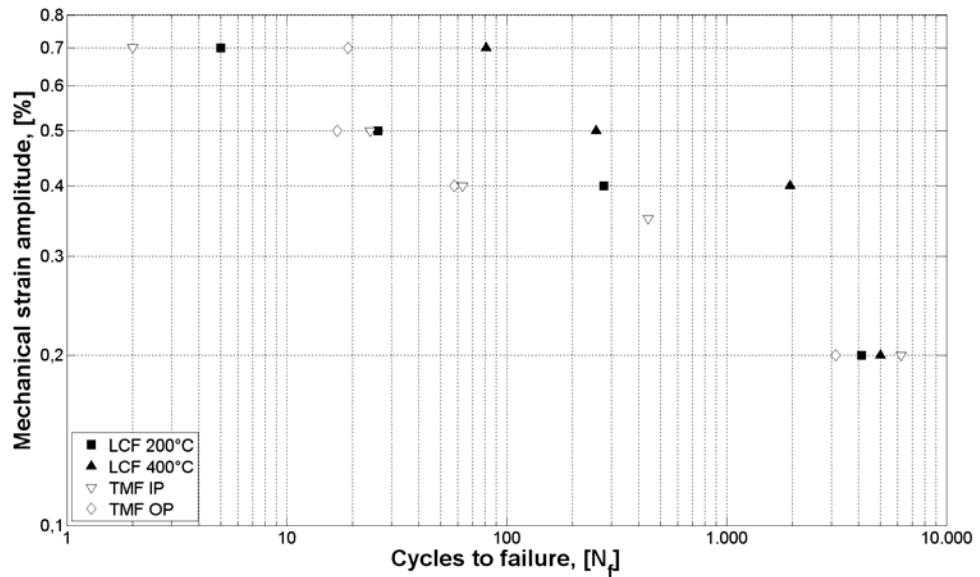


**Figure 6.9:** Mechanical strain amplitude vs.  $N_f$  of AlSi6Cu4-T6 under LCF and TMF test conditions.

The increase in ductility with increasing temperature is also evident in the CER tests. The observed orientation of particles and intermetallic phases in the LCF tests can be attributed to a difference in ductility between the surrounding  $\alpha$ -matrix and secondary phases. The expansion and contraction of the  $\alpha$ -matrix relative to the secondary phases during the tests leads to a radial force acting to change their orientation. Si and  $\alpha$ -phase coarsen more for OP loaded specimens, which can be attributed to higher diffusion rates in a lattice under compression.

At low strain amplitudes, no damage of the particle-matrix-interface could be observed. Given the low strain rate, the matrix has enough time to deform and to transmit stresses to the secondary phases. Furthermore, recovery effects are more evident at low strain rates than at high ones. Since the dislocation densities in the matrix are lower, dislocation movement is easier/ material behaviour is more plastic and can accommodate stresses more easily. This can be seen in the relatively flat stress-strain hysteresis curves for LCF and TMF and the resulting inelastic strain development over the lifetime. In contrast the higher dislocation density induced by higher strain rates cannot be recovered and the matrix is less able to accommodate high stresses, which

leads to decohesion and fracture of the more brittle particles, Figure 6.10. The Si particles appear to escape fracture while both the  $\text{Al}_2\text{Cu}$  and the  $\beta$ -phase reveal fracture.

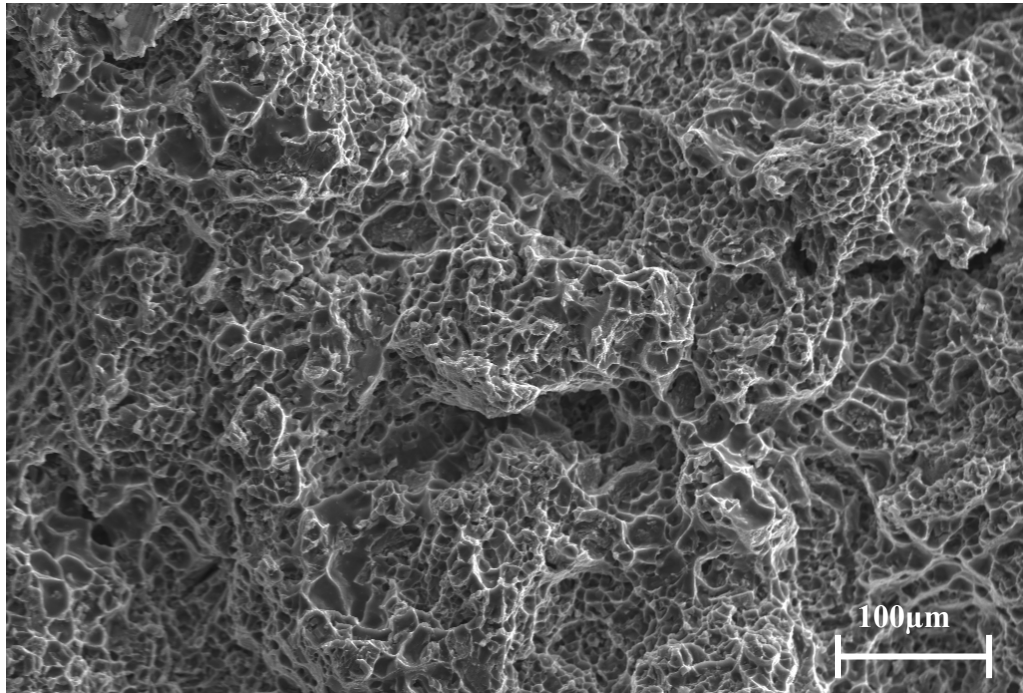


**Figure 6.10:** Brittle fracture surface of AlSi6Cu-T6 under OP-TMF loading at a strain amplitude of 0.6%.

## **6.6 EFFECT OF PRE-TREATMENT ON THERMO-MECHANICAL FATIGUE BEHAVIOUR OF THE ALSI6CU4 REFERENCE ALLOY**

The stress-strain behaviour of the specimen when subjected to each of the three treatments is dominated by decomposition of the metastable  $\theta'$  precipitates and subsequent coarsening of the  $\theta$  phase, which leads to softening with an increasing numbers of cycles (time). In comparison to the ordinary T6 heat treated specimens, the HIP modified specimens exhibit an almost pore free microstructure. This leads to an increase in hardness, strength and ductility, associated with a reduction in number of potential crack initiation sites. The reduction in porosity also leads to longer lifetimes since it takes substantially longer for cracks to initiate. The slightly higher grain size of the HIPed specimens, which can be attributed to their high temperature exposure during the HIP process and the subsequent T6 heat treatment, leads to improved cyclic

deformation behaviour. Although most of the HIP specimens have higher stress amplitudes than the ordinary T6 heat treated specimens, their mean inelastic strain turns out to be nearly equal or higher.

In contrast to the T6 heat treated specimens, the T7 specimens are overaged before testing. During TMF loading, the T7 heat treated specimens have the highest mean inelastic strains, caused by their lower strength and higher ductility. The T7 heat treatment reduces long time resistance, which can be seen in the stress-strain loops as well, where the T7 specimens have a lower  $E_{Sec}$ . Here, no clear difference between IP and OP-TMF loadings can be observed. High mean inelastic strain amplitudes during the tests are related to low strain amplitudes. While mean inelastic strains develop from the initial cycle on for T7 heat treated specimens, mean inelastic strain development is delayed to higher cycle numbers for the ordinary T6 heat treatment and the HIP modification, where overageing only starts at the beginning of the tests.

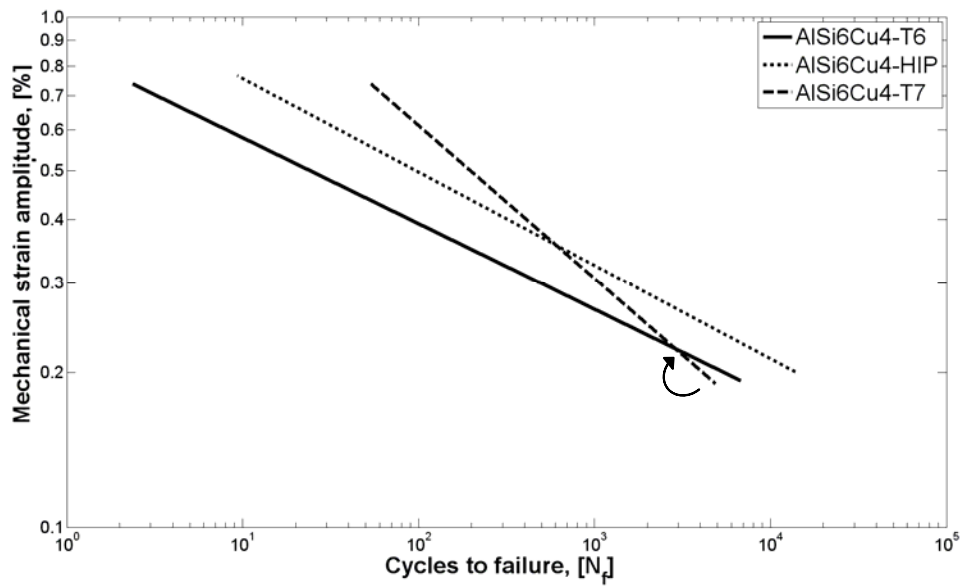
The drift of stresses in the ordinary T6 and HIP+T6 heat treated specimens at strain amplitudes of 0.2% are a result of creep effects. Creep is most pronounced under IP-TMF loading when specimens are under tensile stresses at the higher temperature where plastic processes such as dislocation creep can take place. At a lower temperature, which induces higher stresses, deformation is dominated by dislocation glide, which leads to hardening. The following hot phase of the cycle cannot annihilate or recover all dislocations so that a further increase of dislocation density caused by cyclic loading leads to hardening. With increasing time, a second effect works against this hardening as prolonged exposure at 400°C leads to growth of  $\alpha$ -Al grains and overageing of precipitates. This results in a softening of minimum and maximum stresses and finally leads to fracture. Under OP-TMF loading, these effects have less influence on the cyclic behaviour since diffusion leads to more recovery of dislocations under compression. Furthermore, under OP-TMF loading, compressive stresses under high temperature lead to a reduction of the remaining pore content. For HIP specimens, these effects are still present, although no such behaviour can be observed for T7 specimens. Here, the pre-existing overageing eliminates dislocation-precipitate interaction, leading to rapid softening by coarsening and grain growth.

Because the frequency is constant, the different strain amplitudes give rise to different strain rates. For low strain amplitudes, the particle matrix interface almost does not

reveal any evidence of better stress absorption by the matrix. Apparently, the T7 pre-treatment (or long time exposure at high temperature) has more influence so that the percentage recovery during a single cycle is higher than at higher strain amplitudes. For high strain amplitudes, the hardening caused by dislocation pile-ups during one cycle can be attributed to recovery being no longer complete, and less time being available for the matrix to absorb the high stresses at particle interfaces so that decohesion and particle fracture prevail. This strain rate dependence can also be observed in the gradient of the ductility factor with strain rate, which is lower for lower strain amplitudes than it is for higher strain amplitudes (Figure 5.33). This can be seen in hysteresis loops as well, where, the higher the strain amplitude, the higher is the inelastic strain and, the higher the gradient of ductility is, the higher is the rate of growth of particle damage and decohesion. Summing up, pre-treatment of the AlSi6Cu4 alloy provides it with a higher ductility to withstand higher loadings at higher strain amplitudes.

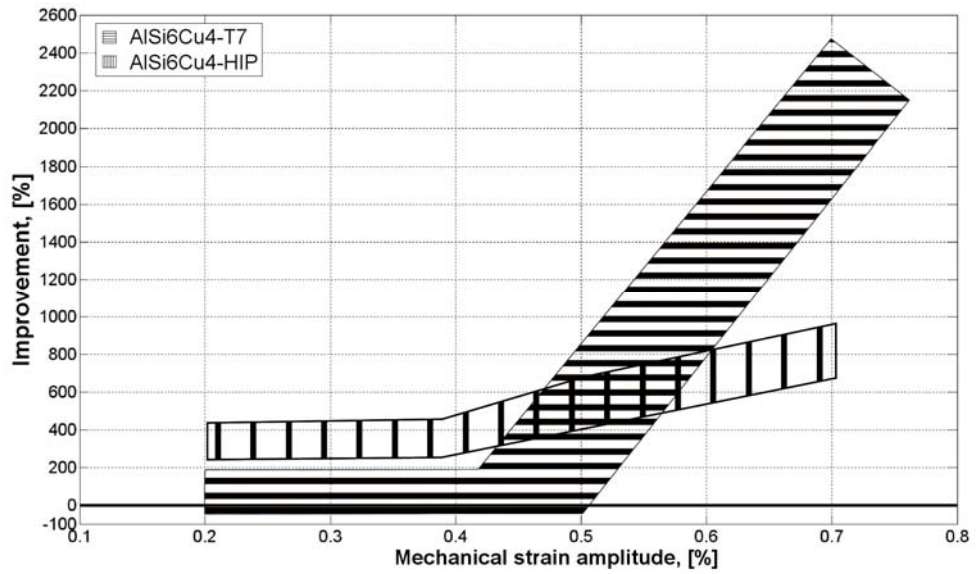
The slight scatter in the lifetime diagram can be attributed to the statistical distribution of damage initiators, such as pores. This is consistent with the application of the HIP process before testing reducing scatter in the data and in the lifetime. Comparing the lifetime curves for IP loading (Figure 6.11), it can be seen that the curves for the T6 and HIP specimens are parallel to each other, whereas that for T7 shows longer lifetimes for high strain amplitudes and shorter lifetimes for low strain amplitudes. This effect can be attributed to the heat treatment. For high strain amplitudes, the increased ductility of T7 specimens leads to higher lifetime because the microstructure can accommodate the resulting stresses better. The lack of heat resistance results in faster damage initiation and shorter lifetimes for low strain amplitudes. The higher lifetimes of the HIP modified specimens compared with T6 are a result of lower porosity and hence the reduced number of damage initiation sites, which affects all strain amplitudes equally.





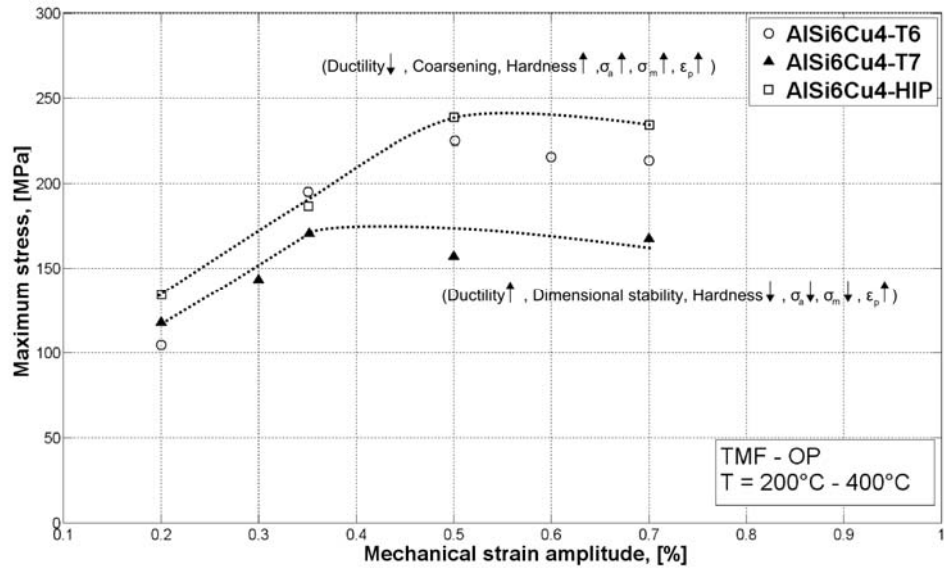
**Figure 6.11:** Relation between lifetimes for AISi6Cu4 with different pre-treatments and under IP-TMF loading.

Figure 6.12 shows the percentage improvement in TMF lifetime over the T6 condition offered by the two pre-treatments as a function of strain amplitude. The T7 pre-treatment leads to a modest deterioration at low strain amplitudes but to a very large (around 20-fold) improvement at high strain amplitudes. The HIP modification shows a more modest but still significant improvement over the whole range of strain amplitude investigated, but with a smaller improvement at higher strain amplitudes.



**Figure 6.12:** Improvement in TMF life offered by two different pre-treatments over the reference condition AISi6Cu4-T6.

Figure 6.13 contrasts schematically the maximum stresses for OP-TMF loading as a function of the controlled mechanical strain of the three treatments. Compared to an ordinary T6 heat treatment at a given strain amplitude, a T7 treatment leads to a reduction of mean stresses, stress amplitudes and hardness values with enhanced ductility and inelastic strains showing a stable condition with no further precipitation. On the other hand, the HIP modification leads to higher stresses and the microstructure has changed due to overageing.



**Figure 6.13:** Effect of pre-treatments on the maximum stresses of AISi6Cu4.

## 6.7 EFFECT OF SDAS ON THERMO-MECHANICAL FATIGUE BEHAVIOUR

The effect of reducing SDAS up to an average value of  $16\mu\text{m}$  can be most clearly seen by comparing the AISi9Cu3 alloy to the reference alloy (Table 5.1), although there may be some effects resulting from the different Cu and Si contents. The finer microstructure confers higher ductility, which can be seen in a higher mean inelastic strain development and a decrease of  $E_{Sec}$  during the TMF tests. The lower Cu content would have a similar effect on ductility although the higher Si content would have the opposite effect. The effect of a different microstructure is particularly pronounced under IP-TMF loading and at higher strain amplitudes, where the lower creep resistance of AISi9Cu3 leads to higher mean inelastic strains. Both a lower Cu content and finer grains would reduce creep resistance and the enhanced Si content would have no influence. Under OP-TMF loading, the evolution of mean inelastic strain for AISi9Cu3 is slightly above and parallel to the evolution of the reference alloy. The difference between the effects on IP and OP-TMF loading is due to the change in creep resistance and is more manifest in IP loading where the higher temperature coincides with higher stresses.

The hysteresis loops show AISi9Cu3 to be weaker than the reference alloy, despite its lower SDAS and higher Si content, both of which would be expected to increase its

strength. This effect, therefore, can be entirely attributed to a lower volume fraction of  $\text{Al}_2\text{Cu}$ , which would also account for the higher ductility.

The lifetime diagram (Figure 5.45) shows the finer microstructure to enhance fatigue life more in the OP tests than in the IP tests. Also, the enhancement is greater at high strain amplitudes (shorter exposure times) as well and the curves all converge at the lowest strain amplitude. The smaller SDAS value results in a reduction of porosity and this, along with the smaller Si particle size, results in a reduced opportunity for crack initiation. While porosity is the main crack initiator in  $\text{AlSi6Cu4}$  specimens, the decreased SDAS and the increased Si content lead to a change of the crack initiation site in  $\text{AlSi9Cu3}$  alloys to the interface between the  $\alpha$ -matrix and the eutectic phase. For lower strain amplitudes (longer lives), coarsening of the Si particles can be observed making them more effective crack initiation sites while, at the same time, the pores in the reference alloy have more time to heal, so that the curves begin to converge.

Reported values of SDAS in the literature range from  $25\mu\text{m}$  to  $100\mu\text{m}$  [77, 221-223, 285, 286], but assessing its effect on lifetime and stress-strain behaviour is very difficult due to the range of different alloys, test conditions and test procedures.

## **6.8 EFFECT OF ALLOYING ELEMENTS ON MICROSTRUCTURE AND THERMO-MECHANICAL FATIGUE BEHAVIOUR**

Most current research [46, 143, 210] is focused on determining the temperature range of one specific alloy or on the effect of heat treatment for specific alloys or alloy types. However, manufacturers need to know how different alloys will perform under specific conditions, and tests conducted by researchers do not usually permit such comparisons. Only once industrial manufacturers have assessed the behaviour of an alloy, will they try to modify the chosen alloy, for example by heat- or pre-treatments. Literature data almost never covers consistent test conditions for a set of candidate alloys and often only contains monotonic test data. It is well known [50, 287] that the strength of an alloy can be increased by enhancing the Si content and so TMF tests were also done on three Al-Si-Mg, where the main compositional differences lie in the silicon content, which incrementally increases from 6% in the reference alloy, through 7, 8 and 9% in the other alloys, and in the replacement of 4% Cu by 0.4-0.5% Mg. The effect of the Si

content can be seen in Table 5.1, where the amount, coarseness and angularity of the Si increase with silicon content. The 4% copper and 0.5%Mg additions might be expected to produce approximately the same volume fractions of the coherent precipitates.

The hysteresis loops for the Al-Si-Mg alloys are all flatter (lower maximum and minimum stresses for a given mechanical strain amplitude) than the reference alloy and the biggest difference is between the group and the reference alloy, indicating that the changeover from Cu to Mg is more significant than the increased Si content. The effects of both Mg and Si are more pronounced in the OP than the IP tests. These changes are reflected in the mean inelastic strain indicating that both the replacement of Cu with Mg and the increase of Si permit more microstructural accommodation by creep, the latter most probably being explicable by the coarser microstructure rather than the increased amount of Si.

As with the AlSi9Cu3 alloy, the Al-Mg-Si alloys show enhanced IP TMF lifetimes over the reference alloy at higher mechanical strain amplitudes, although the curves cross at higher strain amplitudes than for the AlSi9Cu3 and at a strain amplitude that seems to depend on the Si content. The OP TMF lifetime curves are more parallel and the AlSi7Mg0.5 line actually lies below that of the reference alloy. This somewhat confusing picture indicates that the effect of Si content is complex not merely depending upon microstructural coarseness but also depending on coarsening of the Si particles during the TMF tests.

Figure 6.14 summarises the mechanical behaviour of specimens tested under OP-TMF loading. Despite the creep effects at high strain amplitudes, the maximum stresses under OP-TMF loading increase with increasing strain amplitude. This is in contrast to the Al-Si-Cu alloys, where stresses decrease above a strain amplitude of 0.5% and must be associated with the different kinetics of the Mg-Si precipitate ripening.

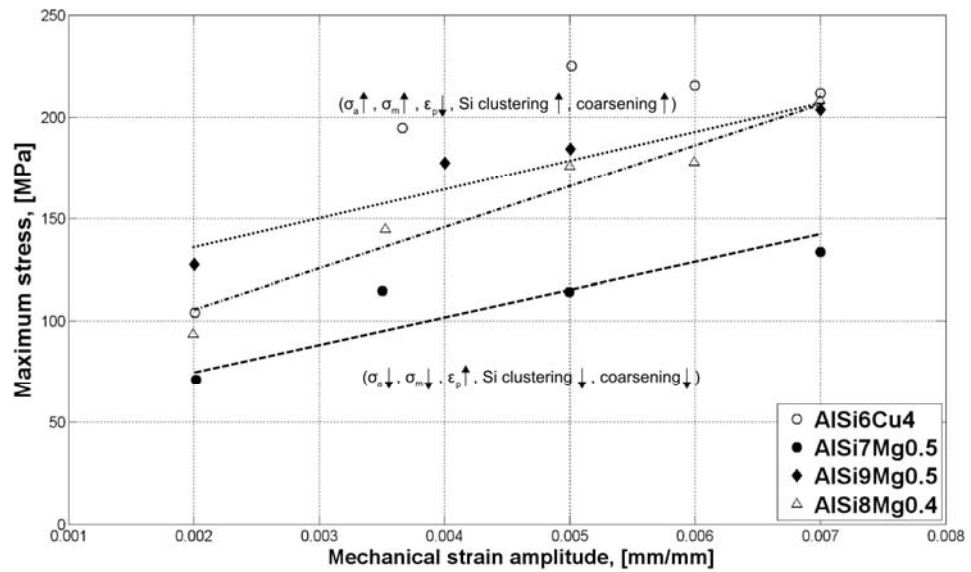


**Figure 6.14:** Maximum stress in OP-TMF tests at  $N=N_f/2$  for the different Al-Si-Mg alloys in relation to AlSi6Cu4.

## 6.9 SUMMARY OF EFFECTS OF ALLOYING AND TREATMENT ON TMF PROPERTIES AND PROSPECTS FOR ALLOY DEVELOPMENT

Figure 6.15 compares the stress amplitudes at  $N=N_f/2$  for all of the alloys, developed during TMF for the mechanical strain amplitudes of 0.2% and 0.5%. The highest stress amplitudes are exhibited by AlSi6Cu4-T6 with and without the HIP modification. The lowest stresses are shown by the AlSi7Mg0.5 alloy, and the stresses increase with Si content in the Al-Si-Mg alloys. The reference alloy in the T7 condition develops around the same stress amplitude as the higher strength Al-Mg-Si alloys. The stress amplitude across the range of alloys tested varies by about a factor of 2 for the reference alloy in the T6 condition over the weakest alloy, indicating that the most effective alloying element is Cu, producing more age-hardening strength increase than Mg-Si. Next most important is silicon, which, for a given age-hardening addition, will increase the stress amplitude in these tests.

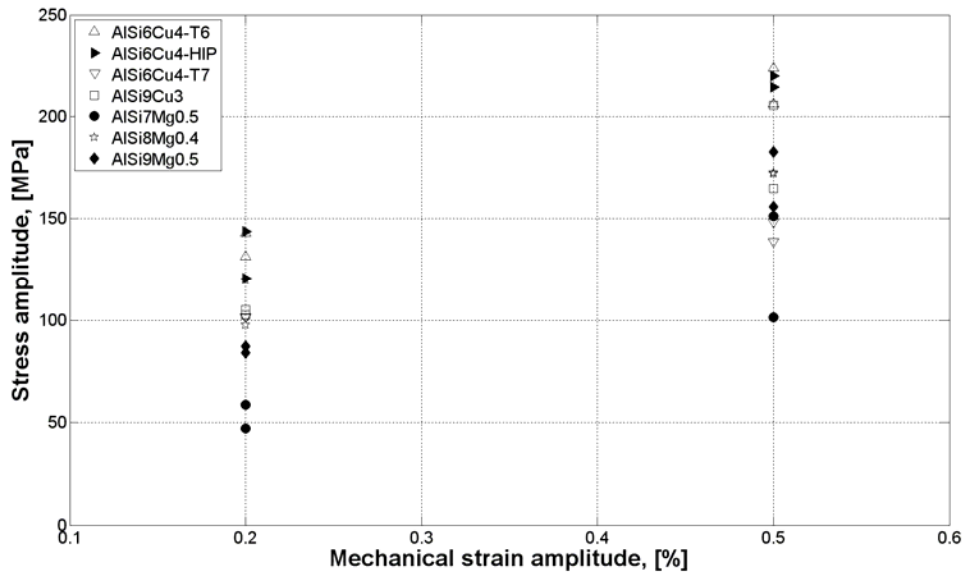


**Figure 6.15:** Comparison of stress amplitudes at mechanical strain amplitudes of 0.2% and 0.5% at  $N=N_f/2$  of alloys tested under TMF loading.

Figure 6.16 shows the TMF lifetimes for all of the alloys at mechanical strain amplitudes of 0.2% and 0.5% for each of the alloys and conditions examined. Although there is some variation in slope of the  $\Delta\varepsilon_{\text{mech}}/2-N$  curves, the reference alloy in the reference condition is consistently one of the poorest-performing alloys, and the AlSi9Cu3 is consistently one of the best. Given that the lifetimes of the Al-Mg-Si alloys appear to decrease with increasing Si content, it seems that the success of the AlSi9Cu3 is attributable to the reduction in the SDAS over the reference alloy outweighing the negative effect of Si cluster formation. Of the two pre-treatments applied to the reference alloy, the HIP treatment appears to have been more effective than the T7 treatment, most probably due to the reduction of crack initiating pores near to the surface.

Table 6.4 summarises the main effects seen in Al-Si-Cu and Al-Si-Mg alloys tested, focusing on the main differences between them. Similarities, such as in the morphology of precipitates and particle orientations, are not mentioned for clarity. It is quite difficult to assess the findings of this research in comparison with literature results, as test results based on the same loading/ test condition are rare. Still, some aspects of aluminium alloy development for TMF resistance can be isolated and these are discussed here. While the observed effects of a decrease in the SDAS on alloy performance are in

agreement with other researchers [222, 288] the reduction in fatigue life with increasing Si content conflicts with the commonly held view [289, 290]. The observation that a decrease in pore size and volume fraction increases the number of cycles to failure is nothing new [93, 291] but this has not until now been linked directly with the influence of a HIP treatment and its effect on the stress-strain behaviour has not been assessed before. It is a key principle of this work that a single application-base test is carried out on different alloys in different conditions using the same procedures, so that, here, a direct comparison can be made from the test results. Furthermore, the increased temperature range and the temperature gradient inside the gauge length are features of the test which cannot be found elsewhere, despite their great significance for the automotive industry. For example, the effect of a T7 treatment on the stress-strain and lifetime behaviour contributes to the common understanding that the treatment leads to a reduction in the cycles to failure [14, 158, 210, 285]. Here, a clearly different behaviour was exhibited, which better reflects the microstructure of hot areas such as the valve bridges in cylinder heads after prolonged operation [32].

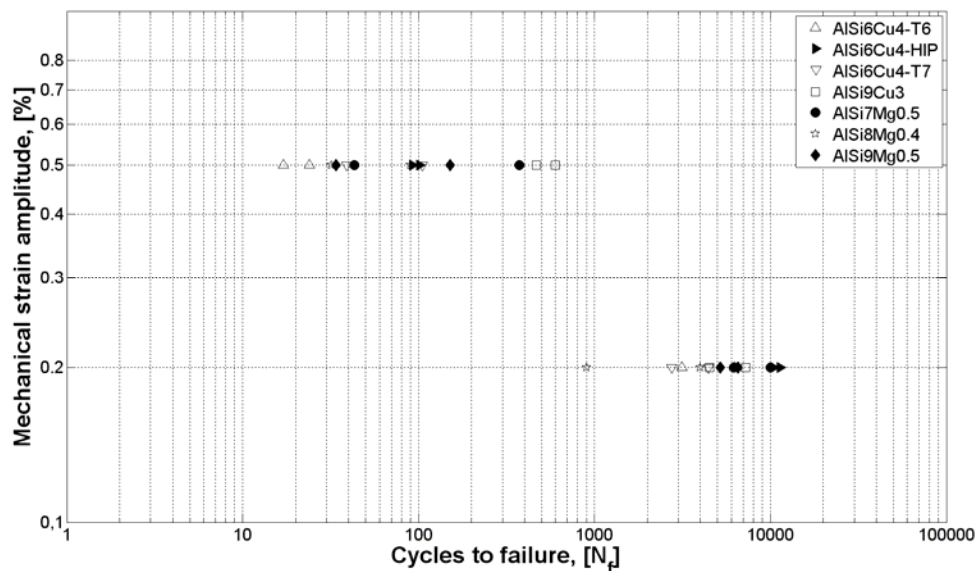


**Figure 6.16:** Mechanical strain amplitude vs. cycles to failure under TMF loading for mechanical strain amplitudes of 0.2% and 0.5% of all alloys tested.



**Table 6.4:** Summary of the main effects on Al-Si-Cu and Al-Si-Mg alloys before and under CERT and TMF conditions.

Alloy/ condition	Main microstructural effects	CERT behaviour	TMF behaviour
<b>AlSi6Cu4-T6</b>	<ul style="list-style-type: none"> <li>- Peak value of hardness</li> </ul>	<ul style="list-style-type: none"> <li>- For tests at 200°C and 400°C the T6 values of UTS, PS and <math>\sigma_y</math> lay between the values of the T7 and the HIP condition</li> </ul>	<ul style="list-style-type: none"> <li>- Sharp form of the hysteresis loop in the transition from tension to compression and backwards</li> <li>- Slight hardening which is followed by softening for low strain amplitudes and softening from the beginning for high strain amplitudes</li> <li>- Transition for compressive mean stresses to tensile mean stresses after <math>N=2</math> which change again after <math>N=15</math> to compressive mean stresses until fracture for strain amplitudes of 0.2% under OP-TMF</li> <li>- Crack initiation at pores near to the surface</li> </ul>
<b>AlSi6Cu4-T7</b>	<ul style="list-style-type: none"> <li>- Overaged microstructure (including grain size, particles, precipitates and particle distances) which results in a more ductile/ stabilized condition</li> </ul>	<ul style="list-style-type: none"> <li>- Lowest UTS, PS and <math>\sigma_y</math> values at 200°C and 400°C for AlSi6Cu4</li> </ul>	<ul style="list-style-type: none"> <li>- Broadening of hysteresis loops</li> <li>- High inelastic strains</li> <li>- Softening for all strain amplitudes</li> <li>- For strain amplitudes <math>\leq 0.2\%</math> under OP-TMF similar behaviour to T6 condition with shift to longer cycles</li> <li>- No further drift in mean stress development for other strain amplitudes</li> <li>- Highest amount of grain coarsening during TMF tests which results in lower creep pores in the microstructure</li> <li>- Cracks propagate through the <math>\alpha</math>-matrix similar to specimens in the T6 condition under long time high temperature exposure</li> <li>- For high strain amplitudes cracks propagate alongside precipitates (<math>\alpha</math>- and <math>\beta</math>-phase) and particles</li> </ul>
<b>AlSi6Cu4-HIP+T6</b>	<ul style="list-style-type: none"> <li>- Lowest content of porosity</li> <li>- Highest hardness values</li> <li>- Slight increase of precipitate sizes caused by a longer exposure time in comparison to the ordinary T6 condition</li> </ul>	<ul style="list-style-type: none"> <li>- Highest UTS, PS and <math>\sigma_y</math> values at 200°C and 400°C for AlSi6Cu4</li> </ul>	<ul style="list-style-type: none"> <li>- Increase of inelastic strain under IP- TMF for strain amplitudes <math>\geq 0.35\%</math> and decrease of inelastic strain for OP-TMF</li> <li>- Slight hardening amplitudes which are followed by softening for low strain and softening for high strain amplitudes from the beginning</li> <li>- For strain amplitudes <math>\leq 0.2\%</math> massive increase of compressive mean stresses from cycle <math>\sim N=100</math> which decreases when reaching cycle <math>\sim N=500</math></li> <li>- Change to crack initiation at Si-particles and precipitates (<math>Al_2Cu</math>)</li> </ul>

**Table 6.4 (contd.):** Summary of the main effects on Al-Si-Cu and Al-Si-Mg alloys before and under CERT and TMF conditions.

<b>AlSi9Cu3-T6</b>	<ul style="list-style-type: none"> <li>- Smallest SDAS and particle values of tested alloys</li> <li>- Fine distribution of Si particles</li> <li>- Higher Fe content leads to cluster formation of <math>\alpha</math>-phase</li> <li>- Highest content of hardening for Al-Si-Cu alloys</li> </ul>	<ul style="list-style-type: none"> <li>- The very small SDAS value leads to the highest work hardening rate at 400°C</li> </ul>	<ul style="list-style-type: none"> <li>- Broadening of the hysteresis loops by a higher inelastic behaviour for IP and OP-TMF</li> <li>- Slight hardening which is followed by softening for low strain amplitudes and softening from the beginning for high strain amplitudes</li> <li>- Nearly constant curve progression of mean stresses under OP-TMF</li> <li>- Notch stresses induced by cluster formation of the <math>\alpha</math>-phase</li> <li>- Crack initiation in Si cluster and oversize <math>\alpha</math>-phase near to the surface</li> <li>- Crack propagation between <math>\alpha</math>-matrix and particles</li> <li>- Decohesion of Si-particles from the matrix</li> <li>- Orientation of precipitates and particles is similar to AlSi6Cu4-T6</li> </ul>
<b>AlSi7Mg0.3(Cu)-T6</b>	<ul style="list-style-type: none"> <li>- Lowest content of hardening of Al-Si-Mg alloys</li> </ul>	-	-
<b>AlSi7Mg0.5-T6</b>	<ul style="list-style-type: none"> <li>- Lowest volume content of fine distributed Si particles of Al-Si-Mg alloys</li> </ul>	<ul style="list-style-type: none"> <li>- Highest work hardening rate of Al-Si-Mg alloys which is similar to AlSi6Cu4-HIP</li> </ul>	<ul style="list-style-type: none"> <li>- Softening for all strain amplitudes</li> <li>- Highest inelastic strains at <math>N=N_f/2</math> for Al-Si-Mg alloys</li> <li>- Lowest coarsening behaviour of Al-Si-Mg alloys</li> <li>- Lowest decohesion behaviour of particles and matrix of Al-Si-Mg alloys under TMF which is induced by an elastic matrix caused by the lower hardness values from the beginning</li> <li>- Highest amount of creep pores formation during TMF of Al-Si-Mg alloys</li> </ul>
<b>AlSi8Mg0.4-T6</b>	<ul style="list-style-type: none"> <li>- Values between AlSi7Mg0.5 and AlSi9Mg0.5</li> </ul>	<ul style="list-style-type: none"> <li>- Values between AlSi7Mg0.5 and AlSi9Mg0.5</li> </ul>	<ul style="list-style-type: none"> <li>- Softening for all strain amplitudes</li> </ul>
<b>AlSi9Mg0.5-T6</b>	<ul style="list-style-type: none"> <li>- Lamellar form of Si particles</li> <li>- Highest amount of Si volume content of Al-Si-Mg alloys which leads to clustering of the Si particles</li> <li>- Highest content of hardening of Al-Si-Mg alloys</li> </ul>	<ul style="list-style-type: none"> <li>- Lowest work hardening rate for all tested alloys</li> </ul>	<ul style="list-style-type: none"> <li>- Softening for all strain amplitudes</li> <li>- For high strain amplitudes similar mean stress behaviour to AlSi6Cu4-T6</li> <li>- Lowest inelastic strain at <math>N=N_f/2</math> for Al-Si-Mg alloys</li> <li>- Notch stress induced by lamellar form of Si-particles</li> <li>- Crack initiation in Si cluster near to the surface</li> <li>- Highest decohesion behaviour of particles and matrix of all Al-Si-Mg alloys under TMF</li> <li>- Highest coarsening behaviour of all Al-Si-Mg alloys</li> <li>- Lowest amount of creep pores formation during TMF of all Al-Si-Mg alloys</li> </ul>

## 6.10 SIMULATION AND MODELLING OF DAMAGE BEHAVIOUR OF ALSI6CU4

In order to provide a demonstration of the applications of the findings of this work, the results were implemented into the FEM tool, Ansys, to simulate IP and OP-TMF loading and into a damage model which is based on 9 parameters and which was developed by Chaboche [238] to simulate LCF behaviour on the test geometries. Finally, TMF loading was applied to a cylinder head geometry. Figure 6.17 illustrates the approach.

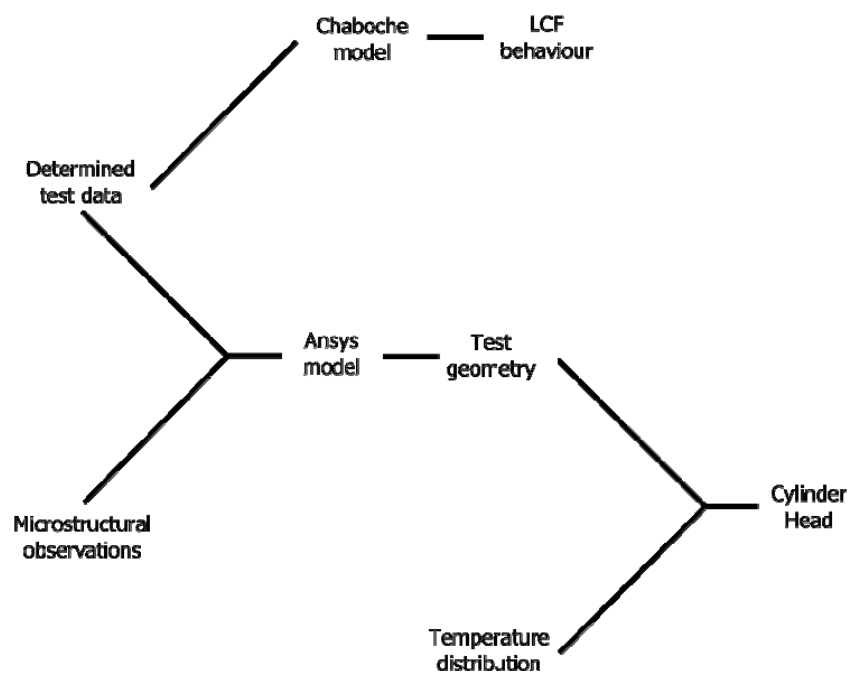


Figure 6.17: Schematic overview of input data and simulation procedure.

### 6.10.1 Modelling and simulation of microstructure during TMF

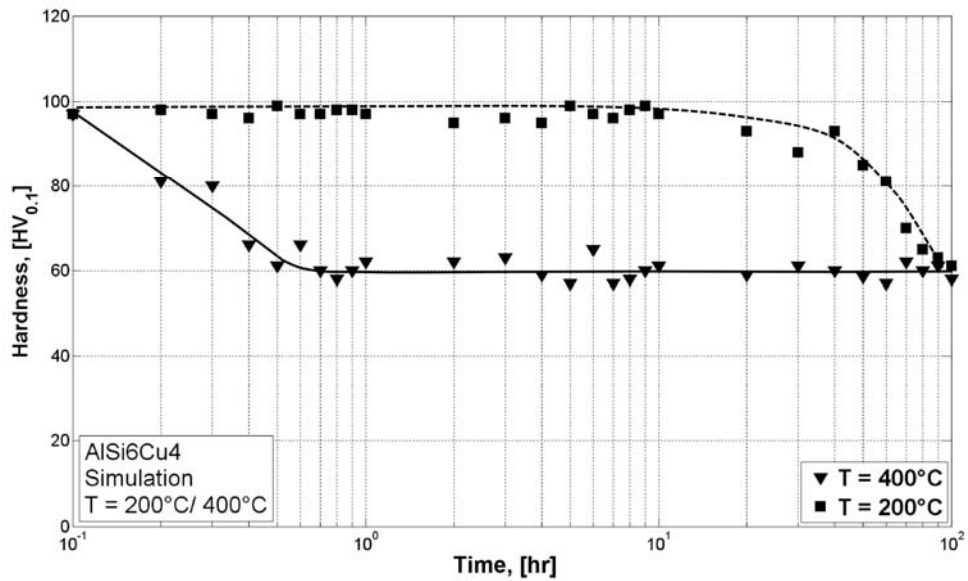
A simulation of hardness, based on the model of Boussac and Calais [161], was carried out for the results of the long-time exposure tests on AlSi6Cu4 starting with either the T6 or T7 condition. Only the minimum and maximum values, 200°C and 400°C, were simulated in order to gain an insight into the material behaviour at the threshold temperatures. Based on the fact that an average TMF test runs for around 5000 cycles, long time exposure tests (and the simulations) were stopped after 100hr.

Figure 6.18 shows the average hardness (20 measurements per specimen) and the simulated hardness for the reference alloy starting with an ordinary T7 heat treatment during long time exposure at 200°C and 400°C. The simulation used the following material constants

at 200°C: A=27, B=0.9, C=153

at 400°C A=18, B=2.5 and C=105

As can be seen, the agreement between the test results and the simulation is excellent, both indicating that, at around 100hr the hardness of an exposure at 200°C approaches that of a 400°C exposure. Applying the simulation to the AlSi7Mg0.3(Cu) revealed a similarly same good correlation between the model and hardness values from the long time exposure tests. This evolution has important implications for TMF lifetimes because it reveals that the softening process is complete within a rather short time compared to the lifetime of an engine block. Furthermore, this must be considered in high temperature tests where a heating up phase or a pre-test can lead to a change of microstructure and so to a different initial microstructure when the test starts. The heating up phase must be kept very short here. In the current work, the direct influence of high test temperature and the associated influences of pre-tests in TMF and the heating up phase in isothermal LCF, could not be observed because of the small amount of specimens.



**Figure 6.18:** Simulation of hardness values of AISi6Cu4 at 200°C and 400°C starting from T7.

Given the potential effect of porosity on TMF life, a FEM study was carried out to assess the influence of pore orientation, pore proliferation and pore form on the likelihood of pore extension under IP and OP-TMF loading. Three orientations, as shown in Figure 6.19, were examined.

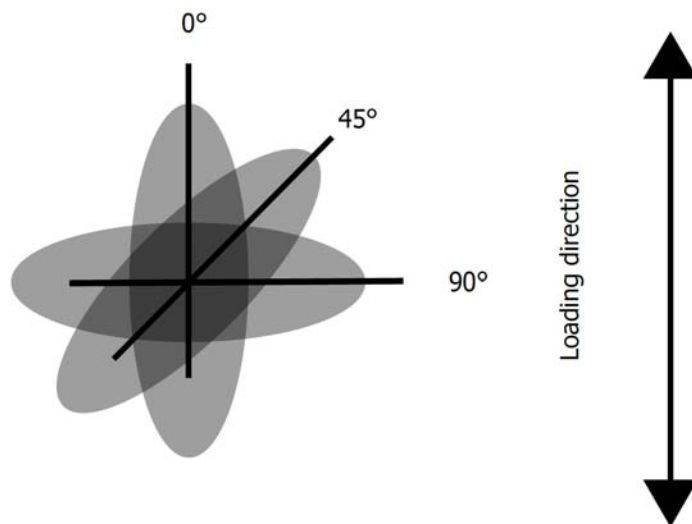


**Figure 6.19:** Orientation of pores relative to the direction of loading.

The material was considered to be a continuum and was modelled by Chaboche in Ansys as a visco-plastic material. Since no creep effects were observed during the TMF tests, it was not considered in the simulation. The Chaboche model used here for the

simulation of the TMF tests was extracted from the CER tests (in 50°C steps) and internally interpolated. As a next step, a geometry volume was defined. The Chaboche model in Ansys simulates non-linear kinematic hardening and consists of 5 sub material models with 11 parameters. These parameters were obtained using an optimisation approach where the simulation and test results were fitted using least squares, first using the CERT and LCF data and, finally, the TMF data. This required the development of a material model with isothermal LCF data from a special multi step test on the same alloy (not part of this thesis). A conflation of the Chaboche model with other material models (e.g. MISO, which is used for isotropic hardening) resulted in a reduction of the 11 parameters.

Globular, elliptical, notch-like and flower-like forms, similar to those observed in the test specimens, were analysed using the elasto-plastic model. It was found that pore geometry has no direct influence on stress intensification, but that the notch tip radius is an important factor. The highest stresses were seen in pores with an orientation of 90°, perpendicular to the loading direction. Figure 6.20 shows the local stress concentration around an elliptical pore oriented at 90° and 0° to the loading direction. As can be seen, the larger active radius for the 90° orientation leads to stresses about four times smaller, not unlike what would be expected in an elastic continuum (Figure 6.21).

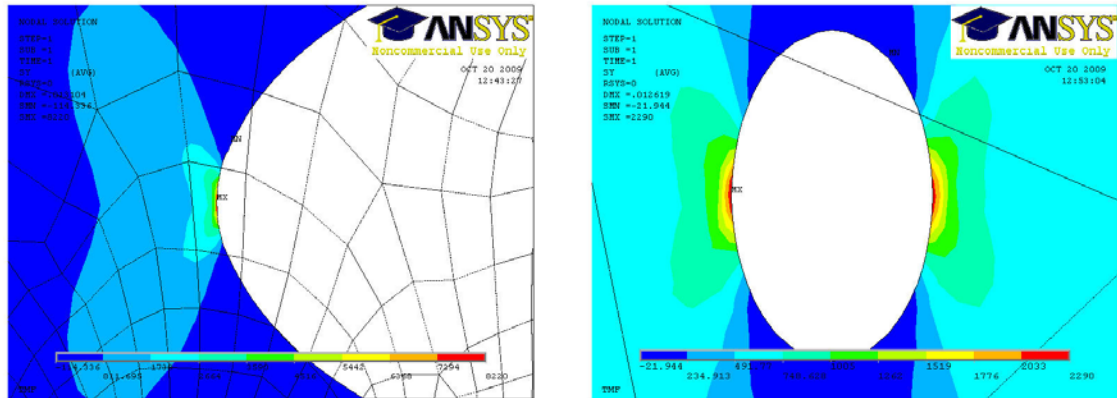


**Figure 6.20:** Stress distribution around an elliptical pore for different orientations: (right) pore aligned in loading direction, (left) pore rotated by 90° relative to the loading direction.

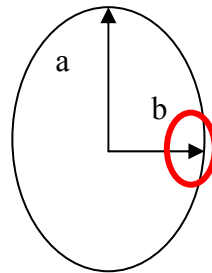


**Figure 6.21:** Pore geometry.

If the pore changes orientation, size or shape (e.g. by HIP or through mechanical deformation) the stress concentration factor (SCF) changes, increasing if the size increases or the radius at the axis perpendicular to the loading axis decreases. Figure 6.22 shows the effect of pore size and radius on the SCF obtained with the material simulated according to the Chaboche model at 400°C with a mechanical strain amplitude of  $\pm 0.5\%$ .

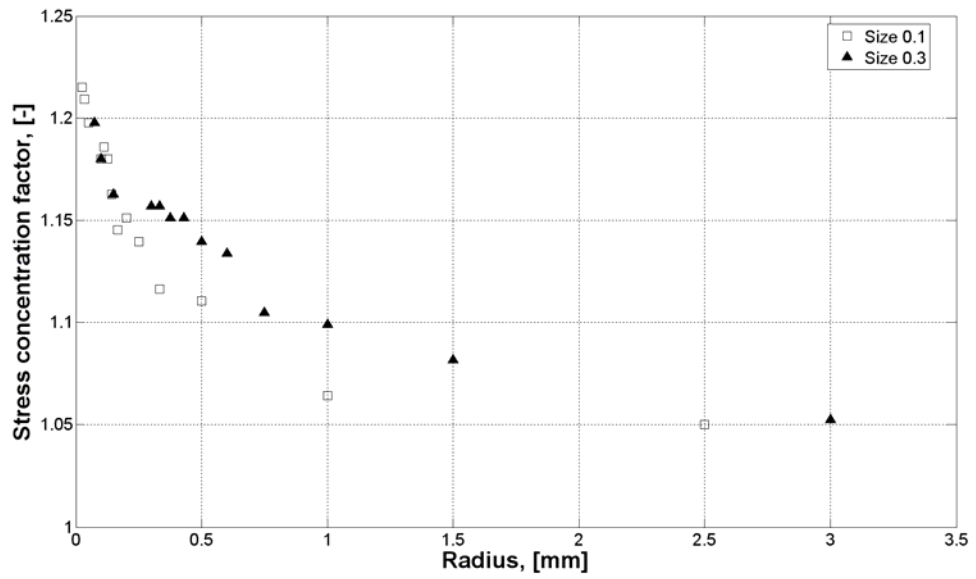


**Figure 6.22:** Stress concentration factor vs. pore radius of two sizes.

A comparison of linear-elastic and Chaboche models for a pore size of  $a=0.1\text{mm}$  and strain amplitude of 0.5% is shown in a single logarithmic plot against radius of curvature in Figure 6.23. Clearly, the stress concentration factor is much lower for the Chaboche model at smaller radii, the two converge of larger ones.



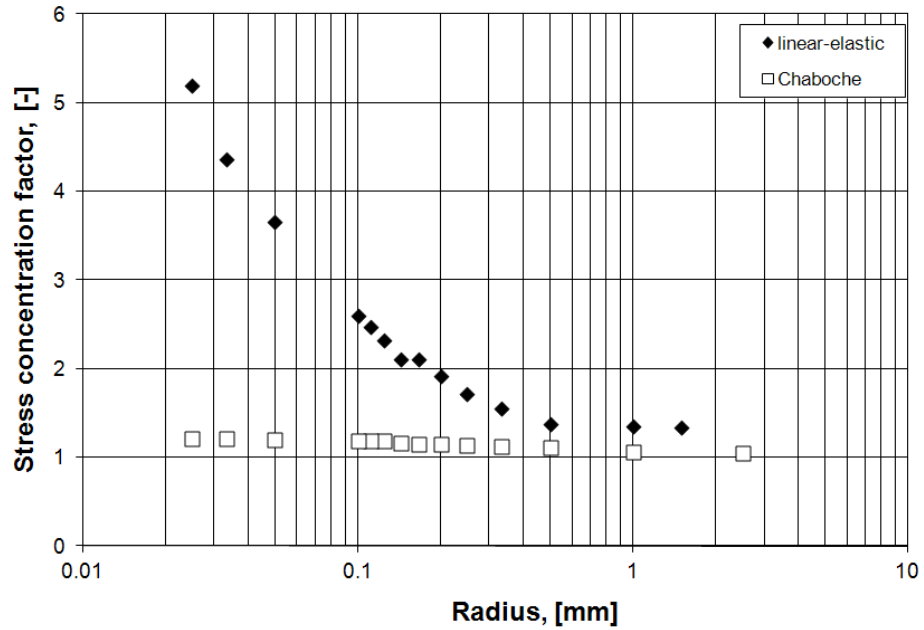


**Figure 6.23:** Stress concentration factors for linear-elastic and Chaboche simulations vs. elliptical pore radius of curvature.

For the IP and OP-TMF loading simulations, it was observed that the inelastic strain at the root of the pore is higher at 200°C than it is at 400°C for a given form and strain amplitude. At first glance, this might appear counter-intuitive because the material starts yielding at a lower stress at higher temperature but, on examination, it was seen that the deformation was distributed over a larger area at 400°C than at 200°C. This means that the pore curvature changes, the pore root becoming blunted. Also, mean inelastic strains under tension were found to be two times higher in tension than in compression and deformation is more concentrated under tension than under compression. On the other hand, pores at the surface exhibit similar behaviour under tension and compression. This is caused by a reduction of the reinforcement offered by the surrounding matrix. Also, pores whose stress fields interact (Figure 6.24) will have a modified propensity to propagate.

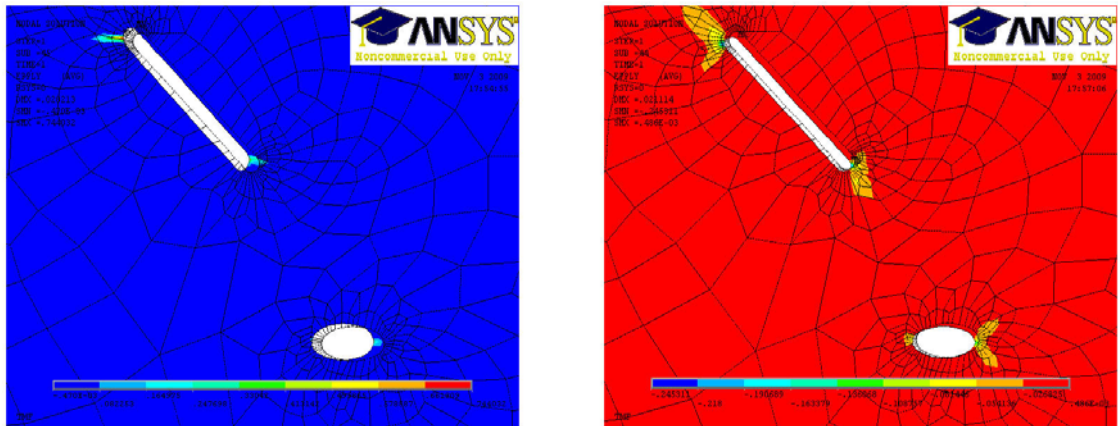


**Figure 6.24:** Interaction of pores under tension (left) and compression (right).

Thus, the behaviour of cast materials under mechanical loading can be understood better using simulation of the microstructure. A HIP treatment, which reduces shrinkage porosity and which leaves behind gas porosity with its globular geometry, results in a bigger notch radius. As a result, the remaining pores have a lower potential for crack initiation potential, hence improving lifetime.

### **6.10.2 Cyclic stress-strain behaviour**

The Chaboche model (summarised in Appendix A) was used to simulate the LCF hysteresis loops for the first 10 cycles in the temperature range between 200°C and 400°C with Matlab. The parameters used here were derived from the results of the special tests [292] using a stochastic approach known as Evolution Strategy which generated a start parameter for a deterministic Levenberg-Marquardt algorithm. The Young's modulus and the yield strength were determined from the CER tests and the viscosity parameter  $K$  and Norton exponent  $n$  were obtained from the creep tests. The cyclic stress-strain curves from the LCF tests and some multi step tests (which are not part of this thesis) led to the kinematic hardening parameters  $C_\infty$  and  $\gamma$ . The isotropic hardening parameters were obtained by analysing the stabilised cycle ( $N=N_f/2$ ). The parameter  $Q_\infty$  is the difference between  $\sigma_{\max}$  of the first cycle and  $\sigma_{\max}$  of the stabilised

cycle. As a start parameter for  $R_0$ , the yield strength of the first cycle was used, and  $b$  can be determined by solving the following equation

$$\frac{\sigma_{\max} - \sigma_{\max 0}}{\sigma_{\max(N=N_f/2)} - \sigma_{\max 0}} = 1 - e^{-2bN\Delta\epsilon^p} \quad (18)$$

As can be seen from Figure 6.25, the parameters used gave a very close fit between test and simulated hysteresis loops.

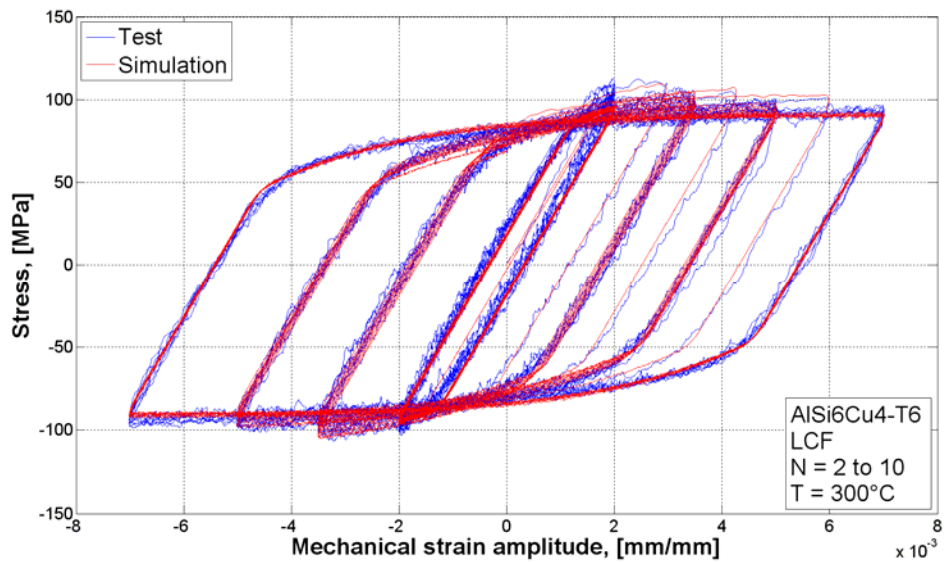


**Figure 6.25:** Comparison of hysteresis loops resulting from simulation with the Chaboche model and from tests.

As seen above, the hysteresis loops from the Chaboche simulation and from the tests were well correlated for LCF behaviour. However, the TMF simulations, for which the model was originally developed, failed at temperatures above 330°C. Here, the relaxation and creep effects observed during isothermal LCF and isothermal CER tests led to a large scatter and translation of the loops. This can be attributed to the different mechanisms which occur during a cycle under LCF and TMF. A further optimization routine would require an increase to around 30 parameters whose determination would require further tests.

As well as the modelling of the microstructure described above, the TMF hysteresis loops (including IP and OP simulations in the temperature range between 200°C and 400°C and strain amplitudes of 0.2% up to 0.7%) were also simulated using Ansys. If the values of Young's modulus, yield strength, ultimate strength and fracture strain are known, a bilinear flow curve (BISO) can be defined. By using all the values from the CER tests a stress-strain curve can be defined. In order to simulate isotropic hardening Ansys offers a multi-linear MISO and a non-linear NLISO isotropic hardening model. The MISO is based on plastic strain and stress whereas NLISO is by an equation of the form:

$$R = k + R_0 \cdot \hat{\varepsilon}_{pl} + R_\infty \cdot \left(1 - e^{-b\hat{\varepsilon}_{pl}}\right) \quad (19)$$

In contrast to the non-linear kinematic variables used by Chaboche, Ansys specifies the variables internally as follows:

$$\dot{X} = \sum_i^n \dot{X}_i = \frac{2}{3} \sum_i^n C_i \cdot \hat{\varepsilon}_{pl} - \gamma_i X_i \cdot \dot{p} + \frac{1}{C_i} \cdot \frac{\partial C_i}{\partial \theta} \cdot \dot{\theta} \cdot X_i \quad (20)$$

$C$  and  $\gamma$  are obtained by a numerical optimisation based on the least squares error method. Overageing and damage to the material during lifetime was implemented as a damage factor,  $D$ :

$$D = 1 - \frac{\sigma_{\max_i}}{\sigma_{\max_1}} \quad (21)$$

where  $\sigma_{\max}$  is the maximum stress in tension in every cycle and  $\sigma_{\max_1}$  is the maximum stress in cycle  $N=1$ . Using this factor leads to a decrease in stresses with increasing lifetime until fracture. Figure 6.26 shows a comparison of data from the test rig along with the Ansys simulation under IP loading. Good agreement was also obtained for all strain amplitudes for OP loadings. A drift of mean stresses for a strain amplitude of 0.5% and the start of yielding is similar to the test values.

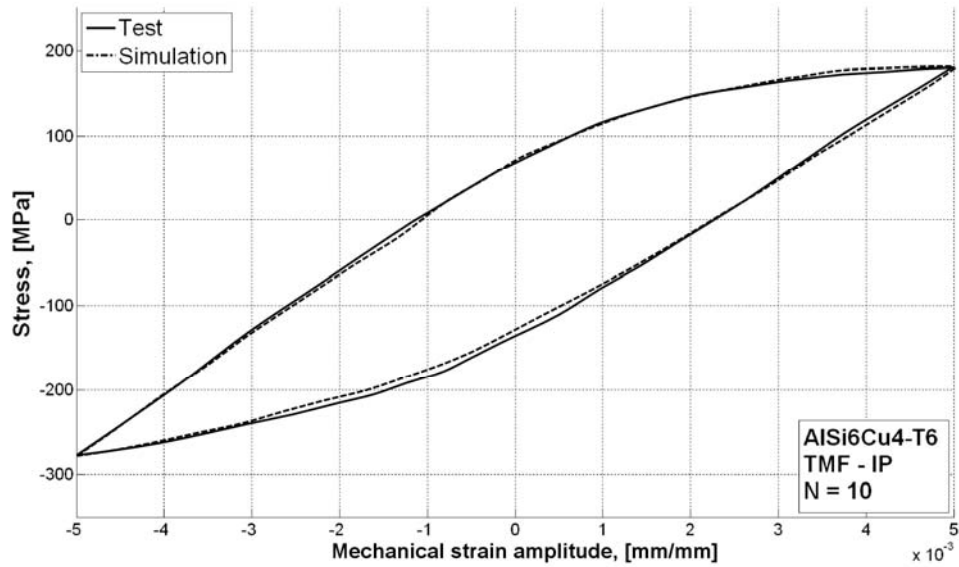


**Figure 6.26:** Comparison of hysteresis loops at  $N=10$  obtained from simulation with Ansys and from tests under IP-TMF loading.

### 6.10.3 Lifetime behaviour

This section applies some of the models for lifetime behaviour described in Section 3.4 to the data for IP and OP loading of the reference alloy, with a view to selecting the best description of lifetime. Next, the selected model is applied to the other TMF data in order to recommend a parametric description of fatigue life for all of the alloys and treatments studied.

Figure 6.27 shows the hysteresis energy at  $N=N_f/2$  calculated from the hysteresis loop for the IP and OP-TMF tests on the reference alloy. As can be seen, low strain amplitudes have the lowest cumulative hysteresis energies and the longest lifetimes, whereas high strain amplitudes show higher cumulative hysteresis energies and shorter lifetimes.

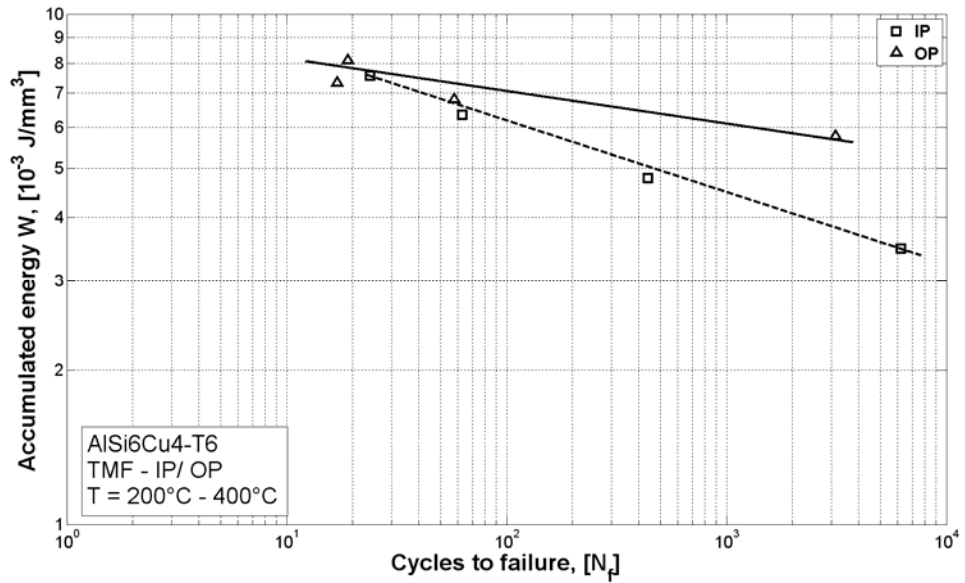


**Figure 6.27:** Accumulated hysteresis energy of AISi6Cu-T6 specimens tested under IP and OP-TMF loading.

By fitting a power law to Figure 6.27, a relationship between fatigue life and the accumulated hysteresis energy can be established. Table 6.5 lists the parameters.

**Table 6.5:** Hysteresis energy parameters for predicting lifetime.

$W = a \cdot N_f^c$	Function	R <sup>2</sup>
IP-TMF	$y = 8.8493 x^{-0.0543}$	0.86
OP-TMF	$y = 11.412 x^{-0.1881}$	0.99

Figure 6.28 shows the dependence of the damage parameters of  $P_{SWT}$  and  $P_{Ost}$  (Equations 8 and 9) calculated at  $N=10$  during fatigue lifetime. Both damage parameters increase and lifetime decreases when the strain amplitude increases for both IP and OP-TMF loading.

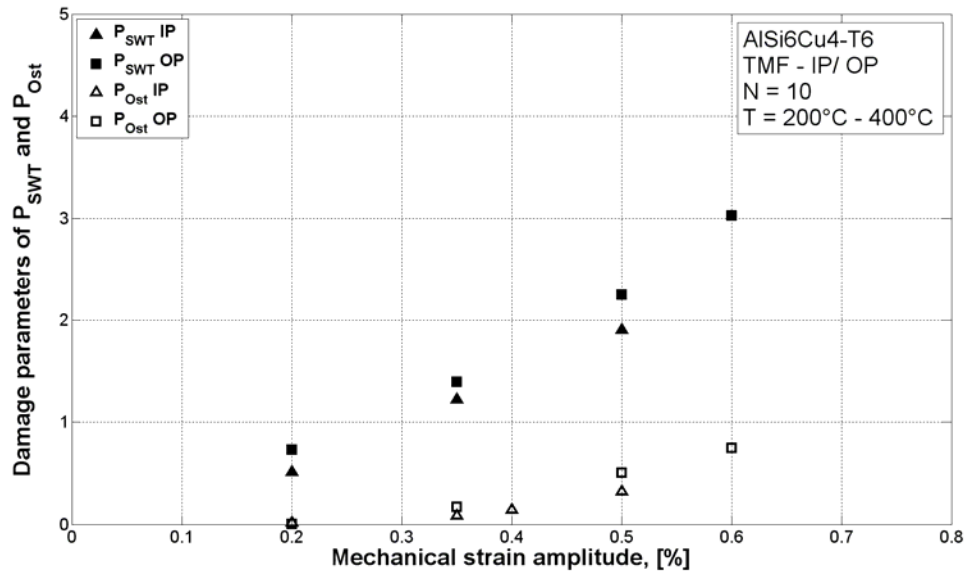


**Figure 6.28:** Damage parameters of Smith-Watson-Topper and Ostergren at  $N=10$  of tested specimens under IP and OP-TMF loading for AISi6Cu4-T6.

The best-fit straight line parameters for Figure 6.28 are summarized in Tables 6.6 and 6.7 for  $P_{SWT}$  and  $P_{Ost}$ , respectively, where  $R^2$  is the coefficient of determination of the fit. The best results are obtained for the  $P_{SWT}$  parameter although both are good.

**Table 6.6:**  $P_{SWT}$  parameters for predicting lifetime.

$P_{SWT}$	Function	$R^2$
IP-TMF	$P_{SWT} = 4.60 \varepsilon_{mech} - 0.403$	0.9997
OP-TMF	$P_{SWT} = 5.69 \varepsilon_{mech} - 0.498$	0.9863

**Table 6.7:**  $P_{Ost}$  parameters for predicting lifetime.

$P_{Ost}$	Function	$R^2$
IP-TMF	$P_{Ost} = 0.986 \varepsilon_{mech} - 0.215$	0.8705
OP-TMF	$P_{Ost} = 1.90 \varepsilon_{mech} - 0.423$	0.9737

Figure 6.29 shows the evolution of damage based on the secant modulus ( $E_{Sec}$ ) (Equation 7). Starting from  $(1-D)=1$ , where the damage,  $D=0$ , and assuming no pre-existing damage in the specimen (e.g. casting defects or other inhomogeneities) the damage induced by cyclic loading and temperature exposure resulting in a decrease in secant modulus, which reflects the decrease in stresses during the lifetime. As can be

seen, damage accumulation is far from linear, the rate increasing towards the end of life. The IP and OP-TMF damage accumulation show similar evolutions at a strain amplitude of 0.2%, whereas higher strain amplitudes show no such similarities.

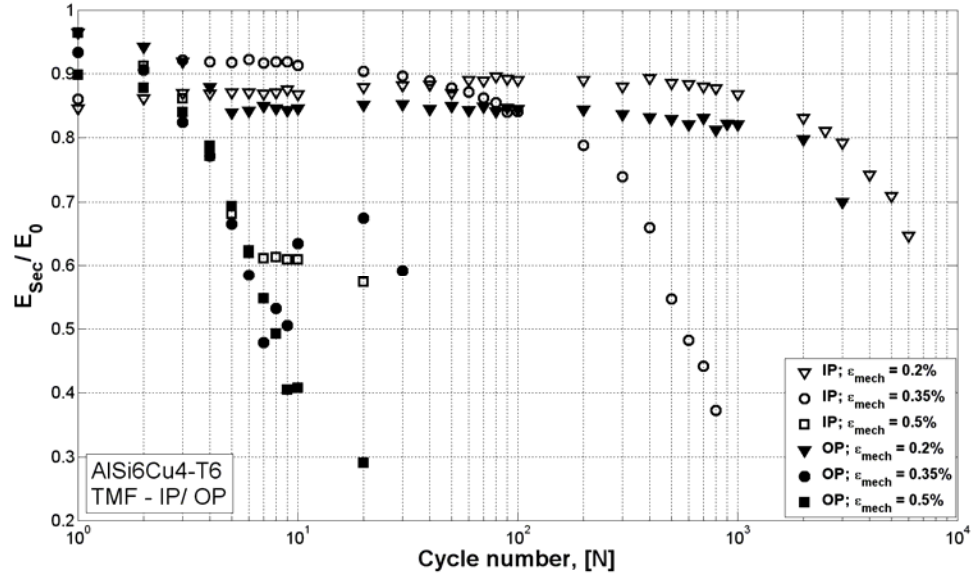


**Figure 6.29:** Evolution of damage based on secant modulus for AlSi6Cu4-T6 under IP and OP-TMF loading.

The scatter at higher strain amplitudes limits the usefulness of the relationship between secant modulus and cycle number. Another approach, is shown in Figure 6.30, which plots the average damage per cycle ( $dD/dN$ ) as a function of the mechanical strain amplitude in a double logarithmic plot. The plots are roughly linear in the log-log plot and the best fit lines are shown in Table 6.8.



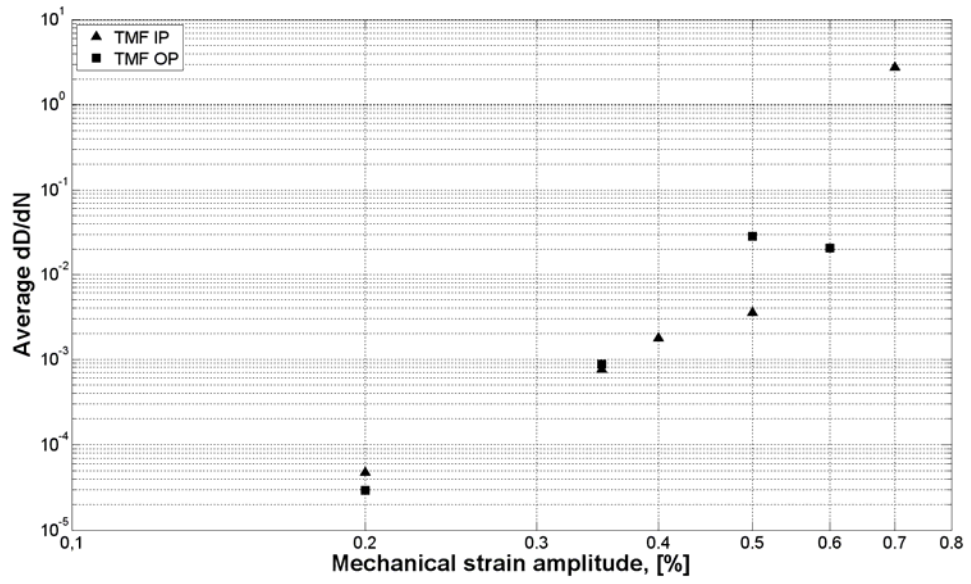


**Figure 6.30:** Average damage per cycle vs. mechanical strain amplitude of AlSi6Cu4-T6 under IP and OP TMF loading.

**Table 6.8:** Best fit lines for average damage per cycle.

Damage	Function	R <sup>2</sup>
IP-TMF	$dD/dN = 6.104 \varepsilon_{mech}^{8.04}$	0.96
OP-TMF	$dD/dN = 1.06 \varepsilon_{mech}^{6.51}$	0.99

Using the relationships in Table 6.8, the fatigue life can be predicted as follows:

$$\frac{dD}{dN} = C \cdot \left( \frac{\Delta \varepsilon}{2} \right)^m \quad (22)$$

$$\log \left( \frac{dD}{dN} \right) = m \cdot \log \left( \frac{\Delta \varepsilon}{2} \right) + \log C \quad (23)$$

$$\int_0^1 dD = \int_0^N C \cdot \left( \frac{\Delta \varepsilon}{2} \right)^m \cdot dN \quad (24)$$

$$1 = C \cdot \left( \frac{\Delta \varepsilon}{2} \right) \cdot N_f \quad (25)$$

$$N_f = \frac{1}{C \cdot \left( \frac{\Delta \varepsilon}{2} \right)^m} \quad (26)$$

The hysteresis area relationship of Schütz [293] and Christ [215], which follows the gradient in the hysteresis loop between  $\sigma_{\varepsilon=0}$  and  $\sigma_{\varepsilon=\varepsilon_{max}}$ , was extended to include the relationship between  $\varepsilon_{\sigma=0}$  and  $\varepsilon_{\sigma=\sigma_{max}}$ , so that not only the change in the hardening or relaxation is considered but also the increase of inelastic strain with increasing cycle time. Following the description of the hysteresis loop by Löhe [217], which explains the microstructural effects which occur during tensile and compressive stresses during one cycle (Figure 3.9), further damage factors can be derived from certain angles in the hysteresis loop. Figure 6.31 gives schematic examples of angles in the upper area of the hysteresis loop (green and pink lines) indicating the different forms the hysteresis loop can take during the lifetime. The red line represents the hardening coefficient, which can also be used, although it does not permit the specific allocation of changes to the controlled strain. The angles which need to be defined for every material and temperature range are a characteristic of damage per cycle and can include creep, relaxation, strengthening and softening or cracking within a cycle and can therefore be accumulated in the same way as was the secant modulus or used to consider the stiffness in the tensile and compressive areas of the loop.

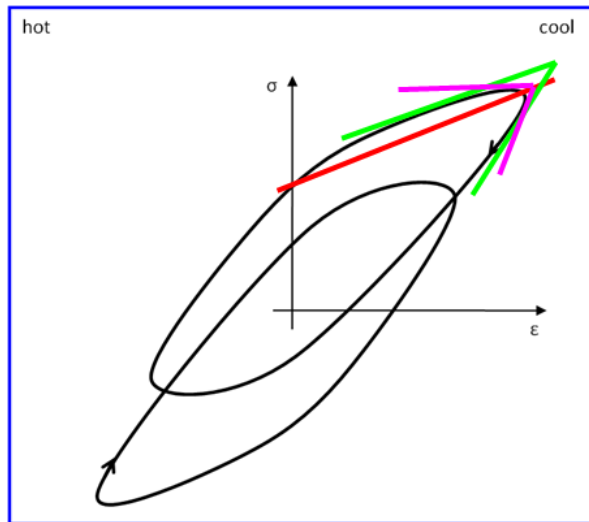


**Figure 6.31:** Specific angles of interest in hysteresis loop under TMF loading.

Figure 6.32 shows the evolution of one of the angular damage parameters and illustrates what happens when a specimen fractures. Here, the drop in the upper angle confirms that the specimen fractured, indicated by a major distortion of the hysteresis loop.

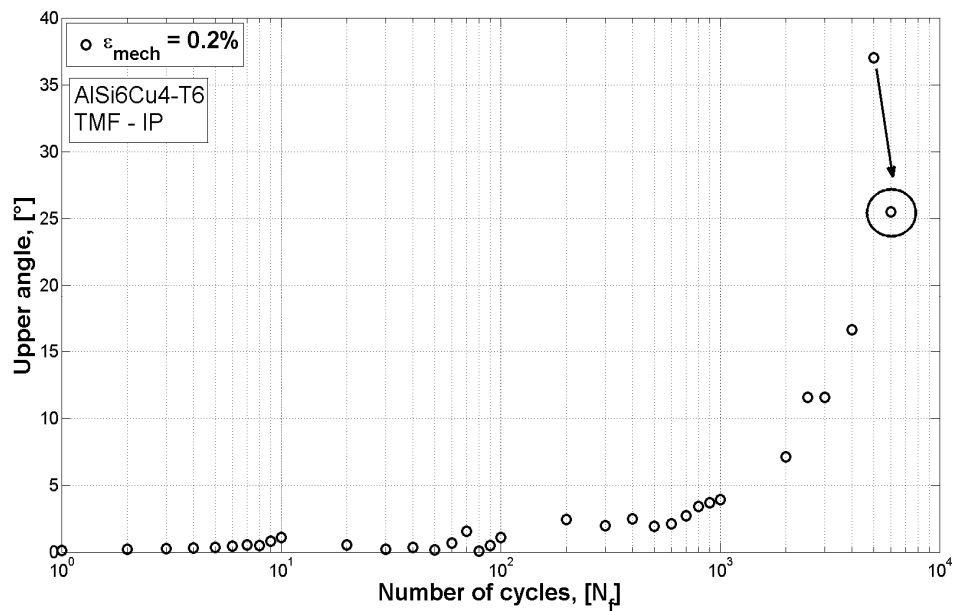


**Figure 6.32:** Example evolution of the upper angle of the hysteresis loop during the lifetime of the reference alloy under IP-TMF loading. The circled point shows the fracture of the specimen.

The change of the upper angle for these types of aluminium alloys during lifetime can only be calculated for small strain amplitudes. The higher strain amplitudes did not

show large enough changes during lifetime to be attributed to overageing, creep or relaxation so that, in the following, this type of damage parameter is neglected. However, this damage parameter could be a helpful alternative for other types of alloys or test parameters on aluminium alloys.

A comparison of all damage parameters and damage factors, shown in Figure 6.33 for IP loading and Figure 6.34 for OP loading, on the reference alloy in its reference state (AlSi6Cu4-T6) revealed that the least scatter between predicted lifetime and measured cycles to failure is obtained with the damage parameter of Ostergren ( $P_{Ost}$ ). Figure 6.35 shows a comparison between all the alloys and conditions using this parameter.

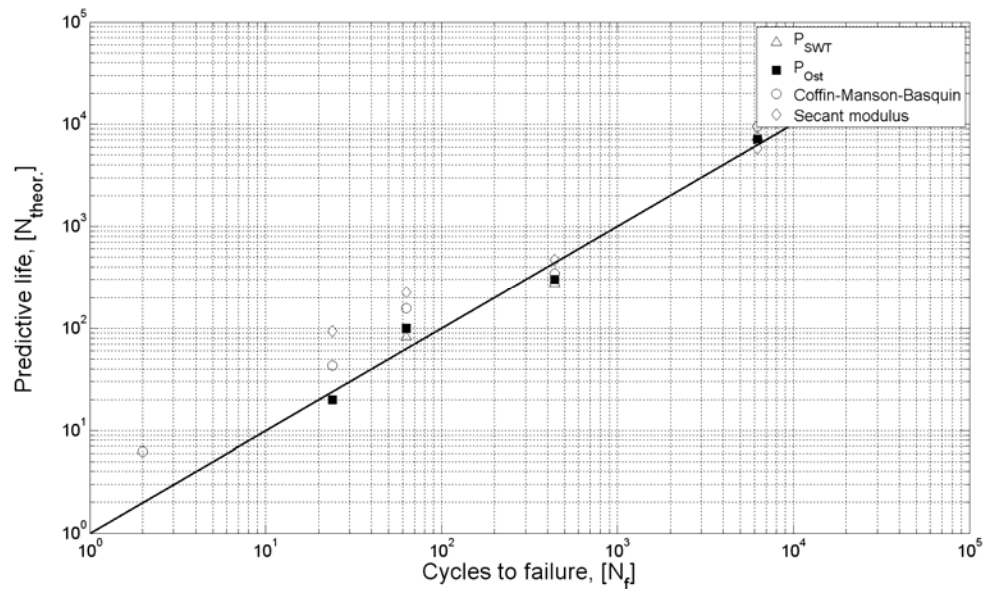


**Figure 6.33:** Predicted life vs. experimentally determined cycles to failure under IP TMF loading of AlSi6Cu4-T6.

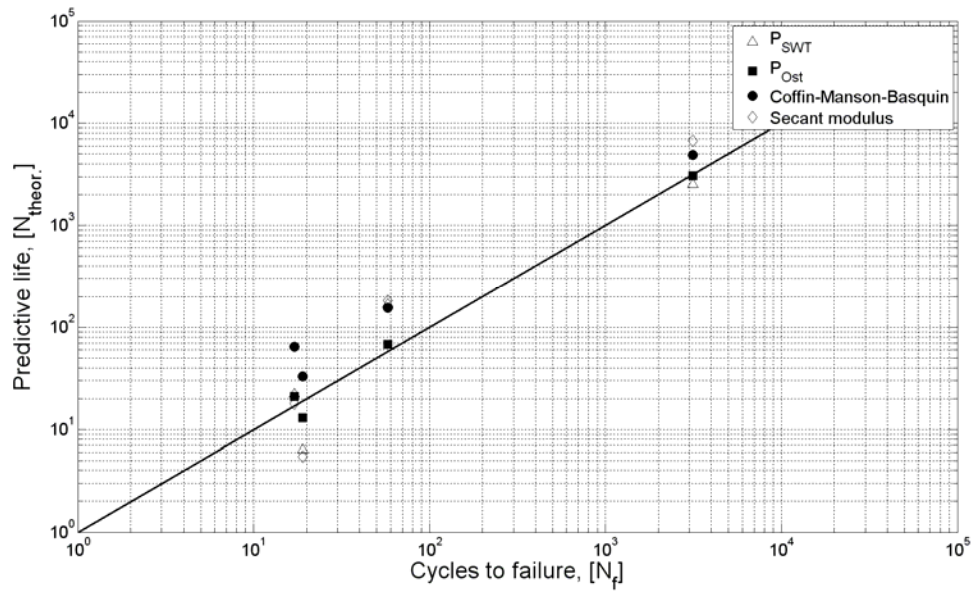


**Figure 6.34:** Predicted life vs. experimentally determined cycles to failure under OP TMF loading of AlSi6Cu4-T6.

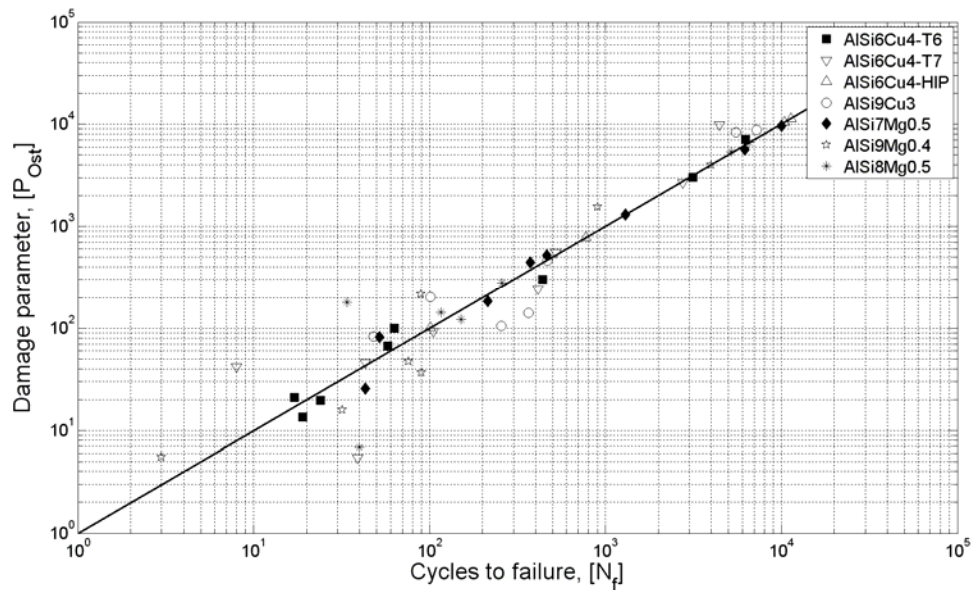


**Figure 6.35:** Damage parameter of Ostergren for all tested alloys under TMF loading.

In order to compare literature data with data and alloys determined in this thesis, Figure 6.36 shows measured data vs. a lifetime calculation based on the method of Manson-Coffin-Basquin (Equation 13). Using this approach, the T7 and T6 conditions for AlSi6Cu4 show a larger deviation from the “ideal” line than was the case using the Ostergren damage parameters. This is because Equation 13 (Manson-Coffin-Basquin)

uses parameters for the penultimate cycle  $N=N_{f-1}$  and  $P_{Ost}$  uses data from  $N=10$  so that different evolutions of inelastic strain can take place.

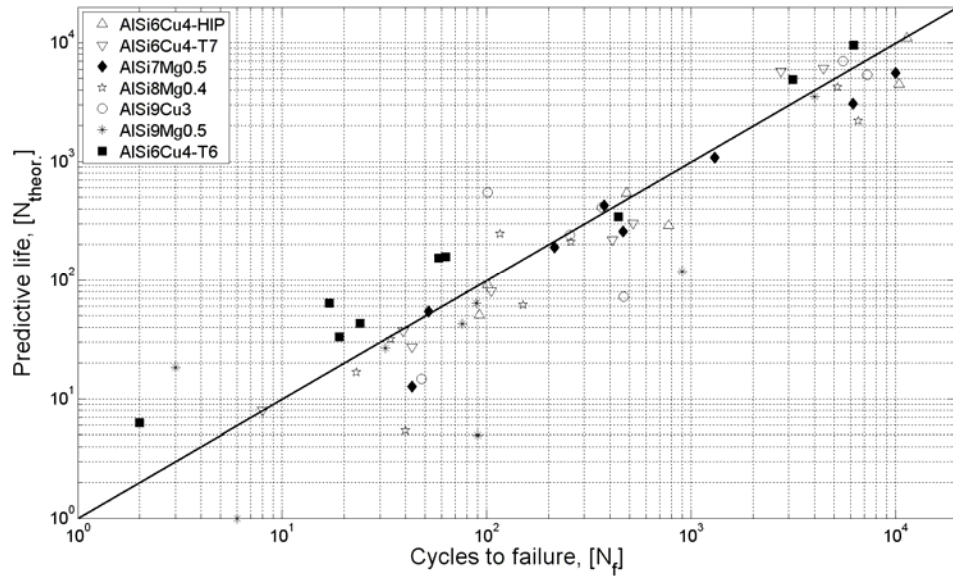


**Figure 6.36:** Measured cycles to failure vs. predicted life using the Manson-Coffin-Basquin equation for all tested alloys under TMF loading.

#### 6.10.4 Application to cylinder head geometry

A published temperature distribution between 200°C and 400°C [294] (Figure 6.37) was used to simulate the IP and OP-TMF stresses in a cylinder head geometry with the Ansys TMF elasto-plastic Chaboche model, which is used above. As can be seen in Figure 6.38, the highest thermal stresses for OP loading lie between the injection nozzle and the exhaust valve.

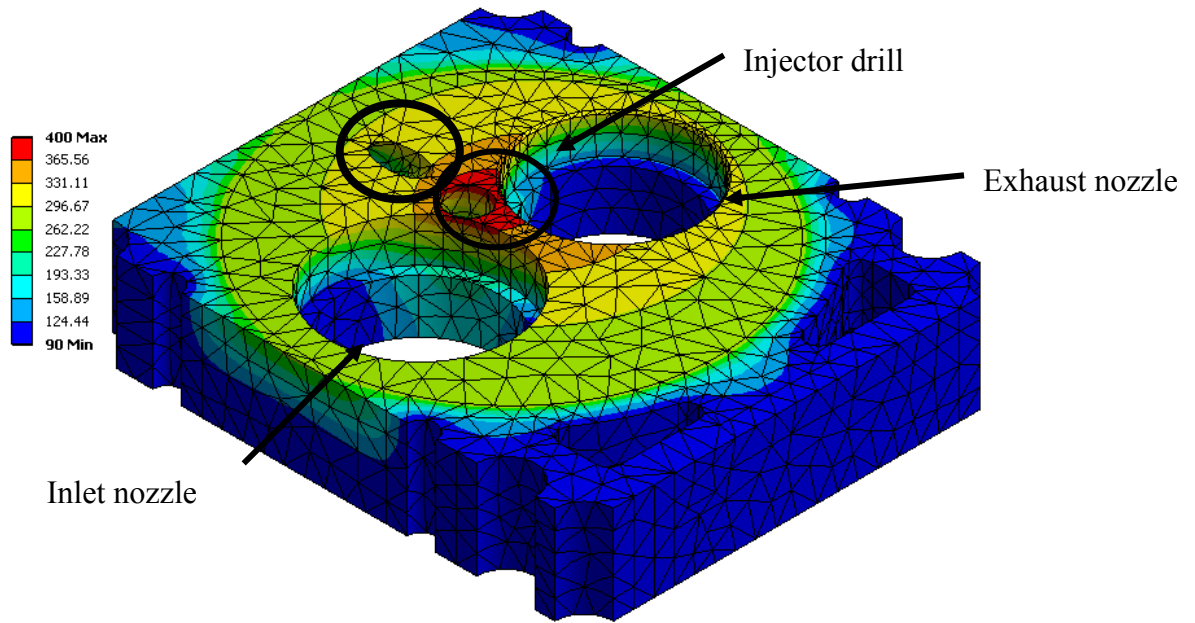


**Figure 6.37:** Cylinder head geometry showing the temperature distribution under OP-TMF loading at 400°C.

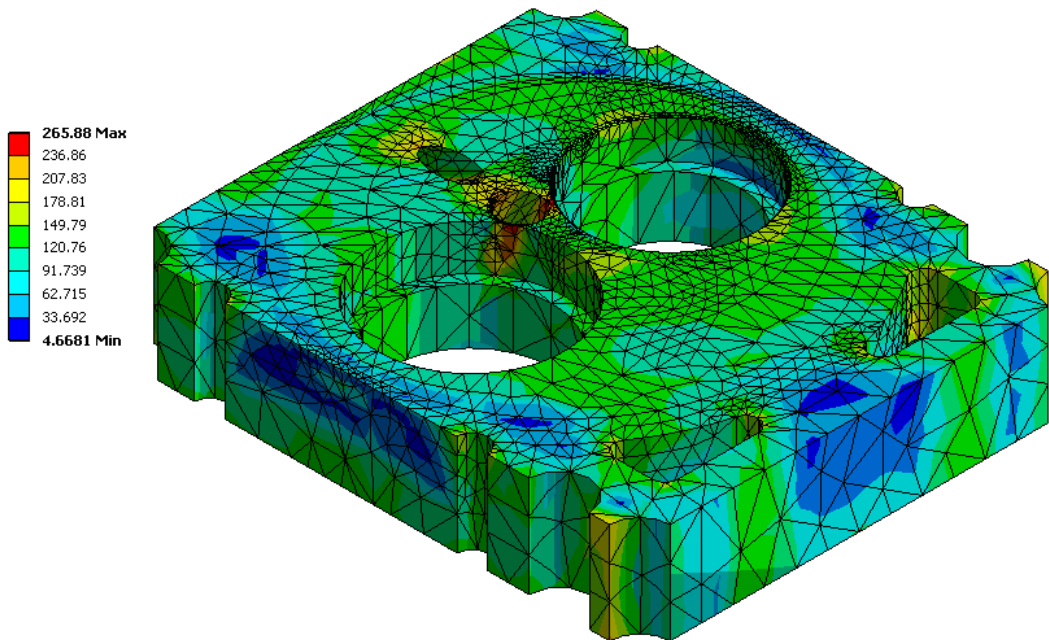


**Figure 6.38:** Results for equivalent stress (von Mises, in MPa) with the global elastic-plastic material model.

Under TMF loading, inelastic strains can be observed between the valve seat and the injector drill and also in the area of the glow plug. The material parameters determined in this work were used with yield stresses in the temperature range 20°C-400°C varying between 231MPa down to 115MPa for this simulation. Figure 6.39 shows a



microstructural observation of a cylinder head with cracks in the areas mentioned above.

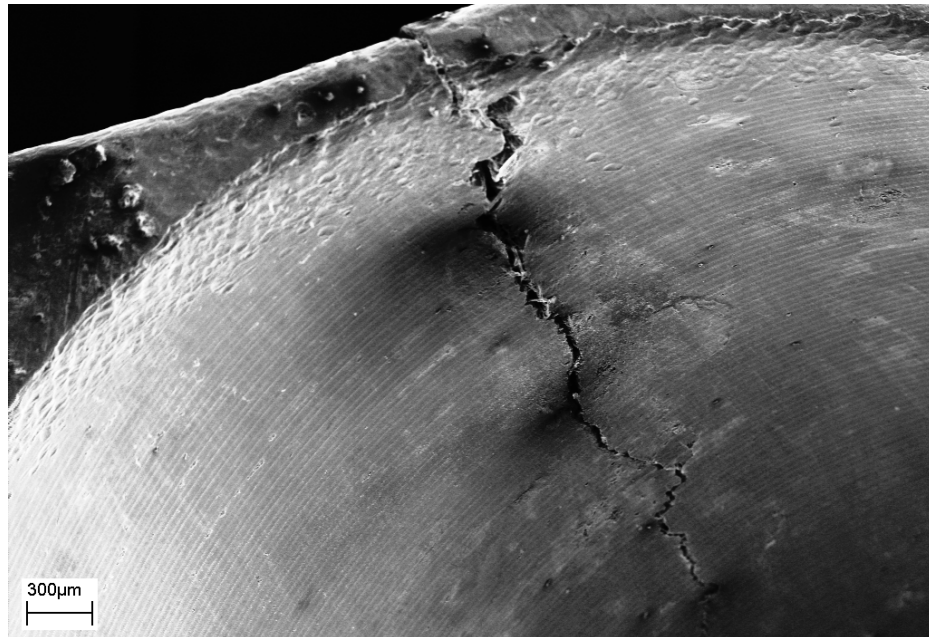


**Figure 6.39:** Crack at the valve bridge of a cylinder head after TMF loading.

The FE Modelling explained above was further extended to a lifetime prediction using the software **FEMFAT**. As an initial step, lifetime was predicted with an ordinary specimen geometry (Figure 4.1) using the elasto-plastic Ansys material model explained above. Next a fatigue calculation on the above mentioned cylinder head geometry was done considering temperature and mean stress development. The calculation [295] determines the cumulative damage using a Miner sum and shows (Figure 6.40) lower safety factors against fatigue fracture in the area between the inlet and injection drillings because of the local plastic deformation. Furthermore, lower safety factors can be identified in the area of the exhaust valve.



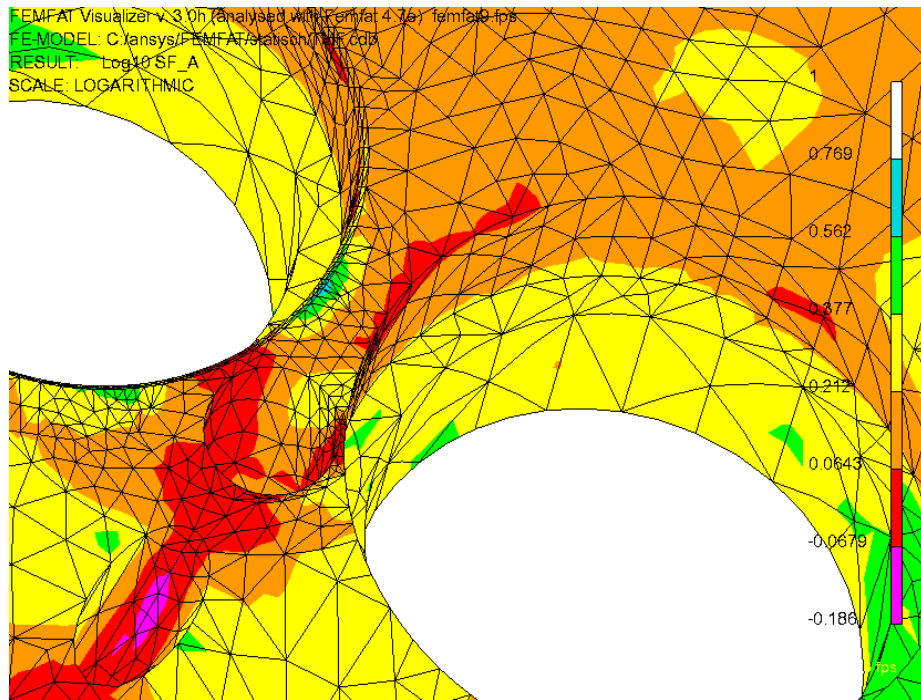


**Figure 6.40:** Results from FEMFAT for fatigue damage (logarithmic scale) applied to cylinder head geometry.

## **CHAPTER 7 - CONCLUSIONS**

The work in this thesis has made contributions to knowledge in four key areas related to aluminium alloy selection and development for an enhanced high temperature specification (temperature range 200-400°C) of automotive engine structures:

1. Observations on the thermally activated processes in Al-Si casting alloys,
2. Assessment of how these processes affect damage evolution under elevated temperature fatigue loading,
3. Development of damage evolution models under TMF for a range of candidate alloys and treatments,
4. A recommendation as to how the findings of this work might be incorporated into the design, material selection and simulation of automotive cylinder heads.

### **7.1 EFFECT OF ALLOYING AND TREATMENT ON RESPONSE TO THERMAL EXPOSURE**

The temper, CER and creep tests have together elucidated the effect of alloy composition and treatment on thermally activated processes going on in candidate casting alloys and the effect that these have on microstructure and mechanical properties. The main microstructural features which changed with alloying and treatment were:

- The volume fraction and morphology of eutectic silicon
- The volume fraction, coherency and average size of precipitation hardening phases (associated with Cu and Mg/Si additions)
- The size of the aluminium grains (as measured by SDAS)
- The amount and average size of pores

Each of these features can change with time during thermal exposure and a comparison to the reference alloy allows the following conclusions to be drawn:

7.1.1 Quite surprisingly, increasing eutectic Si volume fraction resulted in a decrease in both yield stress and work hardening rate at 400°C. The increased Si volume fraction results in more angular Si particles leading to an increased tendency to brittle fracture. Also, there is a nonconformity resulting from the

different thermal expansion coefficients between Si and the  $\alpha$ -matrix and higher stiffness of the Si particles giving enhanced decohesion at higher Si contents. The effect of Si content between the reference alloy and AlSi9Cu3 is obscured by both the change in SDAS and by the change in Cu content. The increased Si content results in little change in yield stress at 400°C, but in a very large increase in work-hardening rate, most likely due to the reduced SDAS.

7.1.2 The amounts of Mg and Cu influence the volume fraction of precipitation hardening phases and also their response to heat treatment and high temperature exposure. Although Si is involved in the formation of the precipitation phase in the Al-Mg-Si alloys, it is always present in significant excess over the amount required to bond with all of the Mg. The temper tests carried out on the reference alloy (Cu as precipitation hardening addition) showed that, for a 400°C exposure, the hardness had fallen to the same low value within 1hr, irrespective of whether the alloy started in the T6 or T7 condition. For the 200°C exposure, complete overageing was delayed to about 100hr for an initial T6 condition, less for an initial T7 condition. These changes in hardness were broadly what one would expect for precipitation-hardening aluminium alloys and the degradation of hardness could be fit by a Boussac-Calais model with parameters  $A=3.2056$ ,  $B=1.3801$ ,  $C=28.8023$  for 200°C and  $A=18.0358$ ,  $B=2.5$ ,  $C=105.897$  for 400°C. These effects are reflected in the CERT behaviour of the reference alloy in the two conditions. While the equilibrium  $Al_2Cu$  volume fraction is 0.038, that of  $Mg_2Si$  in the Al-Si-Mg alloys ranges between 0.0063 and 0.01. The work-hardening rate and yield stress at 400°C for the reference alloy in the T6 condition and AlSi7Mg0.5-T6 are about the same, suggesting that 0.5%Mg has about the same effect on high temperature mechanical properties as does 4%Cu.

7.1.3 As well as affecting ageing, both the T7 heat treatment and longer time exposures lead to grain growth. This is seen as a reduction in yield strength with little effect on work hardening rate at both 200 and 400°C in the CER tests for the reference alloy in the T6 and T7 conditions. HIP treatment reduces the amount of porosity and the size of the pores, and also causes a minor amount of overageing. The consolidation increases proof stress and work hardening rate at both 200 and 400°C despite the overageing.

## 7.2 HIGH TEMPERATURE FATIGUE BEHAVIOUR

The LCF and TMF tests carried out on the reference alloy allow the following conclusions to be drawn on the effect of thermally activated processes on high temperature fatigue behaviour.

7.2.1 Starting in the T6 condition, the overageing in a subsequent 400°C exposure takes place in a very short time so that the ductility is increased and, provided that a fixed mechanical strain amplitude is applied, lower stresses and longer lifetimes result over those at 200°C. The grain coarsening which occurs at 400°C also leads to delayed creep pore formation and so to longer lifetimes. The difference between the brittle behaviour at 200°C and the ductile behaviour at 400°C results in a change of the cyclic stress-strain behaviour and of crack initiation mechanisms. At 200°C hardening mechanisms dominate, based on fracture in the Si, whereas, at 400°C, a change to fracture of the  $\alpha$ -matrix and particle decohesion takes place. Under TMF between 200°C and 400°C, the cyclic stress-strain behaviour resembles that at 400°C, rather than being midway between 200°C and 400°C, indicating a sharp transition between 200°C and 300°C, probably associated with overageing. There is little difference between the IP and OP TMF behaviour, indicating that this transition is associated more with the state of the alloy than the instantaneous temperature of deformation.

7.2.2 Pre-tempering of the reference alloy to T7 leads to improved TMF lifetimes at high strain amplitudes, but essentially the same lifetime at low strain amplitudes. This is due to the fact that the TMF exposure leads to overageing in a relatively short time, so this pre-treatment will only have a substantial effect when the TMF exposure is short. The consolidation effect of the HIP treatment, on the other hand, leads to improved lifetimes at all strain amplitudes, essentially because of the reduction in the number and sizes of crack-initiating pores.

The TMF tests carried out on the reference alloy and other alloys in the T6 condition allows the following conclusions to be drawn on the effect of alloying on high temperature fatigue behaviour.

7.2.3 In the Al-Mg-Si alloys (which all have essentially the same amount and type of precipitation hardening) the stress amplitude during TMF is consistently higher for a given strain amplitude as the Si content increases. The fatigue life also increases with decreasing Si content, this because of the reduced number of crack initiation sites. There is a tendency for fatigue lives to converge at lower strain amplitudes and this effect is more pronounced with the IP tests, indicating that accommodation between the Si and the matrix is important in combating the detrimental effect of a higher Si content.

7.2.4 The AlSi7Mg0.5 alloy shows a much better TMF life than does the AlSi6Cu4, both in the T6 condition. This difference can only be attributed to the different precipitation hardening effects, since the increased Si would be expected to have the opposite effect. Again, there is a tendency for fatigue lives to converge at lower strain amplitudes and again more pronounced with the IP tests, indicating that the accommodation may be affecting hard precipitates in the same way as it does for hard Si particles.

7.2.5 The lower volume fraction of Al<sub>2</sub>Cu in AlSi9Cu3 influences the inelastic strain more than the refinement induced by the lower SDAS does so that AlSi9Cu3 permits higher inelastic strains during the TMF lifetime and longer fatigue life.

### 7.3 DAMAGE EVOLUTION MODELS

7.3.1 The TMF lifetimes measured here can conveniently be described using a Manson-Coffin-Basquin relationship:

$$\varepsilon_{a,t} = \varepsilon_{a,el} + \varepsilon_{a,p} = \frac{c_1}{E} \cdot (2N_f)^{-c_2} + c_3 (2N_f)^{-c_4} \quad (27)$$

The coefficients for the seven alloys/ treatments under IP and OP loading are listed in Table 7.1.

**Table 7.1:** Summary of Manson-Coffin-Basquin lifetime parameters for Al-Si-Cu and Al-Si-Mg alloys tested under TMF.

Alloy	$c_1/E$	$c_2$	$c_3$	$c_4$
AlSi6Cu4-T6 IP	0.004486	-0.138366	0.005203	-0.212994
AlSi6Cu4-T6 OP	0.002090	-0.011705	0.073096	-0.766956
AlSi6Cu4-T7 IP	0.021395	-0.41208	0.001611	-0.016551
AlSi6Cu4-T7 OP	0.010048	-0.267873	0.001312	-0.028025
AlSi6Cu4-HIP IP	0.005699	-0.222540	0.005507	-0.189068
AlSi6Cu4-HIP OP	0.007954	-0.291779	0.005360	-0.138819
AlSi9Cu3 IP	0.008296	-0.257839	0.004216	-0.146481
AlSi9Cu3 OP	0.059743	-0.453924	0.011190	-0.308499
AlSi7Mg0.5 IP	0.007204	-0.200377	0.005501	-0.285202
AlSi7Mg0.5 OP	0.075564	-0.487670	0.001675	-0.075504
AlSi8Mg0.4 IP	0.006488	-0.217588	0.00321	-0.146142
AlSi8Mg0.4 OP	0.007902	-0.236914	0.006591	-0.286524
AlSi9Mg0.5 IP	0.003752	-0.140911	0.002496	-0.13729
AlSi9Mg0.5 OP	0.187174	-1.255679	0.003566	-0.177135

7.3.2 The TMF stress-strain results were also used to generate a series of damage parameters  $\frac{dD}{dN}$  for various cumulative damage equations. A comparison of these equations indicated that the parameter of Ostergren gave the best prediction of lifetime for TMF in the temperature range 200°C to 400°C when fit to a curve of the form  $\frac{dD}{dN} = a\varepsilon_{mech}^b$ . Table 7.2 summarises the values of  $a$  and  $b$  for the alloys and conditions tested.

**Table 7.2:** Summary of the parameters for the equation line of the damage parameter of Ostergren for Al-Si-Cu and Al-Si-Mg alloys tested under TMF.

<b>Alloy</b>	<b>Loading</b>	<b>a</b>	<b>b</b>
AlSi6Cu4-T6	IP	0.82	-0.16
	OP	0.9	-0.19
AlSi6Cu-T7	IP	2.03	-0.29
	OP	0.82	-0.15
AlSi6Cu4-HIP	IP	1.47	-0.22
	OP	1.23	-0.194
AlSi9Cu3	IP	1.53	-0.22
	OP	2.07	-0.26
AlSi7Mg0.5	IP	1.42	-0.23
	OP	3.44	-0.31
AlSi8Mg0.4	IP	1.0	-0.195
	OP	0.92	-.215
AlSi9Mg0.5	IP	1.1	-0.19
	OP	1.064	-0.191

#### **7.4 IMPLICATIONS OF THE WORK FOR THE DESIGN, MATERIAL SELECTION AND SIMULATION OF AUTOMOTIVE CYLINDER HEADS**

Based on the simulations and the TMF results, it is recommended that the following aspects are considered for enhanced high-temperature performance of car cylinder heads:

7.4.1 Increasing test temperature can increase TMF lifetimes so that a reduction of component temperature, brought about, for example, by increasing cooling channel size or improving conduction paths, does not necessarily result in reduced damage.

7.4.2 Components or areas which experience high strain amplitudes/ loadings should be subjected to a HIP procedure to reduce porosity. This would require

developments to reduce the cost and to integrate a HIP procedure into the mass production process for highly loaded cast components (e.g. cylinder heads).

7.4.3 A T7 heat treatment enhances ductility and reduces creep-dominated fatigue.

7.4.4 More effort should be expended to produce higher cooling rates when casting engine parts in order to reduced the SDAS.

7.4.5 Simulations based on CER tests (Ansys) and with the 10 parametric model of Chaboche are representative and reflect the TMF behaviour of aluminium alloy components very well.

7.4.6 For both the IP and OP-TMF loading simulations, it was observed that pores blunt more at 400°C than they do at 200°C. This means that a HIP procedure offers more benefit for lower temperature than higher temperature component, for a given strain amplitude.



## REFERENCES

1. Gemeinschaft, K.d.e. (2008) *Ergebnisse der Überprüfung der Strategie der Gemeinschaft zur Minderung der CO2 Emissionen von Personenkraftwagen und leichten Nutzfahrzeugen*. DOI: [www.uni-mannheim.de/edz/pdf/sek/2007/sek-2007-00190de.pdf](http://www.uni-mannheim.de/edz/pdf/sek/2007/sek-2007-00190de.pdf)
2. Fergusson, M., et al., *Possible Regulatory Approaches to Reducing CO2 Emissions from Cars*. European Environmental Policy, 2007. **070402/2006/452236/MAR/C3**: p. 1-57.
3. Commission, E., *Review of the EU strategy to reduce CO2 emissions and improve fuel efficiency from cars*, D.G. Environment, Editor. 2006. p. 1-16.
4. Armstrong, G.L., *Alloy Selections for Automotive Aluminum Castings*. SAE, 1987. **780249**.
5. Palazzo, F., *The future of Aluminium in the Automotive Industry*. *Alluminio* 1977. **9**: p. 323-334.
6. van Basshuysen, R. and F. Schäfer, *Handbuch Verbrennungsmotoren*. Vol. 2. 2002: Vieweg.
7. von Rüden, K., *Beitrag zum Downsizing von Fahrzeug-Ottomotoren*. *Dissertation, in Verkehrs- und Maschinensysteme*. 2004: Technische Universität Berlin. p. 1-144.
8. Rudolph, F., et al., *The new 1.6l TDI engine from Volkswagen*, in *30<sup>th</sup> International Engine symposium*. 2009: Vienna. p. 82-102.
9. Korte, V., D. Hancock, and H. Blaxill, *The Mahle Downsized Engine as Technology Demonstrator - Concept, Layout and Design*. *MTZ*, 2008. **69**(01).
10. Hoffmann, H., et al., *Cylinder Deactivation for Valve Trains with Roller Finger Follower*. *MTZ*, 2009. **70**(04): p. 7-11.
11. Claus, J., H. Gese, and H. Voggenreiter, *Aluminium-Legierungen im Zylinderkopf und Kolben - eine Herausforderung für Motoren der Zukunft*, in *Anforderung der Automobilindustrie*, E. Ambos, Editor. 2001, VDI: Magdeburg. p. 17-30.
12. Klan, S., *Beitrag zur Evolution von Aluminium-Gusslegierungen für warmfeste Anwendungen*. *Dissertation*. 2004: Universität Freiberg. p. 1-190.
13. Heikel, C., *Werkstoff- und verfahrenstechnische Bewertung von Zylinderköpfen für Dieselmotoren*. *Dissertation, in Mechanical Engineering*. 2005: Otto von Guericke Universität Magdeburg. p. 1-136.
14. Minichmayr, R., *Modellierung und Simulation des thermomechanischen Ermüdungsverhaltens von Aluminiumbauteilen*. *Dissertation, in Product Engineering*. 2005, Montanuniversität Leoben. p. 1-274.

15. Leitner, H., *Simulation des Ermüdungsverhaltens von Aluminiumgusslegierungen. Dissertation.* 2001, Montanuniversität Leoben.
16. Hamm, T., et al., *Zylinderkopfkonzeppte für hohe Spitzendrücke.* MTZ, 2007. 6: p. 526-533.
17. Langmayr, F., M. Howlett, and W. Schöffmann, *Zylinderkopf Konzeption in Abhängigkeit der Werkstoffauswahl,* in *Ventiltrieb und Zylinderkopf.* 2006, VDI Berichte: Leonberg. p. 101-117.
18. Marckwardt, H., *Messtechnische Analyse der thermomechanischen Belastung von Zylinderköpfen. Dissertation.* 1999: Rheinisch Westfälische Technische Hochschule Aachen.
19. Pieper, M., *Konstruktion von Zylinderköpfen für Hochleistungsmotoren in Großserien. Dissertation.* 1992: Rheinisch Westfälische Technische Hochschule Aachen.
20. Widder, T., *Oberflächenmodifikationen und Werkstoffsubstitutionen zur Verbesserung des thermischen Beanspruchungsverhaltens von speziellen Aluminiumlegierungen am Beispiel von Zylinderköpfen für Wirbelkammerdieselmotoren. Dissertation.* 1996: Universität Kaiserslautern.
21. Maaßen, F., M. Loeprecht, and A. Egner-Walter. *Analytical Optimization of Highly Loaded Aluminum Cylinder Heads - Durability Testing Simulation.* in *Aachener Kolloquium Fahrzeug- und Motorentechnik.* 2000.
22. Grzincic, M., *Gießvorgänge beim Kokillenguss von Al-Legierungen. Dissertation.* 2003: Otto von Guericke Universität Magdeburg. p. 1-120.
23. Hoepke, E., et al., *Nutzfahrzeugtechnik.* Vol. 5. 2008: Vieweg Teubner.
24. Köhler, E. and R. Flierl, *Verbrennungsmotoren.* Vol. 5. 2009: Vieweg Teubner.
25. Albert, M., *Werkstoffverhalten unter thermomechanischer Beanspruchung am Beispiel des Zylinderkopf-Ventilsteges. Dissertation.* 1979: Technische Universität Darmstadt.
26. Hoag, K.L., *Vehicular Engine Design.* 2006: Springer.
27. Zima, S., *Motorkolben.* Vol. 1. 2005: Vieweg Teubner.
28. Velji, A., *Der Konflikt zwischen Thermodynamik und Mechanik in der Motorentwicklung.* 2006: Expert Verlag.
29. Urlaub, A., *Verbrennungsmotoren.* 1994: Springer.
30. Krüger, M., *Untersuchung zur thermischen Bauteilbelastung kleiner schnelllaufender Dieselmotoren mit indirekter und direkter Einspritzung. Dissertation.* 1995: Rheinisch Westfälische Technische Hochschule Aachen

31. Loeprecht, M., *Berechnungsverfahren zur Betriebsfestigkeit von Diesel-Zylinderköpfen aus Aluminium. Dissertation.* 2001: Rheinisch Westfälische Technische Hochschule Aachen.
32. Oberbuchner, M., *Damage Analysis of a 1.9 TDI PDE Diesel Engine*, in *LWM.* 2010, University of Applied Sciences: Regensburg. p. 1-72.
33. Babes, F. and J. Gobrecht, *Legierungsoptimierung bei luftgekühlten Aluminium-Zylinderköpfen mittels technologischer Prüfverfahren*, in *7. Internationale Leichtmetalltagung* 1981: Braunau-Ranshofen. p. 208-209.
34. Andrews, J.B. and M.V.C. Seneviratne, *A New, Highly Wear-Resistant Aluminum-Silicon Casting Alloy for Automotive Engine Block Applications.* AFS Transactions, 1984. **92**: p. 209-216.
35. Jonason, P., *Thermal Fatigue of Cylinder Head Alloys.* AFS Transactions, 1992. **92-160**: p. 601-607.
36. Nagayoshi, T. and T. Kodaira, *Analysis of Thermal Fatigue Cracks in Cylinder Heads.* JSAE, 1993. **14**: p. 56-60.
37. Vertin, K.D., C.L. Haller, and S. Lubnow, *A Root Cause Investigation of Cylinder Head Cracking in Large Diesel Engine Standby Power Generators.* SAE, 1995. **950518**: p. 1-12.
38. Koch, F., et al., *Low Cycle Fatigue of Aluminum Cylinder Heads - Calculation and Measurement of Strain under Fired Operation.* SAE, 1999. **1999-01-0645**: p. 43-52.
39. Lee, K.S., et al., *Measurements and Predictions of Steady-State and Transient Stress Distributions in a Diesel Engine Cylinder Head.* SAE, 1999. **1999-01-0973**: p. 1-10.
40. Takahashi, T., Y. Sugimura, and K. Sasaki, *Thermal Plastic-Elastic Analysis in Consideration of Metallurgical Microstructure.* Journal of Manufacturing Science and Engineering, 2004. **126**(1): p. 25-32.
41. Ganser, J., H. Blaxill, and A. Cairns, *High-load EGR in a Turbocharged Gasoline Engine.* MTZ, 2007. **68**(07-08).
42. GDA, *Heat treatment of Aluminium alloys.* 2008: GDA.
43. Aluminium-Zentrale, *Die Wärmebehandlung von Aluminiumgusslegierungen.* 2008, Aluminium-Zentrale.
44. Kammer, C., *Aluminium Taschenbuch II.* Vol. 15. 1996: Aluminium-Verlag.
45. Mondolfo, L.F., *Aluminium Alloys.* 1976, London: Butterworth.
46. Flaig, B., *Isothermes und thermisch-mechanisches Ermüdungsverhalten von GK-AlSi10Mg wa, GK-AlSi12CuMgNi und GK-AlSi6Cu4. Dissertation.* 1995: Universität Karlsruhe.

47. Altenpohl, D., *Aluminium von innen*. Vol. 5. 2005: Aluminium-Verlag.
48. Brunhuber, E. and S. Hasse, *Giesserei Lexikon*. 1988, Schiele & Schoen.
49. Kim, J.M., et al., *Porosity Formation in Relation to the Feeding Behavior of Al-Si Alloys*. AFS Transactions, 1997. **105**: p. 825-831.
50. Riedler, M., *Methodikfindung zur Simulation von thermomechanisch beanspruchten Motorbauteilen aus Aluminiumlegierungen*. Dissertation, in *Product Engineering*. 2005: Montanuniversität Leoben. p. 1-303.
51. Djurdjevic, M., et al., *Quantification of the Impact of Strontium on the Solidification Path of the Aluminum-Silicon-Copper Alloys Using Thermal Analysis Technique*. Practical Metallography, 2009. **46**: p. 137-152.
52. Gupta, A.K., D.J. Lloyd, and S.A. Court, *Precipitation hardening in Al-Mg-Si alloys with and without excess Si*. Materials Science & Engineering A, 2001. **316**: p. 11-17.
53. Johnsson, M., *Grain refinement of aluminium studied by use of a thermal analytical technique*. Thermochemica Acta, 1995. **256**: p. 107-121.
54. Khomamizadeh, F. and A. Ghasemi, *Evaluating of Quality Index of A-356 Aluminum Alloy by Microstructural Analysis*. Scientia Iranica, 2004. **11**(4): p. 386-391.
55. Wang, Q.G., *Effects on the Tensile and Fracture Behavior of Aluminum Casting Alloys A356/357*. Metallurgical and Materials Transactions A, 2003. **34**: p. 2887-2899.
56. Boileau, J.M., et al., *The Dimensional Stability of Cast 319 Aluminum*. SAE International, 2003. **2003-01-0822**: p. 79-84.
57. Boileau, J.M., et al., *The Effect of Porosity Size on the Tensile Properties of a Cast 319-T7 Aluminum Alloy*. AFS Transactions, 2001. **01-045**: p. 419-432.
58. Tash, M., et al., *Effect of metallurgical parameters on the hardness and microstructural characterisation of as-cast and heattreated 356 and 319 aluminum alloys*. Materials Science & Engineering A, 2007. **443**: p. 185-201.
59. Thirugnanam, A., et al., *Effect of Mg on the fracture characteristic of cast Al-7Si-Mg alloys*. Materials Science & Engineering A, 2007. **445-446**: p. 405-414.
60. Ouellet, P. and F.H. Samuel, *Effect of Mg on the ageing behaviour of Al-Si-Cu 319 type aluminium casting alloys*. Journal of Materials Science, 1999. **34**: p. 4671-4697.
61. Caceres, C.H., et al., *The effect of Mg on the microstructure and mechanical behavior of Al-Si-Mg casting alloys*. Metallurgical and Materials Transactions A, 1999. **30**: p. 2611-2618.

62. Taylor, J.A. *The effect of Iron in Al-Si Casting Alloys*. in *35th Australian Foundry Institute National Conference*. 2004.
63. Sreeja Kumari, S.S., R.M. Pillai, and B.C. Pai, *A study on the structural, age hardening and mechanical characteristics of Mn and Ca added Al-7Si-0.3Mg0.6Fe alloy*. *Journal of Alloys and Compounds*, 2008. **453**: p. 167-173.
64. Hwang, J.Y., H.W. Doty, and M.J. Kaufman, *The effects of Mn on the microstructure and mechanical properties of Al-Si-Cu casting alloys*. *Materials Science & Engineering A*, 2008. **488**: p. 496-504.
65. Cáceres, C.H., et al., *The effect of Cu content on the level of microporosity in Al-Si-Cu-Mg casting alloys*. *Scripta Materialia*, 1999. **40**(5): p. 631-637.
66. ASM, *Metals Handbook Ninth Edition: Casting*. Vol. 15. 1988: ASM International.
67. Moustafa, M.A., *Effect of iron content on the formation of  $\beta$ -Al<sub>5</sub>FeSi and porosity in Al-Si eutectic alloys*. *Journal of Materials Processing Technology*, 2009. **209**(1): p. 605-610.
68. Belov, N.A., A.A. Aksenov, and D.G. Eskin, *Iron in Aluminum Alloys*. Vol. 1. 2002: CRC.
69. Ma, Z., et al., *A study of tensile properties in Al-Si-Cu and Al-Si-Mg alloys: Effect of  $\beta$ -iron intermetallics and porosity*. *Materials Science & Engineering A*, 2008. **490**: p. 36-51.
70. Otte, M.O., et al., *Controlling Porosity-Related Casting Rejects: Understanding the Role of Iron in Al-Si alloys*. *AFS Transactions*, 1999. **107**: p. 471-478.
71. Yi, J.Z., et al., *Effect of Fe-content on fatigue crack initiation and propagation in a cast aluminium-silicon alloy (A356-T6)*. *Materials Science & Engineering A*, 2004. **386**: p. 396-407.
72. Nogita, K., M.S. D, and A.K. Dahle, *Modification of Al-Si alloys*. *Materials Forum*, 2004. **28**: p. 945-950.
73. Corbit, S.A. and R.D. Gupta, *Squeeze Cast Automotive Applications and Squeeze Cast Aluminum Alloy Properties*. SAE, 1999. **1999-01-0343**: p. 1-9.
74. Thalmair, S., *Thermomechanische Ermüdung von Aluminium-Silizium-Gusslegierungen unter ottomotorischen Beanspruchungen*. *Dissertation*. 2009: Universität Karlsruhe.
75. DasGupta, R. and D. Killingsworth, *Automotive Applications Using Advanced Aluminum Die Casting Processes*. SAE, 2000. **2000-01-0678**: p. 39-53.
76. Guirao Blank, A., *Standard cast procedures for aluminium cylinder heads*. *Private Communication*. 2010: Wolfsburg.

77. Wang, Q.G., D. Apelian, and D.A. Lados, *Fatigue behaviour of A356/ 357 aluminium cast alloys. Part II - Effect of microstructural constituents*. Journal of Light Metals, 2001. **1**: p. 85-97.
78. Wang, Q.G., D. Apelian, and J.R. Griffiths. *Microstructural Effects on the Fatigue Properties of Aluminium Castings*. in *Materials Solutions Conference on Aluminium Casting Technology*. 1998.
79. Han, Y.S., *Effect of intermetallic Phases on the Mechanical Properties of Cast A356 Alloy Wheels*. IEEEExplore.
80. Garcíá-García, G., J. Espinoza-Cuadra, and H. Mancha-Molinar, *Copper content and cooling rate effects over second phase particles behaviour in industrial aluminium-silicon alloy 319*. Materials & Design, 2007. **28**: p. 428-433.
81. Flemings, M.C., T.Z. Kattamis, and B.P. Bardes, *Dendrite Arm Spacing in Aluminum Alloys*. AFS Transactions, 1991. **99**: p. 501-506.
82. Djurdjevic, M. and J. Pavlovic, *The impact of Major Alloying elements and Refiner on the SDAS of Al-Si-Cu Alloy*. Practical Metallography, 2009. **46**: p. 97-114.
83. Beck, T., *Isothermes und thermo-mechanisches Ermüdungsverhalten von Al<sub>2</sub>O<sub>3</sub> (Saffil) kurzfaserverstärkten Aluminium Gusslegierungen für Verbrennungsmotoren. Technical Report. No. 620*. 1998, Forschungsvereinigung Verbrennungsmotoren Karlsruhe. p. 1-252.
84. Ares, A.E., et al., *Dendrite spacing in Al-Cu and Al-Si alloys as function of growth parameters*. Light Metals, 2002: p. 785-792.
85. Gottstein, G., ed. *Physikalische Grundlagen der Materialkunde*. Vol. 3. 2007, Springer: Aachen.
86. Schatt, W. and H. Worch, *Werkstoffwissenschaft*. Vol. 9. 2007, Dresden: WILEY-VCH.
87. Kubo, K. and R.D. Pehlke, *Porosity Formation in Solidifying Castings*. AFS Transactions, 1986. **94**: p. 753-756.
88. Samuel, A.M. and F.H. Samuel, *Porosity Factor in Quality Aluminum Castings*. AFS Transactions, 1992. **100**: p. 657-666.
89. Gao, Y.X., P.D. Lee, and H.M. Flower, *Scatter in fatigue life due to effects of porosity in cast A356-T6 aluminium alloys*. Metallurgical and Materials Transactions A, 2003. **34**: p. 1879-1890.
90. Gao, X.Y., et al., *The effect of porosity on the fatigue life of cast aluminium-silicon alloys*. Fatigue Fracture Eng. Mater. Struct., 2004. **27**: p. 559-570.
91. Ammar, H.R., A.M. Samuel, and F.H. Samuel, *Effect of casting imperfections on the fatigue life of 319-F and A356-T6 Al-Si casting alloys*. Materials Science & Engineering A, 2008. **473**: p. 65-75.

92. Bangyikhan, K., *Effects of Oxide film, Fe-rich phase, Porosity and their Interactions on Tensile Properties of Cast Al-Si-Mg Alloys*. PhD thesis, in *School of Metallurgy and Materials*. 2005: University of Birmingham.
93. Ikuno, H., S. Iwanaga, and Y. Awano, *Effect of porosity on thermal fatigue lives of AC2B aluminum alloy castings*. 1995. **45**(11): p. 671-676.
94. Paray, F. and J.E. Gruzleski, *Microstructure - mechanical property relationships in a 356 alloy. Part II: Mechanical properties*. *Cast Metals*, 1994. **7**(3): p. 153-163.
95. Brunner, R.W., *Fracture-Positive identification of Internal Defects in Aluminum Castings*. *AFS Transactions*, 1981. **89**: p. 627-632.
96. Hetke, A. and R.B. Gundlach, *Aluminum Casting Quality in Alloy 356 Engine Components*. *AFS Transactions*: p. 367-380.
97. Sigworth, G.K., et al., *Porosity formation in modified and unmodified Al-Si alloy castings*. *AFS Transactions*, 1994. **102**: p. 245-261.
98. Boileau, J.M. and J.E. Allison, *The Effect of Porosity Size on the Fatigue Properties in a Cast 319 Aluminum Alloy*, in *Developments in Lightweight Aluminum Alloys for Automotive Applications*, J.M. Boileau, Editor. 2001, SAE. p. 437-448.
99. Vinarcik, E.J., *Understanding Defects in High Integrity Die Castings*. SAE, 2003. **2003-01-0824**.
100. Fang, Q.T. and D.A. Granger, *Porosity Formation in Modified and Unmodified A356 Alloy Castings* *AFS Transactions*, 1989. **97**: p. 989-1000.
101. Argo, D. and J.E. Gruzleski, *Porosity in Modified Aluminum Alloy Castings*. *AFS Transactions*, 1988. **96**: p. 65-74.
102. Ting, J.C. and F.V. Lawrence, *Modelling the Long-Life Fatigue Behavior of a Cast Aluminum Alloy*. *Fatigue Fracture Eng. Mater. Struct.*, 1993. **16**(6): p. 631-647.
103. Rading, G.O., J. Li, and J.T. Berry, *Fatigue Crack Growth in Cast Al-Cu Alloy A206 With Different Levels of Porosity*. *AFS Transactions*, 1994. **102**: p. 57-61.
104. Major, J.F., *Porosity Control and Fatigue Behavior in A356-T61 Aluminum Alloy*. *AFS Transactions*, 1997. **105**: p. 901-906.
105. Wang, Q.G., D. Apelian, and D.A. Lados, *Fatigue behaviour of A356-T6 aluminum cast alloys. Part I. Effect of casting defects*. *Journal of Light Metals*, 2001. **1**: p. 73-84.
106. Yi, J.Z., et al., *Microstructure-Based Fatigue Life Prediction for Cast A356-T6 Aluminium-Silicon Alloys*. *Metallurgical and Materials Transactions B*, 2006. **37**: p. 301-311.

107. Ammar, H.R., A.M. Samuel, and F.H. Samuel, *Porosity and the fatigue behaviour of hypoeutectic and hypereutectic aluminium-silicon casting alloys*. International Journal of Fatigue, 2008. **30**: p. 1024-1035.
108. Arami, H., et al., *Microporosity control and thermal-fatigue resistance of A319 aluminium foundry alloy*. Materials Science & Engineering A, 2008. **472**: p. 107-114.
109. Lee, M.H., et al., *Effects of HIPing on high-cycle fatigue properties of investment cast A356 aluminum alloys*. Materials Science & Engineering A, 2003. **340**: p. 123-129.
110. Lei, C.S.C., W.E. Frazier, and E.W. Lee, *The Effect of Hot Isostatic Pressing on Cast Aluminum*. JOM, 1997. **Research Summary**: p. 38-39.
111. Chama, C.C., *Elimination of Porosity from Aluminum-Silicon Castings by Hot Isostatic Pressing*. Journal of Materials Engineering and Performance, 1992. **1**(5): p. 773-780.
112. Ceschini, L., A. Morri, and G. Sambogna, *The effect of hot isostatic pressing on the fatigue behaviour of sand-cast A356-T6 and A204-T6 aluminum alloys*. Journal of Materials Processing Technology, 2008. **204**: p. 231-238.
113. Staley, J.T.J., M. Tiryakioglu, and J. Campbell, *The effect of hot isostatic pressing (HIP) on the fatigue life of A206-T71 aluminum castings*. Materials Science & Engineering A, 2007. **465**: p. 136-145.
114. Gubicza, J., et al., *Microstructure and yield strength of ultrafine grained aluminum processed by hot isostatic pressing*. Materials Science & Engineering A, 2007. **458**: p. 385-390.
115. Zhang, B., D.R. Poirier, and W. Chen, *Die Wirkung des HIPens und der Strontiumveredelung auf das Ermüdungsverhalten der Aluminiumlegierung A356.2*. Giesserei-Praxis, 2003. **5**: p. 183-190.
116. Boileau, J.M. and J.E. Allison, *The Effect of Solidification Time and Heat Treatment on the Fatigue Properties of a Cast 319 Aluminum Alloy*. Metallurgical and Materials Transactions A, 2003. **34**: p. 1807-1820.
117. Skrinsky, Y., *Einfluss von heiß- und kaltisostatischem Pressen auf die "statischen" mechanischen Werkstoffkennwerte von Gussteilen aus Aluminiumlegierungen*. Dissertation. 2002: Otto von Guericke Universität Magdeburg.
118. Meyers, C.W. and J.S. Chou, *Experimental Investigations of Deformation in HIPed A356 Aluminum Castings*. AFS Transactions, 1991. **99**: p. 175-186.
119. Zulfia, A., et al., *Effect of hot isostatic pressing on cast A357 aluminium alloy with and without SiC particle reinforcement*. Journal of Materials Science, 1999. **34**: p. 4305-4310.



120. Chama, C.C., *Mechanical Properties of Hot Isostatic Pressed Aluminium-Silicon Castings*. Scripta Metallurgica et Materialia, 1992. **26**: p. 1153-1156.
121. Ermel, D., *Isostatisches Pressen und seine Anwendungsmöglichkeiten, Teil II*. Fachberichte für Metallverarbeitung, 1983. **60**(11-12): p. 497-502.
122. Gilman, P.S. and G.H. Gessinger, *A Method for the Experimental Determination of the Effective Stress in Hot Pressing*.
123. Wakefield, G.R. and R.M. Sharp, *Fatigue properties of hot isostatically pressed Al-10Mg castings*. Materials Science and Technology, 1992. **8**: p. 1125-1129.
124. Mocarski, S.J., G.V. Scarich, and K.C. Wu, *Effect of Hot Isostatic Pressure on Cast Aluminum Airframe Components*. AFS Transactions: p. 77-81.
125. Rooy, E.L., *Hot Isostatic Process*. AFS Transactions: p. 607-612.
126. Widmer, R. and W. Petch, *Present and Future of Casting Densification by Hot Isostatic Pressing*. AFS Transactions, 1983: p. 523-526.
127. Diem, M., W. Graf, and R. Hardt, *Nachbehandlung von Aluminium-Gussteilen*. Giesserei-Praxis, 2004. **91**(11): p. 99-102.
128. Gallo, S., *Liquid Hot Isostatic Pressing Process*. Metallurgical Science and Technology, 2001. **19**(1): p. 1-2.
129. Chandley, D., *Origin of the Liquid Hot Isostatic Pressing Process*. Metallurgical Science and Technology, 2001. **19**(1): p. 3-5.
130. Beghi, M.E., et al., *Microstructural effect of the L.H.I.P. Process on the A356 Aluminium Alloy*. Metallurgical Science and Technology, 2001. **19**(1): p. 6-11.
131. Cabibbo, M. and E. Evangelista, *Microstructural effect of the L.H.I.P. Process on the A356 Aluminium Alloy*. Metallurgical Science and Technology, 2001. **19**(1): p. 12-15.
132. Beghi, M.E., et al., *Microstructural and Mechanical effects of Liquid Hot Isostatic Pressing on AA356 samples I*. Metallurgical Science and Technology, 2001. **19**(1): p. 6-11.
133. Gallo, S., C. Mus, and G. Mortari, *Reasons to develop Liquid Hot Isostatic Pressing*. Metallurgical Science and Technology, 2001. **19**(1): p. 16-20.
134. Romano, E., M. Rosso, and C. Mus, *The effect of Liquid Hot Isostatic Pressing on Fatigue Properties of Al based Castings*. Metallurgical Science and Technology, 2001. **19**(1): p. 21-27.
135. Rosso, M., E. Romano, and S. Barone, *Properties Improvement of Thixoformed parts by Liquid Hot Isostatic Pressing Process*. Metallurgical Science and Technology, 2001. **19**(1): p. 28-34.

136. Antona, P.L. and C. Mapelli, *Hot Isostatic Pressing (HIP): The state of the art & improvement on two steels*. Metallurgical Science and Technology, 2001. **19(2)**: p. 3-7.
137. Mikkola, P.H. and J.A. Redemske, *Optimizing Properties of Automotive Cylinder Heads Cast of Aluminum*. SAE, 1994. **940153**: p. 1-5.
138. Mashl, S.J., et al., *Hot Isostatic Pressing of A356 and 380/383 Aluminum Alloys: An Evaluation of Porosity, Fatigue Properties and Processing*. SAE, 2000. **2000-01-062**: p. 1-6.
139. Scarich, G.V., *Hot Isostatic Pressing of Aluminum Castings*, in *28th National SAMPE Symposium*. 1983, SAMPE: Hawthorne p. 1329-1333.
140. Hanes, H.D., *Hot Isostatic Pressing of Premium Quality Castings*, in *12th National SAMPE Technical Conference* 1980, SAMPE: Dublin, Ohio. p. 1074-1084.
141. Highberger, W.T., G.V. Scarich, and G.R. Chanani, *Advanced Aluminum Metallic Materials and Processes for Application to Naval Aircraft Structures*, in *12th SAMPE Technical Conference*. 1980, SAMPE. p. 554-562.
142. Franetovic, V., R.C. Lints, and J.T. Carter, *Fracture process in semi-solid-formed Al-7% Si based alloys*. Aluminium 2003. 2003: The Minerals, Metals & Materials Society.
143. Henne, I., *Schädigungsverhalten von Aluminiumgusslegierungen bei TMF und TMF/HCF-Beanspruchung. Dissertation*. 2006: Universität Karlsruhe.
144. Association, E.A., *Precipitation hardening*. 1999, TALAT.
145. ASM, *Metals Handbook : Fatigue and Fracture*. Vol. 19. 1996: ASM International.
146. Schneider, W. and F.J. Feikus, *Wärmebehandlung von Aluminium-Gusslegierungen für das Vakuum-Druckgießen*. Giesserei-Praxis, 1996. **83**: p. 21-24.
147. Tillová, E. and M. Panusková, *Effect of solution treatment on intermetallic phases morphology in AlSi9Cu3 cast alloys*. Metallurgija, 2008. **47**: p. 207-210.
148. Chepko, C., et al., *An Experimental and Analytical Study of the Properties of Precipitation Hardening Aluminium Alloys*, in *Research Report*. 2000.
149. Schneider, W. and F.J. Feikus, *Wärmebehandlung von Aluminium-Gusslegierungen für das Vakuum-Druckgießen*. Giesserei-Praxis, 1996. **83(IV)**: p. 23-27.
150. Ratke, L. and P.W. Voorhees, *Growth and Coarsening - Ostwald Ripening in Material Processing*. 2001: Springer.

151. Ringer, S.P. and K. Hono, *Microstructural Evolution and Age Hardening in Aluminium Alloys: Atom Probe Field-Ion Microscopy and Transmission Electron Microscopy Studies*. Materials Characterization, 2000. **44**: p. 101-131.
152. Apelian, D., S. Shivkumar, and G.K. Sigworth, *Fundamental Aspects of Heat Treatment of Cast Al-Si-Mg Alloys*. AFS Transactions, 1989. **89-137**: p. 727-741.
153. Visser, R., et al., *The crystal structure of the  $\beta'$  phase of Al-Mg-Si alloys*. Acta Materialia, 2007. **55**: p. 3815-3823.
154. Andersen, S.J., et al., *The crystal structure of the  $\beta''$  phase in Al-Mg-Si alloys*. Acta Materialia, 1998. **46**(9): p. 3283-3298.
155. EAA, E.A.A., *Precipitation hardening*. 1999, TALAT.
156. ASM, *Metals Handbook Ninth Edition: Heat Treating*. Vol. 4. 1981: ASM International.
157. Firouzdor, V., et al., *Effect of microstructural constituents on the thermal fatigue life of A 319 aluminum alloy*. Materials Science & Engineering A, 2007. **454-455**: p. 528-535.
158. Caton, M.J., J.W. Jones, and J.E. Allison, *The influence of heat treatment and solidification time on the behavior of small-fatigue-cracks in a cast aluminium alloy*. Materials Science & Engineering A, 2001. **314**: p. 81-85.
159. Shercliff, H.R. and M.F. Ashby, *A process model for age hardening of Aluminium Alloys - I. The Model*. Acta Metallurgica et Materialia, 1990. **38**(10): p. 1789-1802.
160. Shercliff, H.R. and M.F. Ashby, *A process model for age hardening of Aluminium Alloys - II. Applications of the Model*. Acta Metallurgica et Materialia, 1990. **38**(10): p. 1803-1812.
161. Boussac, O. and T. Callais, *Influence du Vieillissement Thermique sur les Caractéristiques Mécaniques à Température Ambiante de l'AS7G03 Y39*. Rapport Interne PSA, 1998.
162. Thomas, J.J., et al., *Thermomechanical design in the automotive industry*. Fatigue Fracture Eng. Mater. Struct., 2003. **27**: p. 887-895.
163. Hesse, W., *Aluminium Material Data Sheets*. Vol. 5. 2007: Aluminium Verlag.
164. Hunsicker, H., *Aluminum*, ASM. p. 58-59.
165. Rincón, E., et al., *Effect of temperature on the tensile properties of an as-cast aluminum alloy A319*. Materials Science & Engineering A, 2007. **452-453**: p. 682-687.
166. Schneider, W. and F.J. Feikus, *Wärmebehandlung von Aluminium-Gusslegierungen für das Vakuum-Druckgießen*. Aluminium, 1996. **83**(9): p. 17-22.

167. Tillová, E., M. Panusková, and M. Chalupová, *Metallographische Analyse von Al-Si-Cu Gusslegierungen*. Druckgusspraxis, 2007. **3**: p. 108-111.
168. Seifeddine, S., S. Johansson, and I.L. Svensson, *The influence of cooling rate and manganese content on the  $\beta$ -Al<sub>5</sub>FeSi phase formation and mechanical properties of Al-Si-based alloys*. Materials Science & Engineering A, 2008. **490**: p. 385-390.
169. Meyer, P., D. Massinon, and P. Guerin, *Influence of Microstructure on the Static and Thermal fatigue Properties of 319 Alloys*. SAE, 1997. **970705**: p. 1-8.
170. Döpp, R., H. Wendt, and H.H. Becker, *Beitrag zum Einfluss von Zink und Magnesium auf die gießtechnischen und mechanischen Eigenschaften der Druckgusslegierung GD-AlSi<sub>9</sub>Cu<sub>3</sub> (226)*. Materials & Design, 1996. **18**(4/6): p. 345-347.
171. Zak, H., B. Tonn, and M. Hampl, *Häufig verwendete Al-Si-Sekundärlegierungen*. Giesserei-Praxis, 2008. **5**: p. 167-173.
172. Sarkar, J., et al., *Tensile properties and bendability of T4 treated AA6111 aluminum alloys*. Materials Science and Engineering A, 2004. **369**: p. 258-456.
173. Schneider, W. and F.J. Feikus, *Wärmebehandlung von Aluminium-Gusslegierungen für das Vakuum-Druckgießen*. Aluminium, 1996. **83**(15): p. 17-22.
174. Król, J., *Structure and mechanical properties of age-hardened directionally solidified AlSiCu alloys*. Materials & Design, 1997. **18**(4/6): p. 345-347.
175. Cavaliere, P., E. Cerri, and P. Leo, *Effect of heat treatments on mechanical properties and damage evolution of thixoformed aluminium alloys*. Materials Characterization, 2005. **55**: p. 35-42.
176. Timelli, G., et al., *Effect of Solution Heat Treatments on the Microstructure and Mechanical Properties of a Die-Cast AlSi<sub>7</sub>MgMn Alloy*. Metallurgical and Materials Transactions A, 2008. **39**: p. 1747-1758.
177. Rincón, E., et al., *Temperature Effects on the Tensile Properties of Cast and Heat treated Aluminium Alloy A319*. Materials Science & Engineering A, 2009. **519**: p. 128-140.
178. Caceres, C.H. and J.R. Griffiths, *Damage by the cracking of silicon particles in an Al-7Si-0.4Mg casting alloy*. Acta Metallurgica, 1996. **44**(1): p. 25-33.
179. Dehler, A., et al., *Assessment of creep behaviour of the die-cast cylinder head alloy AlSi<sub>6</sub>Cu<sub>4</sub>-T6*. International Journal of Materials Research, 2006. **97**: p. 1679-1686.
180. Thevenet, D., M. Mliha-Touati, and A. Zeghloul, *Characteristics of the propagating deformation bands associated with the Portevin-Le Chatelier effect in an Al-Szn-Mg-Cu alloy*. Materials Science & Engineering A, 2000. **291**(1-2): p. 110-117.

181. Chen, J.-Z., et al., *Portevin-Le Chatelier effect in an Al-Zn-Mg-Cu-Zr aluminum alloy*. Transactions of Nonferrous Metals Society of China, 2009. **19**(5): p. 1071-1075.
182. Louche, H., P. Vacher, and R. Arrieux, *Thermal observations associated with the Portevin-Le Chatelier effect in an Al-Mg alloy*. Materials Science & Engineering A, 2005. **404**(1-2): p. 188-196.
183. Li, D.M. and A. Bakker, *Strain rate dependence of flow and fracture behavior for a rapidly solidified Al alloy*. Scripta Metallurgica et Materialia, 1994. **30**: p. 1171-1176.
184. Inagaki, A., T. Komatsubara, and H. Inagaki, *Effect of Strain Rate and Temperature of Tensile Test on Lüders Strain in Al-Mg Alloys*. Zeitschrift für Metallkunde, 1999. **90**(6): p. 427-422.
185. Kim, I.S. and C. Chaturvedi, *Serrated Flow in Al-5 wt.% Mg*. Materials Science & Engineering A, 1969. **37**: p. 165-172.
186. McCormick, P.G., *Effect of Grain Size on Serrated Yielding in an Al-Mg-Si Alloy*. Phil. Mag., 1971. **A23**(183): p. 949-956.
187. McCormick, P.G., *The Portevin-Le Chatelier Effect in an Al-Mg-Si Alloy*. Acta Metallurgica, 1971. **19**: p. 463-471.
188. Chan, K.S., T.S. Lui, and L.H. Chen, *Portevin-Le Chatelier Effect of A356 Al Cast Alloy: General Features and Effect of Natural Aging*. AFS Transactions, 1994. **102**: p. 147-150.
189. Harun, H.J. and P.G. McCormick, *Effect of Precipitation Hardening on Strain Rate Sensitivity and Yield Behaviour in an Al-Mg-Si Alloy*. Acta Metallurgica, 1979. **27**: p. 155-159.
190. Odqvist, F.K.G., *Mathematical Theory of Creep and Creep Rupture*. 1974: Oxford
191. Stoeckl, Q.S., *Creep behaviour of cast AlSi6Cu4-T6 with high creep rates*, in *LWM*. 2010, University of Applied Sciences Regensburg.
192. Ashby, M.F., *Strengthening Methods in Metals and Alloys*, in *The Microstructure and Design of Alloys*. 1973: Cambridge. p. 8-42.
193. Ashby, M.F. and D.R.H. Jones, *Engineering Materials 1*. 1991, Oxford: Pergamon
194. Moalla, M., *Isothermes und thermisch-mechanisches Ermüdungsverhalten bei überlagerten LCF/ HCF-Beanspruchungen sowie isothermes Ermüdungsrisssausbreitungsverhalten von NiCr22Co12Mo9 und CoCr22Ni22W14*. Dissertation. 2001: Universität Karlsruhe. p. 1-179.

195. Merckling, G., *Kriech- und Ermüdungsverhalten ausgewählter metallischer Werkstoffe bei höheren Temperaturen*. Dissertation. 1989: Universität Karlsruhe.
196. Kleinpaß, B., *Mikrostrukturen und Schädigung bei NiCr22Co12Mo9 unter thermisch-mechanischer Wechselbeanspruchung*. Dissertation. 1996, Universität Karlsruhe: Karlsruhe. p. 1-196.
197. Krupp, U., *Fatigue Crack Propagation in Metals and Alloys*. 2007: Wiley-VCH.
198. Bürgel, R., *Handbuch Hochtemperatur-Werkstofftechnik*. 2006: Vieweg.
199. Sandström, R., *Creep rupture data for aluminium alloys*. Aluminium, 1993. **69**: p. 2-11.
200. Sandström, R., *Creep rupture strengths up to 100000hours for aluminium alloys*. Aluminium, 1996. **72**: p. 910-917.
201. Chang, C.C. and Q.G. Wang, *Modeling of Bolt Joint Behavior of Cast Aluminum Alloy (A380-T5) by Creep and Plasticity in Finite Element Analysis*. Metallurgical and Materials Transactions B, 2007. **38**: p. 607-613.
202. Jaglinski, T. and R. Lakes, *Creep Behavior of Al-Si Die Cast Alloys*. Transactions of the ASME, 2004. **126**: p. 378-383.
203. Djakovic, A., B.F. Dyson, and M. McLean, *Damage identification in creep of aluminium alloy 2650-T8*. Association of Metallurgical Engineers Serbia and Montenegro: p. 243-250.
204. Requena, G.C., et al., *Microtomographic study of the evolution of microstructure during creep of an AlSi12CuMgNi alloy reinforced with Al<sub>2</sub>O<sub>3</sub> short fibres*. Materials Science & Engineering A, 2008. **487**: p. 99-107.
205. Taleff, E.M., et al. *Creep Fracture during Solute-Drag Creep and Superplastic Deformation*. in *The Minerals, Metals and Materials Society Annual Meeting*. 1997.
206. Ma, Z., et al., *Einfluss des Eisengehalts und der Abkühlgeschwindigkeit auf die Zugfestigkeitseigenschaften von G-AlSi6Cu4-Legierungen im unveredelten Zustand*. Giesserei-Praxis, 2006. **5**: p. 131-138.
207. Sandström, R., *Creep rupture data for aluminium alloys, part I*. Aluminium, 1993. **69**(3): p. 263-268.
208. Holecek, S., K. Stetina, and M. Ruda, *Zur Frage der mechanisch-thermischen Belastbarkeit von Kolbengusslegierungen der Gattung AlSiCu*. Aluminium, 1982. **58**: p. 597-599.
209. Nakajima, T., M. Takeda, and T. Endo, *Accelerated coarsening of precipitates in crept Al-Cu alloys*. Materials Science & Engineering A, 2004. **387-389**: p. 670-673.

210. Luft, J., *Thermisch-mechanische und überlagerte thermisch-mechanische/mechanische Ermüdungsbeanspruchung der Zylinderkopfflegierungen AlSi7Mg und AlSi5Cu3*. Dissertation. 2007, Universität Karlsruhe.
211. Löhe, D., *Thermische Ermüdung*, in *25. Vortragsveranstaltung des DVM-Arbeitskreises Bruchvorgänge*. 1993, DVM. p. 33-48.
212. Radaj, D. and M. Vormwald, *Ermüdungsfestigkeit*. Vol. III. 2007: Springer.
213. Engler-Pinto, C.C., et al., *A Comparative Investigation on the High Temperature Fatigue of Three Cast Aluminum Alloys*. SAE, 2004. **2004-01-1029**: p. 1-6.
214. Rie, K.-T. and R.-M. Schmidt, *Low-Cycle Fatigue (Kurzzeitermüdung) unter besonderer Berücksichtigung der Temperatur und des Umgebungsmediums*, in *Ermüdungsverhalten metallischer Werkstoffe*, D. Munz, Editor. 1984, Deutsche Gesellschaft für Metallkunde: Karlsruhe. p. 397-418.
215. Christ, H.J., *Wechselverformung von Metallen*. 1991: Springer.
216. Mughrabi, H., *Dislocations in Fatigue*. Dislocation and Properties of real Materials. Vol. 323. 1985, London: The Institute of Metals 244-261.
217. Löhe, D., T. Beck, and K.-H. Lang, *Important aspects of cyclic deformation, damage and lifetime behaviour in thermomechanical fatigue of engineering alloys*, in *Fifth International Conference on Low Cycle Fatigue*, P.D. Portella, H. Sehitoglu, and K. Hatanaka, Editors. 2004: Berlin. p. 161-175.
218. Christ, H.J., *Effect of environment on Thermomechanical life*. Materials Science & Engineering A, 2007. **468-470**: p. 98-108.
219. Nitta, A. and K. Kuwabara, *Thermal-Mechanical Fatigue Failure and Life Prediction*. Current Japanes Materials Research, 1988. **3**: p. 203-222.
220. Kuwabara, K., A. Nitta, and T. Kitamura, *Thermal-mechanical fatigue life prediction in high-temperature component materials for power plant*, in *International Conference on Advances in Life Prediction Methods*. 1983. p. 131-141.
221. Smith, T.J., et al., *Modelling High-Temperature Stress-Strain Behavior of Cast Aluminum Alloys*. Metallurgical and Materials Transactions A, 1999. **30**: p. 133-146.
222. Smith, T.J., et al., *The influence of SDAS on the TMF response of Al 319 alloys*, in *International Conference on Low Cycle Fatigue and Elasto-plastic Behaviour of Materials*, K.T. Rie and P.D. Portelle, Editors. 1998, Elsevier. p. 167-172.
223. Sehitoglu, H., T.J. Smith, and H.J. Maier, *Thermo-mechanical Deformation of Al 319-T7B with Small Secondary Dendrite Arm Spacing*, in *Thermo-mechanical Fatigue Behavior of Materials*, H. Sehitoglu, Editor. 2003, ASTM. p. 53-68.

224. Engler-Pinto, C.C., H. Sehitoglu, and H.J. Maier, *Cyclic Behavior of Al 319-T7B under Isothermal and Nonsiothermal Conditions*, in *Thermo-mechanical Fatigue Behavior of Materials*, H. Sehitoglu, Editor. 2006, ASTM. p. 45-64.
225. Sehitoglu, H., C.C. Engler-Pinto, and T. Foglesong, *Thermo-mechanical deformation of Al 319 alloys with different iron contents*, H. Sehitoglu, Editor. 2002, ASM. p. 77-83.
226. Bose-Filho, W.W., et al., *Al-Si cast alloys under isothermal and thermomechanical fatigue conditions*. International Journal of Fatigue, 2007. **29**: p. 1846-1854.
227. Kaneso, M., et al., *Influence of Microstructure on Thermomechanical Fatigue Characteristics and Mechanical Properties of Cast AC4CH Aluminum Alloys*. 2008. p. 699-705.
228. Beck, T., I. Henne, and D. Löhle, *Lifetime of cast AlSi6Cu4 under superimposed thermal-mechanical fatigue and high-cycle fatigue loading*. Materials Science & Engineering A, 2008. **483-483**: p. 382-386.
229. Luft, J., T. Beck, and D. Löhle, *Thermal-Mechanical Fatigue Behaviour of the cast Aluminum alloy AlSi7Mg*. 2003: International Conference on Low Cycle Fatigue. p. 219-225.
230. Beck, T., et al., *Damage mechanism of cast Al-Si-Mg alloys under superimposed thermal-mechanical fatigue and high-cycle fatigue loading*. Materials Science & Engineering A, 2007. **468-470**: p. 184-192.
231. Toyoda, M., et al., *Preferential orientation of precipitates during thermomechanical cyclic loading in an aluminium alloy*. Scripta Materialia, 2007. **56**: p. 377-380.
232. Danzer, R., *Lebensdauerprognose hochfester metallischer Werkstoffe im Bereich hoher Temperaturen*. Materialkundliche Technische Reihe. 1988: Gebrüder Borntraeger.
233. Fatemi, A. and L. Yang, *Cumulative fatigue damage and life prediction theories: A survey of the state of the art for homogeneous materials*. International Journal of Fatigue, 1988. **20**(1): p. 9-34.
234. Neu, R.W. and H. Sehitoglu, *Thermomechanical Fatigue, Oxidation, and Creep: Part II. Life Prediction*. Metallurgical and Materials Transactions A, 1989. **20**: p. 1769-1783.
235. Jiang, Y. and H. Sehitoglu, *Modelling of Cyclic Ratchetting Plasticity, Part II: Comparison of Model Simulations with Experiments*. Transactions of the American Society of Mechanical Engineers, 1996. **63**: p. 726-733.
236. Slavik, D. and H. Sehitoglu, *A constitutive Model for High Temperature Loading Part I - Experimentally Based forms of the Equations*. AMD, 1987: p. 65-73.



237. Chaboche, J.L., *A review of some plasticity and viscoplasticity constitutive theories*. International Journal of Plasticity, 2008. **24**: p. 1642-1693.
238. Lemaitre, J. and J.L. Chaboche, *Mechanics of Solid Materials*. 2002: Cambridge University Press.
239. Chaboche, J.L., *Constitutive Equations for Cyclic Plasticity and Cyclic Viscoplasticity*. International Journal of Plasticity, 1989. **5**: p. 247-302.
240. Chaboche, J.L., *Thermodynamic Formulation of Constitutive Equations and Application to the Viscoplasticity and Viscoelasticity of Metals and Polymers*. International Journal of Solids Structures, 1997. **34**(18): p. 2239-2254.
241. Chaboche, J.L., *Cyclic Viscoplastic Constitutive Equations, Part I: A Thermodynamically Consistent Formulation*. Journal of Applied Mechanics, 1993. **60**: p. 813-821.
242. Chaboche, J.L. and G. Cailletaud, *Integration methods for complex plastic constitutive equations*. Computer methods in applied mechanics and engineering, 1996. **133**: p. 125-155.
243. Tong, J., Z.L. Zhan, and B. Vermeulen, *Modelling of cyclic plasticity and viscoplasticity of a nickel-based alloy using Chaboche constitutive equations*. Int. J. of Fatigue, 2004. **26**: p. 829-837.
244. Seifert, T., *Computational methods for fatigue life prediction of high temperature components in combustion engines and exhaust systems*. Dissertation. 2008, Universität Karlsruhe.
245. Birke, B., et al., *Grafische Ermittlung der Werkstoffparameter einer AlSi6Cu4 Legierung unter Berücksichtigung der Schädigung*, C. Kliemt and F. Wilhelm, Editors. 2009, LWM: Regensburg.
246. Rabotnov, Y.N., *Creep Problems in Structural Members*. 1969, Amsterdam: North Holland Publishing.
247. Kachanov, L.M., *On Creep Rupture Time*. Izv. Akad. Nauk. Otd. Tekh. Nauk. **8**: p. 26-31.
248. Chaboche, J.L., *Lifetime Predictions and Cumulative Damage under High-Temperature Conditions*, in *Low Cycle Fatigue and Life Prediction*. 1982.
249. Dendorfer, S., *Cyclic deformation and fatigue behaviour in cancellous bone*. PhD thesis. 2008: Universität Paderborn.
250. Nihei, M., et al., *Damage Parameters for Constant Strain-Controlled Fatigue Data with Several Levels of Mean Strain and Mean Stress*. 1983, TU Darmstadt.
251. Heitmann, H.H., H. Vehoff, and P. Neumann, *Life prediction for random load fatigue based on the growth behaviour of microcracks*. Advances in Fracture Research, 1986: p. 3599-3606.

252. Smith, K.N., P. Watson, and T.H. Topper, *A stress-strain function for the fatigue of metals*. Journal of Materials, 1970. **4**: p. 767-778.
253. Ostergren, W.J., *A damage function and associated failure equations for predicting hold time and frequency effects in elevated temperature, low cycle fatigue*. Journal of Testing and Evaluation, 1976. **4**(5): p. 327-339.
254. Morrow, J.D., *Fatigue Properties of Metals*. Fatigue Design Handbook. 1968: SAE.
255. Bergmann, J.W. and T. Seeger, *On the influence of Cyclic Stress-Strain-Curves, Damage Parameters, and Various Evaluation Concepts on the Life Prediction by the Local Approach*, in *2nd European Colloquium on Fracture*. 1979, VDI-Fortschrittsberichte: Darmstadt.
256. Erdogan, F. and R. Roberts, Trans. American Soc. Mech. Eng., 1967. **D**(89).
257. Hallstein, R., *Das Verhalten von Gusseisenwerkstoffen unter isothermer, thermischer und thermisch-mechanischer Wechselbeanspruchung*. Dissertation. 1991: Universität Karlsruhe.
258. Golos, M., *A total strain energy density model of metal fatigue*. Strength of Materials, 1995. **27**(1-2): p. 53-64.
259. Skelton, R.P., *Energy Criterion for High Temperature Low Cycle Fatigue*. Materials Science and Technology, 1991. **7**: p. 427-439.
260. Bairstow, L., in *Phil. Trans. Roy. Soc.* 1910: London. p. 35.
261. Morrow, J.D. *Cyclic Plastic Strain Energy and Fatigue of Metals*. in *Internal Friction, Damping and Cyclic Plasticity*. 1964. Philadelphia: ASTM.
262. Feltner, C.E. and J.D. Morrow, *Micro-plastic strain hysteresis energy as a criterion for fatigue fracture*. Journal of Basic Engineering 1961. **83**(D): p. 15-22.
263. Riedler, M., et al., *The use of classical damage parameters for a thermomechanical lifetime assessment*, in *Symposium on Experimental Methods in Solid Mechanics*. 2005.
264. Riedler, M., R. Minichmayr, and W. Eichlseder, *Methods for the thermo-mechanical fatigue simulation based on energy criterions*, in *RELMAS*. 2005: St. Petersburg.
265. Park, J.H. and J.H. Song, *Detailed evolution of methods for estimation of fatigue properties*. International Journal of Fatigue, 1995. **17**(5): p. 365-373.
266. Schubert, R., *Verformungsverhalten und Risswachstum bei Low Cycle Fatigue*. 1989: VDI.
267. Lee, K.S. and J.H. Song, *Estimation methods for strain-life fatigue properties from hardness*. International Journal of Fatigue, 2006. **28**: p. 386-400.

268. Hähner, P., et al., *Validated Code of Practice for Strain-Controlled Thermo-Mechanical Fatigue Testing*. 2006, Institute for Energy: Petten. p. 1-36.
269. Guirao Blank, A., *Temperature Gradients in Aluminium Cylinder Heads. Private Communication*. 2010: Wolfsburg. p. 1.
270. Mücklich, F. and J. Ohser, *Statistical Analysis of Microstructures in Materials Science*. Vol. 1. 2000: John Wiley & Sons.
271. Ripley, B.D., *Spatial Statistics*. 1952: John Wiley & Sons.
272. Underwood, E.E., *Quantitative Stereology*. 1970: Addison-Wesley Publishing Company.
273. DeHoff, R. and F.N. Rhines, *Quantitative Microscopy*. 1968: McGraw-Hill Book Company.
274. Russ, J.C. and R.T. Dehoff, *Practical Stereology*. Vol. 2. 2001: Springer.
275. Lifshitz, I. and V. Slyozov, *The Kinetics of Precipitation from Supersaturated Solid Solutions*. J. Phys. Chem. Solids, 1961. **10**: p. 35-50.
276. Eady, J.A. and D.M. Smith, *Properties and Applications of a New Aluminium Foundry Alloy*. SAE, 1985. **840123**: p. 747-755.
277. Ostermeier, M., H. Hoffmann, and E. Werner, *The Effects of Hot Isostatic Pressing on Aluminium Castings*. Key Engineering Materials, 2007.
278. Kobayashi, T., *Strength and fracture of aluminum alloys*. Materials Science and Engineering, 2000. **A 280**: p. 8-16.
279. Crepeau, P.N., W.T. Whited, and M.E. Hoover, *Automatic Assessment of Dendrite Cell Spacing in Cast Aluminum Microstructures*. AFS Transactions, 1997. **105**: p. 775-781.
280. Linder, J., M. Axelsson, and H. Nilsson, *The influence of porosity on the fatigue life for sand and permanent mould cast aluminium*. International Journal of Fatigue, 2006. **28**: p. 1752-1758.
281. Zhang, L.Y., et al., *Effect of cooling rate on solidified microstructure and mechanical properties of aluminium-A356 alloy*. Journal of Materials Processing Technology, 2008. **207**: p. 107-111.
282. Cáceres, C.H., C.J. Davidson, and J.R. Griffiths, *The deformation and fracture behaviour of an Al-Si-Mg casting alloy*. Materials Science and Engineering, 1995. **A 197**: p. 171-179.
283. Stoeckl, Q., A. Roth, and C. Kliemt, *Creep behaviour of cast AlSi6Cu4-T6 in the high temperature regime*. 2010/ 2011, LWM: Regensburg.
284. Engler-Pinto, C.C., et al., *Thermo-Mechanical Fatigue Behaviour of cast 319 Aluminium Alloys*, in *Temperature Fatigue Interaction*. 2002, Elsevier. p. 3-14.

285. Firouzdor, V., et al., *Effect of microstructural constituents on the thermal fatigue life of A319 aluminium alloy*. Materials Science and Engineering A, 2007. **454-455**: p. 528-535.
286. Stanzl-Tschegg, S.E., et al., *Fatigue and fatigue crack propagation in AlSi7Mg cast alloys under in-service loading conditions*. International Journal of Fatigue, 1995. **17**(2): p. 149-155.
287. Gross, J., *Eigenschaften von Aluminium-Silicium-Legierungen in unterschiedlichen Behandlungszuständen unter besonderer Beachtung des Gefügeeinflusses auf die Festigkeitswerte und auf das Bruchverhalten*. 1992: Wissenschaft und Technik.
288. Lados, D.A. and D. Apelian, *Fatigue crack growth characteristics in cast Al-Si-Mg alloys - Part I. Effect of processing conditions and microstructure*. Materials Science & Engineering A, 2004. **385**: p. 200-211.
289. Kobayashi, T., et al., *Fatigue properties and microstructure of Al-Si-Cu system casting alloys*. Materials Science and Technology, 1999. **15**: p. 1037-1043.
290. Lados, D.A. and D. Apelian, *Relationship between microstructure and fatigue crack propagation paths in Al-Si-Mg cast alloys*. Engineering Fracture Mechanics, 2008. **75**: p. 821-832.
291. Wickberg, A., G. Gustafson, and L.E. Larson, *Microstructural effects on the fatigue properties of a cast AlSi7Mg alloy*. SAE, 1984. **840121**(93): p. 728-735.
292. Birke, B., et al., *Grafische Ermittlung der Chaboche-Werkstoffparameter unter Berücksichtigung der Schädigung*. 2009, LWM: Regensburg.
293. Schützner, P., *Computer-unterstützte Untersuchung des Verhaltens kubisch-flächenzentrierter Metalle und Legierungen bei Wechselverformung. Dissertation*. 1974: Universität Stuttgart.
294. Zieher, F. and F. Langmayr, *Engine Simulation in View of reduced Development Time*. **F02V081**: p. 1-11.
295. Neumann, J., M. Oberneder, and C. Kliemt, *FE Modelling of the TMF behaviour of a Cylinder Head Geometry*. 2010, LWM.
296. Mohr, R., *Modellierung des Hochtemperaturverhaltens metallischer Werkstoffe. Dissertation*. 1999: Technische Universität Hamburg-Harburg.
297. Chaboche, J.L., *Constitutive Equations for Cyclic Plasticity and Cyclic Viscoplasticity*. Int. J. of Plasticity, 1989. **5**: p. 247-302.
298. Chaboche, J.L., *Modelling of ratchetting: Evaluation of various approaches*. European Journal of Mechanics, 1994. **13**(4): p. 501-518.
299. Chaboche, J.L., *On some modifications of kinematic hardening to improve the description of ratchetting effects*. International Journal of Plasticity, 1991. **7**: p. 661-678.

300. Chaboche, J.L. and O. Jung, *Application of a kinematic hardening viscoplasticity model with thresholds to the residual stress relaxation*. International Journal of Plasticity, 1998. **13**(10): p. 785-807.
301. Chaboche, J.L. and F. Gallerneau, *An overview of the damage approach of durability modelling at elevated temperature*. Fatigue Fracture Eng. Mater. Struct., 2001. **24**: p. 405-418.
302. Chaboche, J.L. and D. Nouailhas, *A Unified Constitutive Model for Cyclic Viscoplasticity and Its Applications to Various Stainless Steels*. Transactions of the American Society of Mechanical Engineers, 1989. **111**(424-430).
303. Chaboche, J.L. and G. Rousselier, *On the Plastic and Viscoplastic Constitutive Equations - Part: Rules Developed With Internal Variable Concept*. Journal of Pressure Vessel Technology, 1983. **105**(153-158).
304. Mahnken, R., *Improved implementation of an Algorithm for Non-Linear Isotropic/ Kinematic Hardening in Elastoplasticity*. Communications in Numerical Methods in Engineering, 1999. **15**: p. 745-754.
305. Hartmann, S. and P. Haupt, *Stress Computation and consistent tangent Operator using Non-Linear Kinematic Hardening Models*. International Journal for Numerical Methods in Engineering, 1993. **36**: p. 3801-3814.
306. Seifert, T., *Ein komplexes LCF-Versuchsprogramm zur schnellen und günstigen Werkstoffparameteridentifizierung*, in *Fortschritte der Kennwertermittlung für Forschung und Praxis*, M. Borsutzki and S. Geisler, Editors. 2006: Bad Neuenahr.
307. Seifert, T., et al., *Mechanism-based thermomechanical fatigue life prediction of cast iron. Part II: Comparison of model predictions with experiments*. Int. J. of Fatigue, 2009.
308. Seifert, T. and H. Riedel, *Rechnerische Methoden zur Lebensdauervorhersage von gegossenen Hochtemperaturbauteilen*, in *Abaqus User Meeting*. 2008.
309. Streilein, T., *Erfassung formativer Verfestigung in viskoplastischen Stoffmodellen. Dissertation*. 1997: Carolo-Wilhelmina Universität Braunschweig.
310. Tirpitz, E.R., *Elastoplastische Erweiterung von viskoplastischen Stoffmodellen für Metalle - Theorie, Numerik und Anwendung. Dissertation*. 1992: Carolo-Wilhelmina Universität Braunschweig.

## APPENDIX

### A. - USED EQUATIONS AND FORMULAS FOR CHABOCHE MODELLING AND ANSYS

Chaboche model:

$$\dot{\sigma} = (1 - D)E \cdot \left( \dot{\varepsilon} - \dot{\varepsilon}_{pl} \right) \quad (28)$$

$$\dot{\varepsilon}_{pl} = \dot{p} \cdot \text{sgn}(\sigma - X) \quad (29)$$

$$\dot{p} = \left\langle \frac{\frac{1 - X}{1 - D} - \sigma_y - R}{K} \right\rangle^n \quad (30)$$

$$\dot{R} = b(Q_\infty - R) \cdot \dot{p} \quad (31)$$

$$\dot{X} = \gamma \left( C_\infty \dot{\varepsilon}_{pl} - \dot{p} X \right) \quad (32)$$

$$\dot{D} = \left( \frac{Y}{S} \right)^s \dot{p} \quad (33)$$

For optimisations the gradient method of Levenberg Marquardt and the evolution method of Rechenberg are used. Further details of the Chaboche model, parameter determination, implementation and optimisation can be found in [74, 237, 240-242, 244, 296-310].

Ansys:

$$D = 1 - \frac{\sigma_{\max}}{\sigma_{\max 1}} \quad (34)$$

## B. - BACKGROUND MATERIALS AND METHODS

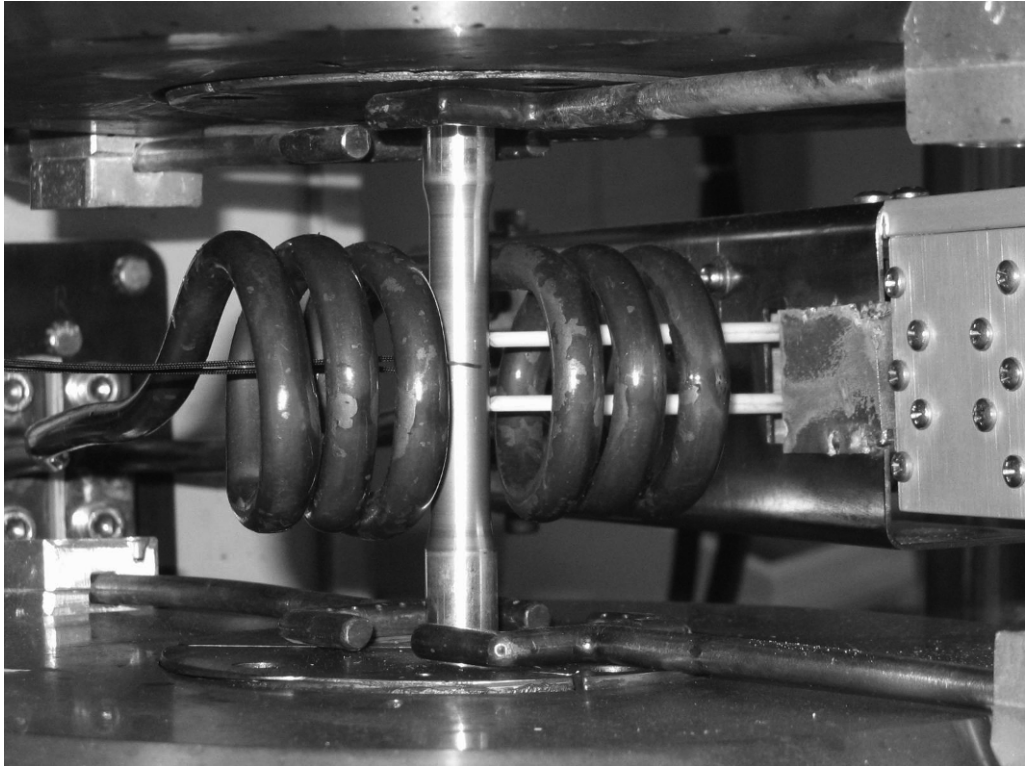


**Figure II.1:** Test rig showing induction coil, specimen, thermocouple and extensometer.

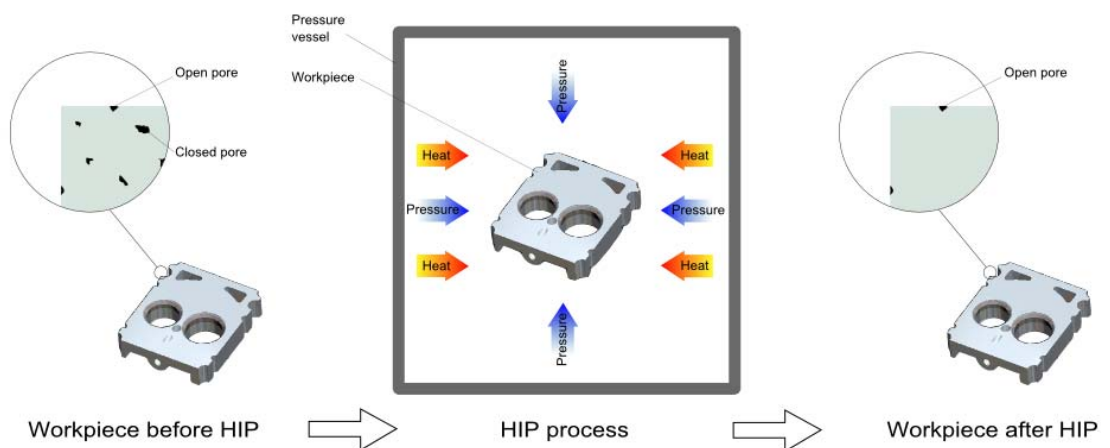


**Figure II.2:** Effect of HIP procedure on a cylinder head.

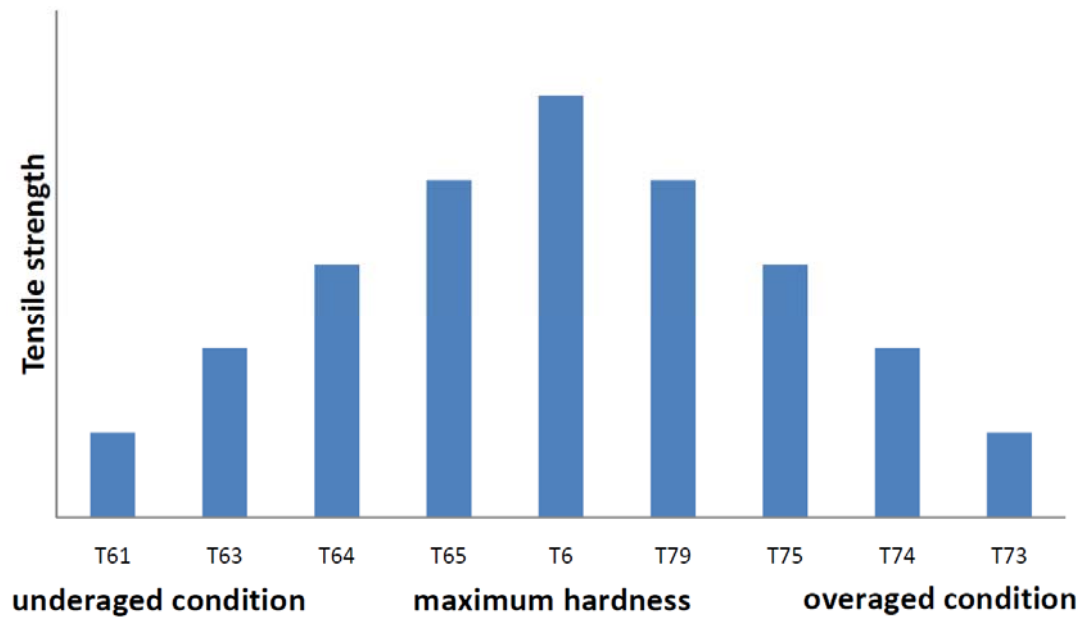


**Figure II.3:** Overview of heat treatments and effects on tensile strength and hardness.



## Used Etchants

**Table II.1:** Overview of used etchants with detailed description of ingredients.

<b>Etchant</b>	<b>Applicability</b>
<ul style="list-style-type: none"> <li>• 1ml HF</li> <li>• 200ml H<sub>2</sub>O</li> </ul>	Examination for identification of constituents
<ul style="list-style-type: none"> <li>• 1g NaOH</li> <li>• 100ml H<sub>2</sub>O</li> </ul>	Macroexamination
<ul style="list-style-type: none"> <li>• 2ml HF</li> <li>• 3ml HCL</li> <li>• 5ml HNO<sub>3</sub></li> <li>• 190ml H<sub>2</sub>O</li> </ul>	Examination for identification of constituents
<ul style="list-style-type: none"> <li>• 5ml HBF<sub>4</sub></li> <li>• 200ml H<sub>2</sub>O</li> </ul>	Examination of grain size and shape, Examination of preferred orientation
<ul style="list-style-type: none"> <li>• 10ml H<sub>3</sub>PO<sub>4</sub></li> <li>• 90ml H<sub>2</sub>O</li> </ul>	Examination for identification of constituents
<ul style="list-style-type: none"> <li>• 50ml Poulton's reagent</li> <li>• 25ml HNO<sub>3</sub></li> <li>• 40ml solution of 3g chromic acid per 10ml of H<sub>2</sub>O</li> </ul>	Examination of grain size and shape, Examination of preferred orientation
<ul style="list-style-type: none"> <li>• 25ml HNO<sub>3</sub></li> <li>• 75ml H<sub>2</sub>O</li> </ul>	Macroexamination, Examination for overageing or poor quench of solution-heat treated alloy
<ul style="list-style-type: none"> <li>• 100ml H<sub>2</sub>O</li> <li>• 2.6 ml HNO<sub>3</sub></li> <li>• 1.6ml HCL</li> <li>• 1ml HF</li> </ul>	Examination for identification of constituents
<ul style="list-style-type: none"> <li>• 20ml H<sub>2</sub>SO<sub>4</sub></li> <li>• 80ml H<sub>2</sub>O</li> </ul>	Examination for identification of constituents
<ul style="list-style-type: none"> <li>• 10g ferrous nitrate</li> <li>• 100ml H<sub>2</sub>O</li> </ul>	Examination for identification of constituents

## C. MICROSTRUCTURAL OBSERVATIONS

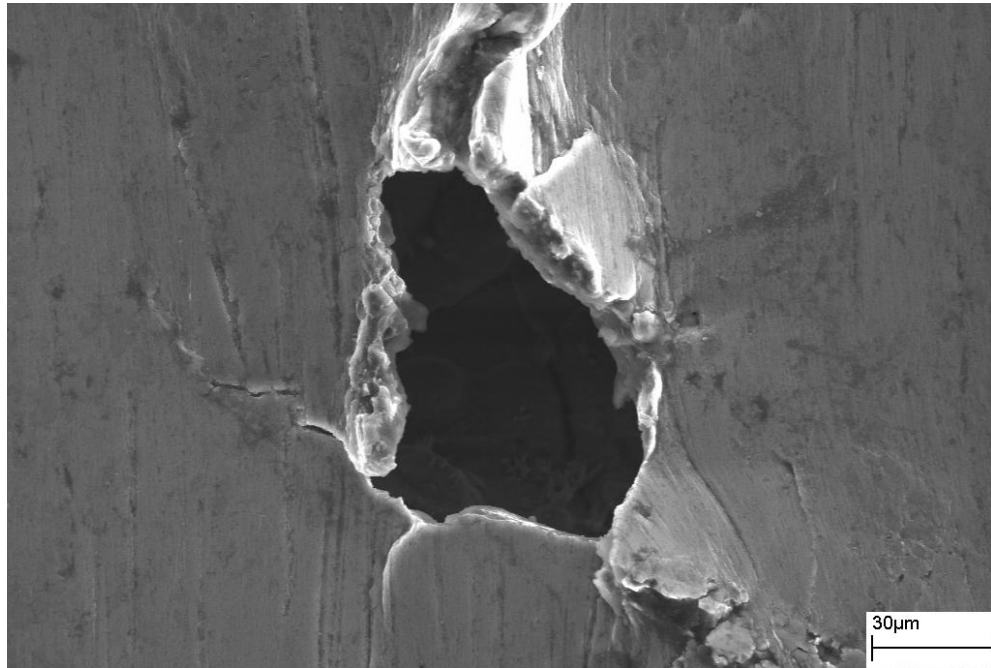


**Figure III.1:** Pore near to the surface of a specimen of cast Al.

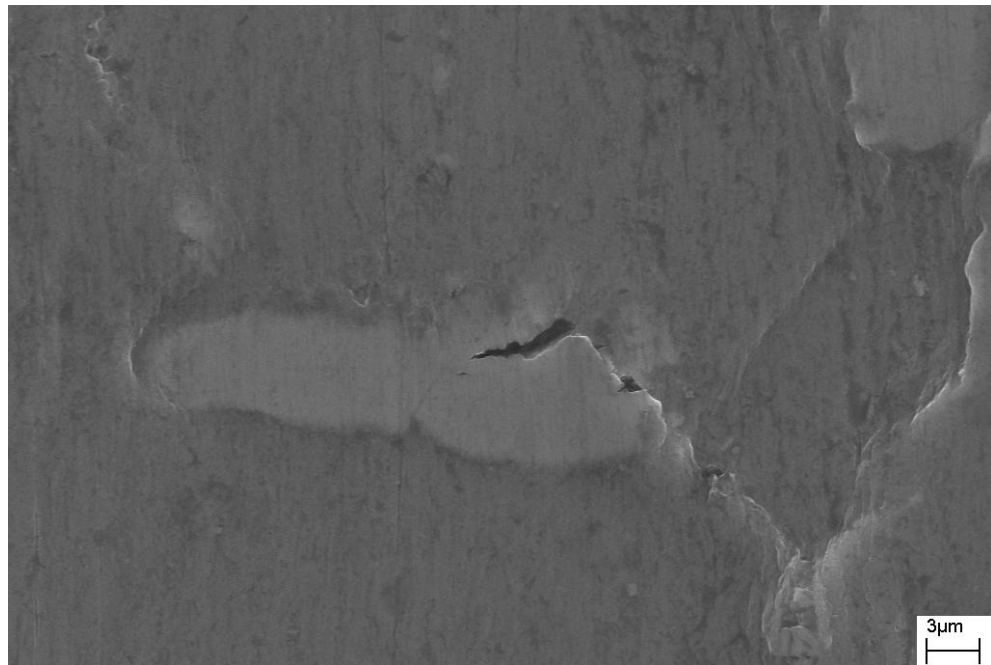


**Figure III.2:** Intermetallic phase on the surface of a specimen with a crack.



**Figure III.3:** Cracks starting from internal voids and pores near to the surface.